Quantum materials explored by neutron scattering

Peter Babkevich

A thesis submitted for the degree of
Doctor of Philosophy

University of Oxford and
Paul Scherrer Institute

Quantum materials explored by neutron scattering

Peter Babkevich
St Hilda's College, University of Oxford and Paul Scherrer Institute
DPhil Thesis, Hilary Term 2012

Abstract

This thesis describes neutron scattering experiments on strongly correlated systems exhibiting a range of emergent phenomena: antiferromagnetism, charge order, superconductivity and multiferroicity. I have examined the La_2CoO_4 compound which is a Mott insulator and orders antiferromagnetically near room temperature. The La_2CoO_4 sample was studied using spherical neutron polarimetry and I present magnetic structure models to describe the two antiferromagnetic phases of the compound. Furthermore, the magnetic fluctuations have been investigated using neutron time-of-flight technique. This has allowed us to extract the dominant exchange interactions in the system. More interestingly, the work on La_2CoO_4 presented in this thesis provides a basis for the experimental evidence of an hourglass dispersion in $La_{5/3}Sr_{1/3}CoO_4$, previously only observed in the copper oxide based superconductors. This dispersion has been understood in terms of a stripe ordered magnetic phase and was found to be well described by a linear spin-wave model.

Neutron scattering experiments were also carried out on the new iron-based high-temperature superconductors, $FeSe_xTe_{1-x}$. A range of compositions were studied, including both antiferromagnetically ordered and superconducting. Below the superconducting phase transition temperature, a spin resonance mode was found centred on the antiferromagnetic wavevector. This is an important feature shared by many unconventional superconductors. The spin resonance intensity was found to reflect the order parameter of the superconducting state. Polarised inelastic neutron scattering experiments have revealed a small anisotropy between the in-plane and out-of-plane magnetic fluctuations at the resonance. This anisotropy cannot be readily explained by the usual anisotropic terms in the Hamiltonian. This could be evidence of new physics in the $FeSe_xTe_{1-x}$ superconductors.

Finally, I have studied CuO – a high-temperature multiferroic. Analysis of polarised neutron diffraction experiments shows that the magnetic domain population can be varied using an externally applied electric field. This unambiguously demonstrates coupling between the magnetic and ferroelectric degrees of freedom. Using representation analysis I derive the incommensurate magnetic structure in the multiferroic phase. The origin of the magnetoelectric coupling is consistent with models based on the inverse Dzyaloshinskii-Moriya interaction.

Acknowledgements

First and foremost I would like to thank my supervisor, Andrew Boothroyd for his good humour and insight throughout my graduate studies and his attempts to evade me by moving to a different country. I am indebted to him for dedicating so many hours of his time to answering my questions. I am grateful to Bertrand Roessli and Seva Gvasaliya who have let me play with the TASP spectrometer and have kept me away from trouble during many experiments together. It is also fitting to acknowledge Seva's nearly superhuman strength when it comes to opening glove boxes amongst other things. The experiments would have been much duller without the samples. I wish to thank Andrew and Bertrand for spending time to proofread this thesis.

Throughout my pursuit of neutron scattering I have come across many good and some bad people. Some of whom tried to steal my belongings and stick them to the ceilings. I expect the plastic cups in the office will remain there until the end of time. We all have Graeme Johnstone to thank for that. Together we have perfected the art of Helium filling. Life in the Clarendon would not be the same were it not for Alice Taylor, Stephen Gaw, Heather Lewtas, Andrew Steele, Isabel Franke, Liam Gannon, Danielle Kaminski and everyone else who I have shared many tea sessions with.

From my time at Paul Scherrer Institute, I would like to thank Gwen Pascua, Tibo Demoulin, Niki Egetenmeyer, Simon Ward, Matthias Thede amongst others. I am grateful to Michael Hess for chauffeuring me on several occasions but not for nearly killing me on the ski slopes. In addition I wish to thank the muon team of Tom Lancaster, Stephen Blundell, Peter Baker, Francis Pratt and Steve Lee for adopting me as one of their own during their many excursions to PSI. Special mention has to be made to Tom and Stephen who helped me evacuate Switzerland by carrying some of my contraband along with them. I wish to thank Jon White on accompanying me in our adventures in seeking spin resonances on the other side of the Atlantic.

The experimental work in this thesis would not have been possible without Prabhakaran Dharmalingam, Ekaterina Pomjakushina, Roger Johnson, Martin Rotter, Lucian Pascut, Ivelisse Cabrera, Amy Poole, Paul Freeman, Rustem Khasanov, Markus Bendele and Sunil Nair.

Lastly, I want to thank my parents and Giorgia.

Definitions of notation

$\boldsymbol{k}_\mathrm{i}$ ($\boldsymbol{k}_\mathrm{f}$)	: Initial (final) neutron wavevector
E_i (E_f)	: Initial (final) neutron energy
$\hbar\omega$ or E	: Energy transferred to or from a crystal in a neutron scattering process, $E = E_\mathrm{i} - E_\mathrm{f}$
$\boldsymbol{Q}$	: Scattering wavevector $\boldsymbol{Q} = \boldsymbol{k}_\mathrm{i} - \boldsymbol{k}_\mathrm{f}$
$\boldsymbol{G}$	: Reciprocal lattice vector
$\boldsymbol{a}$, $\boldsymbol{b}$, $\boldsymbol{c}$	: Real space unit cell parameters
(h, k, l)	: Miller indices
$\boldsymbol{a}^*$, $\boldsymbol{b}^*$, $\boldsymbol{c}^*$	: Reciprocal lattice basis vectors
$\boldsymbol{\kappa}$	: Magnetic propagation vector
$\boldsymbol{\tau}$	: Translation vector in real space
$\boldsymbol{r}$	: Vector in real space
$\boldsymbol{M}(\boldsymbol{r})$	: Magnetisation at position $\boldsymbol{r}$
$\boldsymbol{M}(\boldsymbol{Q})$	: Magnetic structure factor at $\boldsymbol{Q}$
$\boldsymbol{M}_\perp(\boldsymbol{Q})$	: Magnetic interaction vector at $\boldsymbol{Q}$
σ_i (where $i = x, y, z$)	: Pauli spin matrices along x, y, z
$\boldsymbol{\sigma}$	: Pauli spin matrix vector $\boldsymbol{\sigma} = (\sigma_x, \sigma_y, \sigma_z)$
J	: Exchange constant
T_N	: Antiferromagnetic ordering temperature
T_c	: Superconducting phase transition temperature
m_e	: Electron mass
m_n	: Neutron mass
m_p	: Proton mass
μ_N	: Nuclear magneton $\mu_\mathrm{N} = e\hbar/(2m_\mathrm{p})$
$-e$	: Charge on an electron
μ_B	: Bohr magneton $\mu_\mathrm{B} = e\hbar/(2m_\mathrm{e})$
$\sigma(\alpha, \beta)$	: Neutron cross-section where the two indices refer to the direction of the neutron polarisation before and after the sample, respectively
$P_{\alpha\beta}$	: Polarisation matrix component where α and β indicate the polarisation of the incident and final beam
$S(\boldsymbol{Q}, E)$	: Magnetic scattering response function
$\boldsymbol{u}$	: Small displacement of the nucleus from equilibrium position
W	: Exponent for the Debye-Waller factor, $W = \frac{1}{2}\langle(\boldsymbol{Q}\cdot\boldsymbol{u})^2\rangle$
k_B	: Boltzmann constant
P_e	: Electric polarisation
G_0	: Paramagnetic space group
$G_{\boldsymbol{\kappa}}$	: Paramagnetic little group belonging to propagation wavevector $\boldsymbol{\kappa}$
χ^2_ν	: Reduction of the goodness of fit normalised to the number of degrees of freedom ν

Contents

Publications

- P. Babkevich, A. Poole, R. D. Johnson, B. Roessli, D. Prabhakaran and A. T. Boothroyd, *Electric field control of chiral domains in high-temperature multiferroic cupric oxide*, Phys. Rev. B **85**, 134428 (2012)

- P. Babkevich, B. Roessli, S. N. Gvasaliya, L.-P. Regnault, P. G. Freeman, E. Pomjakushina, K. Conder and A. T. Boothroyd, *Spin anisotropy of the resonance peak in superconducting* $FeSe_{0.5}Te_{0.5}$, Phys. Rev. B **83**, 180506(R) (2011)

- A. T. Boothroyd, P. Babkevich, D. Prabhakaran and P. G. Freeman, *Hourglass magnetic spectrum in an insulating, hole-doped antiferromagnet*, Nature **471**, 341 (2011)

- H. Luetkens, M. Bendele, R. Khasanov, P. Babkevich, B. Roessli, *Investigating newly discovered iron-based superconductors with muons and neutrons*, PSI Scientific Report (2010)

- M. Bendele, P. Babkevich, S. Katrych, S. N. Gvasaliya, E. Pomjakushina, K. Conder, B. Roessli, A. T. Boothroyd, R. Khasanov and H. Keller, *Tuning the superconducting and magnetic properties in* $Fe_ySe_{0.25}Te_{0.75}$ *by varying the Fe-content*, Phys. Rev. B **82**, 212504 (2010)

- P. Babkevich, D. Prabhakaran, C. D. Frost and A. T. Boothroyd, *Magnetic spectrum of the two-dimensional antiferromagnet* La_2CoO_4 *studied by inelastic neutron scattering*, Phys. Rev. B **82**, 184425 (2010)

- P. Babkevich, M. Bendele, A. T. Boothroyd, K. Conder, S. N. Gvasaliya, R. Khasanov, E. Pomjakushina and B. Roessli, *Magnetic excitations of* $Fe_{1+y}Se_xTe_{1-x}$ *in magnetic and superconductive phases*, J. Phys.: Condens. Matter **22** 142202 (2010)

- R. Khasanov, M. Bendele, A. Amato, P. Babkevich, A. T. Boothroyd, A. Cervellino, K. Conder, S. N. Gvasaliya, H. Keller, H.-H. Klauss, H. Luetkens, V. Pomjakushin, E. Pomjakushina, and B. Roessli, *Coexistence of incommensurate magnetism and superconductivity in* $Fe_{1+y}Se_xTe_{1-x}$, Phys. Rev. B **80**, 140511(R) (2009)

Chapter 1

Introduction to strongly correlated electron systems

Contents

1.1 Introduction

The magnetic compass is the first technological application of magnetism and one of the oldest instruments for navigation. It was discovered sometime in the 12th century by mariners in China and Europe that a piece of lodestone, a naturally occurring magnetic iron ore, when floated on water, tends to align itself to point in the direction of the polestar [1]. The magnetic property of the iron ore has been known for a long time, since about 500 BC. Nevertheless, a microscopic mechanism to describe magnetism did not emerge until relatively recently when it was shown to be inherently quantum mechanical in origin.

Metals can be thought of as consisting of nearly free electrons, whereas on the other side of the spectrum are insulators where electrons are tightly bound to the positively charged ions contained within the solid. The point at which electrons interact in a cooperative way opens up a broad range of interesting new phenomena. One of these is superconductivity, where electrons in the solid flow without resistance. Many low-temperature superconductors were explained several decades ago by lattice vibrations providing the necessary electron binding. However, subsequently many new materials were discovered whose properties did not obey the conventional theory. The new compounds were found to raise significantly the critical temperature at which superconductivity sets in and has resulted in a lot of interest in the potential technological applications. Although no consensus has been reached on the microscopic origin of high-temperature superconductivity, spin fluctuations are likely to play a crucial role in mediating electron pairing.

1.2 Magnetic and charge ordering

Magnetism is a quantum mechanical phenomenon associated with the motion of electric charges. Interacting magnetic moments in solids exhibit a diverse range of properties and cooperative behaviour between moments is often very different to a system of isolated magnetic moments.

The magnetic moment of an atom originates from the spin $\boldsymbol{s}$ and orbital $\boldsymbol{l}$ angular momentum intrinsic to an electron orbiting a nucleus. The total electronic spin and angular momentum of an ion can be calculated by the vector sum of the moments of the individual electrons, giving $\boldsymbol{S} = \sum_i \boldsymbol{s}_i$ and $\boldsymbol{L} = \sum_i \boldsymbol{l}_i$. In the presence of a perturbing magnetic flux density $\boldsymbol{B}$, the Hamiltonian for a system of electrons at positions $\boldsymbol{r}$ in the atom can be expressed as [2],

$$\mathcal{H} = \mathcal{H}_0 + \mu_{\mathrm{B}}(\boldsymbol{L} + g\boldsymbol{S}) \cdot \boldsymbol{B} + \frac{e^2}{8m_{\mathrm{e}}} \sum_i (\boldsymbol{B} \times \boldsymbol{r}_i)^2, \tag{1.1}$$

where the initial Hamiltonian is $\mathcal{H}_0$. The second and third terms are related to the effect of paramagnetism and diamagnetism. For diamagnetic substances, a magnetic field induces a magnetic moment which opposes the applied magnetic field. Diamagnetism is present in all materials to some extent but is usually very weak.

Paramagnetic behaviour is characterised by magnetic moments which align parallel to the applied magnetic field which causes it. This originates from unpaired electrons in an atom. In the absence of a magnetic field, the magnetic moments are orientated in random directions unless neighbouring atoms interact. The angular momentum on an atom is associated with a total angular momentum $\boldsymbol{J}$, which is defined as $\boldsymbol{J} = \boldsymbol{L} + \boldsymbol{S}$. For an isolated atom, there are many ways of combining the total spin and orbital angular momentum based on different electronic configurations. An estimate of the angular momentum quantum numbers can be found using Hund's rules. In order to reduce Coulomb repulsion between electrons, it is necessary to maximise S followed by L. The value of J can be evaluated using $J = |L - S|$ if the shell is less than half full and $J = |L + S|$ if it is more than half full. This arises from an attempt to minimise the spin-orbit energy but is only applicable in certain circumstances. As will be discussed later, the last of the Hund's rules is violated when the crystal field surrounding an atom dominates over spin-orbit coupling. In the case where Hund's rules hold, the effective magnetic moment, which can be determined from measurements of the paramagnetic susceptibility, is calculated from the spin-orbit interaction as,

$$\mu_{\text{eff}} = g_J \mu_{\text{B}} \sqrt{J(J+1)}, \tag{1.2}$$

where μ_{B} is the Bohr magneton and g_J is the Landé g-factor, which can be found as,

$$g_J = \frac{3}{2} + \frac{S(S+1) - L(L+1)}{2J(J+1)}. \tag{1.3}$$

A magnetic solid consists of atoms carrying a magnetic moment whose net magnetisation $\boldsymbol{M}$ is defined as per unit volume. On length scales considered to be much larger than interatomic distances, the magnetisation is a vector quantity. The magnetic susceptibility χ is in general a tensor which relates the response $\boldsymbol{M}$ to an applied magnetic field $\boldsymbol{H}$. These quantities are related as,

$$M_\alpha = \chi_{\alpha\beta} H_\beta, \tag{1.4}$$

where α, β are spatial directions x, y and z. If the system in the groundstate possesses $J = 0$, no paramagnetic effect would be expected. This would imply that the groundstate energy of the system does not change when a magnetic field is applied and therefore there is no paramagnetic susceptibility [2]. However, this is only true for the groundstate and provided one takes into account the excited states with $J \neq 0$, van Vleck paramagnetism can be created. As in the case of diamagnetism, this effect is small and temperature independent [2].

1.2.1 Exchange interactions

Magnetic order of atoms in solids is possible when interactions between moments of magnetic ions are such that it is energetically favourable for them to order in a periodic arrangement. Magnetic exchange interaction between ions originates from

the differences in the electrostatic energy of different orientations of the magnetic moments. The most probable configuration is one which minimises the total energy of the system. For a system of two interacting electrons at positions $\boldsymbol{r}_1$ and $\boldsymbol{r}_2$ the overall wavefunction has to be antisymmetric to satisfy Pauli exclusion principle. Hence, double occupancy of an orbital is possible for antiparallel electron spins ($\uparrow\downarrow$) but forbidden for parallel spins ($\uparrow\uparrow$). The total wavefunction is made up of the spatial and spin states of the electrons. The spatial part can be described by wavefunctions ψ_a or ψ_b. The spins can either be in a spin singlet state $S = 0$, where the spin part of the wavefunction is antisymmetric χ_{S}, or in a triplet state $S = 1$ with a wavefunction χ_{T}. The total wavefunctions for the singlet (Ψ_{S}) and triplet (Ψ_{T}) states are therefore,

$$\Psi_{\mathrm{S}} = \frac{1}{\sqrt{2}}\chi_{\mathrm{S}}[\psi_a(\boldsymbol{r}_1)\psi_b(\boldsymbol{r}_2) + \psi_a(\boldsymbol{r}_2)\psi_b(\boldsymbol{r}_1)] \tag{1.5}$$

$$\Psi_{\mathrm{T}} = \frac{1}{\sqrt{2}}\chi_{\mathrm{T}}[\psi_a(\boldsymbol{r}_1)\psi_b(\boldsymbol{r}_2) - \psi_a(\boldsymbol{r}_2)\psi_b(\boldsymbol{r}_1)]. \tag{1.6}$$

In order to realise a parallel spin arrangement, one electron must occupy an excited state. The energy required to do so comes from the Coulomb interaction,

$$V_{\mathrm{C}} = \frac{e^2}{4\pi\varepsilon_0|\boldsymbol{r}_1 - \boldsymbol{r}_2|}, \tag{1.7}$$

between two electrons. The Coulomb interaction is spin independent but is larger for electrons in a common orbital ($\uparrow\downarrow$) than in different ones ($\uparrow\uparrow$). The Coulomb interaction indirectly favours the parallel spin alignment and competes against an increase in one-electron energy. The difference between the energies for a spin triplet and singlet states can then be found as,

$$J = E_{\mathrm{T}} - E_{\mathrm{S}} = -2\int \psi_a^*(\boldsymbol{r}_1)\psi_b^*(\boldsymbol{r}_2)\mathcal{H}\psi_a(\boldsymbol{r}_2)\psi_b(\boldsymbol{r}_1)\ \mathrm{d}\boldsymbol{r}_1\mathrm{d}\boldsymbol{r}_2, \tag{1.8}$$

which defines the exchange constant J. The effective spin Hamiltonian can then be expressed as [2],

$$\mathcal{H} = (E_{\mathrm{T}} - E_{\mathrm{S}})\boldsymbol{S}_1 \cdot \boldsymbol{S}_2 = J\boldsymbol{S}_1 \cdot \boldsymbol{S}_2. \tag{1.9}$$

The parameter J is a measure of the strength of interaction between two spins. If $J < 0$, $E_{\mathrm{S}} > E_{\mathrm{T}}$ then the triplet state ($S = 1$) is favoured as the groundstate. Conversely, when $J > 0$, $E_{\mathrm{S}} < E_{\mathrm{T}}$, the singlet state ($S = 0$) is lower in energy. Although the generalisation of this formulation for a many-body system is complicated, it was recognised by Heisenberg that Eq. 1.9 could be applied to all neighbouring atoms where the result, known as the Heisenberg Hamiltonian can be written as,

$$\mathcal{H} = \sum_{ij} J_{ij}\boldsymbol{S}_i \cdot \boldsymbol{S}_j, \tag{1.10}$$

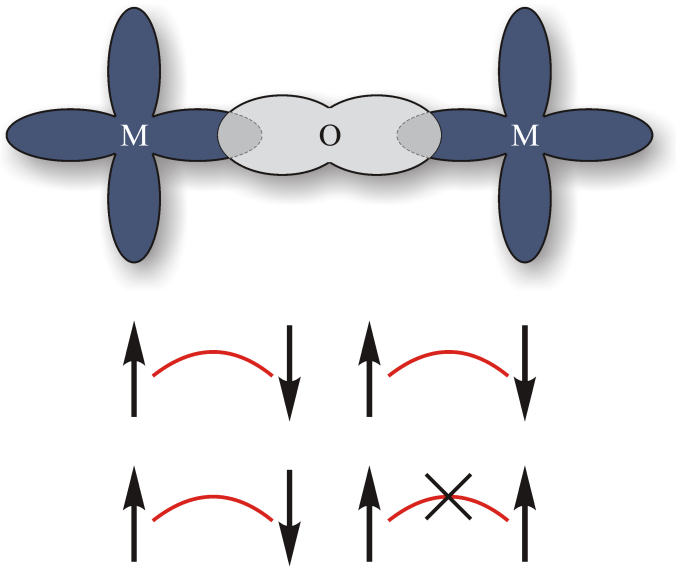

Figure 1.1: Superexchange interaction in transition metal oxides. The orbital lobes of the electron clouds of the transition metal ions are shown in blue and the grey lobes show the electron orbitals of O. The hopping of the electrons is shown in the diagrams below the electron densities. In the antiferromagnetic case the moments on the transition metal ions can freely mix and the electrons are delocalised over the entire M–O–M unit, thereby lowering the kinetic energy. Ferromagnetic alignment of moments on M costs more energy as Pauli exclusion principle excludes the possibility of moments in parallel on the same ion.

for all pairs of spins i and j and J_{ij} is the isotropic exchange constant describing the strength with which the moments are coupled. The interaction between adjacent magnetic moments creates spontaneous alignment. In this convention, $J > 0$ favours antiferromagnetic magnetic order with spins antiparallel to one another and $J < 0$ favours a ferromagnetic alignment of moments where spins are parallel to one another.

Electrons on neighbouring ions can interact directly without the need for an intermediary in a process known as direct exchange. However, in most circumstances this exchange mechanism is not important as there is insufficient overlap between neighbouring electron orbitals. This is true in particular for rare earths where the $4f$ electrons are strongly localised and lie close to the nucleus [2]. The electron orbitals are more extended in transition metals with $3d$ orbitals, however in many transition metal oxides the magnetic ions are separated by O. In these circumstances the indirect exchange interaction becomes important.

The exchange interaction described by coupling parameter J is dependent on the distance between ions and the interaction is normally very short ranged. In ionic solids the most important interaction is known as superexchange, which involves indirect exchange interaction between two ions mediated by a non-magnetic ion between them. The superexchange interactions are usually antiferromagnetic in nature. This is because for antiferromagnetic alignment, the electron are delocalised

over the entire M–O–M configuration, where M is a transition metal ion and O is oxygen. This process is illustrated in Fig. 1.1 for the simple case of one electron in the outer shell on the M ion and two electrons on O. The electrons can hop through the covalent bond joining the atoms. For ferromagnetic alignment, only one electron can hop with the other electron prevented by the exclusion principle. In this simple scenario, the antiferromagnetic state is therefore favourable as it lowers the energy of the system. A full calculation of the superexchange coupling is complicated due to the large number of orbital states involved, however it can be approximated as $J \approx 4t^2/U$ in the physically relevant limit of $U \gg t$ (see § 1.4) [2, 3]. The hopping integral t is proportional to the energy width of the conduction band in a tight-binding approach. The energy cost of making an excited state is provided by the Coulomb energy U.

A semi-empirical set of rules for superexchange interactions was developed by Goodenough and Kanamori [4, 5]. The main features for estimating the sign and relative magnitudes have been formulated into the Goodenough-Kanamori-Anderson rules [6]. The exchange is usually antiferromagnetic but can be ferromagnetic due to direct exchange if the overlap between the atomic orbitals involved is zero by symmetry [7]. Therefore, the geometric shapes of the orbitals play a crucial role in the interatomic interactions.

(i) For a configuration of M–O–M, where the bond angle between the two M ions with half-filled orbitals is 180°, the interaction will be strongly antiferromagnetic.

(ii) When the angle between half-filed orbitals is 90°, a rather weak ferromagnetic interaction can occur.

(iii) Exchange due to overlap between a half-filled and an empty orbital of different symmetry is also weakly ferromagnetic. The electron transfer can be mediated by an intermediate O ion.

It should be noted that superexchange also plays an important role in ferrimagnetism, this is antiferromagnetic coupling of unequal spins on different atomic sites, resulting in a net magnetisation [8].

An important mechanism in oxides with mixed valence is double exchange. In the case of Mn ion in $La_{1-x}Sr_xMnO_3$, doping by Sr^{2+} creates Mn^{3+} and Mn^{4+} valence states. In both the tri- and quadi-positive ions, the low-lying t_{2g} state is occupied by three well-localised $3d$ electrons. But in Mn^{3+} there is an additional e_g electron. A strong single-centre exchange interaction between the e_g electron and three electrons in the t_{2g} level enforces them to be all aligned [2]. The hybridisation with O $2p$ electrons allows the e_g electron to hop and thereby gives a kinetic energy saving. The corresponding spin transfer gives both ferromagnetism and conduction [8].

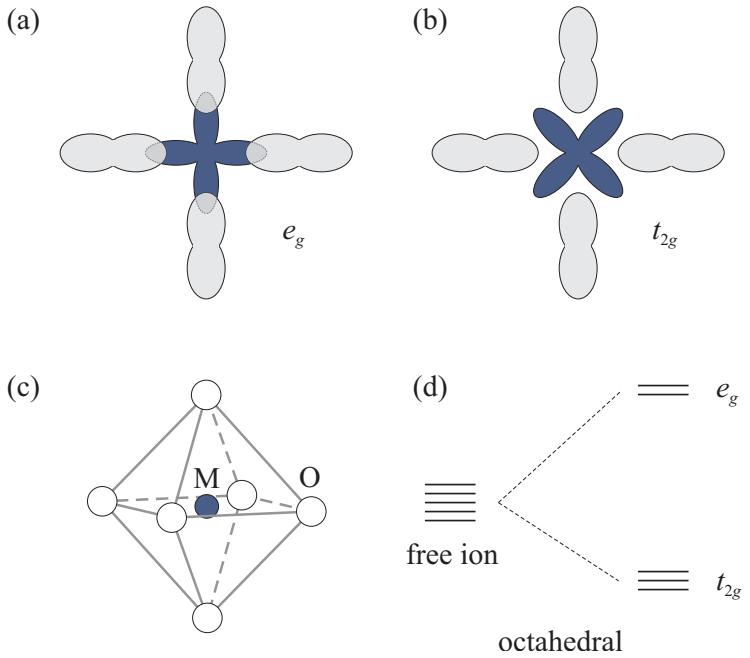

Figure 1.2: The crystal field environment. (a) and (b) Panels showing the electron orbitals in an octahedral environment for e_g (figure shows the $d_{x^2-y^2}$ orbital) and t_{2g} orbitals. (c) The octahedral arrangement of O ions surrounding a transition metal (M) ion. (d) The effect of the crystal field on the energy levels of the ion in the case of an octahedral environment. The t_{2g} orbitals will lower the system's energy with respect to the free ion whereas the e_g energy levels will raise the energy.

1.2.2 Lattice effects

We have already seen that the neighbouring ions greatly influence the magnetic properties of transition metal ions in solids. The formulae 1.2 and 1.3 describe the response of spin and orbital angular momenta to external fields and are very successful in describing the paramagnetic susceptibilities of rare earth systems [3]. The high-temperature susceptibilities of insulating transition metal compounds are described in a similar fashion. The values of the magnetic moment predicted by Eqs. 1.2 and 1.3 do not always appear to agree with experiment (except for the case of $3d^5$ and $3d^{10}$ where $L = 0$). The magnetic moment seems to arise solely from the spin degree of freedom of the $3d$ ions. The orbital contribution is almost completely missing. The reason for this discrepancy is that the free-ion description no longer applies and one needs to consider the $3d$ ions as embedded in a surrounding environment which exerts an electrostatic field on the ion.

1.2.2.1 Crystal field

The crystal field is the electric field originating from the neighbouring atoms in the crystal. The symmetry of the environment is crucial in determining the size and nature of the crystal field [2]. Many transition metal compounds contain transition

metal ions at a centre of octahedron with O ions at each corner, see Fig. 1.2(c). The crystal field arises from the electrostatic repulsion from electrons in the O orbitals. The d orbitals fall into two classes, the t_{2g} orbitals point between $\{x, y, z\}$ axes (these are d_{xy}, d_{xz} and d_{yz} orbitals). The e_g orbitals along these axes – $d_{3z^2-r^2}$ where the lobes are along the z axis and $d_{x^2-y^2}$ orbital which is symmetrical about the x and y axes.

Figures 1.2(a) and (b) illustrate the effect of the surrounding O ions on the transition metal in the centre. The crystal field is largely produced by the p orbitals on the neighbouring atoms. From symmetry of the $3d$ ion orbital, it is clear that the t_{2g} state will have a lower overlap with the p orbitals than e_g. The degeneracy of the free ion energy levels will therefore be lifted with the threefold t_{2g} levels lowered in energy and the e_g levels raised in energy, as shown in Fig. 1.2(d).

The crystal-field Hamiltonian can be expressed using Stevens operators $O_l^m(\boldsymbol{J})$ as,

$$\mathcal{H}_{\mathrm{CF}} = \sum_i \sum_{lm} B_l^m O_l^m(\boldsymbol{J}_i). \tag{1.11}$$

The crystal field parameter B_l^m can in principle be calculated from the charge distribution but in practice it is difficult to obtain meaningful results. The problems arise from uncertainties in the charge distribution surrounding an ion as these can in general be rather asymmetric and spread out in space. The redistribution of charge in the unit cell can modify the electric fields experienced by the $3d$ (or $4f$) electrons. Such shielding effects are very difficult to estimate [3]. A crude estimate can be obtained using the point-charge model, in which an adjustable charge is placed on each lattice site. Alternatively, the B_l^m parameter can be regarded as a quantity to be deduced experimentally. Fortunately, the number of free parameters can be restricted by lattice symmetry.

The crystal field effects are much stronger for $3d$ electrons than for $4f$. The $4f$ orbitals lie deep within the ion core that other occupied shells in the ion screen out the potential of the surrounding ions [3]. For the $4f$ electrons, the external effects on the ion are relatively small and the electrons act as if surrounding a free ion. The $4f$ electrons in rare-earth solids are examples of the weak crystal field where the spin-orbit coupling dominates over the crystal fields. All of Hund's rules hold. The $3d$ transition metal ions are part of intermediate crystal field strength where the crystal field is stronger than the spin-orbit coupling. This means than although L and S are still good quantum numbers and their values are given by Hund's first and second rules, J is no longer a good quantum number. An intermediate crystal field mixes states within a given (L, S) term [3].

The strong crystal fields are comparable to the exchange splitting, which are used to derive the Hund's first and second rules. Such effects can be observed in $4d$ and $5d$ transition metal compounds. The simple ionic model cannot be applied to such cases and mixing of d-orbitals of the transition metal with the p-orbitals of neighbouring ions must be taken into account [3]. Such systems are not dealt with in this thesis and will not be discussed further.

1.2.2.2 Jahn-Teller distortion

If the symmetry of the crystal field is so high that the groundstate of an ion is orbitally degenerate, it is energetically favourable to spontaneously distort the crystal structure in such a way as to remove the orbital degeneracy [9]. The distortion will raise the energy of some orbitals while lowering the energy of others. In the case of partially filled orbitals this effect can be significant. For example, let us consider CuO_6 where the octahedron is elongated in the z-direction. The two O ions will lie farther apart along z, an electron in the $d_{3z^2-r^2}$ orbital will be less repelled by other charges and thus lie at a lower energy than an electron in the $d_{x^2-y^2}$. Therefore the orbitally degeneracy has been lost. The distortion costs an elastic energy of order $\alpha(\delta z)^2$. The splitting of the energy levels is proportional to (δz). The energy of two electrons will be lowered by going into the $d_{3z^2-r^2}$ orbital and one will gain energy by having to be raised to $d_{x^2-y^2}$. The total energy will therefore be $\alpha(\delta z)^2 - \beta\delta z$, which is minimised by the finite distortion $\delta z = \beta/(2\alpha)$ [3]. Although here we have only considered the distortion along z, similar arguments can be made for distortions along arbitrary directions of the crystal.

1.2.3 Charge order

In certain systems with mixed valencies, Coulomb interaction can lead to periodic arrangement of ions. At high temperatures, the excess holes are randomly distributed but on cooling the repulsion between ions of the same valence state forces them to form a unidirectional charge modulation. The ordered charge state is known as charge order and is well known to occur in systems of the form $La_{2-x}Sr_xMO_4$, where M is a transition metal such as Cu, Mn, Ni or Co. Charge order typically occurs at a temperature well above the magnetic ordering transition and has a significant impact on the spin density state. The transition metal ion sits inside an octahedral arrangement of O ions. The difference in valence states in a charge ordered phase will therefore induce slightly different lattice distortions. This alters the lattice periodicity and can be probed by x-ray scattering, however in practice the effect is small and difficult to detect.

1.3 Introduction to excitations in materials

At a finite temperature, the ordered magnetic moments are able to fluctuate about their average positions. The arising excitations are spin waves. Exciting a spin-wave means creating a (bosonic) quasi-particle known as a magnon. Magnons are quantised magnetisation density waves. The magnon dispersion relation can be calculated within theoretical framework of the linear spin-wave theory and thereby the dominant exchange interactions extracted. As an example, let us explore the elementary excitation spectrum of a spin S Heisenberg antiferromagnet whose Hamil-

tonian is given by Eq. 1.10 as,

$$\mathcal{H} = J \sum_{\langle ij \rangle} \boldsymbol{S}_i \cdot \boldsymbol{S}_j, \tag{1.12}$$

where $J > 0$ and the summation is taken over neighbouring sites. The quantum mechanical spin operator at lattice site i is denoted by $\boldsymbol{S}_i$. The system can be considered in terms of a bipartite lattice where the groundstate of the Heisenberg antiferromagnet are close to a staggered spin configuration, known as a Néel state, where all neighbouring spins are antiparallel. The Néel state is not an exact groundstate of the Hamiltonian as the true groundstate exhibits zero-point fluctuations. In the limit of large spin S and at low excitation energies, the ordered phase can be described in terms of small fluctuations of spins around their expected values. The fluctuations can be conveniently expressed in terms of spin raising and lowering operator, $S_i^{-(+)}$ which lowers (raises) the z-component of the spin at site i by one. We can then expand the Hamiltonian in terms of bosonic operators a_i defined as,

$$S_i^z = S - a_i^\dagger a_i, \qquad S_i^- \simeq (2S)^{1/2} a_i^\dagger \qquad \text{and} \qquad S_i^+ \simeq (2S)^{1/2} a_i, \tag{1.13}$$

for the A sublattice and similarly for the B sublattice, related to A by a canonical rotation by 180°, as

$$S_j^z = -S + b_j^\dagger b_j, \qquad S_j^- \simeq (2S)^{1/2} b_j \qquad \text{and} \qquad S_j^+ \simeq (2S)^{1/2} b_j^\dagger, \tag{1.14}$$

derived from the expansion in powers of $1/S$ of the Holstein-Primakoff transformations [10]. The linearised Heisenberg Hamiltonian can then be written as,

$$\mathcal{H} = -z_{\boldsymbol{r}} N J S^2 + JS \sum_{\langle ij \rangle} a_i b_j + a_i^\dagger b_j^\dagger + b_j^\dagger b_j^\dagger + a_i^\dagger a_i, \tag{1.15}$$

where $z_{\boldsymbol{r}}$ is the coordination number and N is the number of spins on each sublattice. In order to diagonalise Eq. 1.15 we have to perform the Fourier transformation,

$$a_{\boldsymbol{Q}} = \frac{1}{\sqrt{N}} \sum_i e^{\mathrm{i}\boldsymbol{Q}\cdot\boldsymbol{r}_i} a_i, \qquad b_{\boldsymbol{Q}} = \frac{1}{\sqrt{N}} \sum_j e^{\mathrm{i}\boldsymbol{Q}\cdot\boldsymbol{r}_j} b_j. \tag{1.16}$$

Eq. 1.15 can then be diagonalised by an appropriate ansatz of linear combination of the operators. To preserve the commutation relations, the transformation must preserve the metric $g = \mathrm{diag}(1, -1)$. This is the Bogoliubov transformation and is known from its relation to superconductivity as,

$$a_{\boldsymbol{Q}} = \quad \cosh\theta_{\boldsymbol{Q}} \alpha_{\boldsymbol{Q}} - \sinh\theta_{\boldsymbol{Q}} \beta_{\boldsymbol{Q}}^\dagger, \tag{1.17}$$

$$b_{-\boldsymbol{Q}} = -\sinh\theta_{\boldsymbol{Q}} \alpha_{\boldsymbol{Q}}^\dagger + \cosh\theta_{\boldsymbol{Q}} \beta_{-\boldsymbol{Q}}. \tag{1.18}$$

All mixed terms can be eliminated provided $\tanh 2\theta_{\boldsymbol{Q}} = \gamma_{\boldsymbol{Q}}$. The Hamiltonian, which takes the form of a quantum mechanical oscillator is described by,

$$\mathcal{H} = -z_{\boldsymbol{r}} NJS(S+1) + \sum_{\boldsymbol{Q}} \omega_{\boldsymbol{Q}} \left(\alpha^{\dagger}_{\boldsymbol{Q}} \alpha_{\boldsymbol{Q}} + \beta^{\dagger}_{\boldsymbol{Q}} \beta_{\boldsymbol{Q}} + 1 \right), \tag{1.19}$$

with the dispersion of the excitations given by,

$$\omega_{\boldsymbol{Q}} = z_{\boldsymbol{r}} JS \left(1 - \gamma^2_{\boldsymbol{Q}}\right)^{1/2}. \tag{1.20}$$

The magnon dispersion function can be defined as $\gamma_{\boldsymbol{Q}} = \sum_{\boldsymbol{\delta}} \exp(\mathrm{i}\boldsymbol{Q} \cdot \boldsymbol{\delta})/z_{\boldsymbol{r}}$, which in this approximation depends only on the positions of the nearest neighbour spins. The derivation also assumes that the lattice possess inversion symmetry such that $\gamma_{\boldsymbol{Q}} = \gamma_{-\boldsymbol{Q}}$. At long wavelengths, the dispersion $\omega_{\boldsymbol{Q}} \propto |\boldsymbol{Q}|$. This follows from Goldstone theorem which states that if a continuous symmetry is broken and the forces are sufficiently short-ranged, then there is a branch of excitations with the property that the energy vanishes in the limit $|\boldsymbol{Q}| \to 0$ [3]. In the present case considered, it is the spin-rotational symmetry which is spontaneously broken by the non-vanishing magnetisation of the groundstate. A long-wavelength magnon is equivalent to a nearly uniform rotation of the spins [3].

The order parameter in the antiferromagnet is the staggered magnetisation. The quantum fluctuations in the groundstate, where no spin waves are excited thermally, reduce the staggered magnetisation from its classical value of S by an amount [3],

$$\Delta S = \frac{1}{2} \left(\int \frac{\mathrm{d}^D \boldsymbol{Q}}{(2\pi)^D} (1 - \gamma^2_{\boldsymbol{Q}})^{-1/2} - 1 \right). \tag{1.21}$$

The integral in Eq. 1.21 depends on the dimensionality D of the system. For a simple cubic lattice,

$$\Delta S = \begin{cases} -0.078 & D = 3 \\ -0.197 & D = 2 \\ \infty & D = 1 \end{cases} \tag{1.22}$$

This demonstrates that in one-dimensional isotropic Heisenberg model, the quantum fluctuations destroy long-range antiferromagnetic order[1] for any spin S. Fluctuations and the mean number of bosons become smaller for larger D or S. The correction is difficult to measure. In the spin wave model including anisotropic terms in the Hamiltonian, ΔS is very sensitive to the anisotropy. A compound that has been used to validate the staggered magnetisation reduction is $RbMnF_3$, which is a three-dimensional Heisenberg antiferromagnet [11, 12]. Due its high-dimensionality and large spin ($S = 5/2$), ΔS is difficult to measure reliably, nevertheless the spin reduction has been confirmed in $RbMnF_3$ [11]. Two-dimensional antiferromagnets are an intermediate case. Linear spin wave theory predicts that for $S = 1/2$ system, only approximately 60% of the classically ordered parameter is left. This is

[1] The result $\Delta S = \infty$ is clearly not meaningful, more careful argument should give $\Delta S = S$.

interesting as it closely corresponds to La_2CuO_4 where the reduction of the ordered moment by quantum fluctuations has been confirmed owing to weak anisotropy effects in the compound [3]. However, it is important to note that the situation where $\Delta S/S \approx 0.4$, places the initial expansion in leading orders of $1/S$ in the spin wave theory in question. This could suggest that higher orders in $(1/S)$ are important or perhaps that long-range order is destabilised completely.

1.4 Local and itinerant picture of magnetism

The interactions considered thus far have been based on the view that the electrons are well localised and at fixed distances from each other. Although this is realised in insulating materials, the situation is clearly quite different in metals where electrons can propagate through the crystal. The kinetic energy of the electrons can be lowered if they are delocalised over the whole of the crystal. However, this competes in certain systems with the on-site Coulomb energy. The strongly interacting many-body system of electrons can be described by the (single-band) Hubbard Hamiltonian as,

$$\mathcal{H}_{\mathrm{H}} = -t \sum_{\langle ij \rangle} \sum_{\sigma} c^{\dagger}_{i\sigma} c_{j\sigma} + U \sum_{i} n_{i\uparrow} n_{i\downarrow}. \tag{1.23}$$

The first term in the Hamiltonian relates to the kinetic energy (electron hopping) which promotes to delocalise the electrons into itinerant states (Bloch states) leading to metallic behaviour. The second term in Eq. 1.23 corresponds to the electron-electron interaction, approximated by on-site Coulomb interaction. The effect of this term is to localise the electrons onto sites, driving the transition to a Mott insulator, which is usually magnetic. The operator $c^{\dagger}_{i\sigma}$ creates an electron in the Wannier state with spin σ. The corresponding occupation number operator is given by $n = c^{\dagger}_{i\sigma} c_{i\sigma}$. The transfer integral between site i and j is denoted by t and U is the Coulomb interaction between two electrons on the same atom in the up- and down-spin-states. The summation $\langle ij \rangle$ is taken over neighbouring lattice sites.

The phase diagram of the Hubbard Hamiltonian is characterised by the dimensionality, the ratio of the Coulomb interaction scale to the bandwidth U/t, the filling fraction $\langle n \rangle$ (average number of electrons per site) and dimensionless temperature T/t. At low temperature and in the dilute limit $\langle n \rangle \ll 1$, the electron wavelength is much larger than the particle separation and the dynamics can be considered as free. The local interactions present only a weak perturbation and the properties of the Hubbard system will mirror those of a weakly interacting nearly free electron system. As long as the interactions are weak, one would expect metallic behaviour to persist. The half-filled system is more interesting. If the interaction is weak $U/t \ll 1$, one would again expect physical properties corresponding to a weakly interacting electron system. If the Fermi wavelength becomes commensurate with the lattice, a transition into an insulating spin-density wave characterised by a small quasi-particle energy gap can be initiated. In the converse case where $U/t \gg 1$, site

double occupancy is inhibited. The mutual Coulomb interaction between electrons drives the system from a metallic into an insulating phase with properties very different to those of conventional band insulators. This has been used to explain why a certain class of materials, known as Mott insulators, which should be conducting assuming usual band theories are in fact insulating.

The application of the Hubbard model to real systems is rather complicated. However, it can successfully explain why La_2CuO_4 is an insulator. In order to understand the electric and magnetic properties of this material, we need to consider only the electronic states lying in the vicinity of the Fermi level. Assuming in La_2CuO_4 that the relevant part of the bands are derived from the Cu $3d$ states lying in between O $2p$ bands, which are completely filled and Cu $4s$ band which is empty [3]. The $3d$ bands are split by the crystal field and we are left with one $d_{x^2-y^2}$ orbital and one electron per Cu atom. Applying the Hubbard model in describing the electrons in this band, in view of the narrowness of the band, the ratio $U_{x^2-y^2}/t_{x^2-y^2}$ is expected to be large [3]. Therefore, in La_2CuO_4, the insulating properties are decided by a subsystem of strongly correlated electrons which occupy the states near the Fermi level.

1.5 Superconductivity

Superconductivity was first observed by Onnes in 1911, three years after he first liquefied He. A property of a superconductor is that when it is cooled below its transition temperature in a magnetic field it expels all magnetic flux from its interior. The phenomena of perfect diamagnetism is known as the Meissner effect and is characteristic of superconductivity. The initial superconducting phase transition temperature was found in Hg at 4.2 K. Much effort, on both theoretical and experimental fronts has since between devoted in trying to understand the mechanism in which the material loses electrical resistivity and to raise the phase transition temperature.

1.5.1 Conventional superconductors

It was not until late 1950s that a satisfactory microscopic description of the phenomena was given by Bardeen, Cooper and Schrieffer – commonly referred to as the BCS theory [13, 14]. This has been very successful in explaining the origin of superconductivity in materials such as Hg, Nb and many others. At low temperatures, the presence of an attractive pairwise interaction can induce an instability of an electron gas towards formation of bound pair of states in the vicinity of the Fermi surface. The entropy of a superconducting state is found from heat capacity measurements to be lower than that of the normal state. This means that the superconducting phase is somehow a more ordered state and agrees with the hypothesis of a pairing interaction.

For the majority of electronic sates, the scattering between electrons induces an effective repulsive interaction of the electrons. However, for a narrow band of

states around the Fermi level, electron-phonon scattering can cause an attractive pairing interaction within the Debye frequency ω_D of the Fermi surface, such that $\hbar\omega_D \ll E_F$. This is because the electron can exploit a lattice distortion created by the passage of a second electron. The coupling of electron degree of freedoms to phonons forms the basis of the phenomena of conventional superconductivity. The BCS theory relies heavily on the accuracy with which the normal state is described by Fermi liquid theory – BCS superconductivity is a Fermi surface instability, which is only meaningful when there is a well defined Fermi surface.

The composite pair of electrons form objects known as Cooper pairs and these behave as bosons. The electron-phonon coupling mechanism correctly explains the isotope effect of T_c found experimentally by substituting atoms in the materials by isotopes. The formation of the Cooper pairs is associated with an energy gap Δ as the energy saved by the Cooper pair formation compared to the normal, unpaired state. The superconducting order parameter can be expressed as $\Delta = e^{i\phi}|\Delta|$, where the energy required to break apart the Cooper pairs at $T = 0$ is $2|\Delta(0)|$ for a gap function which is isotropic in momentum space. At finite temperature, the gap $2|\Delta|$ decreases as temperature increases, above the critical temperature T_c, $2|\Delta| = 0$. At $T = 0$, the gap size can be directly related to T_c, by the famous BCS prediction of

$$2|\Delta(0)| = 3.52 k_B T_c, \tag{1.24}$$

which is obeyed very accurately in a wide range of low-temperature superconductors.

1.5.2 Unconventional superconductors

The progress in raising the superconducting transition temperature stalled for many years, until in 1986 Bendorz and Müller synthesised the first of the copper oxide based superconductors with $T_c \approx 30\,\mathrm{K}$ in a Ba-doped La_2CuO_4 compound [15]. Other compounds were discovered soon after with the current record set at $T_c \approx 130\,\mathrm{K}$ (ambient pressure [16, 17]) and 164 K (under pressure [18]) in Hg doped cuprates.

High-temperature superconductivity, like its low-temperature BCS counterpart, is known to result from electrons forming Cooper pairs. A major challenge remains in trying to understand the microscopic mechanism that binds the electrons together. Estimates of T_c based on phonon-exchange and using experimentally known values of the Debye frequency, electron-phonon coupling and the normal-state density are much lower than the observed critical temperatures in the cuprates. In addition to this, a characteristic of BCS superconductors is that the Cooper pairs have zero orbital angular momentum, they exhibit *s*-wave symmetry. In most hole-doped cuprate superconductors, the Cooper pairs have a non-zero angular momentum, indeed they were found to possess *d*-wave symmetry. The underlying mechanism of superconductivity in cuprates remains an open question although it seems likely that magnetic fluctuations or spin and charge separation are involved. The superconductors which cannot be described by BCS theory are known as unconventional

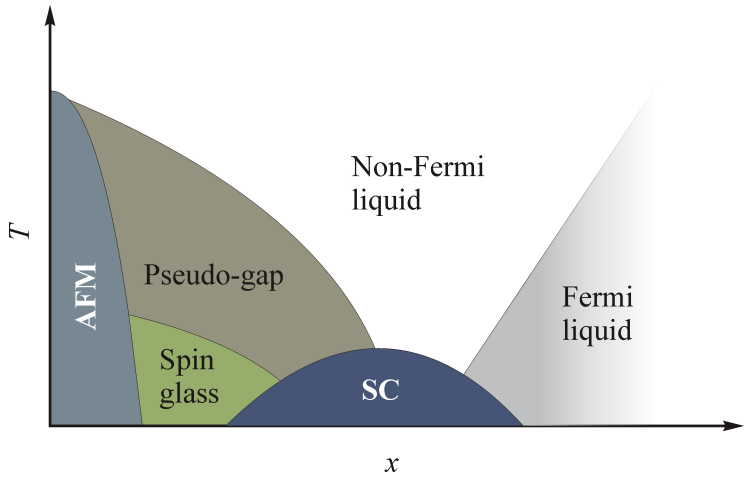

Figure 1.3: Generic phase diagram of an unconventional superconductor. The diagram shows the typical phase diagram of hole-doped cuprate superconductors as a function of hole doping.

superconductors and are actively studied.

1.5.3 Cuprate superconductors

Strong electronic correlations cause diversity in the phase diagram of cuprate superconductors. The simplified phase diagram common to most hole-doped cuprate superconductors is shown in Fig. 1.3 as a function of doping the system with holes. The number of holes is a convenient parameter that can be used to compare different cuprates. Superconductivity can also be obtained through doping with electrons, however these systems are outside of the scope of this thesis.

At low doping levels, the electronic properties are to a large extent controlled by the strong electrostatic repulsion between planar quasi-particles. This causes the d electrons to localise to form a Mott insulator. The effective antiferromagnetic coupling between the spins causes the system to order antiferromagnetically. The magnetic behaviour of these localised spins is well described by a two-dimensional Heisenberg model, where the inter-planar interactions are considered much weaker than the in-plane ones. The antiferromagnetic region is the best understood part of the phase diagram. At increased doping levels the material becomes conducting and the exact temperature and doping determines in which phase of matter the system will be. The addition of holes to the system interferes with long-range antiferromagnetic order and the transition temperature sharply decreases.

Beyond the antiferromagnetic order are the pseudo-gap and spin-glass phases. The pseudo-gap phase is characterised by the existence of an energy gap. All of the cuprates' thermodynamic and electronic-transport properties change by a large amount owing to the material's loss of low-energy excitations [19]. The discovery of the pseudo-gap phase in underdoped cuprates, where the conditions for optimal T_c are not quite established, has presented a major challenge for theorists and a broad

range of ideas have been proposed. The spin-glass phase consists of short-ranged spin correlations which can be ascribed as due to slowly fluctuating spin clusters and are a precursor of antiferromagnetic order [20].

The superconducting phase is eventually reached on sufficient doping with holes. The phase forms a dome on the phase diagram with optimally doped samples displaying the highest superconducting phase transition temperatures. A quantum critical point (QCP) has been postulated to exist at the optimal T_c and connecting the pseudo-gap and Fermi-liquid regions [21, 22]. The QCP affects the behaviour of the system in a wide range of temperatures and might explain some of the properties of the non-Fermi liquid phase, such as linear temperature dependence of resistivity.

In the over-doped region, superconductivity gradually disappears and the material goes into the Fermi-liquid state. The properties of a single electron are renormalised by interactions with other electrons to form quasi-particles. The properties of the material can then be understood in terms of the weak residual interactions between the quasi-particles and their excitations.

At higher temperatures and over a wide range of doping there exists a non-Fermi liquid phase. The thermodynamic properties are in fact similar to the Fermi-liquid behaviour, however, this phase is characterised by power-law dependencies of transport properties as a function of temperature. It is these unusual transport properties which differentiate this phase from the Fermi-liquid. The origin of the non-Fermi-liquid phase is still a matter of debate but could suggest that new physics are required to understand the cuprates.

1.5.4 Discovery of Fe-based superconductors

Ferromagnetism is a mechanism by which certain materials form permanent magnets. It was therefore very surprising when superconductivity was found in LaFePO in 2006 [24] and two years later in LaFeAsO [25] since magnetism is thought to destroy the delicate balance that allows electrons to form Cooper pairs. Both cuprates and Fe-based superconductors have two-dimensional lattices of $3d$ transition metal ions as their building blocks.

All of the Fe-based superconductors that have been discovered belong to a class of poor conductors in the normal state, known as semi-metals. The parent compounds of the cuprates are on the other hand Mott insulators. This suggests that the Mott-Hubbard physics of half-filled Hubbard model is not a good starting point in modelling these systems [23]. This does not exclude the effects of correlations in Fe-based superconductors but they may be moderate or small. A different approach is required. However, in both families, weakening of antiferromagnetism seems to play a role in establishing superconductivity.

The phase diagram of Fe-based superconductors is broadly similar to that of the cuprates. Superconductivity typically emerges at a finite doping in the vicinity of an antiferromagnetic phase. The antiferromagnetic phase, as already mentioned, is metallic suggesting that interactions are generally weaker in the Fe-based superconductors. Because the electrons which carry a magnetic moment travel relatively

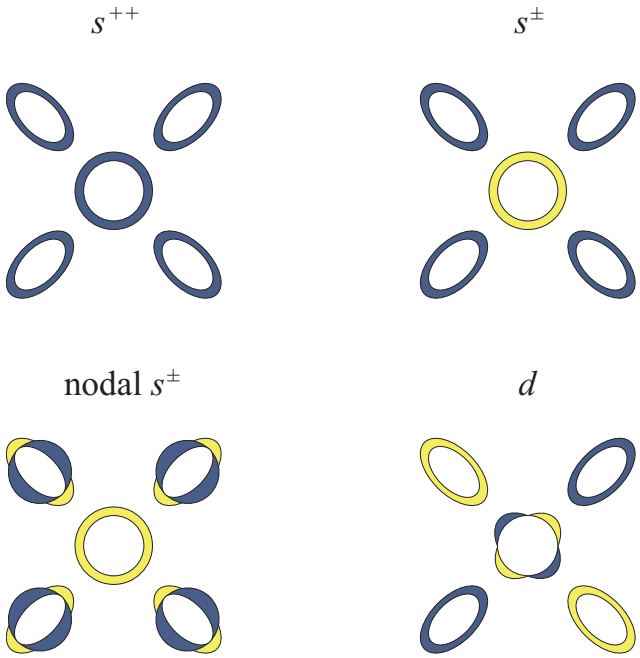

Figure 1.4: Schematic diagram of the symmetries of the order parameters. The order parameter is plotted in the tetragonal basal plane. Different colours indicate different signs of the gap, adapted from Ref. [23].

freely from site to site, the magnetic order is often termed as spin-density-wave, by analogy to Heisenberg antiferromagnets in which the electrons are localised. Unlike in the cuprates, where the long-range magnetic order vanishes before the onset of superconductivity, in Fe-based superconducting materials the competition between these two orders takes several forms. In some systems, including $Fe_ySe_xTe_{1-x}$ which will be discussed in § 5, magnetism can coexist with superconductivity over a small doping range.

The second major difference in the phase diagram of Fe-based superconductors is related to the normal state properties. Underdoped cuprates manifest pseudo-gap behaviour which influences many of the physical properties. In hole-doped cuprates, a strange metal phase near optimal doping is characterised by linear-temperature dependence of resistivity over a wide range of temperatures. In Fe-based superconductors no robust pseudo-gap behaviour is observed in a variety of physical observables [23].

The pairing symmetry and gap structure contain the most relevant information on the superconducting pairing mechanism. In the absence of spin-orbit coupling, the total spin of the Cooper pair is well-defined and can be either $S = 0$ or $S = 1$. Experimental data for Fe-based superconductors appears to rule out the spin-triplet states and we will focus on the singlet groundstate.

In a crystallographic structure with tetragonal symmetry, group theory allows for only five irreducible representations: A_{1g} (s-wave), B_{1g} ($d_{x^2-y^2}$-wave), B_{2g} (d_{xy}-wave), A_{2G} (g-wave) and E_g (d_{xz}- and d_{yz}- wave) according how the order parameter

transforms under symmetry operations of the tetragonal group [23]. Figure 1.4 illustrates the case of s- and $d_{x^2-y^2}$-wave symmetries. All of the order parameters possessing s-wave symmetry are the same under a 90° rotation. The symmetry properties are distinct from the gap structure, which describes the wavevector dependence of the order parameter within a given symmetry class. The isotropic, fully gapped s^{++} and $s^{\pm}$ states only differ by a relative phase of π, which in the later case leads to a change of sign in the order parameter between the hole and electron pockets. The nodal $s^{\pm}$ state shows vanishing of the gap at certain points on the electron pockets. The sign on the electron pockets is still opposite to the hole pockets. The existence of nodes is not obtained from symmetry but from details of the pairing interaction [23].

The d-wave state changes sign when a 90° rotation is applied. The magnitude of the energy gap for the superconductor vanishes at certain points on the Fermi surface. We note that the g-wave states, not shown here, but allowed by symmetry would also have nodes on the electron pockets. However, at present few if any superconductors have been been found to exhibit such gap symmetry and this will not be discussed further. More complicated gap functions with relative phases on different pockets become possible when more pockets are present in the system or when three-dimensional effects are included [23].

It is now well established that the cuprate superconductors possess a d-wave gap symmetry. In contrast, the symmetry of the order parameter appears to be s-type for Fe-superconductors. The presence of hole and electron pockets leads to ambiguities in the sign structure of various states [23]. Assuming spin fluctuations in the paramagnetic phase is the main pairing interaction, it has been argued and confirmed experimentally that a sign changing s-wave gap symmetry produces the necessary pairing of electrons and holes in the newly discovered Fe-based superconductors [26, 27].

The above discussion has been concerned with the spin-singlet groundstate of the Cooper pairs. It should be noted that in the presence of strong ferromagnetic interactions, where parallel spin alignment is favoured, we can expect to find spin-triplet pairing state. Such scenario is likely realised in Sr_2RuO_4 [28] and in some heavy-fermion compounds. The most thoroughly studied case of p-wave ($L = 1$) pairing into a spin-triplet ($S = 1$) is the superfluid state of ^{3}He. The triplet pairing is the consequence of the combination of hard-core repulsion and exchange effects. The hard-core repulsion between ^{3}He atoms can be reduced by forming a paired state with $L > 0$. For parallel alignment, Pauli principle keeps them from occupying the same region which suppresses the effect of hard-core interaction and favours a triplet state [29].

1.6 Brief introduction to multiferroic materials

Multiferroic materials exhibit two or more ferroic properties in the same phase, see Fig. 1.5. The types of order can be ferroelectricity, ferromagnetism, ferroelasticity

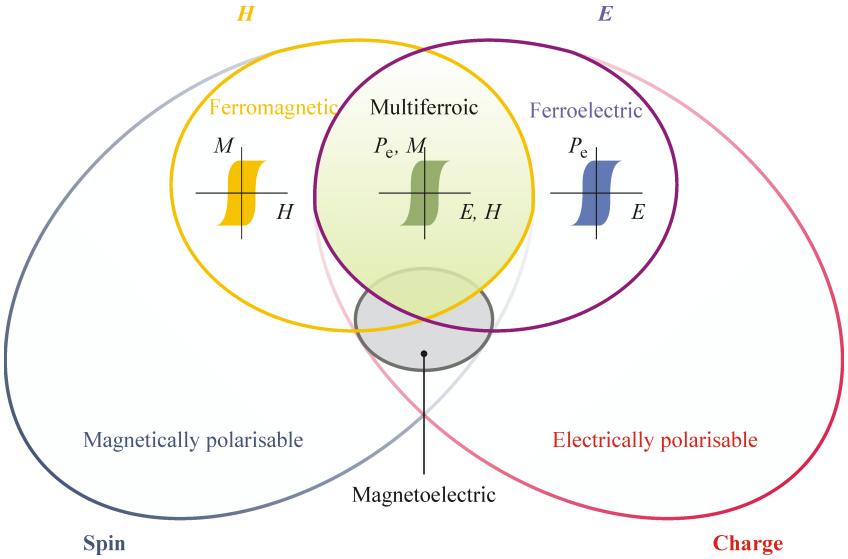

Figure 1.5: Relationship between ferroelectricty and ferromagnetism. In the ideal case, the magnetisation of a ferromagnet shows a hysteresis as a function of applied field H (yellow) and ferroelectrics have a similar response to an electric field E (purple). The grey-shaded area represents the magnetoelectric coupling and the green region is the magnetoelectric multiferroic phase.

and ferrotoroidicity, as well as their anti-ferroic counterparts. This section and subsequent discussions are concerned with the coupling between (anti)ferromagnetism and ferroelectricity – magnetoelectric multiferroics. Ferroelectric materials are an electric analogue of ferromagnetic materials and can spontaneously order below a critical transition temperature. Although there are many magnetic and ferroelectric materials, there are relatively few which exhibit both types of order. Magnetoelectric multiferroics are materials which exhibit spontaneous ferroelectricity and spontaneous magnetic order in a single phase. To simplify the subsequent discussions, magnetoelectric multiferroics will be referred to as simply multiferroics. Magnetoelectric materials are generally different to multiferroics as either electric or magnetic order is not spontaneous.

1.6.1 Magnetoelectric effect

The magnetoelectric effect quite generally describes the coupling between electric and magnetic fields in matter, that is the induction of magnetisation $\boldsymbol{M}$ by an applied electric field $\boldsymbol{E}$ or polarisation $\boldsymbol{P}_\mathrm{e}$ caused by magnetic field $\boldsymbol{H}$. Within the Landau theory, the expansion of the free energy for a magnetoelectric system about the groundstate free energy F_0 is [30],

$$\begin{aligned} F(E,H) = F_0 - P_i^\mathrm{s} E_i - M_i^\mathrm{s} H_i - \frac{1}{2}\varepsilon_0\varepsilon_{ij} E_i E_j - \frac{1}{2}\mu_0\mu_{ij} H_i H_j \\ - \alpha_{ij} E_i H_j - \beta_{ijk} E_i H_j H_k - \gamma_{ijk} H_i E_j E_k - \ldots, \end{aligned} \tag{1.25}$$

the polarisation is then given as,

$$P_i(\boldsymbol{E},\boldsymbol{H}) = -\frac{\partial F}{\partial E_i} = P_i^{\mathrm{s}} + \frac{1}{2}\varepsilon_0\varepsilon_{ij}E_j + \alpha_{ij}H_j + \frac{1}{2}\beta_{ijk}H_jH_k + \gamma_{ijk}H_iE_j + \ldots, \quad (1.26)$$

and analogously the magnetisation can be derived to be,

$$M_i(\boldsymbol{E},\boldsymbol{H}) = -\frac{\partial F}{\partial H_i} = M_i^{\mathrm{s}} + \frac{1}{2}\mu_0\mu_{ij}H_j + \alpha_{ij}E_j + \beta_{ijk}H_jE_i + \frac{1}{2}\gamma_{ijk}E_jE_k + \ldots, \quad (1.27)$$

where the subscripts (i, j, k) refer to orthogonal spatial coordinates, P^{s} and M^{s} denote the spontaneous polarisation and magnetisation, ε_0 and μ_0 are the dielectric and magnetic susceptibilities of vacuum, ε_{ij} and μ_{ij} the second-order tensors of dielectric and magnetic susceptibilities and β_{ijk} and γ_{ijk} are third-order tensor coefficients. The α_{ij} corresponds to the induction of polarisation by a magnetic field or of magnetisation by an electric field [31]. This corresponds to the linear magnetoelectric effect. The majority of research is focused on the linear magnetoelectric effect [31]. Although Landau theory proves that ferroelectricity can be induced by magnetic order, it does not say anything about the microscopic origin.

The vast number of multiferroics has led to the classification into two broad groups. The type-I (or proper) multiferroics contains materials in which ferroelectricity and magnetism arise from different sources and appear largely independent of one another, although there is some coupling between them. The ferroelectricity typically appears at a higher temperature than magnetism and the spontaneous polarisation is often large $10 - 100\,\mu\mathrm{C/cm^2}$ [32]. The second group is the type-II (improper) multiferroics in which magnetism and ferroelectricity emerge concomitantly, implying there is strong coupling between the two degrees of freedom. The polarisation is however usually much smaller than observed in type-I systems of order $10^{-2}\,\mu\mathrm{C/cm^2}$. The later compounds are of fundamental interest but have little practical use at the moment due to their low critical parameters. A goal of research in this area is to find a type-II multiferroic that operates at room temperature.

Coupling between ferroelectricity and magnetism is governed by the symmetries of the two order parameters. The polarisation $\boldsymbol{P}_{\mathrm{e}}$ can be considered to be caused by a local electric dipole moments where positive and negative charges lie asymmetrically about an atomic site within the unit cell such that there is no net charge. The sign of polarisation will change under spatial inversion $\boldsymbol{r} \to -\boldsymbol{r}$ but not under time-reversal $t \to -t$. The magnetisation transforms in the opposite way. Here the local magnetic moments can be considered to be due to circulating currents. Spatial inversion will leave the moments unchanged, whereas time-reversal will cause a change of sign. The difference in transformation properties means that for a system to become multiferroic it must break simultaneously spatial- and time-reversal symmetries. Out of 233 Shubnikov magnetic point groups [2], only 13 allow the si-

[2] A Shubnikov group leaves the magnetic structure invariant, it is a subgroup of the direct product of a space group and the time inversion group in a way that does not contain time reversal operator alone but only in combination with other symmetry elements [33].

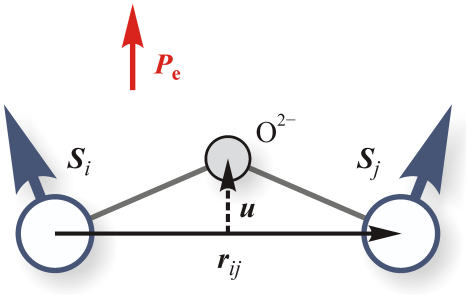

Figure 1.6: Effects of the Dzyaloshinskii-Moriya interaction. The Dzyaloshinskii-Moriya interaction depends on the position of the negative O ion located between two transition metal ions carrying spin $\boldsymbol{S}$ and connected by vector $\boldsymbol{r}$. A local electric dipole is generated as positive and negative charges are displaced by $\boldsymbol{u}$ transverse to $\boldsymbol{r}$.

multaneous appearance of polarisation and magnetisation: 1, 2, 2′, m, m', 3, $3m'$, 4, $4m'm'$, $m'm2'$, $m'm'2'$, 6 and $6m'm'$ [30]. The restrictions in the crystallographic symmetries means that multiferroics are rare in nature.

Linear coupling between $(\boldsymbol{P}_\mathrm{e}, \boldsymbol{E})$ and $(\boldsymbol{M}, \boldsymbol{H})$ is only possible when these vectors vary in both space and time [34]. Coupling between static $\boldsymbol{P}_\mathrm{e}$ and $\boldsymbol{M}$ can only be non-linear and results from competing charge, spin, orbital and lattice degrees of freedom [34].

Most of the type-II multiferroics that have been discovered to date possess a non-collinear magnetic structure. A helicoidal spin structure spontaneously breaks time-reversal as well as spatial inversion symmetries. Therefore, a helicoidal magnetic state allows for the simultaneous presence of multiferroicity. The precise microscopic mechanism responsible for the emergence of ferroelectricity is complex and several models have been proposed, these are summarised below.

Inverse Dzyaloshinskii-Moriya interaction A prominent model to account for non-collinear spins driving the system into a ferroelectric state has been proposed based on the antisymmetric Dzyaloshinskii-Moriya (DM) interaction [35, 36]. Ferroelectricity is the inverse effect, resulting from lattice relaxation in a magnetically ordered state. In this mechanism, which is a relativistic correction to the usual superexchange interaction, O ions are displaced from equilibrium positions driven by the DM interaction between neighbouring transition metal ions. Figure 1.6 shows the symmetry breaking interaction leading to ferroelectricity. The Hamiltonian can be expressed as,

$$\mathcal{H}_\mathrm{DM} = \sum_{ij} \boldsymbol{D}_{ij} \cdot (\boldsymbol{S}_i \times \boldsymbol{S}_j)\,, \tag{1.28}$$

where $\boldsymbol{D}$ is the DM factor related to the O displacement away from the line joining two spins $\boldsymbol{S}_i$ and $\boldsymbol{S}_j$. It is proportional to the spin-orbit coupling λ and the amount by which the O is shifted, expressed as $\boldsymbol{D}_{ij} \propto \lambda \boldsymbol{u} \times \boldsymbol{r}_{ij}$. The interaction shifts the O in the direction perpendicular to the spin chain and

this results in an electric polarisation. This term therefore can give rise to a small canting of the moments. In antiferromagnets, it can result in a weak ferromagnetic moment perpendicular to the antiferromagnetic alignment, as in the case of La_2CuO_4. The DM vector vanishes where there is a centre of inversion between the ith and jth sites.

Spin-current model The spin current model serves as the second microscopic explanation of multiferroicity in helicoidally arranged spin systems, proposed by Katsura *et al.* [37]. The coupling between the spin current and an internal electric field has the same form as the DM interaction [38]. Spontaneous spin-current flows between mutually canted spins, $\boldsymbol{j}_{ij} \propto \boldsymbol{S}_i \times \boldsymbol{S}_j$ produced by the superexchange interaction mediated by an O atom between two transition metal atoms. In analogy to charge currents generating a magnetic field, the spin current induces an electric dipole moment between the pairs of spins given by $\boldsymbol{P}_\mathrm{e} \propto \boldsymbol{r}_{ij} \times \boldsymbol{j}_{ij}$, where spins are connected by vector $\boldsymbol{r}$. The implication of this model is that electric polarisation can occur when there exists non-collinear spin arrangement between adjacent transition metal atoms and the spin rotation axis is not parallel to the magnetic propagation wavevector. Although this model gives simple predictions to the direction in which electric polarisation is generated, it is limited in two important ways. Firstly, the model lacks quantitative prediction results and secondly the concept of spin current in spin-orbital coupled system is not well defined [39].

Electric current cancellation model In systems with strong spin-orbit coupling, ferroelectricity can be induced by non-collinear magnetism through an electric current cancellation process [39]. This model is derived from first principles and gives quantitative predictions to the size of the ferroelectrically induced response. The total ferroelectricity can be written as [39],

$$\boldsymbol{P}_\mathrm{e} = \frac{\varepsilon_0 g}{2 m_\mathrm{e} e \lambda M_0^2} \langle \boldsymbol{M} \times \nabla \times \boldsymbol{M} \rangle, \tag{1.29}$$

where λ is the effective spin-orbit coupling parameter, M_0 is the magnitude of the magnetic moment on an atom site and the $\langle \ldots \rangle$ denote spatial average over the sample volume. The model predicts that the size of the magnetisation does not increase ferroelectricity, which is against what is expected in the phenomenological Ginzburg-Landau theory [39]. It also shows that ferroelectricity is inversely proportional to the spin-orbit coupling. A semi-quantitative estimation gives polarisation of approximately $100\,\mu\mathrm{C/m^2}$ for a typical manganite system [30].

Despite their apparent differences, the three models give a similar prediction that $\boldsymbol{P}_\mathrm{e} \propto \boldsymbol{r}_{ij} \times \boldsymbol{S}_i \times \boldsymbol{S}_j$ and canted spin structure is a prerequisite for ferroelectricity. However, not all helicoidal magnets are ferroelectric. For example Cs_2CuCl_4 has a magnetic structure consisting of counter-rotating spirals [40]. Ferroelectricity is not observed in this compound.

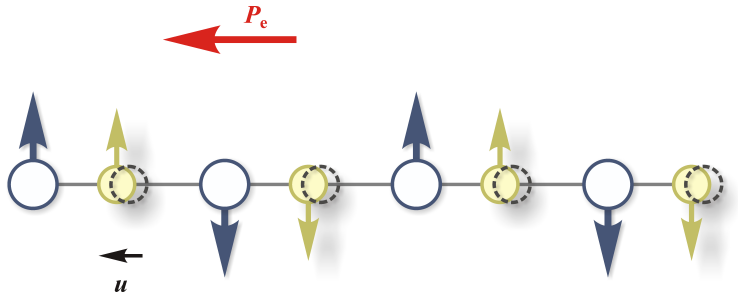

Figure 1.7: One dimensional chain of atoms leading to ferroelectricity through magnetostriction. The dashed grey outline shows the equilibrium position of yellow ions. Due to magnetostriction, they are displaced towards blue ions with moments in the same direction. The yellow and blue ions carry different charges and therefore the distortion results in polarisation observed along the direction of the bonds.

Ferroelectricity can also emerge in type-II multiferroics with collinear magnetic order, without necessarily involving spin-orbit interaction. The origin of polarisation in such materials is due to exchange striction, which is the inverse effect of the symmetric superexchange interaction combined with the effect of charge order. Let us consider the case of a one dimensional Ising spin chain with competing nearest-neighbour ferromagnetic interactions J_{F} and next-nearest-neighbour antiferromagnetic interaction J_{AF}. The groundstate of such a system will be of $\uparrow\uparrow\downarrow\downarrow$ provided $|J_{\mathrm{AF}}/J_{\mathrm{F}}| > 1/2$ in an arrangement shown in Fig. 1.7. The exchange striction associated with the symmetric superexchange interaction will lower the system's energy by shortening the bonds between parallel spins and lengthening those where spins are antiparallel. This breaks the spatial inversion symmetry and polarisation is created along the bond direction, as per $\boldsymbol{P}_{\mathrm{e}} \propto (\boldsymbol{S}_i \cdot \boldsymbol{S}_j)\boldsymbol{r}_{ij}$. A realisation of such a state is found in Ca_3CoMnO_6 [41]. The structure of Ca_3CoMnO_6 consists of alternating Co^{2+} and Mn^{4+} ions. At high temperature the bond distances are the same but as the material orders magnetically, exchange striction distorts the crystal structure and the material becomes ferroelectric.

Although the effect in Ca_3CoMnO_6 relies on transition metal ions of different valencies, this need not be the case. The same effect can be observed in $R\mathrm{MnO}_3$ perovskites where R is small rare earth. The Mn ions order in a $\uparrow\uparrow\downarrow\downarrow$ fashion in the basal plane but exchange striction shifts O ions perpendicular to the Mn–Mn bonds producing a polarisation in the direction of the distortion [32].

The physics of type-II multiferroics where non-collinear spin structure drives the system into a ferroelectric state illustrate that magnetic order is often a result of competing magnetic interactions. This competition usually reduces the ordering temperature of conventional spin-ordered phase [30]. Therefore, relatively few non-collinear multiferroics are observed above 40 K, far below room temperature where their properties would be applicable for practical use in devices.

The search for such materials continues but it seems one possible way of increasing the phase transition temperature is to search for materials with very strong com-

peting interactions. In cuprates, the superexchange interaction J favours collinear arrangement of Cu–O–Cu bonds when $\phi \approx 180°$. The value of J is found to decrease monotonically for decreasing bond angle eventually becoming negative at $\phi \approx 95°$ [30]. Therefore, in cuprates deviations of ϕ from 180° results in competition with higher-order superexchange interactions, often leading to non-collinear magnetic structures. A good example of this effect is CuO investigated in this thesis. The dominant exchange interaction is along Cu–O–Cu bonds with $\phi = 146°$ [42]. Incommensurate magnetic order and ferroelectricity have been found at relatively high temperatures in the range from 213 to 230 K. Therefore, it is interesting to try to understand the mechanism leading to multiferroicity in CuO.

1.7 Work presented in this thesis

Strongly correlated electron systems exhibit a wide range of intriguing physical phenomena due to a multitude of competing order parameters. The studies presented in this thesis examine the roles of magnetism, superconductivity and multiferroicity. Using a combination of experimental techniques we gain a deeper understanding of the processes leading to these properties. The main projects of interests which will be discussed herein are outlined below.

Magnetism and dynamics in Sr doped La_2CoO_4

Hole-doped transition metal oxide antiferromagnets exhibit a range of physical properties due to competing ordered phases. At certain dopings, holes segregate into unidirectional density-wave states which can involve coexistence of charge and magnetic order. Such correlations are often termed as stripes and have been discussed extensively in connection with copper oxide superconductors.

The $La_{2-x}Sr_xCoO_4$ family of compounds, which although not superconducting, share many features with holed-doped copper oxide superconductors. Furthermore, the Co^{3+} ions forming the charge stripes adopt the low spin $S = 0$ state and therefore layered cobaltates offer the chance of investigating fundamental interactions and excited states in an ordered stripe phase.

In order to quantify the dominant exchange interactions we have looked at the parent La_2CoO_4 phase using time-of-flight neutron scattering technique on MAPS instrument at ISIS, UK to comprehensively map out the excitations up to 250 meV. The spectrum was found to be well described by a model which includes the spin and orbital degrees of freedom of Co ions in a crystal field environment. This was then used to explain the magnetic excitations in $x = 1/3$ which display an hourglass-like dispersion analogous to some of the cuprate superconductors.

Interplay of magnetism and superconductivity in $Fe_ySe_xTe_{1-x}$

The recent discovery of Fe-based superconductors raises the interesting question of its origin and relation to cuprate superconductors. One common feature is the emergence of a sharp peak in the magnetic spectrum localised in wavevector upon cooling into the superconducting phase. Using the crystal growth expertise and a combination of magnetometery, μSR and neutron scattering techniques at PSI, Switzerland we have studied extensively the phase diagram of $Fe_ySe_xTe_{1-x}$.

The focus has been looking at the low-energy dynamics. We found that stark contrasts exist between superconducting and purely magnetic phases of $FeSe_xTe_{1-x}$. A resonant mode was found to develop at 6.5 meV centred at $(0.5, 0.5, 0)$ in reciprocal space, whilst the non-superconducting sample showed incommensurate excitation branches in the vicinity of this wavevector. We also demonstrated using polarised inelastic neutron scattering on IN22, ILL, France with the CryoPAD setup that spin fluctuations in and out of the plane of Fe layers are nearly isotropic in

the superconducting phase. This result is consistent with the singlet pairing state of $s^{\pm}$ symmetry.

Multiferroicity in CuO

The superexchange interaction between copper ions coordinated by oxygen as found in low-dimensional copper oxide based superconductors have been extensively studied for many years. Yet, the building block of these materials, CuO, is different in character. In 2008, CuO was found to possess coupling between magnetic and ferroelectric degrees of freedom. Owing to a large superexchange interaction, a ferroelectric response was measured up to 230 K. Although this material has been studied previously in the context of antiferromagnetism, the discovery of multiferroicity has led to a number of theoretical models to be postulated on the possible origin of this phenomenon.

To this end we have carried out careful measurements with an applied electric field to see if we can control the magnetic domains related by inversion symmetry to unambiguously show that magnetism and ferroelectricity are coupled. These measurements were made using polarised neutron diffraction with the MuPAD device installed on the TASP instrument at SINQ, PSI, Switzerland. A group theory based approach was developed to account for the experimental results and has been shown to provide a unique and rigorous solution to the magnetic structure.

Chapter 2

Experimental techniques

Contents

2.1 Introduction

Neutrons are elementary particles which were identified in 1932 by J. Chadwick [43]. The value of the neutron as a probe of condensed matter derives from the fact in the thermal energy range, its de Broglie wavelength is of the same order as interatomic distances in solids and liquids. Interference can occur and this provides information on the scattering system.

The precise mechanism by which an incoming particle is scattered by a compound depends on the properties of the probe such as its charge, spin, energy and so on. In this thesis only neutron scattering has been employed. The neutrality of neutrons allow them to probe the bulk of the sample as neutrons interact with the nucleus of an atom via the strong force. Although it is inherently powerful, the range over which the strong force acts is rather small and therefore the probability of neutron scattering is rather low. Owing to its magnetic dipole moment, a neutron can couple to magnetic field distribution in a crystal thereby probing both nuclear and magnetic structure. The complementary technique of x-ray scattering relies on the electromagnetic interaction between the electron charge clouds surrounding the nuclei. The strength with which an atom scatters x-rays is therefore related to the number of electrons it possesses. Light elements are difficult to detect using x-rays. Conversely, the neutron scattering strength does not vary systematically with the atomic number and is invariant for different valence states.

Neutron diffraction makes possible for the study of crystallographic and magnetic structures, whilst inelastic neutron scattering provide information on spin or lattice excitations. Consequently, neutrons can be used to look at order and dynamics in compounds. This section will introduce the concepts to neutron scattering theory and the technical aspects which allow us to use neutron scattering as a probe of condensed matter systems.

2.2 Concepts of scattering theory

A rigorous theoretical treatment of the process of neutron scattering is given in detail in many textbooks such as Refs. [44–48]. Here I shall present the main features in calculating magnetic cross-sections for elastic and inelastic neutron scattering. In a neutron scattering experiment, an incident neutron with wavevector $\boldsymbol{k}_{\mathrm{i}}$ is scattered by a sample through an angle of 2θ into a final wavevector $\boldsymbol{k}_{\mathrm{f}}$. In this process the momentum, spin and energy of the neutron can change. From conservation of momentum and energy during a scattering process,

$$\boldsymbol{Q} = \boldsymbol{k}_{\mathrm{i}} - \boldsymbol{k}_{\mathrm{f}}, \tag{2.1}$$

$$E = E_{\mathrm{i}} - E_{\mathrm{f}}, \tag{2.2}$$

where $\hbar\boldsymbol{Q}$ and E are the momentum and energy imparted to the crystal, respectively. The latter can be expressed in terms of the initial and final neutron wavevec-

tors, where m_n is the mass of the neutron

$$E = \frac{\hbar^2}{2m_\mathrm{n}}\left(k_\mathrm{i}^2 - k_\mathrm{f}^2\right). \tag{2.3}$$

The elastic scattering process is one in which $k_\mathrm{i} = k_\mathrm{f}$. In inelastic neutron scattering $k_\mathrm{i} \neq k_\mathrm{f}$ and the neutrons can either gain or lose energy by exciting modes in the sample. The condition for a plane wave to be diffracted by a family of planes is given by Bragg's law as, $n\lambda = 2d\sin\theta$, where d is the lattice spacing, λ is the wavelength of the diffracting radiation and n is an integer describing the order of the reflection.

In a neutron scattering experiment, the count rate C as measured by a detector which subtends a solid angle $\Delta\Omega$, with an energy acceptance range of ΔE_f around nominal value E_f and efficiency η is given by,

$$C = \eta\Phi_0 \frac{\mathrm{d}^2\sigma}{\mathrm{d}\Omega\mathrm{d}E_\mathrm{f}}\Delta\Omega\Delta E_\mathrm{f} \tag{2.4}$$

The double differential cross-section $\mathrm{d}^2\sigma/\mathrm{d}\Omega\mathrm{d}E_\mathrm{f}$ gives the probability that a normalised flux of neutrons Φ_0 with incident wavevector $\boldsymbol{k}_\mathrm{i}$ is scattered into a solid angle $\mathrm{d}\Omega$ perpendicular to the direction $\boldsymbol{k}_\mathrm{f}$ and the neutron energy falls within a range between E_f and $E_\mathrm{f} + \mathrm{d}E_\mathrm{f}$.

The double differential cross-section for unpolarised neutrons can be separated into the coherent and incoherent parts,

$$\frac{\mathrm{d}^2\sigma}{\mathrm{d}\Omega\mathrm{d}E_\mathrm{f}} = \left.\frac{\mathrm{d}^2\sigma}{\mathrm{d}\Omega\mathrm{d}E_\mathrm{f}}\right|_\mathrm{coh} + \left.\frac{\mathrm{d}^2\sigma}{\mathrm{d}\Omega\mathrm{d}E_\mathrm{f}}\right|_\mathrm{inc}. \tag{2.5}$$

Generally, the coherent part provides information on the cooperative effects among atoms such as elastic Bragg scattering or inelastic scattering by phonons or magnons. The incoherent part is related to the time correlations of the individual atoms.

The cross-section can be calculated from first principles using quantum mechanics for the cases of elastic, inelastic and polarised neutron scattering. As the neutron probes matter, it acts as a very weak perturbation of the scattering system. A neutron can excite a transition between quantum states, but it does not modify the nature of the states themselves [46]. In the Born approximation, where both incident and outgoing neutrons can be treated as plane waves, the differential cross-section between λ_i and λ_f states and neutron spin states σ_i and σ_f can be expressed as,

$$\left.\frac{\mathrm{d}^2\sigma}{\mathrm{d}\Omega\mathrm{d}E_\mathrm{f}}\right|_{\lambda_\mathrm{i},\sigma_\mathrm{i}\to\lambda_\mathrm{f},\sigma_\mathrm{f}} = \frac{k_\mathrm{f}}{k_\mathrm{i}}\left(\frac{m_\mathrm{n}}{2\pi\hbar^2}\right)^2 |\langle\lambda_\mathrm{f}\sigma_\mathrm{f}|V(\boldsymbol{Q})|\lambda_\mathrm{i}\sigma_\mathrm{i}\rangle|^2\delta(E + E_\mathrm{i} - E_\mathrm{f}), \tag{2.6}$$

where the Fourier transform of the effective interaction potential is given by,

$$V(\boldsymbol{Q}) = \int V(\boldsymbol{r})e^{\mathrm{i}\boldsymbol{Q}\cdot\boldsymbol{r}}\,\mathrm{d}\boldsymbol{r}, \tag{2.7}$$

such that the scattering centres are at positions $\boldsymbol{r}$. Summing over all final states of the sample λ_f and final polarisation states σ_f and taking an average over the initial states λ_i, which occur with a probability p_{λ_i} and over all initial states of the neutron whose probability is p_{σ_i}, we obtain

$$\frac{\mathrm{d}^2\sigma}{\mathrm{d}\Omega\mathrm{d}E_\mathrm{f}} = \frac{k_\mathrm{f}}{k_\mathrm{i}}\left(\frac{m_\mathrm{n}}{2\pi\hbar^2}\right)^2 \sum_{\lambda_\mathrm{f},\sigma_\mathrm{f}}\sum_{\lambda_\mathrm{i},\sigma_\mathrm{i}} p_{\lambda_\mathrm{i}} p_{\sigma_\mathrm{i}} \mid \langle \lambda_\mathrm{f}\sigma_\mathrm{f} \mid V(\boldsymbol{Q}) \mid \lambda_\mathrm{i}\sigma_\mathrm{i}\rangle \mid^2 \delta(E + E_\mathrm{i} - E_\mathrm{f}). \quad (2.8)$$

Energy conservation considerations lead to the δ-function. Equation 2.8 is general and can be applied for different interaction potentials. In the case of unpolarised neutron beam Eq. 2.8 reduces to

$$\frac{\mathrm{d}^2\sigma}{\mathrm{d}\Omega\mathrm{d}E_\mathrm{f}} = \frac{k_\mathrm{f}}{k_\mathrm{i}} S(\boldsymbol{Q}, E), \quad (2.9)$$

where the response function $S(\boldsymbol{Q}, E)$ is defined as,

$$S(\boldsymbol{Q}, E) = \frac{1}{2\pi\hbar}\left(\frac{m_\mathrm{n}}{2\pi\hbar^2}\right)^2 \int_{-\infty}^{\infty} \langle V(\boldsymbol{Q}, 0) V(-\boldsymbol{Q}, t)\rangle e^{-\mathrm{i}Et/\hbar}\, \mathrm{d}t. \quad (2.10)$$

This corresponds to the time and space Fourier transform of the interaction potential. We have used angle brackets $\langle \ldots \rangle$ to denote the average over initial states and t is time. The factor $S(\boldsymbol{Q}, E)$ does not depend on the properties of the neutron. Instead it describes the property of the system of interest and depends on the relative motions of the particles or spins in the system. The aim of most neutron scattering experiments is to measure the response function $S(\boldsymbol{Q}, E)$ and thereby determine microscopic properties of the system.

2.2.1 Nuclear interaction

When neutrons are incident on a sample, they can undergo elastic scattering from the nuclei through the strong nuclear force. Since the strong force acts over extremely short distances, the nuclear potential for an assembly of atoms can be approximated by a spherically symmetry Fermi pseudo-potential (in the absence of nuclear spin) as,

$$V_\mathrm{N}(\boldsymbol{r}) = \frac{2\pi\hbar^2}{m_\mathrm{n}} \sum_j b_j \delta(\boldsymbol{r} - \boldsymbol{r}_j), \quad (2.11)$$

where a neutron at position $\boldsymbol{r}$ interacts with the jth nucleus at position $\boldsymbol{r}_j$. The scattering length b_j represents the strength with which the neutrons are scattered at position $\boldsymbol{r}_j$. In general this quantity is complex as at resonance, the nucleus can absorb the neutron. This is only significant in a few strongly neutron absorbing materials such ^{103}Rh, ^{113}Cd, ^{157}Gd, and so on. The scattering length in such cases becomes strongly dependent on neutron energy. However, in most materials the imaginary part of the scattering length is small and will not be discussed further.

In crystalline solids, the neutrons can interfere with planes of atoms in the

lattice to give Bragg peaks. The scattering cross-section for the elastically scattered neutrons ($E_\mathrm{i} = E_\mathrm{f}$) can be calculated by evaluating Eq. 2.8 using the scattering potential in Eq. 2.11. The coherent differential cross-section is therefore

$$\begin{aligned}\left.\frac{\mathrm{d}^2\sigma}{\mathrm{d}\Omega\mathrm{d}E_\mathrm{f}}\right|_\mathrm{coh}^\mathrm{el} &= |N(\boldsymbol{Q})|^2\delta(E) \\ &= n\frac{(2\pi)^3}{V_0}|F_\mathrm{N}(\boldsymbol{Q})|^2\delta(\boldsymbol{Q}-\boldsymbol{G})\delta(E),\end{aligned} \tag{2.12}$$

where n and V_0 is the number and size of the unit-cell, respectively. The Fourier transform of a crystal lattice $N(\boldsymbol{Q})$ will will give rise to finite intensity only when the scattering wavevector $\boldsymbol{Q}$ is equal to the reciprocal lattice wavevector $\boldsymbol{G}$. The nuclear structure factor $F_\mathrm{N}(\boldsymbol{Q})$ is given by,

$$F_\mathrm{N}(\boldsymbol{Q}) = \sum_j \langle b_j\rangle e^{\mathrm{i}\boldsymbol{Q}\cdot\boldsymbol{r}_j}e^{-W_j}, \tag{2.13}$$

where we consider the coherent scattering length $\langle b\rangle$ of the jth atom. In practice the lattice is not a rigid structure and atoms will fluctuate about their equilibrium positions due to thermal motion. This causes a reduction of the Bragg intensities which is parameterised by the Debye-Waller factor W. In the scope of this thesis, this effect is not important for measurements performed below about 100 K and will not be discussed further.

2.2.2 Magnetic interaction

The scattering of neutrons by atomic magnetic moments can be calculated in similar fashion to nuclear scattering by Eq. 2.8. The relevant interaction is between the dipole magnetic moment of the neutron and the internal magnetic fields of the sample produced by spin and angular momentum of unpaired electrons. The neutron moment is given by,

$$\boldsymbol{\mu}_\mathrm{n} = -\gamma\mu_\mathrm{N}\boldsymbol{\sigma}, \tag{2.14}$$

where the nuclear magneton is $\mu_\mathrm{N} = e\hbar/2m_\mathrm{p}$ and the gyromagnetic ratio $\gamma = 1.913$. The Pauli spin operator $\boldsymbol{\sigma}$ has eigenvalues of ±1. The spin angular momentum and Pauli spin operators for the neutron are related to each other by a factor of two, $\boldsymbol{\sigma} = 2\boldsymbol{s}_\mathrm{n}$. A dipole in an inhomogeneous field $\boldsymbol{B}$ from the sample will experience a potential,

$$V_\mathrm{M}(\boldsymbol{r}) = -\boldsymbol{\mu}_\mathrm{n}\cdot\boldsymbol{B}(\boldsymbol{r}). \tag{2.15}$$

The magnetic field at a distance $\boldsymbol{R}$ from an electron with momentum $\boldsymbol{p}$ and magnetic dipole moment $\boldsymbol{\mu}_\mathrm{e} = -2\mu_\mathrm{B}\boldsymbol{s}$ due to its spin angular momentum $\boldsymbol{s}$ (in units of $\hbar$) is the sum of the magnetic field contributions due to the electron's spin and orbital motion,

$$\boldsymbol{B} = \boldsymbol{B}_S + \boldsymbol{B}_L = \frac{\mu_0}{4\pi R^2}\left(\nabla\times\boldsymbol{\mu}_\mathrm{e}\times\hat{\boldsymbol{R}} - \frac{2\mu_\mathrm{B}}{\hbar}\boldsymbol{p}\times\hat{\boldsymbol{R}}\right). \tag{2.16}$$

The Fourier transform of the magnetic interaction potential can be found to be

$$V_{\mathrm{M}}(\boldsymbol{Q}) = -\mu_0 \boldsymbol{\mu}_{\mathrm{n}} \cdot \boldsymbol{M}_{\perp}(\boldsymbol{Q}). \tag{2.17}$$

The Fourier transform of the real-space magnetisation $\boldsymbol{M}(\boldsymbol{r})$ is defined as $\boldsymbol{M}(\boldsymbol{Q})$, where the component of magnetisation perpendicular to $\boldsymbol{Q}$ is related as $\boldsymbol{M}_{\perp}(\boldsymbol{Q}) = \hat{\boldsymbol{Q}} \times \boldsymbol{M}(\boldsymbol{Q}) \times \hat{\boldsymbol{Q}}$, or

$$\boldsymbol{M}_{\perp}(\boldsymbol{Q}) = -2\mu_{\mathrm{B}} \sum_j e^{\mathrm{i}\boldsymbol{Q}\cdot\boldsymbol{r}_j} \left(\hat{\boldsymbol{Q}} \times \boldsymbol{s}_j \times \hat{\boldsymbol{Q}} + \frac{\mathrm{i}}{\hbar|\boldsymbol{Q}|} \boldsymbol{p}_j \times \hat{\boldsymbol{Q}} \right), \tag{2.18}$$

where the jth electron is located at position $\boldsymbol{r}_j$ and possesses spin and momentum $\boldsymbol{s}_j$ and $\boldsymbol{p}_j$. In the case of unpolarised neutron scattering, it is convenient to separate the differential cross-section into two components belonging to elastic and inelastic scattering as

$$\frac{\mathrm{d}^2\sigma}{\mathrm{d}\Omega \mathrm{d}E_{\mathrm{f}}} = \frac{k_{\mathrm{f}}}{k_{\mathrm{i}}} \left(\frac{\gamma r_0}{2\mu_{\mathrm{B}}} \right)^2 \left[|\boldsymbol{M}_{\perp}(\boldsymbol{Q})|^2 \delta(E) + \tilde{S}(\boldsymbol{Q}, E) \right], \tag{2.19}$$

where $r_0 = \mu_0 e^2/(4\pi m_{\mathrm{e}})$ is known as the classical radius of the electron. The elastic part in Eq. 2.19 is the time-averaged value of magnetisation and measures static correlations should be expressed as the expectation value, $\langle \boldsymbol{M}_{\perp}^{\dagger}(\boldsymbol{Q}) \rangle \langle \boldsymbol{M}_{\perp}(\boldsymbol{Q}) \rangle$. However, in order to simplify the notation, I shall hereafter refer to this quantity as $|\boldsymbol{M}_{\perp}(\boldsymbol{Q})|^2$. The inelastic part is denoted by $\tilde{S}(\boldsymbol{Q}, E)$ and is (to within a constant factor) the dynamical part of $S(\boldsymbol{Q}, E)$ defined in Eq. 2.10.

2.2.2.1 Elastic neutron scattering

The first term in Eq. 2.19 describes the elastic neutron scattering differential cross-section. In analogy to nuclear interaction, the magnetic scattering intensity is given by,

$$\begin{aligned} \left. \frac{\mathrm{d}^2\sigma}{\mathrm{d}\Omega \mathrm{d}E_{\mathrm{f}}} \right|_{\mathrm{coh}}^{\mathrm{el}} &= \left(\frac{\gamma r_0}{2\mu_{\mathrm{B}}} \right)^2 |\boldsymbol{M}_{\perp}(\boldsymbol{Q})|^2 \delta(E) \\ &= n \frac{(2\pi)^3}{V_0} |\boldsymbol{F}_{\perp \mathrm{M}}(\boldsymbol{Q})|^2 \delta(\boldsymbol{Q} - \boldsymbol{G}_{\mathrm{M}}) \delta(E), \end{aligned} \tag{2.20}$$

where $\boldsymbol{G}_{\mathrm{M}}$ is the reciprocal lattice wavevector of the magnetic structure and can be related to the magnetic propagation wavevector $\boldsymbol{\kappa}$ as $\boldsymbol{G}_{\mathrm{M}} = \boldsymbol{G} \pm \boldsymbol{\kappa}$. A magnetic reflection is therefore only allowed when $\boldsymbol{Q} = \boldsymbol{G} \pm \boldsymbol{\kappa}$. In the dipole-dipole approximation the magnetic structure factor is given by,

$$\boldsymbol{F}_{\perp \mathrm{M}}(\boldsymbol{Q}) = \hat{\boldsymbol{Q}} \times \boldsymbol{F}_{\mathrm{M}}(\boldsymbol{Q}) \times \hat{\boldsymbol{Q}}, \tag{2.21}$$

$$\boldsymbol{F}_{\mathrm{M}}(\boldsymbol{Q}) = \sum_j f_j(\boldsymbol{Q}) \boldsymbol{\mu}_j e^{\mathrm{i}\boldsymbol{Q}\cdot\boldsymbol{r}_j} e^{-W_j}. \tag{2.22}$$

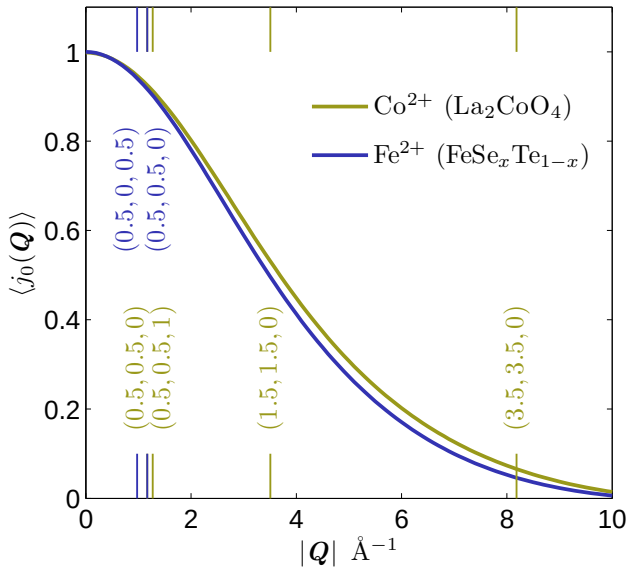

Figure 2.1: Free-ion magnetic form factor for Co^{2+} and Fe^{2+} ions. The variation of the zeroth order spherical Bessel function $\langle j_0(\boldsymbol{Q})\rangle$ with $\boldsymbol{Q}$ is plotted for the case of Co^{2+} and Fe^{2+}. The (h, k, l) indices refer to the reciprocal lattice of the two compounds studied, namely La_2CoO_4 and $FeSe_xTe_{1-x}$. The values of coefficients defining $\langle j_0(\boldsymbol{Q})\rangle$ are taken from Ref. [49].

The effective magnetic moment on site j is described by $\boldsymbol{\mu}$, as discussed in § 2.2.2, both spin and angular momentum of electrons can contribute to the magnetic moment. The magnetic form factor $f(\boldsymbol{Q})$ is obtained from the Fourier transform of the magnetisation distribution of a single magnetic atom [49]. For magnetisation with a unique direction,

$$\boldsymbol{\mu} \int m(\boldsymbol{r}) e^{\mathrm{i}\boldsymbol{Q}\cdot\boldsymbol{r}} \, \mathrm{d}\boldsymbol{r} = \boldsymbol{\mu} f(\boldsymbol{Q}), \tag{2.23}$$

where $m(\boldsymbol{r})$ is a normalised scalar function describing how the intensity of magnetisation varies over the volume of the atom [49]. In the dipole approximation, that is when the magnitude of $\boldsymbol{Q}$ is much smaller than the reciprocal of the mean radius of the wavefunction for the unpaired electrons, it can be shown that for a single atom [50],

$$\boldsymbol{M}(\boldsymbol{Q}) \approx -2\mu_{\mathrm{B}} \left[\langle j_0(\boldsymbol{Q})\rangle \boldsymbol{S} + \frac{1}{2} \left(\langle j_0(\boldsymbol{Q})\rangle + \langle j_2(\boldsymbol{Q})\rangle \right) \boldsymbol{L} \right], \tag{2.24}$$

where $\boldsymbol{S}$ and $\boldsymbol{L}$ are the total spin and orbital angular momentum operators.

For $3d$ transition metal ions the crystal field is usually much stronger than the spin-orbit coupling. The orbital moment $\boldsymbol{L}$ is usually quenched, but the spin-orbit interaction can induce a small component of $\boldsymbol{L}$ in a direction parallel or anti-parallel to the spin $\boldsymbol{S}$. It can be shown that in this case $\boldsymbol{L}$ is replaced by $(g-2)\boldsymbol{S}$ and the

magnetisation in Eq. 2.24 reduces to,

$$\boldsymbol{M}(\boldsymbol{Q}) \approx -g\mu_{\mathrm{B}} f(\boldsymbol{Q})\boldsymbol{S} = \boldsymbol{\mu} f(\boldsymbol{Q}), \tag{2.25}$$

where $g = 2$ when the orbital angular momentum is fully quenched. The dipole magnetic form factor can then be approximated as,

$$f(\boldsymbol{Q}) = \langle j_0(\boldsymbol{Q})\rangle + \frac{2-g}{g}\langle j_2(\boldsymbol{Q})\rangle. \tag{2.26}$$

The $4f$ ions usually have both spin and orbital degrees of freedom and the total angular momentum J is a good quantum number. From Eq. 2.24, the magnetisation is written as,

$$\boldsymbol{M}(\boldsymbol{Q}) \approx -g_J\mu_{\mathrm{B}} f(\boldsymbol{Q})\boldsymbol{J} = \boldsymbol{\mu} f(\boldsymbol{Q}), \tag{2.27}$$

and g_J is the Landé splitting factor, defined in Eq. 1.3. The magnetic form factor defined in Eq. 2.26 has the same form but we must replace g by g_J.

The radial distribution of magnetisation surrounding a single magnetic atom can be approximated by nth order spherical Bessel functions $\langle j_n(Q)\rangle$. These in turn can be approximated by a sum of suitable analytical expressions for d electrons of the $3d$ and $4d$ series and the f electrons of some rare earth and actinide ions [49]. In this approximation,

$$\langle j_0(s)\rangle = A_1 e^{\alpha_1 s^2} + A_2 e^{\alpha_2 s^2} + A_3 e^{\alpha_3 s^2} + A_0 \tag{2.28}$$

$$\langle j_{n>0}(s)\rangle = \left(A_1 e^{\alpha_1 s^2} + A_2 e^{\alpha_2 s^2} + A_3 e^{\alpha_3 s^2} + A_0\right) s^2, \tag{2.29}$$

where $s = |\boldsymbol{Q}|/(4\pi) = \sin\theta/\lambda$, the neutron wavelength is denoted by λ. The numerical values of the coefficients A_n and α_n are tabulated in Ref. [49]. Figure 2.1 illustrates how the leading order approximation of the magnetic form factor varies as a function of reciprocal lattice wavevector $\boldsymbol{Q}$. The plotted function is spherically symmetric reflecting the real-space magnetisation decreasing monotonically away from the ion. This need not always be the case and the octahedral ligand field such as in structures containing CuO_6 can cause significant asymmetry in the magnetic form factor, as found in $PrBa_2Cu_3O_{6+x}$ for example [51]. However, for magnetic structures considered hereafter such effects are not considered to be important.

2.2.2.2 Inelastic neutron scattering

Ordered magnetic moments can fluctuate about their average orientations. It costs energy to create the fluctuations and the variation of magnetic excitation energy E as a function of wavevector $\boldsymbol{Q}$ can be measured using inelastic neutron scattering. The response function $S(\boldsymbol{Q}, E)$ is related to the Fourier transform of the time-

dependent correlation function for the magnetisation, and can be written as

$$S(\boldsymbol{Q},E) = \left(\frac{\gamma r_0}{2\mu_\mathrm{B}}\right)^2 \sum_{\alpha\beta}(\delta_{\alpha\beta} - \hat{Q}_\alpha\hat{Q}_\beta)S^{\alpha\beta}(\boldsymbol{Q},E), \tag{2.30}$$

$$S^{\alpha\beta}(\boldsymbol{Q},E) = \frac{1}{2\pi\hbar}\int_{-\infty}^{\infty}\langle \boldsymbol{M}_\alpha(-\boldsymbol{Q},0)\boldsymbol{M}_\beta(\boldsymbol{Q},t)\rangle e^{-\mathrm{i}Et/\hbar}\,\mathrm{d}t, \tag{2.31}$$

where $\{\alpha,\beta\} = \{x,y,z\}$ are Cartesian components of the magnetisation operator. Therefore, the scattering is dependent on the magnetic fluctuations in the system. Unlike scattering from nuclei, the magnetic interaction contains a term $(\delta_{\alpha\beta}-\hat{Q}_\alpha\hat{Q}_\beta)$ which selects the component of the magnetisation which is perpendicular to the momentum transfer $\boldsymbol{Q}$.

A response function for a macroscopic system relates the change in the ensemble-average physical quantity (i.e. magnetisation) to an external force (i.e. oscillating magnetic field) [52]. In the limit where the external force is sufficiently small, the physical observable changes linearly with applied force. Furthermore, the initial state of the system must be in thermal equilibrium before the force is applied. These conditions form the basis of the linear response theory which can be applied to condensed matter systems as a means of comparing theoretical models to observable spectra.

In a realistic system in a thermal bath at temperature T, a neutron exciting a lower state in energy is more likely than a neutron losing energy through an energy loss process with equal but opposite wavevector and energy transfer. The proportion in which the two states are thermally populated is directly related by the Boltzmann factor. Therefore, the response function will be related by the principle of detailed balance as [52],

$$S(\boldsymbol{Q},E) = e^{E/k_\mathrm{B}T}S(-\boldsymbol{Q},-E). \tag{2.32}$$

In addition, the fluctuation-dissipation theorem relates the imaginary part of the generalised susceptibility $[\chi(\boldsymbol{Q},E) = \chi'(\boldsymbol{Q},E) + \mathrm{i}\chi''(\boldsymbol{Q},E)]$ to the dynamical part of $S(\boldsymbol{Q},E)$ by,

$$\tilde{S}(\boldsymbol{Q},E) = \frac{1}{\pi}[1+n(E)]\chi''(\boldsymbol{Q},E), \tag{2.33}$$

where the Bose-Einstein thermal population factor is $n(E) = [\exp(E/k_\mathrm{B}T) - 1]^{-1}$. The imaginary part of the susceptibility corresponds to the absorption of energy from an external field, in this case due to magnetic fluctuations. The physical interpretation resulting in absorption is because in thermal equilibrium transitions from lower to higher energy states are more likely than transitions from higher to lower energy.

Type	Contribution	Description
N	$\boldsymbol{P}_\mathrm{i} NN^*$	Incident polarisation is conserved when only considering atomic structure
M	$-\boldsymbol{P}_\mathrm{i}(\boldsymbol{M}_\perp \cdot \boldsymbol{M}_\perp^*)$ $+ \boldsymbol{M}_\perp(\boldsymbol{P}_\mathrm{i} \cdot \boldsymbol{M}_\perp^*)$ $+ \boldsymbol{M}_\perp^*(\boldsymbol{P}_\mathrm{i} \cdot \boldsymbol{M}_\perp)$	Incident polarisation is spin flip except for the component with $\boldsymbol{P}_\mathrm{i} \parallel \boldsymbol{M}_\perp$
C	$-\mathrm{i}\boldsymbol{M}_\perp^* \times \boldsymbol{M}_\perp$	Intensity is dependent on the initial polarisation, the chiral term is non-zero whenever $\boldsymbol{M}_\perp$ is not parallel to $\boldsymbol{M}_\perp^*$, as for helicoidal magnetic structures
I	$N\boldsymbol{M}_\perp^* + N^*\boldsymbol{M}_\perp -$ $\mathrm{i}\left[(N\boldsymbol{M}_\perp^* - N^*\boldsymbol{M}_\perp) \times \boldsymbol{P}_\mathrm{i}\right]$	Polarisation is created along $\boldsymbol{M}_\perp$ when nuclear and magnetic Bragg peaks coincide.

Table 2.1: Description of the four terms contained in Eq. 2.35 for elastic polarised neutron scattering. The types are labeled as: (N) nuclear, (M) magnetic, (C) magnetic chiral and (I) nuclear-magnetic interference, from Ref. [53].

2.2.3 Polarised neutron scattering

The previous section have been primarily concerned with unpolarised neutron scattering, where only the change in the momentum is considered. Polarised neutron scattering makes use of the incident and outgoing neutron spin state to provide additional information on the magnetic system. The polarisation of a neutron beam is a statistical quantity defined as the normalised expectation value of an ensemble of neutron spins. Scattering from a sample can in general reorient the neutron moment from one orientation to any other orientation in three dimensions. This process can be described by a polarisation matrix $P_{\alpha\beta}$ which is a second rank tensor. The equations for elastic neutron polarimetry based on standard theory of neutron interaction with matter have been established in the 1960s by Blume and Maleyev [54, 55]. Although these equations are useful in gaining insight into how different scattering processes affect the terms in the polarisation matrix, the formulation cannot be used directly when dealing with more realistic systems with different magnetic domains. The total neutron cross-section due to a single domain for incident polarisation $\boldsymbol{P}_\mathrm{i}$ of the neutron beam is,

$$\sigma = NN^* + \boldsymbol{M}_\perp \cdot \boldsymbol{M}_\perp^* + \boldsymbol{P}_\mathrm{i} \cdot (\boldsymbol{M}_\perp N^* + \boldsymbol{M}_\perp^* N) + \mathrm{i}\boldsymbol{P}_\mathrm{i} \cdot (\boldsymbol{M}_\perp^* \times \boldsymbol{M}_\perp), \tag{2.34}$$

where the $\boldsymbol{Q}$-dependencies have been omitted for clarity. The polarisation of the beam after elastic scattering from the sample $\boldsymbol{P}_\mathrm{f}$ relative to the original polarisation has contributions primarily from nuclear, magnetic, magnetic chiral and magnetic-

nuclear interference terms and is of the form,

$$\boldsymbol{P}_{\mathrm{f}}\sigma = (\boldsymbol{P}_{\mathrm{f}}\sigma)_{\mathrm{N}} + (\boldsymbol{P}_{\mathrm{f}}\sigma)_{\mathrm{M}} + (\boldsymbol{P}_{\mathrm{f}}\sigma)_{\mathrm{C}} + (\boldsymbol{P}_{\mathrm{f}}\sigma)_{\mathrm{I}}, \tag{2.35}$$

where the main contributions to elastic neutron scattering are listed in Table 2.1. It can be observed that scattering neutrons from mixed nuclear-magnetic Bragg reflections or from a helicoidal magnetic structure can create polarisation of the neutron beam [56]. The former is the method by which single-crystal polarisers § 2.4.3 can be created.

The central equation describing neutron scattering is given by Eq. 2.8 where the differential scattering cross-section,

$$\frac{\mathrm{d}^2\sigma}{\mathrm{d}\Omega\mathrm{d}E_{\mathrm{f}}} \propto |\langle\lambda_{\mathrm{f}}\sigma_{\mathrm{f}}|V(\boldsymbol{Q})|\lambda_{\mathrm{i}}\sigma_{\mathrm{i}}\rangle|^2\delta(E + E_{\mathrm{i}} - E_{\mathrm{f}}). \tag{2.36}$$

This can be shown to lead to the Blume-Maleyev equations but can also be used to determine the scattering cross-sections for multi-domain structures as well as inelastic polarised scattering processes. We have already established that the interaction potential is in general $V(\boldsymbol{Q}) = V_{\mathrm{N}}(\boldsymbol{Q}) + V_{\mathrm{M}}(\boldsymbol{Q})$ defined in Eqs. 2.11 and 2.17. For an interaction potential that contains both nuclear and magnetic contributions, due to the square of the matrix element of $V(\boldsymbol{Q})$, the cross-section can be separated into three terms – purely nuclear, purely magnetic and one involving nuclear-magnetic interference. Unpolarised neutron scattering is not sensitive to nuclear-magnetic interference as these terms vanish on averaging of spin states. It is useful to define the polarisation matrix where a neutron with initial spin state $|\beta\rangle$ scatters from the interacting potential into a final state $|\alpha\rangle$ as,

$$P_{\alpha\beta} = \frac{|\langle\alpha|V(\boldsymbol{Q})|\beta\rangle|^2 - |\langle\alpha|V(\boldsymbol{Q})|\bar{\beta}\rangle|^2}{|\langle\alpha|V(\boldsymbol{Q})|\beta\rangle|^2 + |\langle\alpha|V(\boldsymbol{Q})|\bar{\beta}\rangle|^2}, \tag{2.37}$$

where the cross-section can be measured in a polarised neutron scattering experiment and the weighted difference between non-spin-flip and spin-flip channels compared to magnetic structure models. It is convenient to define the frame of reference as x the direction parallel to $\boldsymbol{Q}$, z perpendicular to the scattering plane and y completing the right-handed coordinate system, such that $\{\alpha, \beta\} = \{x, y, z\}$. In the trivial case where the reflection which is probed by polarised neutrons is purely due to nuclear scattering, the interaction potential leaves the incident neutron spin invariant. The polarisation matrix, for ideal beam polarisation, is therefore $P_{\alpha\beta} = \delta_{\alpha\beta}$. Let us now consider the purely magnetic interaction potential where the Fourier transform of the magnetisation $\boldsymbol{M}(\boldsymbol{Q}) = (M_x, M_y, M_z)$ and the $\boldsymbol{Q}$-dependence of the components has been neglected for clarity. Since the neutron can only probe magnetic correlations perpendicular to the scattering wavevector, for a given reflection, it is not possible to probe the M_x component of the magnetisation. The cross-section for polarised neutron scattering from magnetic correlations is therefore reduced to be proportional to $|\langle\alpha|\sigma_y M_y + \sigma_z M_z|\beta\rangle|^2$. The matrix element can

therefore allow us to separate the different components of $\boldsymbol{M}_\perp$. The Pauli spin matrices are defined for a spin-1/2 particle to be,

$$\sigma_x = \begin{pmatrix} 0 & 1 \\ 1 & 0 \end{pmatrix}, \qquad \sigma_y = \begin{pmatrix} 0 & -\mathrm{i} \\ \mathrm{i} & 0 \end{pmatrix}, \qquad \sigma_z = \begin{pmatrix} 1 & 0 \\ 0 & -1 \end{pmatrix}. \tag{2.38}$$

The polarisation matrix for a magnetic reflection in the absence of nuclear-magnetic interference and for $|\boldsymbol{P}_\mathrm{i}| = 1$, i.e. perfect incident beam polarisation, can then be found as,

$$P = \begin{pmatrix} -1 & 0 & 0 \\ H & -K & L \\ H & L & K \end{pmatrix} \tag{2.39}$$

$$\begin{aligned} HD &= \mathrm{i}(M_y M_z^* - M_y^* M_z), \\ KD &= |M_z|^2 - |M_y|^2, \\ LD &= M_y M_z^* + M_y^* M_z, \\ D &= |M_y|^2 + |M_z|^2. \end{aligned} \tag{2.40}$$

There are several important consequences of these equations. The polarisation matrix can in principle be calculated for both static and dynamic correlations as already discussed, Eq. 2.36 used in the derivation is rather general. The P_{xx} term can be readily used to identify the nature of scattering, a nuclear reflection will give $P_{xx} = 1$ whereas for a magnetic reflection $P_{xx} = -1$. This relates the fact that nuclear interaction, as defined in Eq. 2.11, does not contain operators which act on the neutron spin. Therefore, in a coherent scattering process, the neutron spin will not be flipped by such a nuclear interaction whereas a spin-flip will occur when the neutron experiences a magnetic dipolar interaction. It should be noted that nuclear spin incoherent scattering can flip the spin and thereby contribute to a featureless spin-flip background.

The chiral term in Eq. 2.40 can be equivalently expressed as $HD = -\mathrm{i}(\boldsymbol{M}_\perp^* \times \boldsymbol{M}_\perp)$, as in Table 2.1, and is a signature of non-collinear magnetic order. Complicated magnetic structures can be solved using spherical neutron polarimetry to determine the polarisation matrix. Usually this requires collection of polarisation matrices at several non-equivalent reflections and knowledge of the crystal symmetry in order to account for depolarisation of the matrix elements due to the presence of domains. For a single magnetic domain the summation $H^2 + K^2 + L^2 = 1$ will hold for ideal beam polarisation.

Magnetic domain structures occur whenever the symmetry of the ordered magnetic structure is lower than that of the paramagnetic phase [48]. Some of the possible domains are as follows:

Configuration domains or $\boldsymbol{\kappa}$-domains Domains in which the translational symmetry has been lost. This is when the magnetic propagation wavevector $\boldsymbol{\kappa}$ is not transformed into $\boldsymbol{G} \pm \boldsymbol{\kappa}$ on applying symmetry operations of the param-

agnetic group. The symmetry elements of the space group that change the propagation wavevector and are related by a rotation form the arms of the star of $\boldsymbol{\kappa}$. The symmetry elements that produce $\boldsymbol{\kappa}$-domains belong to $\{G_0 - G_{\boldsymbol{\kappa}}\}$. The energy of the domains is equivalent.

180° domains When a material orders magnetically, time inversion symmetry is lost. These are always present in antiferromagnetically ordered systems and cannot be distinguished by neutron scattering.

Spin domains These domains occur when the lattice has symmetry equivalent directions, for example moments on a square motif cannot have a unique direction. From symmetry considerations these are the domains which belong to the little group where $G_{\boldsymbol{\kappa}} \in G_0$, in which the symmetry operations leave $\boldsymbol{\kappa}$ unchanged but are part of the paramagnetic space group G_0.

Chiral domains In non-collinear magnetic structures, chiral domains can occur. The paramagnetic space group is centrosymmetric but the ordered magnetic structure is not. They are a special type of $\boldsymbol{\kappa}$-domains in which $+\boldsymbol{\kappa} \neq -\boldsymbol{\kappa}$. Polarised neutron scattering is capable of distinguishing between the chiral domains.

2.3 Representation analysis of magnetic structures

The technique that will be presented here is the application of group theory to magnetic structures and is termed representational analysis [33, 57–65]. The pieces of information that are required for these calculations are the propagation wavevector $\boldsymbol{\kappa}$, the crystallographic space group and the atomic coordinates of the magnetic atoms in the paramagnetic phase. The representational analysis is a powerful theoretical technique which allows for the determination of possible magnetic structures as imposed by the crystallographic symmetry and the magnetic ordering wavevector. Comprehensive analysis can be made using the SARAh [66] and BasiReps [67] program packages.

The formal definition of a group G containing elements g_i with an operation $\circ$ acting on g_i, satisfies the following axioms.

Associativity $[g_i \circ (g_j \circ g_k) = (g_i \circ g_j) \circ g_k]$ The multiplication is associative

Identity $[g_i \circ E = E \circ g_i = g_i]$ There exists a unique identity element E

Closure $[g_i \circ g_j = g_k$ such that $g_k \in G]$ The group is closed, the multiplication of two elements produces an element which is a member of the same group

Inverse $[g_i \circ g_i^{-1} = g_i^{-1} \circ g_i = E]$ Every element g_i has an inverse g_i^{-1}

Some groups have the additional property of commutation and are termed abelian, the non-commutative groups are referred to as non-abelian. Commutation satisfies the relation that the product of two elements in the group is the same regardless of the order in which they are combined.

Each space group contains a set of symmetry operations g_n which act on a general position vector $\{x, y, z\}$ in the cell, which is defined with respect to the crystallographic axes $\{\boldsymbol{a}, \boldsymbol{b}, \boldsymbol{c}\}$. The symmetry elements can be described by a combination of unitary transformation matrix R and a translation $\boldsymbol{\tau}$, such that the position 3-vector $\boldsymbol{x}$ can be related to $\boldsymbol{x}'$ as $\boldsymbol{x}' = \{R|\boldsymbol{\tau}\}\boldsymbol{x} = R\boldsymbol{x} + \boldsymbol{\tau}$. The symmetry elements g_n which leave the crystallographic unit cell unchanged under their action form the paramagnetic space group G_0.

The effect of applying a symmetry operation on an atom and its magnetic moment is to simultaneously change the atom's position and moment direction. The magnetic moment is an axial vector, i.e. one which does not change under an inversion operation. Conversely, polar vectors are reversed by an inversion. The symmetry arguments presented hereafter for the magnetic structure can equally well be applied to the problem of phonon modes, whose origin – atomic displacements – are polar vectors. Both polar and axial vectors have the same transformation properties for rotations, as illustrated in Fig. 2.2.

The paramagnetic little group $G_{\boldsymbol{\kappa}}$ is a subset of elements within the G_0 group ($G_{\boldsymbol{\kappa}} \subseteq G_0$) which leave the propagation vector invariant under operation R. The star of $\boldsymbol{\kappa}$ is defined as the set of non-equivalent propagation vectors produced by the action of symmetry elements of the space group. The set of matrices which

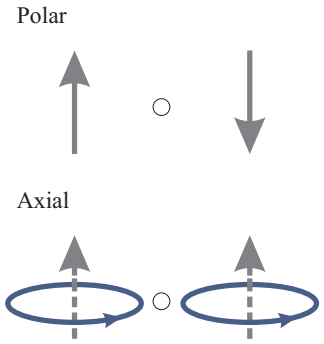

Figure 2.2: Polar and axial vectors under improper rotations. Diagram to show the difference between polar and axial vectors under an inversion operator $\bigcirc$.

describe the transformation of the magnetic structure by symmetry elements in the $G_{\boldsymbol{\kappa}}$ group is the representation of $G_{\boldsymbol{\kappa}}$. However, it is convenient to transform the representation of $G_{\boldsymbol{\kappa}}$ into the irreducible representations which are orthogonal to one another. A character table can be constructed by considering the effect of the symmetry operations within $G_{\boldsymbol{\kappa}}$ on the magnetic structure $|\Psi\rangle$ for each of the irreducible representations. The structure should transform as $R(g)|\Psi\rangle = \chi(g)|\Psi\rangle$, where χ is the character and can in general be complex.

The magnetic representation Γ_{mag} is the result of the symmetry operations on magnetic (axial) and position (polar) vectors. The two effects are independent and can be treated separately. The symmetry elements of group $G_{\boldsymbol{\kappa}}$ permute the atomic positions such that,

$$g_n \boldsymbol{x}_i = \boldsymbol{x}_j. \tag{2.41}$$

It is possible that the symmetry operation takes the atom outside of the zeroth unit cell. In such case, a phase factor of $e^{\mathrm{i}\boldsymbol{\kappa}\cdot(\boldsymbol{x}_j - \boldsymbol{x}_i)}$ is required. The matrix which identifies the permutation of atom labels and a phase change is the permutation representation Γ_{perm}.

The magnetic moments must obey the axial vector property and remain invariant under an inversion. Therefore, the magnetic vector of an atom $\boldsymbol{\mu} = (\mu_a, \mu_b, \mu_c)$ is related to the rotational part of the symmetry element of $G_{\boldsymbol{\kappa}}$ as,

$$\boldsymbol{\mu}' = |R| R \boldsymbol{\mu}, \tag{2.42}$$

where $|R|$ is the determinant of R required to conserve the symmetry of the axial vector under improper rotations. The axial representation Γ_{axial} relates how the moment vector is altered by the symmetry operations and is a 3×3 matrix. The character of permutation and axial vector representations is simply given by the trace of the respective representations. The magnetic representation Γ_{mag} is then a tensor product of the permutation and axial representations,

$$\Gamma_{\text{mag}} = \Gamma_{\text{perm}} \times \Gamma_{\text{axial}}, \tag{2.43}$$

$$\chi_{\text{mag}} = \chi_{\text{perm}} \chi_{\text{axial}}, \tag{2.44}$$

where Γ_{mag} has dimensions of $3N \times 3N$. Any magnetic representation is reducible to block-diagonal form by a summation over the irreducible representations Γ_ν,

$$\Gamma_1\mu_1 + \Gamma_2\mu_2 + \ldots + \Gamma_\nu\mu_\nu = \begin{pmatrix} \Gamma_1 & 0 & \ldots & 0 \\ 0 & \Gamma_2 & \ldots & 0 \\ \vdots & \vdots & & \vdots \\ 0 & 0 & \ldots & \Gamma_\nu \end{pmatrix} \begin{pmatrix} \mu_{\Gamma_1} \\ \mu_{\Gamma_2} \\ \vdots \\ \mu_{\Gamma_\nu} \end{pmatrix}. \tag{2.45}$$

Each of the matrices Γ_ν acts only on a subspace of $3N$-spin components μ_{Γ_ν}. The magnetic representation can then be described as,

$$\Gamma_{\text{mag}} = \sum_\nu n_\nu \Gamma_\nu, \tag{2.46}$$

$$n_\nu = \frac{1}{n(G_{\boldsymbol{\kappa}})} \sum_{g \in G_{\boldsymbol{\kappa}}} \chi_{\text{mag}}(g)\chi_{\Gamma_\nu}(g)^*, \tag{2.47}$$

The value of n_ν tells us how many distinct basis vector we can expect for each irreducible representation. The basis vectors $\boldsymbol{\psi}$ are calculated using the projection operator technique by using a trial functions along crystallographic axes $\boldsymbol{m}_a = (1,0,0)$, $\boldsymbol{m}_b = (0,1,0)$ and $\boldsymbol{m}_c = (0,0,1)$. The projection operator formula to find the basis vector $\boldsymbol{\psi}$ for magnetic representation Γ_ν is given as,

$$\boldsymbol{\psi}_{\alpha\nu} = \sum_{g \in G_{\boldsymbol{\kappa}}} \chi^*_\nu(g) \sum_n \delta_{n,g_n} |R(g)| R(g)\boldsymbol{m}_\alpha \tag{2.48}$$

where $\chi(g)$ is the character of the little group $G_{\boldsymbol{\kappa}}$. In general, any linear combination of the basis vectors will have the symmetry of the irreducible representation. The moment distribution $\boldsymbol{M}_j$ of jth atom can be expressed as the Fourier transform of the linear combination of basis vectors $\boldsymbol{\Psi}_j = \sum_\alpha C_\alpha \boldsymbol{\psi}_\alpha$,

$$\boldsymbol{M}_j = \sum_{\boldsymbol{\kappa}} \sum_\alpha C_\alpha \boldsymbol{\psi}_\alpha e^{-\mathrm{i}\boldsymbol{\kappa}\cdot\boldsymbol{\tau}}, \tag{2.49}$$

where C_α, which can be complex, is the coefficient describing the mixing of the basis vectors and the summation is taken over all possible propagation vectors $\boldsymbol{\kappa}$. This can lead to the unphysical result of a complex moment on an atom. The basis vectors can be brought into a form in which they are completely real by forming a linear combination of each basis vector with a basis vector whose ordering is described by $-\boldsymbol{\kappa}$. These basis vectors are the complex conjugates of $+\boldsymbol{\kappa}$ deduced from the projection of test functions [68],

$$\boldsymbol{M}_j = \sum_\alpha \left(C_\alpha \boldsymbol{\psi}_\alpha e^{-\mathrm{i}\boldsymbol{\kappa}\cdot\boldsymbol{\tau}} + C^*_\alpha \boldsymbol{\psi}^*_\alpha e^{\mathrm{i}\boldsymbol{\kappa}\cdot\boldsymbol{\tau}} \right), \tag{2.50}$$

which is equivalent to,

$$\boldsymbol{M}_j = 2\sum_{\alpha} |C_\alpha| \hat{\boldsymbol{v}}_\alpha \cos\left(\boldsymbol{\kappa}\cdot\boldsymbol{\tau} + \omega_\alpha + \theta_\alpha\right), \tag{2.51}$$

where the basis vectors in a direction $\hat{\boldsymbol{v}}$ can be expressed as $\boldsymbol{\psi} = e^{-\mathrm{i}\omega}\hat{\boldsymbol{v}}$ and the complex coefficient as $C = |C|e^{-\mathrm{i}\theta}$. The phase contribution ω is restricted by the symmetry of the space group, whereas θ is a free parameter.

2.4 Instrumentation

The field of neutron scattering techniques is vast and the choice of instruments depends on the problem which is tackled. The majority of the work in this thesis was carried on triple-axis spectrometers: TASP at SINQ, Paul Scherrer Institut (PSI), Switzerland and IN22 and IN8 at Insitut Laue-Langevin (ILL), France. The time-of-flight measurements were carried out using the MAPS spectrometer at ISIS, UK.

2.4.1 Neutron sources

There are two methods of high flux neutron production for use in scattering experiments – spallation (PSI, ISIS) and reactor sources (ILL). A spallation source produces relatively lower flux of neutrons than a reactor source but with a broad range of energies. Retrospectively, the spallation process is about an order of magnitude more efficient in producing neutrons [69]. In order to produce neutrons by this method, protons are accelerated to high energies in pulses before colliding with a heavy metal target. The proton beam can be produced in a number of ways, such as [49],

(i) Linear accelerators such as LAMPF at Los Alomos. However, the long pulses or high frequencies cannot be used effectively in neutron scattering experiments. Particle storage rings are required to compress the pulses.

(ii) Cyclotrons such as SINQ at PSI produce continuous neutron beam by the spallation reaction.

(iii) Synchrotrons as used at ISIS where are H^- ions are initially accelerated by linear accelerator which then injects protons into the synchrotron for further acceleration. Typically an initial pulse width of approximately 1 μs at a frequency of 10–50 Hz is used in the neutron production [46].

The fragmentation of the target due to collisions with the protons produces high energy neutrons. At SINQ, the target is located inside a heavy water moderator tank which slows the neutrons down to required energies. The resulting neutrons are then guided through beam lines to the instruments.

The alternative method to produce neutrons is through controlled fission process in specially designed research reactors. The uranium-235, which comprises as only 0.7% of the naturally occurring uranium undergoes fission when bombarded by thermal neutron, producing on average 2.4 fast neutrons and releasing approximately 177 MeV of energy per fission. One of the equations for the fission process may be written as

$$^{235}_{92}\mathrm{U} + \mathrm{n}_{\mathrm{thermal}} \rightarrow {}^{144}_{56}\mathrm{Ba} + {}^{89}_{36}\mathrm{Kr} + 2.4\mathrm{n}_{\mathrm{fast}} + \mathcal{Q} \tag{2.52}$$

Neutrons produced from the reaction are similarly moderated to a particular temperature with an energy profile described by Maxwell-Boltzmann statistics with

an effective temperature of around 300 K, they are always higher than the physical moderator temperature as true equilibrium is never achieved in a finite sized moderator [49]. The Maxwellian peaks in intensity at an energy of about 25 meV for a room temperature moderator [49]. Research reactors are not designed to produce electricity and therefore have very small nominal thermal power compared to nuclear power plants. The radiation protection is provided by borated concrete and steel structure which surrounds the reactor. Some of the moderated neutrons escape the core region to be used for neutron scattering experiments.

Thermal neutrons have energies in the range of 5–100 meV. However, using liquid H_2 or CH_4, the neutrons can be moderated for studies with cold neutrons ($T \approx 20$ K) of 0.1–10 meV [46]. Spallation sources have a large epithermal neutron contribution (>100 meV) than reactor based ones and are suitable for exploring these energies. However, a moderator such as graphite heated to 2400 K, as used at ILL, can shift the neutrons to the hot energy range.

2.4.2 Triple-axis spectrometer

The triple-axis spectrometers are capable of measuring very precisely the change of momentum and energy of neutrons that scatter from samples. This is useful in looking at excitations in the crystal such as spin-waves or when high resolution elastic scans are required. As a result this technique has been used for decades in understanding of condensed matter systems. A typical spectrometer configuration is shown in Fig. 2.3.

The initial neutron beam is polychromatic. The incident neutron wavevector $\boldsymbol{k}_\mathrm{i}$ is selected by Bragg reflections on a single-crystal monochromator. Different wavevectors can be chosen by varying the scattering angle $2\theta_\mathrm{M}$ and thereby the neutrons which fulfil the Bragg scattering condition. Typically, the monochromator and analyser are made of pyrolytic graphite (PG), Cu, Si or Heusler crystals. The later are particularly important when spin-polarising the neutron beam. The scattered neutrons can then be selected in analogous fashion by using reflections from the analyser which correspond to the $\boldsymbol{k}_\mathrm{f}$ wavevector.

The monitors are simply low-efficiency detectors. They are placed along the neutron beam path to normalise the counts in the detector and serve as a check for certain spurious scattering (see below). Typically ^{3}He gas single-detectors are used to measure the number of counts for a given monitor rate. When a neutron enters the detector, it will be absorbed by ^{3}He and emit a proton, as per the reaction,

$$\mathrm{n} + {}^3\mathrm{He} \rightarrow {}^3\mathrm{H} + {}^1\mathrm{H} + \mathcal{Q}, \tag{2.53}$$

where $\mathcal{Q} = 0.76$ MeV. The protons ionise the gas and the electrons produced drift towards the central anode. The signal is multiplied by a Townsend avalanche and the count is registered. The ^{3}H nucleus eventually decays to form another ^{3}He nucleus and so the detector is self sufficient. However, due to a finite relaxation time, the detector signal saturates when neutron flux is too high.

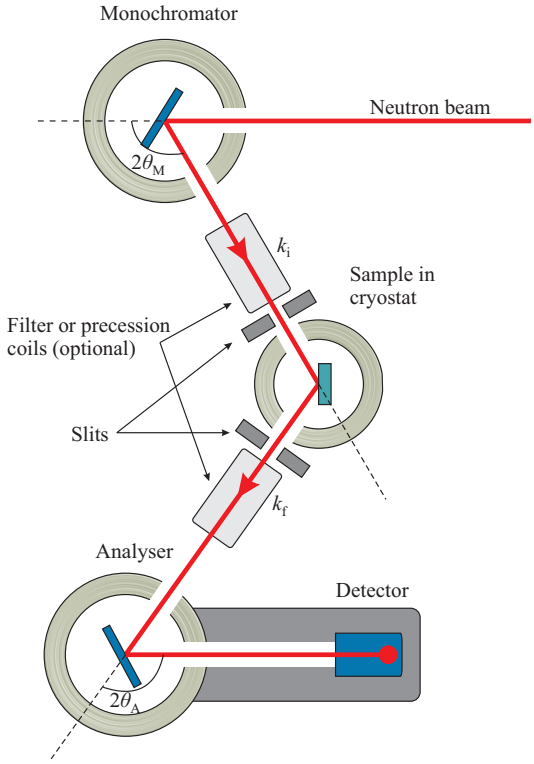

Figure 2.3: Schematic of a triple-axis spectrometer. The neutrons contributing to the signal at the detector are shown by the red line. The monochromator, analyser and sample are able to rotate to achieve the required momentum and energy transfer. In order to eliminate higher order neutron wavelengths, a Be or graphite filter can be mounted. Monitors are placed between monochromator–sample and sample–analyser to normalise the detector counts and as checks for spurious scattering. In addition to this, in polarised neutron scattering experiments, precession coils can be added to finely adjust the incident and reflected neutron polarisation.

The measurements of a given $(\boldsymbol{Q}, E)$ point can be performed in an infinite number of ways due to the flexibility of the instrument configuration. However, in reality not all configurations are equivalent as they lead to different intensity or resolution characteristics. The quantity which we measure in neutron scattering experiments is the double-differential cross-section with respect to solid angle Ω and scattered neutron energy E_f,

$$\frac{\mathrm{d}^2\sigma}{\mathrm{d}\Omega\,\mathrm{d}E_\mathrm{f}} = \frac{k_\mathrm{f}}{k_\mathrm{i}} S(\boldsymbol{Q}, E), \tag{2.54}$$

where the response function $S(\boldsymbol{Q}, E)$ is the physical quantity of the sample which we wish to extract in neutron scattering experiments. Generally, the final wavevector $\boldsymbol{k}_\mathrm{f}$ is held fixed and $\boldsymbol{k}_\mathrm{i}$ is allowed to vary. This is for a number of good reasons. Often varying $\boldsymbol{k}_\mathrm{i}$ results in a decreasing incident neutron flux on the sample. Also, in qualitative analysis of the integrated intensities in constant-$\boldsymbol{Q}$ scans, the intensity

is proportional to the factor $F(k_\mathrm{f})$ which is given as [46],

$$F(k_\mathrm{f}) = R_\mathrm{A}(k_\mathrm{f}) k_\mathrm{f}^3 \cot\theta_\mathrm{A}, \tag{2.55}$$

where R_A is the reflectivity of the analyser and θ_A is the scattering angle, defined in Fig. 2.3. This factor accounts for the changes in analyser response and resolution volume as a function of k_f. Therefore, in instrument setup where k_f is varied, a significant k_f-dependent correction correction must be taken care of. Over a large range of k_f, the analyser reflectivity will also become important. The variable-k_f mode is useful in measurements which require a very low background as higher-order neutrons can be filtered out of the incident beam [46].

By contrast, in the fixed-k_f scattering mode, which is more frequently used, the factor $F(k_\mathrm{f})$ becomes constant. That is not to say that the resolution volume is not changing but rather, as the incident beam monitor efficiency is inversely proportional to k_i, the neutron count rate normalised to the monitor counts is then directly proportional to the response function $S(\boldsymbol{Q}, E)$, from Eq. 2.54.

2.4.2.1 Spurious signals

The beam size is typically larger than the sample mounted in the cryostat, therefore some neutrons can scatter off the cryostat wall or sample holder. This is undesirable as it may produce spurious signals. Slits or diaphragms are placed before and after the sample along beam path to reduce this effect and are adjusted in size for optimal count rate at detector.

In the absence filters in the beam, higher-order neutrons can create spurious diffraction peaks when the analyser and monochromator are of the same crystal. A series of diffraction peaks will then be observed corresponding to the fundamental wavevector and higher-order harmonics which fulfil the Bragg scattering condition. In inelastic neutron scattering, accidental reflections can occur due to diffraction of different harmonics at the monochromator (with wavevectors $2k_\mathrm{i}$, $3k_\mathrm{i}$,...) and analyser (with wavevectors $2k_\mathrm{f}$, $3k_\mathrm{f}$,...). The contribution of the unfiltered harmonics to the monitor count-rate (in the constant-k_f mode) can lead to scan profiles being distorted. The harmonics can also lead to spurious signal when $nk_\mathrm{i} = mk_\mathrm{f}$ with $n, m = 1, 2, 3, \ldots$ due to elastic (coherent or incoherent) scattering from the sample (or its environment) [49]. For identical monochromator and analyser crystals, a spurious reflection will occur when the spectrometer is set for an energy transfer,

$$E_\mathrm{spurion} = \left(1 - \frac{n^2}{m^2}\right) E_\mathrm{i}. \tag{2.56}$$

The false-peak conditions can therefore result in a large, sharp peak at a distinct energy transfer. To avoid this, a useful condition of working with $2/3 < k_\mathrm{i}/k_\mathrm{f} < 3/2$ can be considered [49]. An inelastic scattering event may also occur due to phonons in the monochromator or analyser (thermal diffuse scattering). This can lead to a strong signal if the beam is scattered elastically in the sample.

A number of artifacts can arise from the sample environment. Most trivial example is Bragg scattering from the sample holder or cryostat. Typically Al is used for many applications in neutron scattering experiments the neutron beam will be Bragg scattered. Finally, it is worth mentioning that condensation of He exchange gas can be observed by inelastic neutron scattering. Although the scattering cross-section of ^{4}He is low, with enough sensitivity it can lead to an inelastic temperature-dependent background [46].

2.4.2.2 Filters

To eliminate the unwanted spurious scattering it is also useful to use pyrolytic graphite or cooled Be to suppress higher order harmonics. For thermal neutrons, a PG filter can effectively suppress the second order of neutrons of particular wavevectors, $k = 2.66\,\text{Å}^{-1}$ and $4.1\,\text{Å}^{-1}$. The polycrystalline Be cooled below 80 K only transmits neutrons with $k < 1.57\,\text{Å}^{-1}$ [70]. Cooling of Be is required to reduce the inelastic phonon scattering. Such filter is useful when working with neutrons in the cold energy range.

2.4.2.3 Resolution function

In analysing the neutron scattering data it is important to properly take into account the experimental resolution. The calculation of the resolution function is rather complicated as it depends on many instrument parameters and generally an anisotropic four-dimensional ellipsoid in (Q_x, Q_y, Q_z, E)-space is used in the approximation. The details are discussed at length in Ref. [46] and programs such as ResLib can be used to calculate the resolution function of triple-axis spectrometers [71].

The calculations involve determining the reciprocal space distribution functions $p_\text{i}(\boldsymbol{k}_\text{i})$ and $p_\text{f}(\boldsymbol{k}_\text{f})$ which describe the transmission of the monochromator and analyser arms, respectively. The measured intensity at nominal position $(\boldsymbol{Q}_0, E_0)$ is then given in general by a four-dimensional convolution,

$$I(\boldsymbol{Q}_0, E_0) = N\langle A(\boldsymbol{k}_\text{i})\rangle \int R(\boldsymbol{Q} - \boldsymbol{Q}_0, E - E_0) S(\boldsymbol{Q}, E)\ \mathrm{d}\boldsymbol{Q}\,\mathrm{d}E, \tag{2.57}$$

where N is the number of particles in the irradiated sample volume and $\langle A(\boldsymbol{k}_\text{i})\rangle$ is the average source spectrum function and the normalised resolution function is given by,

$$\int R(\boldsymbol{Q} - \boldsymbol{Q}_0, E - E_0)\ \mathrm{d}\boldsymbol{Q}\,\mathrm{d}E = \int p_\text{i}(\boldsymbol{k}_\text{i}) p_\text{f}(\boldsymbol{k}_\text{f})\ \mathrm{d}\boldsymbol{k}_\text{i}\,\mathrm{d}\boldsymbol{k}_\text{f}. \tag{2.58}$$

In an experiment there is always a compromise that has to be reached between highest possible resolution and sufficiently short counting time. Focusing the neutron beam can be used to increase the flux on the sample. A vertical focusing monochromator increases the beam divergence and can allow for a flux increase of around four times without seriously deteriorating the in-plane momentum and

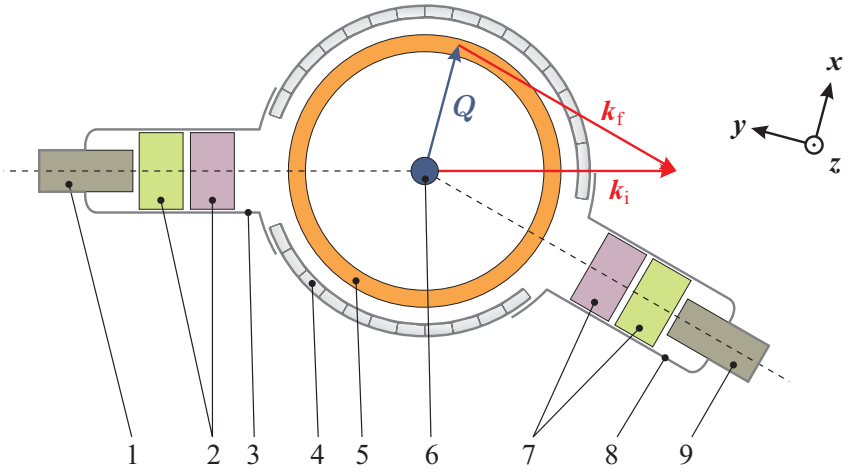

Figure 2.4: Polarisation analysis setup using MuPAD. The zero-field chamber setup used in spherical neutron polarimetry is shown centred on the sample (6) inside a cryostat (5). The polarisation of the incident spin-polarised neutrons is maintained by guide-fields before (1) and after (9) the sample. The neutron moments can be rotated into arbitrary direction by the Helmholtz coils (2) and (7) which generate a magnetic field in orthogonal directions. As the spectrometer moves to access different scattering wavevectors $\boldsymbol{Q}$, the instrument arms (3) and (8) together with the shielding of the sample space also change position. The Cartesian x, y, z coordinate system, usually adopted in describing polarisation analysis, is also plotted. The standard definition is used where x is parallel to scattering wavevector $\boldsymbol{Q}$. The z axis is chosen to be perpendicular to the scattering plane and y completes the right-handed axes.

energy resolution [46]. In similar fashion a vertically bent crystal can be used as an analyser. A horizontally bent monochromator or analyser will degrade the in-plane momentum. This is sometimes acceptable when studying short-ranged magnetic correlations whose response is weak and broad, for example.

2.4.3 Polarimetry using triple-axis spectrometer

In the preceding section we have only considered using the triple-axis spectrometer to analyse the change in momentum and energy of an incident neutron. However, since neutrons carry a magnetic moment, additional information can be extracted about a system by looking at the change in the spin-state of the neutron using spherical neutron polarimetry.

Various techniques have been developed for producing and analysing polarised neutron beams. The most common methods are (i) diffraction from single-crystal polarisers, (ii) reflection from magnetised thin films or supermirrors and (iii) spin-state selective absorption by ^{3}He [56].

Single-crystal polarisers An applied magnetic field saturates magnetic moments in a centrosymmetric crystal such that the moments are perpendicular to $\boldsymbol{Q}$. From Eqs. 2.34 and 2.35, an initially unpolarised neutron beam ($\boldsymbol{P}_i = 0$) can

be fully polarised provided $|\boldsymbol{M}_\perp| = |N|$ [56]. Conversely, the case of $|\boldsymbol{M}_\perp| = 0$ leaves the polarisation of the neutron ensemble unchanged.

Supermirrors The initial beam polarisation is obtained using total reflection of neutrons from a magnetised ferromagnetic thin film, the critical angle is given by

$$\theta_c^{\pm} = \lambda\sqrt{n(b \pm p)/\pi}. \tag{2.59}$$

Here n denotes the particle density and b and p are the nuclear and magnetic scattering lengths, respectively. The reflection angle of θ_c^- (θ_c^+) corresponds to neutrons with (anti)-parallel to the direction of magnetisation of the film. The critical angle can be increased by constructing supermirrors of alternating ferromagnetic and non-magnetic layers.

^{3}He spin filter These filters use optical pumping of meta-stable ^{3}He whose transmission is polarisation dependent. They allow a wider energy band of neutrons to be polarised, however, the efficiency of the filters decreases with time and they must be replaced [56].

The first spherical polarisation analysis setup CryoPAD was developed at ILL and was used in diffraction measurements of complicated magnetic structures [72, 73]. This setup was later modified to allow for inelastic polarised neutron scattering [74, 75]. The region around the sample is shielded from external magnetic fields by double Meissner shields of Nb. Incident neutron are spin-polarised by a Cu_2MnAl Heusler crystal. Nutation and precession fields then rotate the neutron spin into an arbitrary direction. An alternative to CryoPAD is the MuPAD instrument [76]. Instead of using the Meissner-Ochsenfeld effect of a superconductor to expel the magnetic field out of the sample volume, a shielding composed of highly permeable material is used.

The MuPAD device is shown in Fig. 2.4. The polarisation of the incident neutrons is conserved using a magnetic guide field. Without this, stray fields will quickly depolarise the neutron beam. Precession coils are placed before the sample which allow for the manipulation of the neutron spins into any direction by the application of transverse magnetic fields. Scattering of the neutrons by the sample will will change the initial spin state of the neutron. The spin state of the scattered neutrons can be analysed by rotating the magnetic moments to examine a particular polarisation channel. The number of counts is then recorded by the detector.

In this thesis both MuPAD and CryoPAD have been employed to perform spherical neutron polarimetry. This technique is valuable as analysis of the change in the neutron spin-state provides us with additional information on the scattering processes in the sample. It is a very good method for unambiguously separating the coherent magnetic and nuclear scattering contributions to a signal at a given $(\boldsymbol{Q}, E)$ position. The method suffers from the serious drawback that ferromagnetic materials cannot be analysed as these will rapidly depolarise the beam. Although this can be useful in showing a material entering a ferromagnetic phase, it can also

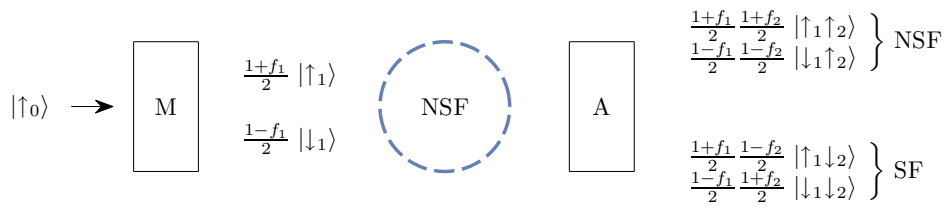

Figure 2.5: Schematic diagram of beam depolarisation in a measurement of a nuclear reflection using polarised neutrons. An initially perfectly polarised neutron beam $|\uparrow_0\rangle$ will be depolarised such that most neutrons will be in spin-up $|\uparrow_1\rangle$ but some will be in the spin-down $|\downarrow_1\rangle$ state before reaching the sample. Similarly, when the scattered neutrons are analysed, neutrons in the $|\uparrow_1\rangle$ state can be reflected with the spin in the $|\downarrow_2\rangle$ state. Therefore, a signal will be measured in the spin-flip channel which is not related to the sample.

be detrimental to analysis of crystals with even small ferromagnetic impurities from the growth process. Spherical neutron polarimetry is therefore largely restricted to studies of antiferromagnets. In addition, in order to use polarised neutron analysis, a large decrease in the count-rate has to be sacrificed – usually a factor of around 20 compared to unpolarised scattering process.

2.4.3.1 Finite spin-flip ratio correction

In practice, due to stray magnetic fields a neutron beam will never be 100% polarised such that an incident and scattered beam will have polarisation efficiency $0 < f_1, f_2 < 1$, respectively. This will cause some neutrons to be scattered into the wrong channel such that a purely nuclear (magnetic) reflection will have a finite component in the spin-flip (non-spin-flip) channel. However, this effect can be compensated for provided one measures a Bragg reflection which is either purely nuclear or magnetic in origin. It is useful to define the spin-flip ratio, R for a nuclear reflection as

$$R = \left(\frac{I_{\mathrm{NSF}}}{I_{\mathrm{SF}}}\right)_{\mathrm{measured}} = \frac{1 + f_1 f_2}{1 - f_1 f_2}, \tag{2.60}$$

by measuring the intensity in the spin-flip I_{SF} and non-spin-flip channels I_{NSF}. A flipping ratio of 10 will then correspond to a neutron beam polarisation of 82%. The corrected intensity coming from the sample in each channel can then be related as follows,

$$\begin{pmatrix} I_{\mathrm{NSF}} \\ I_{\mathrm{SF}} \end{pmatrix}_{\mathrm{corrected}} = \frac{1}{R-1} \begin{pmatrix} R & -1 \\ -1 & R \end{pmatrix} \begin{pmatrix} I_{\mathrm{NSF}} \\ I_{\mathrm{SF}} \end{pmatrix}_{\mathrm{measured}}. \tag{2.61}$$

This is particularly important when the flipping ratio R is small or ratios of intensities are needed to calculate polarisation matrices.

2.4.4 Time-of-flight spectrometer

An alternative to the triple-axis spectrometers, in which initial and final neutron wavevectors are selected by Bragg reflections, is the time-of-flight technique. Unlike

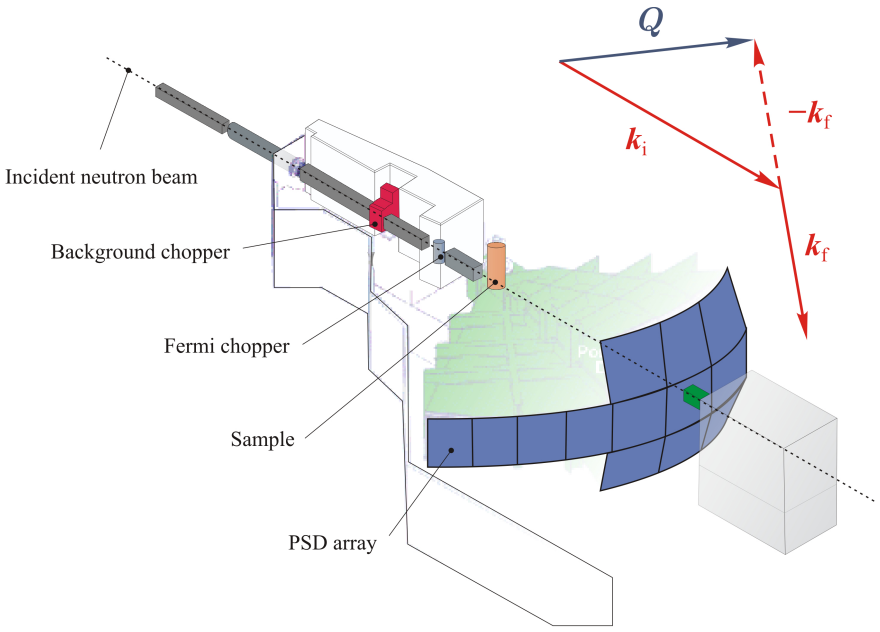

Figure 2.6: Schematic diagram of MAPS spectrometer at ISIS as an example of a time-of-flight instrument. The initial neutron beam is pulsed and two choppers as used to select a particular incident wavevector $\boldsymbol{k}_i$. The scattered neutrons are recorded by a large array of position sensitive detectors located some distance away from the sample. Monitors (not shown) are placed before background chopper, after Fermi chopper and at very end of the beam after the detectors. The scattering triangle for this setup is shown on the top right.

the triple-axis spectrometer which probes a specific point in $(\boldsymbol{Q}, E)$ space, the time-of-flight technique is capable of collecting many energy spectra simultaneously for a wide range of wavevectors by using position sensitive detector (PSD) arrays. Pulsed sources are therefore ideally suited for time-of-flight techniques. Although a reactor source can be adopted to use time-of-flight if the source beam is pulsed by using a chopper or a series of choppers.

The time-of-flight measurements can be made in two settings of geometry:

Direct geometry spectrometer The incident neutron energy E_i is defined by a crystal or a chopper and the final energy E_f is found from time-of-flight.

Indirect geometry spectrometer The sample is illuminated by a polychromatic beam and E_f is defined by a crystal or filter. The incident energy E_i is determined by time-of-flight.

Only a direct geometry spectrometer has been used in the work presented in this thesis and will be discussed further.

In the classical limit where the neutron wavelength is much smaller than the slits the neutron encounters along its path, neutrons can be treated as an ensemble of particles of mass m_n traveling with a velocity v for a time interval of t. The velocity of thermal neutrons is of order of km/s and consequently their energy can be determined by measuring their time-of-flight over a distance of a few meters. This is achieved as follows. Figure 2.6 shows the typical time-of-flight setup using the MAPS instrument at ISIS as an example. An initial pulse of neutrons from the spallation source contains neutrons with velocities $\langle v\rangle \pm \delta v$, where $\langle v\rangle$ is the average velocity and velocity distribution is δv. As the neutrons propagate the pulse width will increase. To reduce the background initial background choppers are used to block fast neutrons produced in the instant of proton spallation. A Fermi chopper is then placed to monochromate the incident beam further. The chopper is a rotating drum synchronised to the neutron pulse which consists of layers of highly absorbing (such as B) and transparent material (such as Al). Only a narrow range of neutrons with desired energy are allowed to pass, with the remainder of neutrons absorbed by the chopper. The energy width of the pulse is varied by adjusting the frequency of the rotation of the chopper. Using a higher frequency will improve the energy resolution but reduce the beam intensity.

The monochromatic beam is then incident on the sample and will be scattered into the position sensitive detector banks. The neutron position can be determined to within about 1 cm and the neutron arrival time is measured to a precision of around 1 ns. When the chopper–sample and sample–detector distances are L_1 and L_2, respectively, and the neutron transverses this distance in a time interval of t_{12}, the final energy can be found by solving,

$$t_{12} = \left(\frac{m_\mathrm{n}}{2}\right)^{1/2} \left(\frac{L_1}{E_\mathrm{i}^{1/2}} + \frac{L_2}{E_\mathrm{f}^{1/2}}\right). \tag{2.62}$$

The scattering wavevector can then be calculated since the position of the detector is known. However, unlike in the triple-axis experiments, the momentum and energy transfer are coupled. Resolving the scattering wavevector parallel and perpendicular to $\boldsymbol{k}_\mathrm{i}$ as $(Q_\parallel, Q_\perp)$, it can be shown that,

$$E = -\frac{\hbar^2}{2m_\mathrm{n}}\left(Q_\parallel^2 + Q_\perp^2 + 2Q_\parallel Q_\perp \cot 2\theta\right), \tag{2.63}$$

where 2θ is the angle between $\boldsymbol{k}_\mathrm{i}$ and $\boldsymbol{k}_\mathrm{f}$. Therefore, for a given $Q_\perp$ the predetermined values of E_i and E_f can be used to calculate $Q_\parallel$. The variation of $Q_\parallel$ with E is not a problem when analysing two-dimensional systems, as in the case of La_2CoO_4 which will be discussed later. When the dispersion is three-dimensional, rotation of the crystal about the axis perpendicular to the scattering plane is necessary and software is available to reconstruct the full $(\boldsymbol{Q}, E)$ excitation spectrum.

The resolution function given in Eq. 2.57 also holds for the time-of-flight spectrometers. However, a good approximation to the energy dependent part of the resolution can be calculated using the width of the elastic line. Treating the wavevector and energy resolutions separately. At a fixed detector position, the uncertainty in the energy transfer can be expressed as,

$$\delta E = \frac{\partial E}{\partial E_\mathrm{i}}\delta E_\mathrm{i} + \frac{\partial E}{\partial E_\mathrm{f}}\frac{\partial E_\mathrm{f}}{\partial E_\mathrm{i}}\delta E_\mathrm{i}. \tag{2.64}$$

In order for neutrons to arrive at the same time t_{12}, from Eq. 2.62, E_i and E_f are coupled. Using the width of the elastic line, δE_0, we can eliminate δE_i from Eq. 2.64 to obtain,

$$\delta E = \frac{\delta E_0}{1 + L_1/L_2}\left[1 + \frac{L_1}{L_2}\left(\frac{E_\mathrm{f}}{E_\mathrm{i}}\right)^{3/2}\right]. \tag{2.65}$$

The wavevector resolution is to mainly dependent on the beam divergence $\delta\phi$ for an incident neutron of energy E_i, the wavevector broadening can be approximated as,

$$\delta|\boldsymbol{Q}| \approx k_\mathrm{i}\delta\phi. \tag{2.66}$$

Another advantage of time-of-flight measurements is that the excitation spectrum can be readily converted into absolute units which can then be compared to theoretical models. This can be achieved by comparing the data measured to the same instrument parameter measurements on a standard V calibration.

2.5 Bulk properties measurements

Magnetisation and pyroelectric current measurements are two of many bulk techniques. These two methods were employed in the work presented in this thesis. Magnetisation measurements are important in characterising the bulk magnetism of compounds as a function of temperature and applied magnetic field. This can be used to identify phase transitions and can be combined with neutron scattering

measurements to provide a more comprehensive understanding of the system. Pyroelectric current measurements provides us with information about the ferroelectric order in a compound. This form of measurement probes the dielectric properties of the material which cannot be deduced from neutron scattering measurements.

2.5.1 SQUID magnetometry

The magnetic susceptibility was measured using a Quantum Design MPMS XL Superconducting Quantum Interference Device (SQUID). The SQUID magnetometer is an instrument which is very sensitive to small magnetic fields and operates on the principle of Josephson junctions to measure trapped flux quanta. The magnetic dynamic susceptibility, as measured by neutrons, can be directly related to the static susceptibility χ'_0 measured in a SQUID magnetometer by [77],

$$\chi'_0 = \lim_{Q\to 0} \frac{1}{\pi} \int_{-\infty}^{\infty} \frac{\chi''(\boldsymbol{Q}, E)}{E} \, \mathrm{d}E, \tag{2.67}$$

where we have made use of the Kramers-Kronig relation to relate the real and imaginary parts of the general susceptibility [52].

The magnetisation of a sample can be measured provided a magnetic field is applied to induce a net magnetic moment in the sample. The SQUID is capable of measuring the magnetic susceptibility of samples from 400 K to a base temperature of 2 K. Measurements can be made in a static magnetic field from about 10 G up to a maximum of 70000 G.

An assembly of second-derivative detector array, isolation transformer and SQUID sensors form the basis of the magnetic field measurements. The sample is placed inside detection loops which are configured as a highly-balanced coil set made from superconducting wire. Pairs of coils are wounded in opposite senses in order to reduce noise in the detection unit. The pick-up coils in which a current is induced by the sample are isolated from the SQUID loop by a transformer. The superconducting transformer includes a small heater to drive the SQUID input circuit into the normal state in order to eliminate persistent currents induced in the pick-up loops when changing the applied magnetic field. The SQUID device then measures the magnetic flux. A constant biasing current is maintained in the device, the measured voltage oscillates with changes in phase between two Josephson junctions and in turn depends on the change in the magnetic flux.

There are several techniques which can be used to measure the sample magnetisation. The reciprocating sample option (RSO) and direct current (DC) methods have been employed in the work presented in this thesis. In RSO measurements, the sample is oscillated from the centre of the main sensing coils. The DC method involves moving the sample through the detector coils. In both methods, the SQUID output is measured as a function of the sample's position. The resulting signal is fitted using a theoretical curve for a point-like sample. The amplitude of the recorded signal is taken to be the magnetisation of the sample. Since the sample is usually mounted inside a plastic straw, moving the sample through the detector

coils to a large extent eliminates the background contribution from the straw. The RSO technique is more sensitive and in general is used in preference to the DC method.

Operating at large applied fields can cause a residual magnetic field to persist in the superconducting magnet when measuring in low magnetic fields. Therefore, it is necessary to reset the magnet by heating a small portion of it. A chain reaction drives the entire magnet into the normal state thereby quenching it. This reduces the remnant field to less than 2 G.

2.5.2 Measurements of the electric polarisation

Measurements of the electric polarisation involve the measurement of the pyroelectric current as a function of temperature. Small, plate-like samples are used and electrical contacts are made to opposing flat faces of the crystal. The custom sample insert has been used together with a Quantum Design PPMS, which acts as a cryostat. The measurements are made as follows. A large electric field is applied using a high-voltage power supply at a temperature above the ferroelectric phase transition in the paraelectric phase. The sample is then cooled with the applied electric field into the ferroelectric phase. On reaching a base temperature, the electric field is switched off.

It is important to remove the charge deposited onto the surface of the sample due to the application of the electric field. The sample is therefore usually left to discharge for approximately 30 min. The sample can then be warmed up and an electrometer measures the pyroelectric current as function of temperature. The electrometer is highly sensitive and allows currents of order 10^{-12} A to be measured. This introduces practical issues of eliminating possible stray fields or ground loops. The temperature dependence of the pyroelectric current is measured upon warming (or cooling) out of the multiferroic phase into the paraelectric one. At the phase transition, a sharp spike is usually observed in the pyroelectric current I_e. The electric polarisation P_e can then be found for a parallel plate arrangement by integrating the pyroelectric current measured as a function of time t and temperature T as,

$$\begin{aligned} P_\mathrm{e} &= \frac{Q_\mathrm{e}}{A} \\ &= \frac{1}{A}\int I_\mathrm{e}\,\frac{\mathrm{d}t}{\mathrm{d}T}\,\mathrm{d}T, \end{aligned} \tag{2.68}$$

where Q_e and A are total charge released and the surface area of the sample, respectively. The warming (or cooling) rate of the sample after the field has been removed is set to be very slow e.g. 1 K/min to allow the sample to thermalise and to obtain more points around the sharp phase transitions. Since the cryostat may not warm at a uniform rate, especially at the start of the measurement, the rate of heating (or cooling) has to be accounted for in the integration. A third-order polynomial has been found to provide a good approximation this effect.

Chapter 3

Magnetic order and fluctuations in La_2CoO_4

Contents

3.1 Introduction

The evolution from antiferromagnetism to high-temperature superconductivity with carrier doping of the layered copper oxides [15] has inspired a vast literature on the electronic, structural, dynamical and chemical properties of related materials. It has become clear from these studies that superconductivity and commensurate antiferromagnetic order are only two out of many different competing ordering tendencies found in systems of strongly interacting electrons.

Nematic phases in doped Mott insulators are characterised by unidirectional density-wave states involving combined charge and spin order. Such 'striped' phases were first identified many years ago in hole-doped $(La, Nd)_2CuO_4$ (Ref. [78]) and La_2NiO_4 (Refs. [79–82]), but their significance for high-temperature superconductivity has been the subject of a continuing debate. Although much of the focus has been on the cuprates, the nickelates have contributed to this debate on account of their relatively well correlated and stable stripe order which is amenable to experimental investigation. One drawback, however, is that holes localised on Ni^{3+} ions in hole-doped La_2NiO_4 carry a spin which can interact magnetically both with other spins in the charge stripes and with the surrounding antiferromagnetic matrix of Ni^{2+}. The influence of these interacting magnetic degrees of freedom on the properties of stripes in nickelates has yet to be fully evaluated, although spin correlations associated with both Ni sites have been observed [83] and there remain some unexplained features in the spin excitation spectra [84].

Recently, evidence has been presented for the existence of stripe phases in the layered cobaltate system $La_{2-x}Sr_xCoO_4$ (Ref. [85]), which is isostructural with hole-doped La_2CuO_4 and La_2NiO_4. The cobaltate system has an advantage over the nickelates in that only the Co^{2+} site is magnetic. The Co^{3+} ions adopt the low spin ($S = 0$) state at low temperatures and are therefore not magnetically active [86, 87]. Hence, the layered cobaltates offer the chance to investigate the fundamental interactions and excited states of an ordered stripe phase in which the doped holes do not possess low-energy spin degrees of freedom.

The aim of the work presented in this chapter is to determine the magnetic structure of La_2CoO_4, which is regarded as a canonical $S = 3/2$ two-dimensional antiferromagnet. It is interesting to establish whether the magnetic order is a simple collinear antiferromagnet, as has been assumed up to now, or whether there could be a more complex non-collinear magnetic order caused by the alternate tilting of the CoO_6 octahedra. Furthermore, in order to understand electronic phases in $La_{2-x}Sr_xCoO_4$ we require some basic knowledge of La_2CoO_4. Although the structural and magnetic ordering of La_2CoO_4 has been previously examined, no measurements of the magnetic excitation spectrum have been reported until now [88]. Our work has been able to establish the energy scale and characteristics of the magnetic excitations and to map out the complete spin-wave spectrum in sufficient detail to extract the values of the dominant exchange interactions.

3.2 Crystal growth description

A single crystal sample of La_2CoO_4 with a mass of approximately 5 g was grown in Oxford by Dr Prabhakaran using the optical floating-zone method. Polycrystalline La_2CoO_4 was prepared from high-purity (> 99.99%) La_2O_3 and Co_3O_4 by solid-state reaction. Stoichiometric amounts of the oxides were mixed and reacted at 1050°C for 48 hours under a flowing atmosphere of CO/CO_2 mixed in the ratio 1:10. A reducing atmosphere is needed to avoid the formation of $LaCoO_3$. The powder was re-ground and sintered at 1100°C in a flow of argon for a further 48 hours. No impurity phases could be detected in the product by x-ray powder diffraction. The La_2CoO_4 powder was isostatically pressed into rods of diameter 12 mm and length 120 mm. The rods were sintered in an argon atmosphere at 1250°C for 24 hours. Crystal growth was carried out in a four-mirror image furnace (Crystal Systems Corporation) in flowing argon at a growth speed of approximately 2 mm/hr with counter-rotation of the feed and seed rods at 25 rpm.

Crystals grown by this method contain an excess of oxygen. To achieve stoichiometry the as-grown crystal was annealed at 850°C for 72 hours in flowing CO/CO_2 (1:10 ratio). A fragment of the annealed crystal was ground to a powder and subjected to a thermogravimetric analysis. From the measured weight loss we determined the oxygen nonstoichiometry to be $\delta = -0.03 \pm 0.02$. This suggests that the crystal is close to the ideal stoichiometry, if anything slightly oxygen-deficient.

3.3 Crystal and magnetic structure of La_2CoO_4

In common with the stoichiometric La_2CuO_4 and La_2NiO_4 compounds, La_2CoO_4 exhibits three different structural phases [89]:

(i) $T > T_1$ high-temperature tetragonal (HTT), space group $I4/mmm$;

(ii) $T_2 < T < T_1$ low-temperature orthorhombic (LTO) [1] , space group $Cmca$;

(iii) $T < T_2$ low-temperature tetragonal (LTT), space group $P4_2/ncm$.

The tetragonal body-centred unit cell of La_2CoO_4 is shown in Fig. 3.1(a). The Co atoms are found in an octahedral environment surrounded by O ions with four nearest-neighbour O1 sites in the ab-plane of CoO_2 and two more displaced O2 ligands along the c direction. The La and Sr atoms are found displaced along the c direction from the O2 sites which act to separate the CoO_2 layers. Throughout this chapter I shall use the conventional $I4/mmm$ unit cell as a basis for the reciprocal lattice. The low temperature lattice constants referred to this cell are $a = b = 3.91$ Å and $c = 12.6$ Å.

The structural transition temperatures for La_2CoO_4 are $T_1 \approx 900$ K (Ref. [85]) and $T_2 = 120 - 135$ K (Ref. [89]). The latter is reported to be first order. The ideal

[1] The orthorhombic distortion occurs in the ab-plane with cell parameters a and b only differing by approximately 2%.

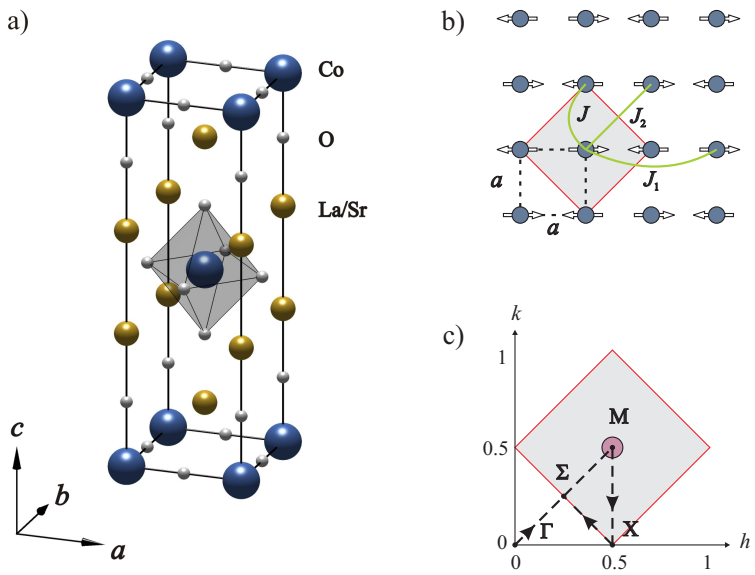

Figure 3.1: Crystal and magnetic structure of La_2CoO_4. (a) The tetragonal ($I4/mmm$) crystal structure of La_2CoO_4. (b) In-plane magnetic structure of La_2CoO_4. The dashed square shows the conventional $I4/mmm$ unit cell of the HTT phase, and the filled square represents the magnetic unit cell, which coincides with the $\sqrt{2} \times \sqrt{2}$ chemical unit cell of the LTT phase. The exchange interactions used to model the magnetic spectrum are indicated. (c) Diagram of the reciprocal space lattice corresponding to the $I4/mmm$ cell. The filled square indicates the magnetic Brillouin zone centred on $(0.5, 0.5)$. The dashed lines show the path through reciprocal space along high-symmetry directions used for detailed analysis of the magnetic excitation spectrum.

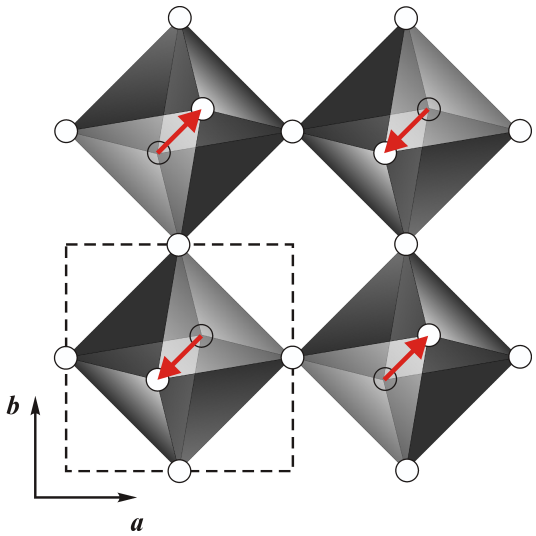

Figure 3.2: Tilt of the oxygen octahedra in the LTO phase. The white circles denote the O located at the vertices of the octahedra surrounding Co ions in La_2CoO_4. The red arrows indicates the tilt of the octahedra away from the tetragonal axis and the conventional unit cell is shown by the dashed line.

single-layered crystal structure above T_1 is distorted by the tilt of the corner-sharing CoO_6 octahedra along the $[1,1,0]$ direction, as shown in Fig. 3.2. The rotations about the $[1,-1,0]$ direction form an antiferrodistortive structural arrangement in the LTO and LTT phases. Such tilting is found in other systems of the form La_2MO_4 where M is Cu or Ni [89]. The tilted structure forms a periodic arrangement characterised by a tetragonal unit cell whose in-plane dimensions are $\sqrt{2}\times\sqrt{2}$ larger than those of the $I4/mmm$ pseudo-cell. This modulation of the nuclear structure can be probed by neutron scattering giving rise to weak superlattice reflections. Refinement of single-crystal neutron diffraction measurements have shown that the tilt angle is approximately 10° for La_2CoO_4 and 4.2° for the related Cu compound [89]. In the LTT phase the octahedra tilts alternate by 90° from one layer to layer along the $\boldsymbol{c}$ axis.

The transition to magnetic order occurs at $T_N \approx 275\,K$, and a magnetic reorientation occurs at T_2 coincident with the LTO–LTT structural transition. The antiferromagnetic structure has an ordering wavevector $\boldsymbol{q}_m = (0.5, 0.5, 0)$, with ordered moments lying in the CoO_2 plane. Assuming collinear order, the difference between the magnetic structures in the LTT and LTO phases is that in the LTT phase the moments are perpendicular to $\boldsymbol{q}_m$ whereas in the LTO phase they are are parallel to $\boldsymbol{q}_m$. Another possibility is that the structure is collinear within the layers but the moment direction rotates by ±90° from one layer to the next – following the CoO_6 octahedral distortion [89]. In the absence of inter-layer coupling all these structures have the same energy. Our inelastic neutron scattering measurements (discussed in § 3.7) did not observe any evidence in the excitation spectrum for inter-layer coupling we will treat the magnetic order as two-dimensional. Figure 3.1(b) shows the in-plane magnetic order with the moments arbitrarily chosen to point along the horizontal axis.

3.4 Bulk properties measurements

The temperature dependence of the FC and ZFC susceptibility ($\chi = M/H$) is shown in Fig. 3.3(a). Both curves show a change in slope at approximately 276 K consistent with the antiferromagnetic transition, and sharp anomalies at 124 K close to the temperature T_2 at which the LTO–LTT structural transition is expected. The onset of antiferromagnetism at $T_N \approx 276\,K$ is confirmed by the temperature dependence of the neutron diffraction intensity recorded at the magnetic Bragg peak positions, shown in Fig. 3.3(b). To estimate T_N, the data was fitted to a power law $I \propto (1 - T/T_N)^{2\beta}$, assuming a Gaussian distribution of Néel temperatures about the mean value $\langle T_N \rangle$ with standard deviation of σ_T. This function was found to give a good description of diffraction data near T_N in Ref. [89]. The parameters obtained from our spherical neutron polarimetry data were $\langle T_N \rangle = 273.5(5)\,K$, $\sigma_T = 1.24(7)\,K$ and $\beta = 0.186(2)$. The transition temperatures measured on the La_2CoO_4 sample are consistent with previously reported values of $T_N = 275\,K$ and $T_2 \approx 135\,K$ for a nominally stoichiometric crystal [89]. Although there is some discussion in

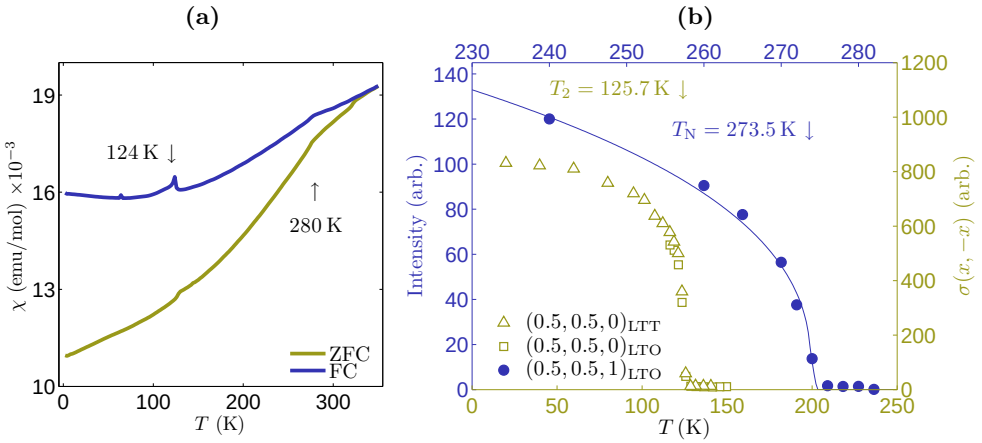

Figure 3.3: Temperature dependence of magnetisation in La_2CoO_4. (a) Field-cooled (FC) and zero-field-cooled (ZFC) magnetic susceptibility of La_2CoO_4 recorded with a measuring field of 1000 Oe applied parallel to the c axis. The magnetic ordering transition and the LTO–LTT structural transition are indicated by arrows. (b) Temperature dependencies of the $(0.5, 0.5, 0)$ (△, □) and $(0.5, 0.5, 1)$ (●) magnetic Bragg peak of La_2CoO_4 showing the onset of magnetic order at $T_N \approx 274$ K measured in the $x\bar{x}$ polarisation channel. The solid blue line shows a power law fit to data with a Gaussian distribution of Néel temperatures. The △ and □ symbols denote measurements at $\boldsymbol{Q} = (0.5, 0.5, 0)$ with lattice parameters corresponding to the LTT and LTO structural phases, respectively.

the literature about the precise composition of La_2CoO_4 prepared under different conditions [89–92], we can at the very least be confident that our crystal is close in composition to the one used in Ref. [89]. The critical exponent of magnetisation deduced for La_2CoO_4 is consistent with materials such as $BaNi_2(PO_4)_2$, Rb_2CrCl_4, K_2CuF_4 and $Cu(pyz)_2(BF_4)_2$ which have differing crystallographic structures and magnetic moments yet have β in the range of 0.18 to 0.26 [93, 94]. Theoretically it has been demonstrated that $\beta = 0.23$ is a universal signature realised in two-dimensional XY models [93].

The FC and ZFC susceptibility curves separate below 350 K, which is not expected in the paramagnetic phase. This indicates that the sample contains a small amount of ferromagnetic impurity. The FC–ZFC separation was not observed in the as-grown crystal. The most probable explanation is that a tiny amount of elemental Co was formed during the CO/CO_2 annealing step. This is consistent with the slight oxygen deficiency found from the thermogravimetric analysis. As there is no unexplained secondary signal in the measured neutron scattering spectra this impurity must be present in very small quantities so is of no consequence to our neutron results, but it does mean that the susceptibility curves shown in Fig. 3.3(a) contain a background signal in additional to the signal from pure La_2CoO_4.

3.5 Magnetic structure analysis using spherical neutron polarimetry

Interest in La_2CoO_4 stems from its crystal structure [Fig. 3.1(a)] which is one of the isomorphous compounds of La_2CuO_4. In this section, I shall describe the attempts to solve the magnetic structure in the LTT and LTO phases using spherical neutron polarimetry measurements.

3.5.1 Experimental setup

The 5.1 g single-crystal sample was grown by the method described in § 3.2 and is the same crystal as used for inelastic neutron scattering measurements, § 3.7. The sample was mounted on a non-magnetic microgoniometer in two orientations to allow access to (h, h, l) and $(h, k, 0)$ scattering planes. Spherical neutron polarimetry analysis was carried out using the MuPAD/TASP spectrometer configuration at SINQ, PSI [76, 95, 96]. The instrument is optimised for neutron wavelength $\lambda = 3.2\,\text{Å}$, however in order to access high-order reflections, $\lambda = 2.9\,\text{Å}$ was also utilised. The flipping ratio, as measured on the (110) and (002) peaks, was found to be around 17 for both neutron wavelengths used. Therefore, the beam polarisation is sufficiently high that experimental data presented here have not been corrected for this effect. Furthermore, the high spin-flip ratio demonstrates that the ferromagnetic impurity found in the susceptibility measurements, shown in Fig. 3.13 (inset), are negligible. The modelled polarisation matrices take the non-ideal beam polarisation into account. Complete normal $P_{\alpha\beta}$ and negative $P_{-\alpha\beta}$ polarisation matrices were measured in the LTT phase at 1.6 K and in the LTO phase at 150 K.

3.5.2 Magnetic phase transitions in La_2CoO_4

Comprehensive analysis of the spin structure has previously been made on a single crystal of La_2CoO_4 using unpolarised neutron scattering [89]. It revealed that La_2CoO_4 exhibits two antiferromagnetic ordered phases below the Néel temperature T_N and the study attempted to ascertain the details of the crystallographic and magnetic phases. The nature of the reflections found in La_2CoO_4 is depicted in Fig. 3.4. The peaks corresponding to the $\sqrt{2} \times \sqrt{2}$ superstructure are formed by the tilts of the CoO_6 octahedra in the LTO and LTT phases, which breaks the in-plane symmetry. Owing to the tetragonal crystal lattice symmetry, the magnetic and superlattice peaks in the LTT phase overlap and since their structure factors are approximately equal it is difficult to resolve their individual contributions to the peak intensity when performing unpolarised neutron diffraction. The LTO phase is simpler in this respect as the magnetic and superlattice peaks will split sufficiently to be resolved experimentally. The open and filled triangles in Fig. 3.4 denote the two magnetic domains in La_2CoO_4 related to each other by a rotation of 90° about the c axis. The measurements by Yamada *et al.* [89] demonstrate that in the LTO phase, the magnetic structure is of La_2NiO_4-type with spins aligned perpendicular to the

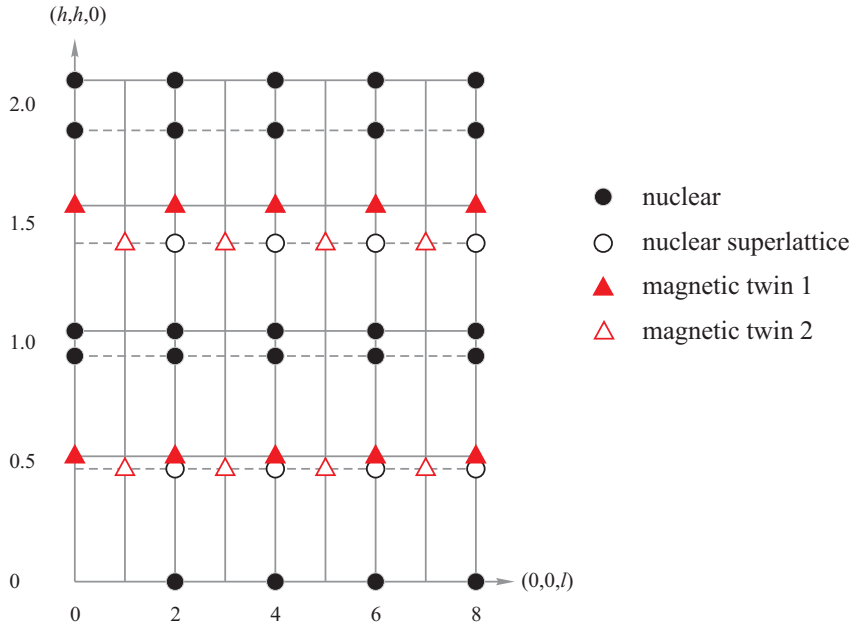

Figure 3.4: Nuclear and magnetic reciprocal lattice of La_2CoO_4. Schematic diagram to show the nature of the nuclear and magnetic order present in La_2CoO_4 in the (h, h, l) scattering plane. The distortion in the *ab*-plane in the LTO phase is denoted by the dashed lines forming the reciprocal lattice. In the LTT phase, the dashed line is coincident with the full line, from Ref. [89].

propagation wavevector $\boldsymbol{q}_\mathrm{m}$. The LTT phase is less well understood, it could be either in the form of a simple collinear La_2CuO_4 magnetic structure with moments parallel to $\boldsymbol{q}_\mathrm{m}$ or more complicated non-collinear spin structure in which moments along c are rotated by 90°. A further complication arises due to a residual LTT structure persisting into the LTO phase and a hysteresis in the LTO phase due to stacking faults in La_2CoO_4 [89].

Polarised neutron diffraction measurements collected in the spin-flip and non-spin-flip x polarisation channels agree with the phase diagram of La_2CoO_4 proposed by Yamada *et al.* [89], see Fig. 3.5. The reflection at $\boldsymbol{Q} = (0.5, 0.5, 0)$ is found to disappear above the LTT–LTO phase transition. Polarised neutrons confirm that the peak must be due to magnetic order as, within beam polarisation efficiency correction, non-spin-flip channel contains negligible counts. The correlation length is found to be approximately 42 Å along $(h, h, 0)$ and 57 Å along c. This does not include corrections for the instrumental resolution hence the values of correlation lengths underestimate the true static correlations. It is therefore clear that the magnetic order is long-ranged in La_2CoO_4. No significant change in peak width (and thus correlation length) has been found in the temperature range investigated, including close to phase transitions. The temperature evolution of this peak is found from the counts recorded at the peak position shown in Fig. 3.3(b). The first-order nature of LTT–LTO phase transition is evident in the sharp discontinuity observed in the $\boldsymbol{Q} = \boldsymbol{q}_\mathrm{m}$. The $(h, h, 0)$ scans in Figs. 3.5(c)–(e) at $T > T_2$ show that the peak

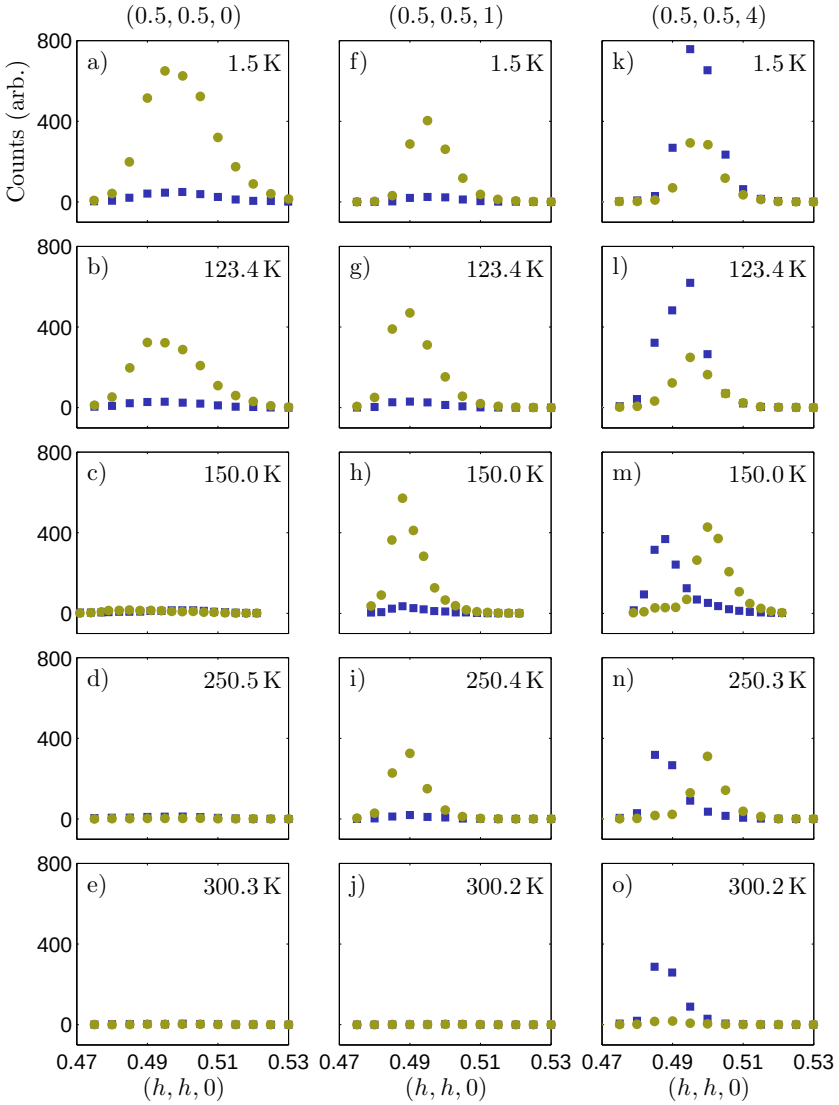

Figure 3.5: Temperature evolution of superlattice and magnetic order in La_2CoO_4 Temperature dependence of reflections at $\boldsymbol{Q} = (0.5, 0.5, 0)$ [(a)–(e)], $(0.5, 0.5, 1)$ [(f)–(j)] and $(0.5, 0.5, 4)$ [(k)–(o)] from 2 to 300 K. Figures show the the counts recorded in the non-spin-flip (■) and spin-flip (●) polarisation channels parallel to $\boldsymbol{Q}$. Diagram in Fig. 3.4 illustrates that the peaks at $\boldsymbol{Q} = (0.5, 0.5, 0)$ and $(0.5, 0.5, 1)$ arise from purely magnetic scattering, whereas reflection at $(0.5, 0.5, 0)$ has both nuclear and magnetic character. Magnetic phase transition temperature for La_2CoO_4 are found to be $T_2 \approx 125\,\mathrm{K}$ and $T_N = 234\,\mathrm{K}$.

does not simply shift in $\boldsymbol{Q}$ but completely vanishes.

The reflection at $\boldsymbol{Q} = (0.5, 0.5, 1)$ does not change significantly at $T = T_2$ and persists in the the LTO phase [Fig. 3.5(f)–(i)]. This peak is also purely of magnetic origin and therefore reliable when characterising the magnetic structure. The temperature dependence of this reflection is used to define the onset of magnetic order in Fig. 3.3(b). Above T_N, only weak scattering is observed in the non-spin-flip channel corresponding to the nuclear superlattice, as shown in Fig. 3.5(o).

Figures 3.5(m) and (n) show that in the LTO phase the magnetic and nuclear superlattice peaks can be resolved by polarised neutron scattering due to the slight in-plane orthorhombic distortion of the lattice. This can be understood in terms of twin domains related by a 90° rotation such that the magnetic and structural distortion modulation wavevectors are orthogonal to one another. In other words, if it were possible to untwin the crystal in the LTO phase such as by applying uniaxial pressure, either magnetic or nuclear reflections would appear at $(0.5, 0.5, 4)$. The transition into the tetragonal phase $T < T_2$ results in nuclear and magnetic reflections sitting on top of each other and therefore unpolarised neutron scattering cannot determine the magnetic and nuclear superlattice structure factors at reflections such as $(0.5, 0.5, l)$ when l is even.

3.5.3 Low-temperature orthorhombic phase, LTO

Polarised neutron scattering measurements were made at 150 K in the (h, h, l) scattering plane. Complete polarisation matrices were shown to have negligible off-diagonal elements and therefore the measurements have been focused on $P_{\alpha\alpha}$ components only. Measurements were made with incident neutron spin parallel and antiparallel to the polarisation axes and away from the superlattice reflections depicted in Fig. 3.4. In total 30 polarisation matrices were found to give reliable results with little nuclear contamination, a selection is found in Fig. 3.6. We find that within the beam polarisation efficiency, the elements take values of ± 1. The reflection measured at $\boldsymbol{Q} = (0.5, 0.5, 0)$ is an exception to this, with elements that show some depolarisation. However, Fig. 3.5 clearly shows that the reflection at this position in reciprocal space is extremely weak may not give reliable polarisation matrix elements.

In trying to understand the spin arrangement we must consider the possible domains that are energetically equivalent but can give different magnetic structure factors. To simplify the problem, let us consider a tetragonal crystallographic structure with magnetic ordering modulated by $\boldsymbol{q}_\mathrm{m} = (0.5, 0.5, 0)$. From irreducible representation analysis, the Co^{2+} magnetic moments are allowed to be orientated in an arbitrary direction. However, as stated previously, the strong anisotropy constrains them to be in the ab-plane. We can consider moments at Co(1): $(0, 0, 0)$ and Co(2): $(0.5, 0.5, 0)$ within the unit cell to lie either parallel to perpendicular to $\boldsymbol{q}_\mathrm{m}$.

The action of the four-fold rotation about the c-axis allows a magnetic structure to have $\boldsymbol{q}_\mathrm{m} = (0.5, -0.5, 0)$ magnetic propagation wavevector, completing the star of

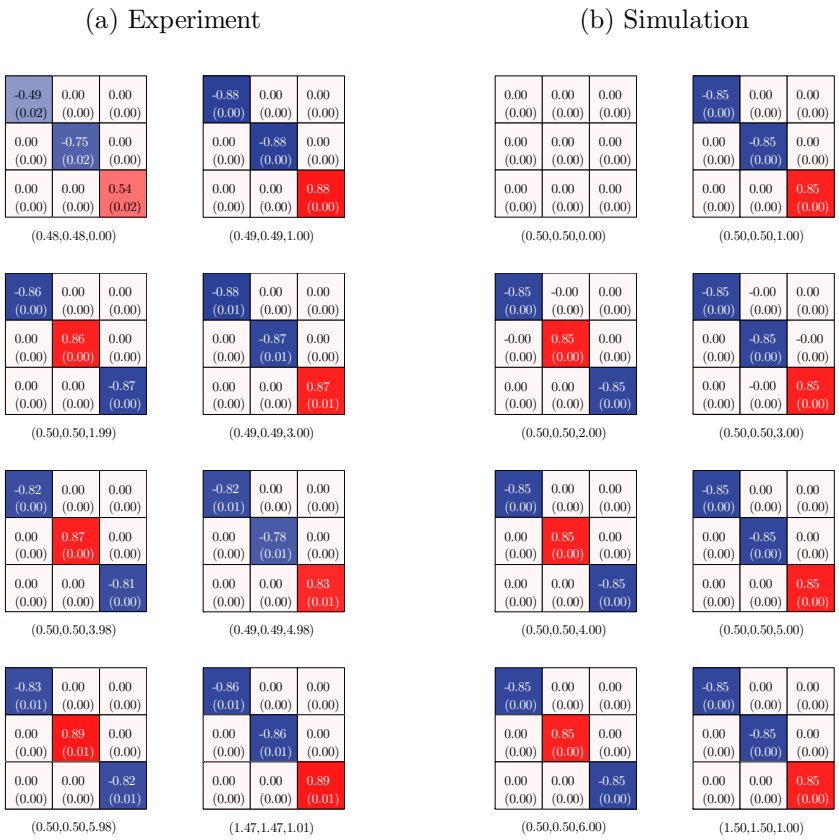

Figure 3.6: Comparison of polarisation matrices observed and calculated in the LTO phase. A sample of the polarisation matrices collected at 150 K in the (h, h, l) scattering plane. The panels to the left show the $P_{\alpha\beta}$ components and on the right are the respective simulations based on the best fit model described in the text and corrected for non-ideal beam polarisation. The errors, as deduced from peak intensities are shown in parenthesis. The red (blue) colours represent $+1$ (-1) values of the matrix elements.

the propagation wavevectors. For the LTO phase, we can consider just two magnetic domains related by a four-fold rotation about c.

The model which best describes the data is shown together with the experimental measurements in Fig. 3.6. The spin structure consists of moments aligned perpendicular to $\boldsymbol{q}_{\mathrm{m}}$ with Co^{2+} moments at the origin and body centre aligned ferromagnetically – see Fig. 3.8(b). The magnetic structure model describes the experimental data with a goodness of fit of $\chi^2_\nu \approx 37$. The reflection at $\boldsymbol{Q} = (0.5, 0.5, 0)$ is predicted to be forbidden. In contrast, experimentally we found a weak reflection at this position. It is likely to be due to a small amount of LTT magnetic structure remaining in the LTO phase. Based on the intensity of the $(0.5, 0.5, 0)$ peak, only approximately 2.5% of the LTT spin structure survives above T_2 in the LTO phase. The incomplete transition was also noted by previous study of La_2CoO_4 concluding that a small amount of approximately 5% of residual LTT phase is present above

T_2 [89]. From analysis of the LTT phase, the reflection at $\boldsymbol{Q} = \boldsymbol{q}_\mathrm{m}$ is also by far the strongest. The analysis of the polarimetry data recorded at this and other scattering wavevector is thus unlikely to be aversely affected by this contribution. The best-fit magnetic structure is agrees with that found in Ref. [89].

Other spin structures were also considered but these were found to give significantly worse fits. For example, setting the spins to be aligned along the a axis, gives a fit of $\chi^2_\nu = 26000$. We can conclude that the the polarisation matrices recorded in the LTO phase place tight constraints on the magnetic structure.

3.5.4 Low-temperature tetragonal phase, LTT

We now turn to the analysis of the low-temperature tetragonal phase in La_2CoO_4 below $T_2 \approx 125\,\mathrm{K}$. The refinement of the magnetic structure in this phase is more complicated due to overlap of the superlattice and magnetic reflections (Fig. 3.4).

Complete positive and negative polarisation matrices were recorded at 1.6 K. Two scattering geometries were employed to probe the (h, h, l) and $(h, k, 0)$ reflections. Figure 3.7 shows a selection of the polarisation matrices collected. The propagation wavevector in LTT phase is unchanged from LTO but moments at Co(2) position can be at 90° to the moments in the basal plane. Taking non-collinear magnetic moment arrangement into account means that more domains must be considered which can give inequivalent magnetic structure factors. The tetragonal crystal symmetry of La_2CoO_4 and strong anisotropy restrict the number of possible domains. The symmetry operations of the identity and mirror plane along $\boldsymbol{a} = \boldsymbol{b}$ leave the propagation wavevector unchanged. The other $\boldsymbol{\kappa}$-domain contains the four-fold rotation about c-axis and mirror in the ac-plane, which transform the wavevector into $(0.5, -0.5, 0)$. There are therefore two $\boldsymbol{\kappa}$-domains each containing two spin-domains for a total of four domains that must be taken into account.

The comparison between the magnetic structure model and experiment cannot be compared without also considering the effect of the superlattice reflections. Polarisation matrices measured at $\boldsymbol{Q} = (0.5, 0.5, l)$, where l is even show that P_{xx} term in the polarisation matrix is far from -1 as would be expected for scattering of magnetic origin. Elements of $P_{xx} \approx 0$ signify that the magnetic and superlattice structure factors are nearly the same. Standard unpolarised neutron scattering, as employed in Ref. [89], cannot separate the nuclear and magnetic structure factors. Conveniently, spherical neutron polarimetry can go some way in obtaining meaningful results.

When a neutron is incident on a sample, the direction of the neutron spin will not be affected by nuclear scattering whereas the presence of internal magnetic fields in the sample will flip the neutron spin. Considering just the spin-flip parallel and anti-parallel to $\boldsymbol{Q}$, the cross-sections for the non-spin-flip $[\sigma(x, x)]$ and spin-flip $[\sigma(x, -x)]$ polarisation channels are,

$$\sigma(x, x) \propto N^2(\boldsymbol{Q}) + b_\mathrm{NSF}, \qquad \sigma(x, -x) \propto M^2_\perp(\boldsymbol{Q}) + b_\mathrm{SF}, \tag{3.1}$$

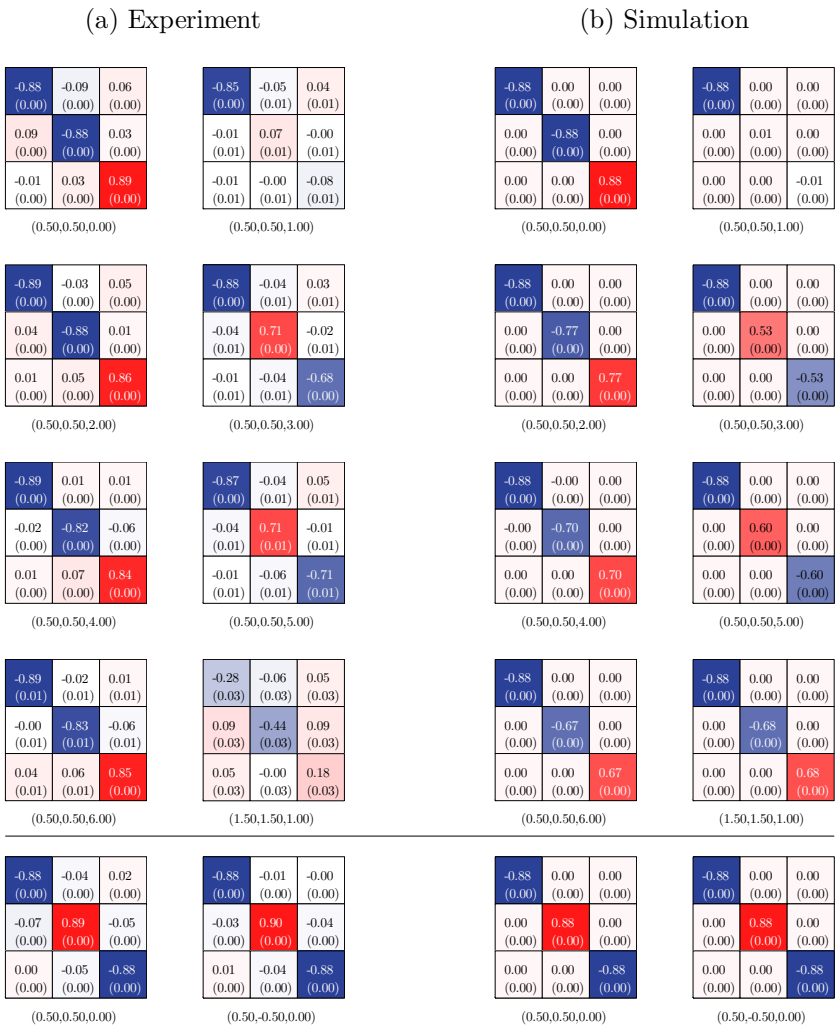

Figure 3.7: Comparison of polarisation matrices observed and calculated in the LTT phase. Some of the polarisation matrices collected in the LTT phase of La_2CoO_4 at 2 K. The polarisation matrices above and below the horizontal line represent measurements and simulations in the (h, h, l) and $(h, k, 0)$ scattering planes, respectively. The panels on the right show the best fit obtained by setting the in-plane angle $\phi = 23.5°$. The errors, as deduced from peak intensities are shown in parenthesis. The red (blue) colours represent $+1$ (-1) values of the matrix elements.

where $N^2(\boldsymbol{Q})$ is the coherent nuclear cross-section and the magnetic structure factor is $M_\perp(\boldsymbol{Q})^2$. The background can in general be different in each channel and is denoted by b_{NSF} and b_{SF}. From our measurements we find these terms are negligible compared to the strength of the nuclear and magnetic signal. Analogously, $\sigma(y, y)$ and $\sigma(z, z)$ will have a $N^2(\boldsymbol{Q})$ dependence. Since polarisation matrix elements are calculated as the difference between NSF and SF channels, a finite $N^2(\boldsymbol{Q})$ contribution will depolarise $P_{\alpha\alpha}$ elements, as found in La_2CoO_4.

To subtract the nuclear superlattice scattering from the polarisation matrices

it necessary to correct the intensities for non-ideal beam polarisation in the Blume frame of reference, as

$$\begin{bmatrix} \sigma_c(\alpha,\beta) \\ \sigma_c(\alpha,-\beta) \end{bmatrix} = \left[I - C^{-1}(R)(\delta_{\alpha\beta},0)C(R) \right] \begin{bmatrix} \sigma(\alpha,\beta) \\ \sigma(\alpha,-\beta) \end{bmatrix}, \tag{3.2}$$

where I is the identity matrix and $C(R)$ is a 2×2 matrix, which is dependent on the flipping ratio, to correct the number of counts in NSF (SF) channel wrongly analysed in the SF (NSF) polarisation channel (see § 2.4.3.1).

The full polarisation matrices obtained at $\boldsymbol{Q} = (0.5, 0.5, l)$ for $l = 2, 4, 6$, shown in Fig. 3.7, were corrected for the effect of the nuclear superlattice contamination using Eq. 3.2. Using a data set of 62 complete polarisation matrices collected at 1.7 K it is possible to compare these measurements to theoretical spin structure models. Setting the moments on Co(1) and Co(2) ions to be parallel, a fit of $\chi^2_\nu = 300$ is obtained when the moments are at angle of $\psi_1 = \psi_2 = 23.5°$ to the a axis. The fitting was done using the simulated annealing algorithm in the MuFit program [97]. However, an identical fit can be obtained by allowing both Co(1) and Co(2) moments to rotate. In this case a solution is found when $\psi_1 = -21.7°$ and $\psi_2 = 68.7°$, which corresponds to spins in adjacent layers along c to be aligned perpendicular to one another. A spin structure with spins aligned at $\psi_1 = 0°$ and $\psi_2 = 132.8°$ can also be used to describe the polarimetry data. The goodness-of-fit may not truly reflect the quality of the fit as errors are assumed to be given by Poisson statistics. In La_2CoO_4 it appears that we have reached a limit where the main source of uncertainty is due to systematic errors on a level of approximately 0.02 demonstrated by off-diagonal polarisation matrix elements in Fig. 3.7.

It does not appear to be possible to deduce which of the spin arrangements is realised in the LTT phase. The presence of domains ensures that all three structures are equivalent. The ambiguity was also found in the previous study [89]. It was found that the tilt of the CoO_6 octahedra determined the spin direction in the LTO phase. In the LTT phase, the octahedra rotate by 90° in alternate layers. Thus it would not seem unreasonable if the spin structure were to follow this in the low temperature phase. It was not possible to use the polarimetry data at base temperature to estimate the residual LTO spin structure, from Yamada *et al.* [89] this is reported to be about 5%, which should have little bearing on the spin structure determination presented here.

So far the analysis has focused on symmetry equivalent domains which have been assumed to occur in equal proportions. Due to the slight structural distortion in La_2CoO_4, this assumption may not necessarily hold true. Allowing the spin orientations and domain population to vary independently produces further possible magnetic structures. However, restricting the spin models to only the La_2CuO_4-like structure, where $\psi_1 = \psi_2 = 45°$, and allowing the domain population to vary does not appear to reproduce polarisation matrices of sufficiently good fit. Similarly staggering the spins from layer to layer along c by a 90° rotation with domain population set as free parameters also does not explain the polarimetry data. We

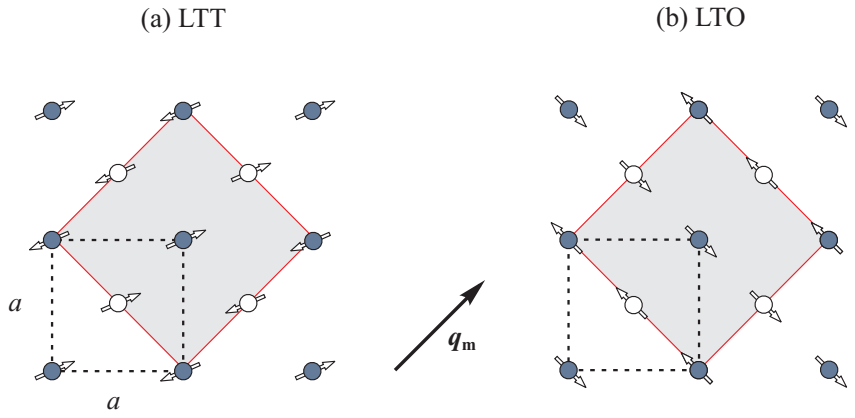

Figure 3.8: Magnetic structure of La_2CoO_4 in the LTT and LTO phases. The filled circles correspond to the moments in the $z = 0$ plane and the empty circles denote moments at the body-centred position, at $z = 0.5$. (a) Spin arrangement in the LTT phase deduced from polarimetry. The structure in the LTT phase could not be uniquely identified, spin arrangement shown here corresponds to the case where the moments on Co(1) and Co(2) atoms are parallel and at an angle of 23.5° to the a-axis. (b) Magnetic structure of La_2CoO_4 in the LTO phase with spins aligned perpendicularly to the propagation wavevector $\boldsymbol{q}_m$. The dashed line shows the crystallographic unit cell. The filled grey region represents the magnetic unit cell.

can therefore conclude that although it is not possible to rule out other spin arrangements, the data does provide clues on which structures can be ruled out which would otherwise not be possible using unpolarised neutron scattering.

3.5.5 Discussion

Spherical neutron polarimetry has been used in this section to ascertain the nature of the magnetic order in the two antiferromagnetic phases of La_2CoO_4. Directly below T_N, a simple antiferromagnetic spin arrangement develops with moments perpendicular to $\boldsymbol{q}_m$ and moments on the Co(1) and Co(2) ions parallel, as shown in Fig. 3.8(b). A first-order structural and magnetic transition is found at T_2. The magnetic structure in the LTT phase is found to be either collinear with a simple spin-rotation in the ab-plane with angle to the a axis of 23.5° [Fig. 3.8(a)], or a non-collinear arrangment which follows the tilts of the CoO_6 octahedra with moments rotating by 90° from layer to layer. The results are consistent with unpolarised neutron scattering measurements on La_2CoO_4 [89]. A symmetry breaking mechanism such as application of in-plane magnetic field may resolve the issue of the domain averaging.

The reason behind the rotation of the spins away from the a axis is unclear but must be related to competing exchange interactions in the system. In a similar compound of $La_{3/2}Sr_{1/2}CoO_4$ which orders antiferromagnetically in the basal plane, polarised neutron scattering measurements have demonstrated that the spin which is initially aligned along $\boldsymbol{a}$ slowly rotates by an angle of 12° on lowering of temperature [98]. In La_2CoO_4 the magnetic phase transition is of first order but it may be

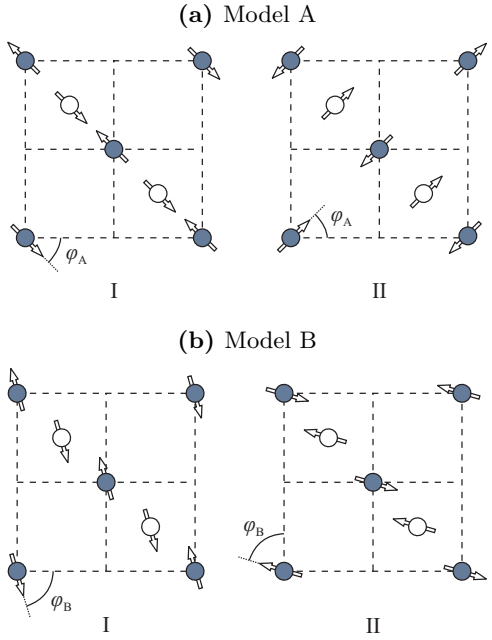

Figure 3.9: Magnetic structure models for $La_{3/2}Sr_{1/2}CoO_4$. The are cells shown in the CoO_2 plane are of size $2a \times 2a \times c$ with spin moments of Co^{2+} in the $z = 0$ plane represented by full circles and $z = 0.5$ layer denoted by empty circles. The non-magnetic Cu^{3+} ions are not shown in this diagram. (a) The angle ϕ_A at which the moment lies to the CoO bond is set to 45°. (b) Alternative model of the groundstate assumes there are almost equal population of domain BI and BII related to one another by a mirror plane perpendicular to $[1, \bar{1}, 0]$ The angle from the $\boldsymbol{a}$ axis is found to be 73.5°.

possible that the groundstate of La_2CoO_4 is similar to that of $La_{3/2}Sr_{1/2}CoO_4$.

3.6 $La_{3/2}Sr_{1/2}CoO_4$ examined by spherical neutron polarimetry

The crystal structure of $La_{3/2}Sr_{1/2}CoO_4$ can be described by the $I4/mmm$ space group with cell parameters, $a = 3.84$ Å and $c = 12.5$ Å. At this doping, Co^{2+} and Co^{3+} are found in equal proportions and the electrostatic repulsion between ions results in a checkerboard arrangement of charge and magnetic order. The magnetic structure consists of collinear moments confined to the ab plane due to strong planar anisotropy. The spins form antiferromagnetic stripes described by propagation wavevector $\boldsymbol{\kappa} = (0.25, 0.25, 0)$ along $[1, 1, 0]$ separated by a body centered Co^{3+} ion and ferromagnetic layers along $[1, \bar{1}, 0]$ modulated by antiferromagnetically aligned moments with respect to $z = 0$ plane at body centered position [98]. Previous measurements show that the magnetic order in the $z = 1/2$ layer is related to $z = 0$ by a translation vector $(1.5, 0.5, 0.5)$, however, the precise nature of the in-plane order has not been established [98]. The magnetisation is found to change as the sample is

h	k	l	$\boldsymbol{P}_i$			Polarisation matrix			Model A			Model B		
0.25	0.25	1.00	1	0	0	-0.70 (2)	-0.02 (2)	0.05 (2)	-0.81	0.00	0.00	-0.81	0.00	0.00
0.25	0.25	1.00	0	1	0	0.01 (2)	-0.53 (2)	0.01 (2)	0.00	-0.63	0.00	0.00	-0.63	-0.02
0.25	0.25	1.00	0	0	1	0.07 (2)	0.05 (2)	0.59 (2)	0.00	0.00	0.63	0.00	-0.02	0.63
0.25	0.25	-1.00	1	0	0	-0.75 (3)	-0.04 (3)	0.05 (3)	-0.81	0.00	0.00	-0.81	0.00	0.00
0.25	0.25	-1.00	0	1	0	0.04 (3)	-0.58 (3)	0.10 (3)	0.00	-0.63	0.00	0.00	-0.63	0.02
0.25	0.25	-1.00	0	0	1	0.07 (3)	0.10 (3)	0.72 (3)	0.00	0.00	0.63	0.00	0.02	0.63
0.25	0.25	3.00	1	0	0	-0.90 (2)	-0.12 (2)	0.08 (2)	-0.81	0.00	0.00	-0.81	0.00	0.00
0.25	0.25	3.00	0	1	0	0.06 (2)	-0.53 (2)	-0.02 (2)	0.00	-0.48	0.00	0.00	-0.48	-0.02
0.25	0.25	3.00	0	0	1	0.00 (2)	-0.02 (2)	0.52 (2)	0.00	0.00	0.48	0.00	-0.02	0.48
0.25	0.25	-3.00	1	0	0	-0.90 (3)	-0.03 (3)	0.10 (3)	-0.81	0.00	0.00	-0.81	0.00	0.00
0.25	0.25	-3.00	0	1	0	0.04 (3)	-0.46 (3)	0.04 (3)	0.00	-0.48	0.00	0.00	-0.48	0.02
0.25	0.25	-3.00	0	0	1	0.07 (3)	0.08 (3)	0.50 (3)	0.00	0.00	0.48	0.00	0.02	0.48
0.75	0.75	1.00	1	0	0	-0.75 (5)	-0.10 (5)	0.09 (5)	-0.81	0.00	0.00	-0.81	0.00	0.00
0.75	0.75	1.00	0	1	0	-0.09 (6)	-0.78 (5)	0.09 (5)	0.00	-0.77	0.00	0.00	-0.77	-0.01
0.75	0.75	1.00	0	0	1	-0.08 (5)	0.03 (5)	0.60 (6)	0.00	0.00	0.77	0.00	-0.01	0.77
0.75	0.75	-1.00	1	0	0	-0.89 (7)	-0.07 (7)	0.05 (7)	-0.81	0.00	0.00	-0.81	0.00	0.00
0.75	0.75	-1.00	0	1	0	0.06 (8)	-0.92 (7)	0.03 (7)	0.00	-0.77	0.00	0.00	-0.77	0.01
0.75	0.75	-1.00	0	0	1	-0.04 (7)	-0.03 (7)	0.80 (9)	0.00	0.00	0.77	0.00	0.01	0.77
-0.25	-0.25	1.00	-1	0	0	0.77 (2)	0.00	0.00	0.81	0.00	0.00	0.81	0.00	0.00
-0.25	-0.25	1.00	0	-1	0	0.00	0.60 (2)	0.00	0.00	0.63	0.00	0.00	0.63	0.02
-0.25	-0.25	1.00	0	0	-1	0.00	0.00	-0.66 (2)	0.00	0.00	-0.63	0.00	0.02	-0.63
0.25	0.25	3.00	-1	0	0	0.84 (3)	0.00	0.00	0.81	0.00	0.00	0.81	0.00	0.00
0.25	0.25	3.00	0	-1	0	0.00	0.47 (2)	0.00	0.00	0.48	0.00	0.00	0.48	0.02
0.25	0.25	3.00	0	0	-1	0.00	0.00	-0.54 (3)	0.00	0.00	-0.48	0.00	0.02	-0.48
0.25	0.25	-3.00	-1	0	0	0.81 (3)	0.00	0.00	0.81	0.00	0.00	0.81	0.00	0.00
0.25	0.25	-3.00	0	-1	0	0.00	0.53 (4)	0.00	0.00	0.48	0.00	0.00	0.48	-0.02
0.25	0.25	-3.00	0	0	-1	0.00	0.00	-0.47 (3)	0.00	0.00	-0.48	0.00	-0.02	-0.48
0.75	0.75	1.00	-1	0	0	0.74 (8)	0.00	0.00	0.81	0.00	0.00	0.81	0.00	0.00
0.75	0.75	1.00	0	-1	0	0.00	1.12 (12)	0.00	0.00	0.77	0.00	0.00	0.77	0.01
0.75	0.75	1.00	0	0	-1	0.00	0.00	-0.74 (10)	0.00	0.00	-0.77	0.00	0.01	-0.77
0.75	0.75	-1.00	-1	0	0	0.76 (7)	0.00	0.00	0.81	0.00	0.00	0.81	0.00	0.00
0.75	0.75	-1.00	0	-1	0	0.00	0.74 (8)	0.00	0.00	0.77	0.00	0.00	0.77	-0.01
0.75	0.75	-1.00	0	0	-1	0.00	0.00	-0.61 (8)	0.00	0.00	-0.77	0.00	-0.01	-0.77

Table 3.1: Comparison of measured and simulated polarisation matrices for $La_{3/2}Sr_{1/2}CoO_4$ measured at the (h, k, l) scattering wavevector. The incident neutron polarisation vector is denoted by $\boldsymbol{P}_i$. Models A and B, shown in Fig. 3.9, give qualitatively good fits demonstrated by $\chi^2_\nu = 3.7$.

cooled below 30 K [98]. One possibility is that at lower temperatures the moments rotate away from the $\boldsymbol{a}$ axis by 12° in the ab-plane. However, the neutron data [98] can also be explained in terms of a change in the population of inequivalent magnetic domains.

Polarised neutron diffraction is a valuable technique in understanding complex magnetic structures. Using the MuPAD/TASP instrument at PSI [76, 95, 96], spherical neutron polarimetry experiment was carried out on $La_{3/2}Sr_{1/2}CoO_4$ single crystal (0.873 g) with a final neutron wavelength of 3.2 Å. The sample was aligned in the (h, h, l) scattering plane. The crystal was cooled to 1.6 K at which complete normal and negative polarity polarisation matrices were recorded, shown in Table 3.1. Background subtraction was carried out away from the Bragg peaks by approximate displacement of $(0.1, 0.1, 0)$ from the peak centre, however due to the broad nature of the peaks, in some cases this proved to be insufficient.

We first consider Model A [Fig. 3.9(a)] for which moments lie parallel and perpendicular to the propagation vector $\boldsymbol{\kappa} = (0.25, 0.25, 0)$ along the easy axes of the system [98]. Such domains AI and AII, shown in Fig. 3.9(a), are not related by symmetry and therefore will in general be energetically different. The domains in such a model need not be populated equally and therefore setting this as a free parameter, we find a fit to the data with $\chi^2_\nu = 3.7$ where domain AI constitutes 63% and domain AII 37% of the volume of the sample. The simulated polarisation matrices using this model are shown in Table 3.1.

Representation analysis shows that the little group $G_{\boldsymbol{\kappa}}$ contains 8 symmetry elements that correspond to $\boldsymbol{\kappa}$. The star of $\boldsymbol{\kappa}$ is completed by symmetry operations contained in $\{G_0 - G_{\boldsymbol{\kappa}}\}$ group, which transform the propagation wavevector into $\boldsymbol{\kappa}' = (0.25, -0.25, 0)$. Furthermore, as the spins are assumed to lie in the ab plane, the relevant symmetry operators are reduced to four per propagation vector. Therefore, we find that each κ-domain contains two spin-domains, which are found by time reversal operator. It is therefore sufficient to consider domains BI and BII [Fig. 3.9(b)] which are related by a mirror plane normal to $[1, \bar{1}, 0]$ such that $\boldsymbol{a} \leftrightarrow \boldsymbol{b}$. An equally good fit ($\chi^2_\nu = 3.7$) to model A is found when the domain population is 50:50 and the moments are aligned at angle away from the $\boldsymbol{a}$ axis $\phi_B = 73.5°$. The rotation angle ϕ_B is in good agreement to the previously reported value of 12° [98]. However, the polarimetry data does not provide a unique solution to the magnetic structure. Indeed, simulations of polarisation matrices in other scattering planes are unable to distinguish between these models.

3.7 Magnetic excitations in La_2CoO_4

Attempts to understand the electronic phases in $La_{2-x}Sr_xCoO_4$ will require some basic knowledge of the parent antiferromagnet La_2CoO_4. The La_2CoO_4 system can then be used in trying to understand the unusual hourglass dispersion found in $La_{5/3}Sr_{1/3}CoO_4$ described in § 4. Although the crystal structure and magnetic order of La_2CoO_4 have been studied in detail [89] no measurements of the magnetic

excitation spectrum have been reported before now [88].

3.7.1 Experimental setup

Unpolarised-neutron inelastic scattering measurements were performed on the direct-geometry chopper spectrometer MAPS (shown in Fig. 2.6) at the ISIS facility [99]. Neutron time-of-flight instruments with large position sensitive detector arrays such as MAPS allow sampling of vast regions of $(\boldsymbol{Q}, E)$ space simultaneously, where $\boldsymbol{Q}$ and E are respectively the wavevector and energy transferred from the neutron to the sample. This is very advantageous in studies where the excitation spectrum is required throughout the Brillouin zone.

In preparation for the inelastic neutron measurements the La_2CoO_4 crystal (mass of 5.1 g) was sealed in a thin-walled aluminium can containing helium exchange gas and aligned with the c axis parallel to the direction of the incident neutron beam. Cooling was provided by a closed-cycle refrigerator. Data were collected with incident-neutron energies of 51, 86, 111, 152 and 303 meV. The energy resolution was typically 5% of the incident energy (full width at half maximum) at zero energy transfer, decreasing slightly with increasing energy transfer. Under the chosen experimental conditions the wavevector resolution is largely determined by the divergence of the incident neutron beam which is approximately 0.5°. Spectra from La_2CoO_4 were recorded at several temperatures between 6 K and 300 K. Separate measurements of a standard vanadium sample were made at each incident energy to normalise the spectra and place them on an absolute intensity scale.

For presentation and analysis, the neutron data were transformed from raw time-of-flight spectra into an intensity map as a function of $\boldsymbol{Q}$ and E. With a fixed sample orientation, only three out of the four components of $(\boldsymbol{Q}, E)$ are independent. Setting the two in-plane wavevector components $(Q_x, Q_y) = (h, k) \times 2\pi/a$ and energy as the independent variables, means that the out-of-plane wavevector $Q_z = l \times 2\pi/c$ varies implicitly with energy transfer. For a two-dimensional scattering system, however, there is no dispersion in the out-of-plane direction and the gradual variation of scattering intensity with Q_z can be included in a model (and was done so in this chapter). The justification for treating La_2CoO_4 as a two-dimensional magnetic system is that the magnetic spectra show no discernible periodic modulation in intensity with Q_z (i.e. with E).

In order to quantify the magnetic dispersion a series of constant-energy and constant-wavevector cuts are made through the data volume along high-symmetry directions [shown in Fig. 3.1(c)] using the MSLICE software [100]. Before performing these cuts, data at symmetry-equivalent wavevectors were averaged to improve the signal.

3.7.2 Results

Figure 3.10 provides an overview of the excitation spectrum of La_2CoO_4 measured by unpolarised inelastic neutron scattering at 6 K. Panels (a)–(c) are constant-

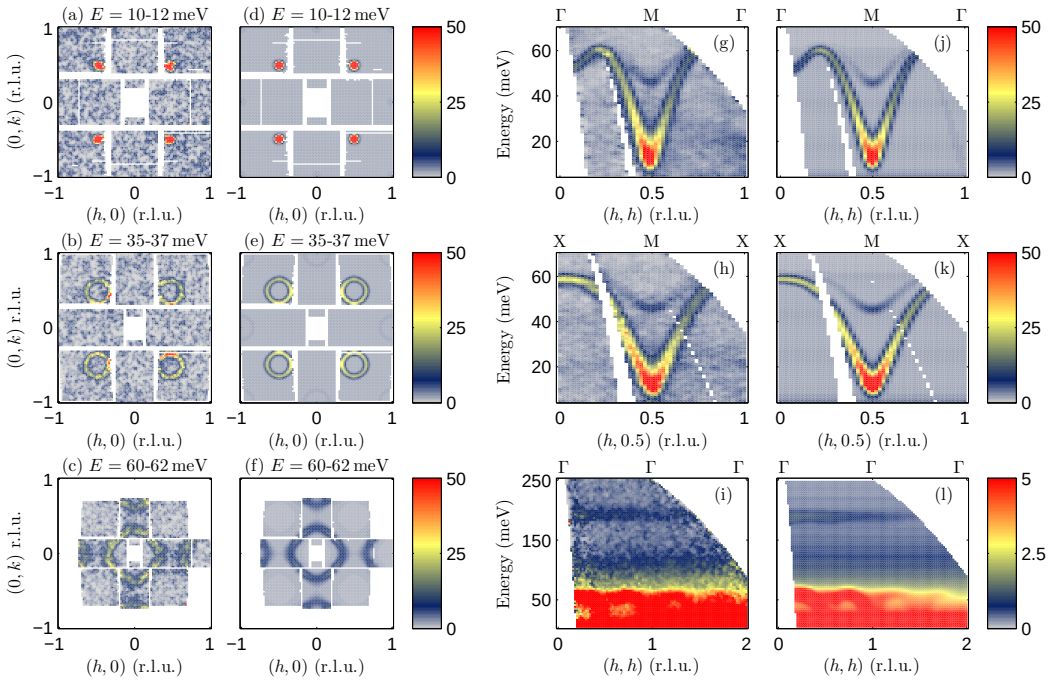

Figure 3.10: Measured and simulated magnetic spectra of La_2CoO_4 at 6 K. Panels (a)–(c) show intensity maps averaged over 2 meV energy ranges centred on different energies as indicated, with the corresponding calculated spectra shown in (d)–(f). The magnetic dispersion along two high-symmetry directions is displayed in (g)–(i), with corresponding simulations in (j)–(l). Data in (a)–(h) were measured with an incident neutron energy $E_i = 86$ meV, whilst (i) was measured with $E_i = 303$ meV. The units of intensity indicated by the colourbars are mb sr^{-1} meV^{-1} f.u.$^{-1}$. The simulated spectra are calculated from the spin-orbital spin-wave model. Reprinted figure with permission from Babkevich *et al.*, Phys. Rev. B **82**, 184425 (2010) [88]. Copyright © (2010) by the American Physical Society.

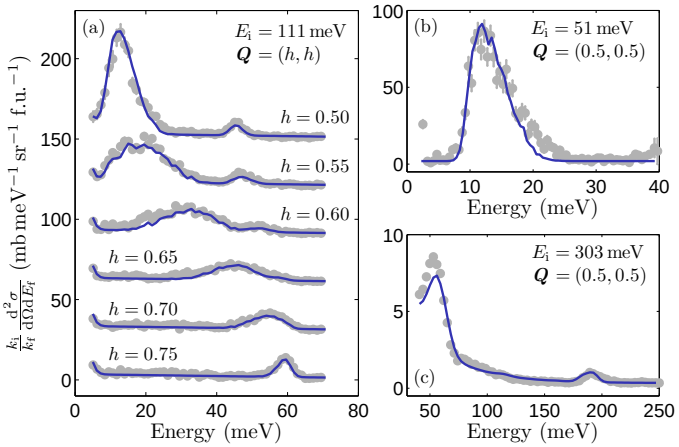

Figure 3.11: Constant-Q cuts taken through the measured and simulated spectra. Panel (a) shows a series of cuts following the dispersion from the zone center $(0.5, 0.5)$ to the antiferromagnetic zone boundary at $(0.75, 0.75)$ measured with incident energy 111 meV. Panel (b) shows the spin gap of ∼10 meV at $(0.5, 0.5)$ measured with an incident energy of 51 meV which gave an improved energy resolution. Panel (c) shows the measured and simulated excitation mode at ∼ 190 meV. These data were obtained with $E_i = 303$ meV. Reprinted figure with permission from Babkevich *et al.*, Phys. Rev. B **82**, 184425 (2010) [88]. Copyright © (2010) by the American Physical Society.

energy transfer E slices at three different energies, and panels (g)–(i) are energy transfer–$\boldsymbol{Q}$ slices to illustrate the magnetic dispersion. The spectrum is dominated by a spin-wave-like conical dispersion which rises from the in-plane antiferromagnetic ordering wavevector $\boldsymbol{q}_m = (0.5, 0.5)$ and equivalent positions [the M-points of the square-lattice Brillouin zone — see Fig. 3.1(c)]. This mode has a gap of approximately 10 meV at the M-point and rises to a maximum energy of 60 meV at the Σ-point on the Brillouin zone boundary. A much weaker branch, displaying an upwards dispersion with a minimum energy at M of 46 meV, corresponds to the first mode translated by $\boldsymbol{q}_m$. The large splitting of the modes at M shows that the anisotropy is strongly XY-like. The lower and upper modes correspond to in-plane and out-of-plane fluctuations, respectively. Fig. 3.10(i) shows data up to the maximum energy explored in our experiment. This reveals only one other significant feature — a band of scattering in a narrow range of energies close to 190 meV.

Figure 3.11 shows examples of constant-$\boldsymbol{Q}$ cuts taken through the data volumes measured with incident energies $E_i = 51$, 111 and 303 meV. To extract the magnetic dispersion in a form suitable for fitting to a model we performed a large number of such constant-energy cuts at wavevectors along the reciprocal-space paths indicated in Fig. 3.1(c). The peaks in these as well as some additional constant-wavevector cuts were fitted with Gaussian functions on a linear background. The peak centres determined this way are plotted along high-symmetry directions in Figs. 3.14 and 3.15.

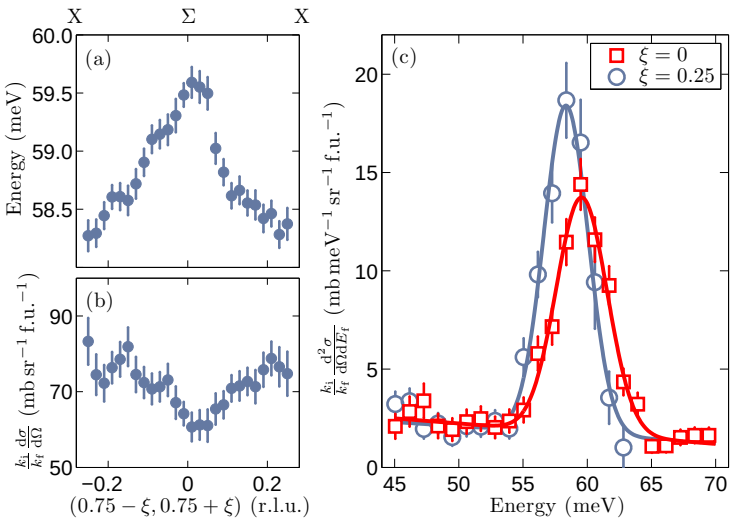

Figure 3.12: Dispersion of the magnon peak along the magnetic zone boundary in La_2CoO_4. Variation of (a) the peak position and (b) the integrated intensity of the magnon peak in constant-$\boldsymbol{Q}$ cuts. (c) Constant-$\boldsymbol{Q}$ cuts at $\boldsymbol{Q} = (0.75, 0.75)$ and $(0.5, 1)$ fitted with Gaussian lineshapes. The data are from the run with incident energy 111 meV and sample temperature 6 K. Reprinted figure with permission from Babkevich *et al.*, Phys. Rev. B **82**, 184425 (2010) [88]. Copyright © (2010) by the American Physical Society.

An interesting behavior is observed along the magnetic zone boundary: the energy of the magnon branch is not constant but varies by approximately 1.5 meV. As shall be discussed, this is significant because a dispersion along the zone boundary indicates a need to go beyond a linear spin-wave model with nearest-neighbor interactions only. This effect is emphasised in Fig. 3.12(a) the energy and (b) the integrated intensity of the magnon peak along the entire length of a zone boundary (XΣX). The maximum in the dispersion at Σ is seen to coincide with a minimum in its intensity. Because the dispersion surface forms a ridge along the zone boundary care was taken to select an appropriately-sized box in $\boldsymbol{Q}$ over which to average the data so as to avoid systematic errors from the curvature of the dispersion surface while at the same time having good enough statistics to extract the peak energies and integrated intensities. Figure 3.12(c) shows energy cuts taken at an X-point and a Σ-point to illustrate the difference between the magnon peaks at the zone corner and zone edge.

Finally, it is worth noting the temperature dependence of the magnetic spectrum. Figures 3.13(a)–(c) show maps of the magnetic scattering measured at $T = 6$, 150 and 300 K, and Fig. 3.13(d) displays constant-$\boldsymbol{Q}$ cuts at the magnetic zone centre for the same temperatures. On increasing the temperature from 6 to 150 K the 11 meV peak increases in intensity due to the increasing thermal population but remains at the same energy, while the 46 meV peak broadens and shifts to lower energy [Fig. 3.13(d) inset]. Although La_2CoO_4 undergoes a first-order phase transition coincident with a magnetic reorientation at $T_2 \approx 125$ K, the in-plane lattice

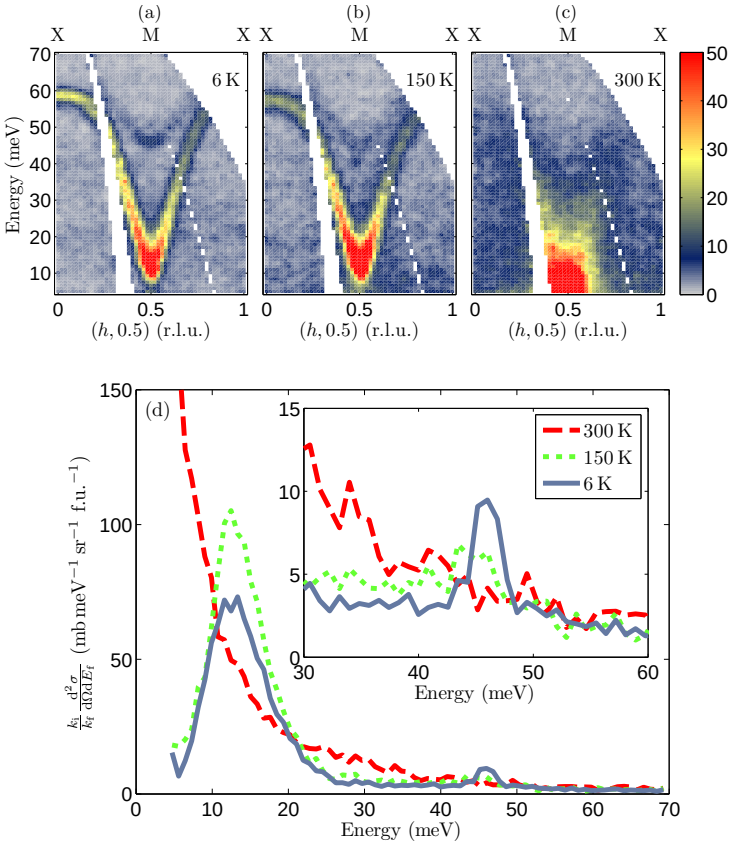

Figure 3.13: Temperature dependence of the magnetic spectrum of La_2CoO_4. The upper panels (a)–(c) show intensity maps measured at 6, 150 and 300 K along the $(h, 0.5)$ direction. (d) Magnetic spectrum at the antiferromagnetic ordering wavevector $(0.5, 0.5)$ (M-point) measured at 6, 150 and 300 K. Inset: temperature evolution of the higher-energy magnon mode. Reprinted figure with permission from Babkevich *et al.*, Phys. Rev. B **82**, 184425 (2010) [88]. Copyright © (2010) by the American Physical Society.

parameters in the LTO phase differ only slightly from those in the LTT phase, and the change in the magnetic structure only affects the stacking along the c axis. It is not surprising, therefore, that the transition does not significantly affect the magnetic spectrum. At $T = 300\,\mathrm{K}$, the spectrum has become quasielastic and there are no longer any sharp inelastic peaks. This indicates the absence of long-range magnetic correlations for $T > T_\mathrm{N}$.

3.7.3 Linear spin-wave model

As a suitable starting point in analysing the low energy part of the excitation spectrum ($E < 60\,\mathrm{meV}$) of La_2CoO_4 it is worth to consider the standard linear spin-wave theory for an effective spin-$\frac{1}{2}$ antiferromagnet, which neglects the orbital component of the modes. Using the same model as described in Ref. [98] in which the magnetic anisotropy is described by anisotropic nearest-neighbor exchange interactions $J_x = J(1+\varepsilon)$, $J_y = J$ and $J_z = J(1-\delta)$. The parameters ε and δ control the in-plane and out-of-plane anisotropy, respectively. The more distant interactions J_1 and J_2 were included too, but because they are relatively small we treated these as isotropic. The paths of the exchange interactions are shown in Fig. 3.1(b).

3.7.3.1 Linear spin-wave theory

A more generalised Hamiltonian given in Eq. 1.10 describing the exchange interaction between spins can be expressed as, $\mathcal{H} = \sum_{\langle ij \rangle} \sum_\alpha J_\alpha S_i^\alpha S_j^\alpha$, where the summation is taken over different spatial directions $\alpha = x$, y and z and includes an exchange anisotropy. The Hamiltonian $\mathcal{H}_m$ of mth magnetic unit cell can be considered to be due to anisotropic antiferromagnetic interactions (AFM, J_i^A) and ferromagnetic (FM, J_i^F) between collinear spins, such that

$$\begin{aligned}\mathcal{H}_m \;=\; & \sum_{\boldsymbol{r}} J_x^\mathrm{A} S_{\boldsymbol{m}}^x S_{\boldsymbol{m}+\boldsymbol{r}}^x + J_y^\mathrm{A} S_{\boldsymbol{m}}^y S_{\boldsymbol{m}+\boldsymbol{r}}^y + J_z^\mathrm{A} S_{\boldsymbol{m}}^z S_{\boldsymbol{m}+\boldsymbol{r}}^z \\ & + \sum_{\boldsymbol{R}} J_x^\mathrm{F} S_{\boldsymbol{m}}^x S_{\boldsymbol{m}+\boldsymbol{R}}^x + J_y^\mathrm{F} S_{\boldsymbol{m}}^y S_{\boldsymbol{m}+\boldsymbol{R}}^y + J_z^\mathrm{F} S_{\boldsymbol{m}}^z S_{\boldsymbol{m}+\boldsymbol{R}}^z, \end{aligned} \tag{3.3}$$

where spins of opposing alignment are connected by $\boldsymbol{r}$ and nearest neighbour same spins are joined by $\boldsymbol{R}$. The Holstein-Primakoff transformations [10] can be used to transform the spin operators to Bose operators by considering the spins to lie on bipartite sublattices A and B such that the exchange interaction is AFM between A and B and FM within each sublattice. For quantisation axis along x,

$$\begin{array}{ll} \textbf{Sublattice A} & \textbf{Sublattice B} \\ S_i^x = (S - a_i^\dagger a_i) & S_j^x = -(S - b_j^\dagger b_j) \\ S_i^y = \sqrt{S/2}(a_i + a_i^\dagger) & S_j^y = \sqrt{S/2}(b_j + b_j^\dagger) \\ S_i^z = -\mathrm{i}\sqrt{S/2}(a_i - a_i^\dagger) & S_j^z = \mathrm{i}\sqrt{S/2}(b_j - b_j^\dagger). \end{array} \tag{3.4}$$

Expressing the Hamiltonian in terms of the spin operators up to quadratic terms followed by the Fourier transform as defined in § A.2 would give the Hamiltonian, in the general matrix form as,

$$\mathcal{H} = \mathcal{H}_0 + \frac{1}{2}\sum_{\boldsymbol{Q}} X^{\dagger}_{\boldsymbol{Q}} H_{\boldsymbol{Q}} X_{\boldsymbol{Q}}, \tag{3.5}$$

where $X_{\boldsymbol{Q}}$ is a vector of magnon creation and annihilation operators for the two sublattices, $X^{\dagger}_{\boldsymbol{Q}}$ is its transposed Hermitian adjoint. The solution to this type of problem is known and is described in Ref. [101]. The Hamiltonian $H_{\boldsymbol{Q}}$ of the form of Eq. 3.5, $X_{\boldsymbol{Q}}$ will in general contain all the appropriate operators and their adjoints. Thus if $X_{\boldsymbol{Q}}$ is composed of $1 \ldots n$ elements that are independent annihilation $(a_{\boldsymbol{Q}})$ and $(n+1) \ldots 2n$ corresponding to the creation operators $(a^{\dagger}_{-\boldsymbol{Q}})$

$$X_{\boldsymbol{Q}} = \left[a_1(\boldsymbol{Q}), \ldots, a_n(\boldsymbol{Q}), a^{\dagger}_1(-\boldsymbol{Q}), \ldots, a^{\dagger}_n(-\boldsymbol{Q})\right]^{\mathrm{T}}, \tag{3.6}$$

with Boson operators obeying $[a_\alpha(\boldsymbol{q}), a^{\dagger}_\beta(\boldsymbol{q}')] = \delta_{\alpha\beta}\delta_{\boldsymbol{q}\boldsymbol{q}'}$ then the $H_{\boldsymbol{Q}}$ takes the form,

$$H_{\boldsymbol{Q}} = \begin{pmatrix} H_{11}(\boldsymbol{Q}) & H_{12}(\boldsymbol{Q}) \\ H^{*}_{12}(-\boldsymbol{Q}) & H^{*}_{11}(-\boldsymbol{Q}) \end{pmatrix}, \tag{3.7}$$

where H_{11} and H_{12} are $n \times n$ matrices. Quadratic in the bosonic operators, the Hamiltonian can be diagonalised by a canonical transformation. In order to preserve the commutation relations, the transformation must preserve the metric g,

$$\left[X_{\boldsymbol{Q}}, X^{\dagger}_{\boldsymbol{Q}}\right] = g, \qquad g = \begin{pmatrix} I & 0 \\ 0 & -I \end{pmatrix}, \tag{3.8}$$

such that I is the $n \times n$ identity matrix. New operators $X'_{\boldsymbol{Q}}$ may be introduced, such that $X_{\boldsymbol{Q}} = S_{\boldsymbol{Q}} X'_{\boldsymbol{Q}}$. The Hamiltonian can then be solved as an eigenvalue problem, $|gH_{\boldsymbol{Q}}S_{\boldsymbol{Q}} - \lambda S_{\boldsymbol{Q}}| = 0$.

The total Fourier-transformed Hamiltonian $H_{\boldsymbol{Q}}$ can be expressed in the form of Eq. 3.5 by considering a set of operators defined in $X_{\boldsymbol{Q}}$

$$X_{\boldsymbol{Q}} = \begin{pmatrix} a_{\boldsymbol{Q}} \\ b_{\boldsymbol{Q}} \\ a^{\dagger}_{-\boldsymbol{Q}} \\ b^{\dagger}_{-\boldsymbol{Q}} \end{pmatrix}, \qquad H_{\boldsymbol{Q}} = \begin{pmatrix} A_{\boldsymbol{Q}} & B_{\boldsymbol{Q}} & C_{\boldsymbol{Q}} & D_{\boldsymbol{Q}} \\ B_{\boldsymbol{Q}} & A_{\boldsymbol{Q}} & D_{\boldsymbol{Q}} & C_{\boldsymbol{Q}} \\ C_{\boldsymbol{Q}} & D_{\boldsymbol{Q}} & A_{\boldsymbol{Q}} & B_{\boldsymbol{Q}} \\ D_{\boldsymbol{Q}} & C_{\boldsymbol{Q}} & B_{\boldsymbol{Q}} & A_{\boldsymbol{Q}} \end{pmatrix} \tag{3.9}$$

where the Fourier coefficients are found for the case of La_2CoO_4 to be,

$$\begin{aligned} A_{\boldsymbol{Q}}/S &= 4J_x - 4J_1 - 4J_2 \\ &\quad + 2J_1\left(\cos 2\boldsymbol{Q}\cdot\boldsymbol{a} + \cos 2\boldsymbol{Q}\cdot\boldsymbol{b}\right) \\ &\quad + 2J_2\left[\cos\boldsymbol{Q}\cdot(\boldsymbol{a}-\boldsymbol{b}) + \cos\boldsymbol{Q}\cdot(\boldsymbol{a}+\boldsymbol{b})\right] \qquad (3.10) \\ B_{\boldsymbol{Q}}/S &= (J_y - J_z)\left(\cos\boldsymbol{Q}\cdot\boldsymbol{a} + \cos\boldsymbol{Q}\cdot\boldsymbol{b}\right) \qquad (3.11) \\ C_{\boldsymbol{Q}}/S &= 0 \qquad (3.12) \\ D_{\boldsymbol{Q}}/S &= (J_y + J_z)\left(\cos\boldsymbol{Q}\cdot\boldsymbol{a} + \cos\boldsymbol{Q}\cdot\boldsymbol{b}\right) \qquad (3.13) \end{aligned}$$

The Hamiltonian can be diagonalised leading to expressions for the two modes with spin-wave dispersion relations given by,

$$E_{\pm}(\boldsymbol{Q}) = \left[\left(A_{\boldsymbol{Q}} \pm B_{\boldsymbol{Q}}\right)^2 - \left(C_{\boldsymbol{Q}} \pm D_{\boldsymbol{Q}}\right)^2\right]^{1/2}. \qquad (3.14)$$

A more comprehensive discussion of applying the linear spin-wave theory is given in Appendix A.

3.7.3.2 Simulated annealing algorithm

The comparison between a spin-wave model and the measured dispersion can be made by allowing the exchange interactions to be varied. Such model, however, suffers from having many free parameters and most standard fitting routines such as Levenberg-Marquardt or gradient search optimisation algorithms fail to converge to meaningful solutions as they become quickly trapped in local, rather than global χ^2 minima. A suitable strategy to overcome these problems is to use simulated annealing method, which mimics the process in which materials become ordered when they are slowly cooled. To do this, the method of importance sampling developed in Ref. [102] is implemented to allow the solver to explore a larger space of possible solutions. The difference between the previously ascertained goodness-of-fit χ_i^2 and another χ_j^2 is accepted with a probability function P described by,

$$P = \begin{cases} e^{-(\chi_i^2 - \chi_j^2)/\theta} & \text{if } (\chi_i^2 - \chi_j^2) > 0, \\ 1 & \text{otherwise.} \end{cases} \qquad (3.15)$$

A temperature parameter θ is then lowered to slowly allow the system to converge to the true global minimum, representing the optimal fit of the model to the measured data.

3.7.3.3 Simulations of the magnetic excitation spectrum using spin-only spin-wave model

The main features of the low-energy excitation spectrum of La_2CoO_4 can be captured by the linear spin-wave model using methods outlined in the preceding sections. Figure 3.14 shows a fit to the dispersion which qualitatively agrees with the

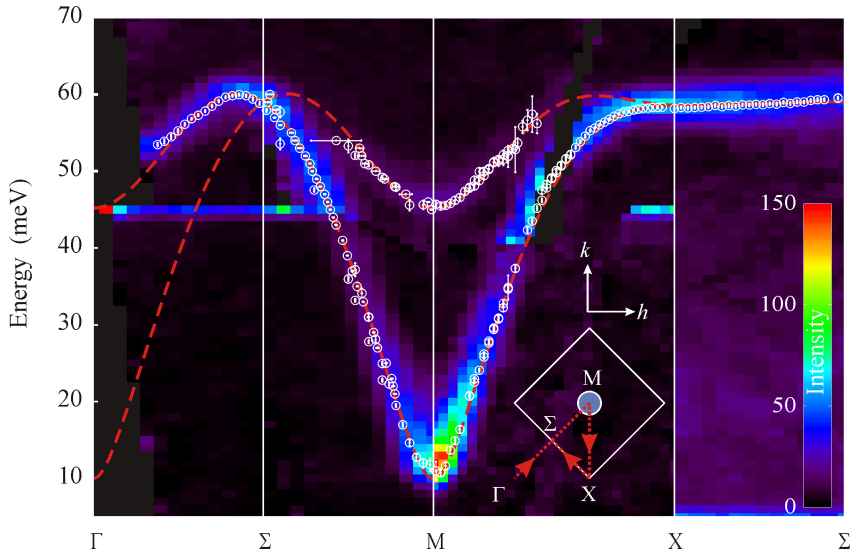

Figure 3.14: Simulation of the dispersion relation in La_2CoO_4 using linear spin-wave model. Intensity map constructed from measurements made with incident neutron energies of 51, 86 and 111 meV along high-symmetry directions indicated in the inset. The open white data points are $(\boldsymbol{Q}, E)$ points used to fit the dispersion using linear spin-wave model, shown in dashed red lines. The fit parameters were $J = 8.30\,\text{meV}$, $J_1 = -0.353\,\text{meV}$, $J_2 = -0.634\,\text{meV}$, $\varepsilon = 0.0241$ and $\delta = 0.383$.

measurements. In fact, an equally good description of the data (as reflected in the value of χ^2) could be found with sets of parameters in which J_1 and J_2 are both positive or both negative: (i) $J = 9.89(1)\,\text{meV}$, $J_1 = 0.04(1)\,\text{meV}$, $J_2 = 0.13(1)\,\text{meV}$, $\varepsilon = 0.013(1)$, $\delta = 0.283(4)$, or (ii) $J = 8.30(6)\,\text{meV}$, $J_1 = -0.35(2)\,\text{meV}$, $J_2 = -0.63(3)\,\text{meV}$, $\varepsilon = 0.024(1)$, $\delta = 0.383(5)$. Using the spin-only spin-wave model to model the dispersion along the magnetic zone boundary, shown in Fig. 3.12(c), the observation that the mode at X is found to be at lower energy than at Σ, or $E_X/E_\Sigma < 1$, is satisfied if,

$$J_2 > 2J_1 \qquad \text{iff } J_1, J_2 > 0, \text{or} \tag{3.16}$$

$$J_2 < 2J_1 \qquad \text{iff } J_1, J_2 < 0. \tag{3.17}$$

This demonstrates that in principle there could be other solutions for the exchange interaction strengths. As will be demonstrated in the next section, a model which includes the full magnetic degrees of freedom of Co^{2+} does indeed provide a good description of the magnetic excitation spectrum. Another drawback of the effective spin–$\frac{1}{2}$ linear spin-wave model is that the intensities are not accurately described because of the neglect of the orbital degrees of freedom.

3.7.4 Spin-orbital many-level model

Magnetism in Co^{2+} compounds like La_2CoO_4 is generally influenced to a significant degree by unquenched orbital angular momentum which is responsible for, among

other things, the strong anisotropy in the susceptibility observed in many such compounds. In a recent study [98] of the magnetic excitations in the half-doped cobaltate $La_{3/2}Sr_{1/2}CoO_4$, which is also an antiferromagnet, a model was developed to describe the magnetic spectrum including both the spin and orbital angular momentum of the Co^{2+} in the high-spin configuration ($3d^7$, $S = 3/2$, $L = 3$). The model is an advance over conventional (spin-only) spin-wave theory, described in § 3.7.3, in that it includes level-mixing within the ^{2S+1}L term caused by the ligand and exchange fields, and hence the parameters that describe the single-ion anisotropy and exchange interactions are physically realistic. As far as the magnetic spectrum is concerned, the admixture of basis states means that excitations to levels above the first excited single-ion level can propagate and can be observed by neutron scattering. Moreover, the orbital component of the single-ion states needs to be included for an accurate calculation of the neutron cross section.

The model employs the Hamiltonian [2]

$$\begin{aligned}\mathcal{H} &= \sum_{\langle jk\rangle} J_{jk}\boldsymbol{S}_j \cdot \boldsymbol{S}_k \\ &\quad + \sum_j \left[\sum_{l,m} B_l^m O_l^m(\boldsymbol{L}_j) + \lambda \boldsymbol{L}_j \cdot \boldsymbol{S}_j + \boldsymbol{H}_j^{\mathrm{a}} \cdot \boldsymbol{S}_j\right].\end{aligned} \tag{3.18}$$

The first term describes an isotropic Heisenberg exchange interaction between pairs of $S = 3/2$ spins. For La_2CoO_4 we include only the nearest-neighbour and next-nearest-neighbour exchange interactions J, J_1 and J_2, as defined in Fig. 3.1(b). The remaining terms in Eq. 3.18 are single-ion terms. The first of these represents the crystal (ligand) field acting on the Co^{2+} ions. The O_l^m are Stevens operator-equivalents with B_l^m the corresponding crystal-field parameters. The axially-distorted octahedral crystal field from the neighboring O^{2-} ions is described by the operators O_2^0, O_4^0 and O_4^4. We kept the same values for the parameters B_4^0 and B_4^4 as found for $La_{1.5}Sr_{0.5}CoO_4$ in Ref. [98]: $B_4^0 = -1.35\,\mathrm{meV}$ and $B_4^4 = -8.00\,\mathrm{meV}$. These are estimated from a point-charge calculation and scaled to match the cubic crystal field splitting observed in CoO [103]. The parameter B_2^0 controls the out-of-plane anisotropy and was adjusted to obtain a good fit to the magnetic spectrum. Its final value (see below) differs from that deduced for $La_{3/2}Sr_{1/2}CoO_4$ by only ∼10%. The term $\lambda\boldsymbol{L}\cdot\boldsymbol{S}$ is the spin-orbit coupling. The coupling constant $\lambda = -18.7\,\mathrm{meV}$ used here has been deduced from reflectivity measurements of CoO by optical spectroscopy [103]. The final term $\boldsymbol{H}^{\mathrm{a}}\cdot\boldsymbol{S}$ represents a small uniaxial anisotropy which defines the in-plane orientation of the moments and produces a spin gap at the Γ-point (and, equivalently, the M-point). We chose the moments to lie along the x axis, and to achieve this the anisotropy field $\boldsymbol{H}^{\mathrm{a}}$ points along $+x$ on one of the antiferromagnetic sublattices and along $-x$ on the other.

Spherical neutron polarimetry discussed in § 3.5 concluded that the spins are

[2] The diagonalisation of Eq. 3.18 was carried out using ExcitonQ program written by A.T. Boothroyd, more details on this are found in Ref. [98].

aligned parallel or perpendicular to $\boldsymbol{q}_\mathrm{m}$ in La_2CoO_4. However, within the spin-wave models considered here where spins are along a, the inclusion of domains means that the excitation spectrum appears to be the same whether moments are aligned along a or lie at $\pm 45°$ to a. Hence, the analysis of the polarimetry and inelastic neutron scattering experiments are not contradictory.

The partial differential scattering cross-section depends on the response functions $S^{\alpha\alpha}(\boldsymbol{Q},\omega)$ describing $\alpha\alpha$ magnetic correlations. In the dipole approximation the relation for one-magnon excitation is [44]

$$\frac{k_\mathrm{i}}{k_\mathrm{f}}\frac{\mathrm{d}^2\sigma}{\mathrm{d}\Omega \mathrm{d}E_\mathrm{f}} = \left(\frac{\gamma r_0}{2}\right)^2 f^2(Q)\,\mathrm{e}^{-2W}\sum_\alpha (1-\hat{Q}_\alpha^2) S^{\alpha\alpha}(\boldsymbol{Q},\omega), \tag{3.19}$$

where

$$S^{\alpha\alpha}(\boldsymbol{Q},\omega) = \sum_j |\langle j|M^\alpha(\boldsymbol{Q})|0\rangle|^2 \delta[\omega-\omega_j(\boldsymbol{Q})]. \tag{3.20}$$

Here, k_i and k_f are initial and final neutron wavevectors, $(\gamma r_0/2)^2 = 72.8\,\mathrm{mb}$, $f(Q)$ is the dipole magnetic form factor of Co^{2+}, e^{-2W} is the Debye-Waller factor which is close to unity at low temperatures, and $\hat{Q}_\alpha = Q_\alpha/|\boldsymbol{Q}|$ is the α component of a unit vector in the direction of $\boldsymbol{Q}$. The response function (per La_2CoO_4 f.u.) described in Eq. 3.20 takes into account both the spin and orbital magnetisation $\boldsymbol{M} = -(\boldsymbol{L}+2\boldsymbol{S})$ in the transition matrix element connecting the ground state to an excited mode j. The procedure to diagonalise the Hamiltonian (3.18) to obtain the dispersion and response functions of the magnetic modes is described in detail in Ref. [98]. In order to make a comparison between measured and predicted intensities, it is necessary to account for the broadening of the spectrum due to the instrumental resolution effects and also apply corrections for the absorption and self-shielding effects. These are briefly discussed next.

3.7.4.1 Approximate form of the resolution function

In order to approximate the resolution function of the MAPS spectrometer we can consider the wavevector and energy broadening separately. Assuming the angular beam divergence is the limiting broadening with FWHM of $\delta\phi \approx 0.5°$, for an incident energy E_i, we can calculate the wavevector-dependent broadening to be $\delta|\boldsymbol{Q}| \approx k_\mathrm{i}\delta\phi$. Using this result we convolute the simulated spectrum by a Gaussian function with width given by Eq. 3.7.4.1. For $E_\mathrm{i} = 100\,\mathrm{meV}$, this would correspond to a broadening of approximately $\delta|\boldsymbol{Q}| \approx 0.03\,\mathrm{r.l.u.}$ along the a axis. The energy-dependent broadening is governed by,

$$\delta E = \frac{\delta E_0}{1+L_1/L_2}\left[1+\frac{L_1}{L_2}\left(\frac{E_\mathrm{i}-E}{E_\mathrm{i}}\right)^{3/2}\right], \tag{3.21}$$

where δE_0 is the elastic linewidth and E is the energy transfer, see § 2.4.4 for more details. For the MAPS spectrometer the target-sample (L_1) and sample-detector

	σ_{abs} (b)	σ_{coh} (b)	σ_{inc} (b)
La	8.97	8.53	1.13
Co	37.18	0.78	4.8
O	0	4.23	0
La_2CoO_4	**55.1**	**34.8**	**7.1**

Table 3.2: Absorption, coherent scattering and incoherent scattering cross-sections given in units of barn. The absorption cross-section is quoted for incident 25 meV neutrons, from Ref [104].

(L_2) distances are assumed to be 12 and 6 m respectively. The full-width at half-maximum of the elastic peak at (0.5, 0.5) as a function of incident energy are found to be:

E_i (meV):	51	86	111	303
δE_0 (meV):	2.5	4.6	5.9	20.7

Equation 3.21 shows that the resolution of the spectrometer increases at large energy transfer.

3.7.4.2 Absorption and self-shielding effects

A neutron incident on the sample can be either be absorbed or be scattered multiple times as it transverses the crystal. Both effects lower the transmission of neutrons and a correction to the simulated spectrum calculated using Eq. 3.19 must be applied.

The process of multiple scattering arises when the neutron is scattered more than once within the bulk of the sample. The most probable process is for two elastic scattering events as coherent scattering cross-section σ_{coh} are larger than incoherent σ_{inc} ones in general. However, this is irrelevant as we are interested in the inelastic neutron spectrum. The process in which an elastic scattering event is either followed or preceded by inelastic event are more problematic. The energy transfer would appear to be the same as an inelastic scattering event, the direction of the scattered neutron will differ. Two inelastic scattering events can be considered to be negligible.

The total cross-section per formula unit $\sigma_{tot}(E)$ of La_2CoO_4 for neutron of energy E can be calculated as,

$$\sigma_{tot}(E) = \sigma_{abs}(E) + \sigma_{inc} + f\sigma_{coh}, \tag{3.22}$$

where f relates the fraction of neutrons lost through coherent scattering. Spectra calculated in this chapter assume $f \approx 0.1$. The values of the coherent and incoherent scattering cross-sections as well as the absorption cross-section σ_{abs} are shown in Table 3.2. The absorption cross-section, in the low energy limit (< 1 eV), is inversely proportional to the neutron velocity, or $\sigma_{abs} \propto 1/\sqrt{E}$.

The transmission function $\mathcal{T}$ can be found by considering a uniform rectangular sample of thickness d in which an incident neutron is scattered, changing energy from E_i to E_f,

$$\mathcal{T} = \frac{1}{d}\int_0^d e^{-n\sigma_\mathrm{tot}(E_\mathrm{i})x} e^{-n\sigma_\mathrm{tot}(E_\mathrm{f})(d-x)}\,dx, \tag{3.23}$$

where n is the number of formula units per unit volume. Neutrons with an incident energy of 100 meV irradiating a 5 mm thick sample will result in a transmission factor of 0.82 and 0.64 when E is 10 and 95 meV, respectively.

3.7.4.3 Simulating the magnetic excitations

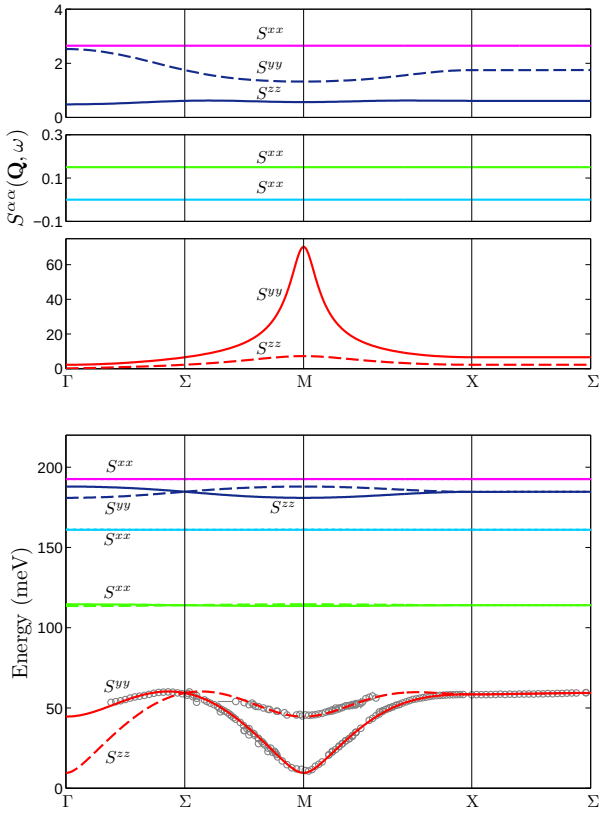

Figure 3.15: Spin-wave dispersion calculated using spin-orbital many-level model for La_2CoO_4. The lower figure shows the dispersion of the magnetic excitations of La_2CoO_4 along high symmetry directions in the 2D Brillouin zone defined in Fig. 3.1(c). Open circles are points extracted from cuts through the measured data volume. The lines show the dispersion of the modes calculated with the many-level spin-wave model described in the text. The upper figure shows the response functions $S^{\alpha\alpha}$ for each mode calculated from the many-level model. The normalisation of the response functions is per formula unit of La_2CoO_4. Reprinted figure with permission from Babkevich *et al.*, Phys. Rev. B **82**, 184425 (2010) [88]. Copyright © (2010) by the American Physical Society.

The parameters of the spin-orbital many-level model were refined from a fit to the measured dispersion carried out by a simulated-annealing algorithm (§ 3.7.3.2). Because of the computer time required to diagonalise the Hamiltonian for the complete set of $2 \times \{(2L+1)(2S+1) - 1\} = 54$ excited states (twice the number of single-ion excited states because we have two magnetic sublattices) we restricted the number of observables included in the fit to just enough to represent all the important features of the data, including the high-energy signal at ∼190 meV. The parameters varied in the fit were B_2^0, J, J_1, J_2, and H^{a}. The best fit was achieved with parameters $B_2^0 = 14.6(1)$ meV, $J = 9.69(2)$ meV, $J_1 = 0.14(2)$ meV, $J_2 = 0.43(1)$ meV, and $H^{\mathrm{a}} = 0.66(6)$ meV. By contrast to the spin-only model discussed in § 3.7.3, the spin-orbital many-level model clearly favours the case with J_1 and J_2 both positive. The model can discriminate the two cases because of the inclusion of the higher excited levels. Only the parameter set with J_1 and J_2 both positive fits the low energy modes ($E < 60$ meV) *and* reproduces the peak in the spectrum at ∼190 meV and absence of any other measurable peaks between 60 and 250 meV.

The calculated dispersion and response functions of the magnetic modes are shown in Fig. 3.15 together with the full set of data points for the lowest energy modes determined from the measurements. The agreement is seen to be very good. The fit indicates that the next-nearest-neighbour exchange constants J_1 and J_2 are very small but not zero. As a test, the fit was repeated with J_1 and J_2 fixed to zero. The quality of best fit in such model worsened, as indicated by the goodness-of-fit parameter χ^2 per degree of freedom which increased from 4.5 to 11.1. Therefore, the obtained values of J_1 and J_2, though small compared to the dominant nearest-neighbour interaction, are still significant.

To further visualise and assess the model intensity maps and cuts have been calculated to simulate those obtained from the experiment. Figures 3.10 and 3.11 show the simulations alongside the corresponding experimental data. The quantity plotted is $(k_{\mathrm{i}}/k_{\mathrm{f}})\mathrm{d}^2\sigma/\mathrm{d}\Omega\mathrm{d}E_{\mathrm{f}}$ per formula unit (f.u.), i.e., the partial differential cross section multiplied by a factor $k_{\mathrm{i}}/k_{\mathrm{f}}$ as defined in Eq. 3.19. The dipole magnetic form factor of Co^{2+} and the direction of $\boldsymbol{Q}$ that determines the weighting of the different response functions are included in the simulated spectra. The simulations also take into account a number of other experimental factors: (i) average over a 50:50 mixture of equivalent magnetic domains in which the ordered moments point along the x and y axes, respectively; (ii) the spectra are broadened in energy and wavevector by the estimated resolution of the MAPS spectrometer (see § 3.7.4.1); (iii) an estimate of the absorption and self-shielding of the neutron beam by the sample is included as well, which reduces the intensity by a factor of typically 0.65–0.80 depending on the incident neutron energy and E, as described in § 3.7.4.2. An additional scale factor of 0.4 was applied uniformly to all calculated spectra in order to match the measured absolute scattering intensity.

The simulations show that the model provides a very good description of the entire observed spectrum of La_2CoO_4. The relative intensities of the magnetic excitations are reproduced to within 10–20 %, including the band of scattering at

$\sim$190 meV, which from Fig. 3.15 is seen to originate from a mode with longitudinal (xx) character together with some less-intense transverse modes. Magnetic excitations are also present in the model at around $\sim$115 and $\sim$165 meV but are predicted to carry negligible spectral weight and are not observed – see Fig. 3.11(c). The additional scale factor of 0.4 needed to match the absolute intensity is similar to that required for $La_{1.5}Sr_{0.5}CoO_4$ (Ref. [98]). It is accounted for partly by the size of the ordered moment. The observed ordered moment is 2.9 μ_B [89] whereas the ordered moment in the (ionic) model is 4.1 μ_B. The difference between observed and calculated moments may be an effect of covalency, which would also modify the magnetic form factor relative to the free ion form factor in such a way that could cause an additional reduction in intensity, as recently found in Sr_2CuO_3 – a cuprate chain compound [105].

3.7.5 Discussion

It is interesting to compare the magnetic spectrum of La_2CoO_4 with that of other two-dimensional, square-lattice, antiferromagnetic insulators, particularly in relation to the anomalous dispersion along the zone boundary. The anomalous refers to the zone-boundary dispersion which cannot be described within the framework of an antiferromagnetic spin-wave model in the linear approximation with only nearest-neighbour interactions. Inclusion of (i) interactions with more distant neighbours, or (ii) terms beyond the linear approximation, are two ways in which a zone-boundary dispersion can be obtained. Other layered antiferromagnets which exhibit zone-boundary dispersion include La_2CuO_4 (Refs. [106, 107]), $Sr_2Cu_3O_4Cl_2$ (Ref. [108]) and $Cu(DCOO)_2 \cdot 4D_2O$ (CFTD, Refs. [109, 110]). These are all realisations of highly two-dimensional, $S = \frac{1}{2}$ Heisenberg antiferromagnets with almost isotropic interactions, and it is thought that the zone-boundary dispersion is caused by non-linear terms in the nearest-neighbour Heisenberg model. For example, in La_2CuO_4 a model with a four-spin ring exchange was employed [106] and for CFTD a resonating-valence-bond model describing entangled spin-dimer states was proposed to explain the data [110]. Interestingly, the behaviour along the zone boundary is different in these two materials: in La_2CuO_4 both the energy and intensity are higher at X than at Σ, whereas in CFTD both the energy and intensity are higher at Σ than at X. In La_2CoO_4, on the other hand, the energy is a maximum at Σ while the intensity is a maximum at X (see Fig. 3.12). By contrast, there is virtually no zone-boundary dispersion at all in $S = 5/2$ square-lattice system Rb_2MnF_4 [111]. The analysis of La_2CoO_4 outlined here suggests that although the zone boundary dispersion can be satisfactorily reproduced with an appropriate choice of J_1 and J_2, the corresponding intensity does not have the deep minimum at Σ found in the experiment [Fig. 3.12(b)]. Therefore, whether the zone boundary dispersion of La_2CoO_4 is due to interactions with more distant spins or arises from quantum effects in a non-linear nearest-neighbour model remains an open question.

3.8 Conclusions

In this chapter, we have dealt with the magnetic static order and the spin fluctuations in La_2CoO_4. Spherical neutron polarimetry was able to demonstrate that a solution to the magnetic structure in the two magnetic phases of La_2CoO_4 is possible. The polarised neutrons allow for a separation of coherent nuclear and magnetic scattering cross-sections and goes beyond previous experimental work using unpolarised neutron scattering. However, the presence of magnetic domains means that the finding a unique solution is difficult due to several equivalent structures that can describe the experimental results equally well. The data nevertheless places tight constraints on any future models of La_2CoO_4.

The excitation spectrum of single-crystal La_2CoO_4, an excellent realisation of a two-dimensional XY antiferromagnet. Using the combination of the experimental results with numerical simulations it is possible to achieve a very good description of the magnetic spectrum throughout the entire Brillouin zone, up to an energy of 250 meV. The magnetic anisotropy is strongly XY-like, but a small uniaxial anisotropy is present which will make the low temperature magnetic properties Ising-like. An anomalous dispersion along the antiferromagnetic zone boundary is observed and can be reproduced by including exchange interactions beyond the nearest-neighbours but which could also be a manifestation of quantum fluctuations in a nearest-neighbour model.

Chapter 4

Correlations in stripe ordered $La_{5/3}Sr_{1/3}CoO_4$

Contents

4.1 Introduction

The extent to which stripe correlations are important in high-temperature superconducting cuprates is still a matter of controversy. Static magnetic stripe order competes with superconductivity in the cuprates, suppressing superconductivity [112, 113]. Conversely, fluctuating stripes are thought by some to play a crucial role in the mechanism which leads to superconductivity in many unconventional superconductors. Inelastic neutron scattering is powerful technique which has shown that, rather surprisingly many hole-doped layered copper oxide superconductors exhibit a universal magnetic excitation spectrum which in momentum-energy space resembles the shape of an hourglass. Its origin has been the subject of debate for some time depending on whether one considers the system in the local-moment or itinerant scheme.

In this chapter I shall examine the experimental and theoretical work carried out on $La_{5/3}Sr_{1/3}CoO_4$. This composition is derived from the parent Mott insulator La_2CoO_4 discussed in § 3. The parent compound is an excellent realisation of two-dimensional antiferromagnet which has been well understood using many-level spin-orbit model. $La_{5/3}Sr_{1/3}CoO_4$ shares a crystal structure with La_2MO_4 (M = Co, Cu, Ni), where planes of CoO_2 are well separated along c giving the system low-dimensional properties. The presence of Co^{3+}, created by doping with Sr, allows the system to charge order, but importantly, Co^{3+} does not carry a magnetic moment and therefore cannot interact magnetically. This creates an ideal model system which can be used to understand some of the competing interactions in more complicated copper oxide based systems.

4.2 Crystal Growth

Two single crystals of $La_{5/3}Sr_{1/3}CoO_4$ were studied, with masses 3.7 g and 11.5 g. The majority of the neutron scattering measurements were made on the smaller crystal. Cross-checks were made, and results from the two crystals are consistent to within experimental error. The crystals were grown by D. Prabhakaran in Oxford by the floating-zone method. Polycrystalline $La_{5/3}Sr_{1/3}CoO_4$ was prepared from La_2O_3, $SrCO_3$ and Co_3O_4 (>99.99% purity) by solid-state reaction. The starting materials were reacted in air at 1200°C for 48 hours, reground, and sintered in air at 1225°C for 48 hours. No impurity phases were detected in the product by x-ray powder diffraction. The powder was pressed into rods and sintered in air at 1250°C for 24 hours. Crystals were grown in a four-mirror image furnace in flowing argon at a growth speed of 2 mm/hr with counter-rotation of the feed and seed rods at 25 rpm. Thermogravimetric analysis gave $\delta = 0.01 \pm 0.02$ for an assumed composition $La_{5/3}Sr_{1/3}CoO_{4+\delta}$. The mosaic of the crystals measured in rocking curves on different reflections by neutron diffraction was in the range 0.6° to 0.8° (full-width at half-maximum).

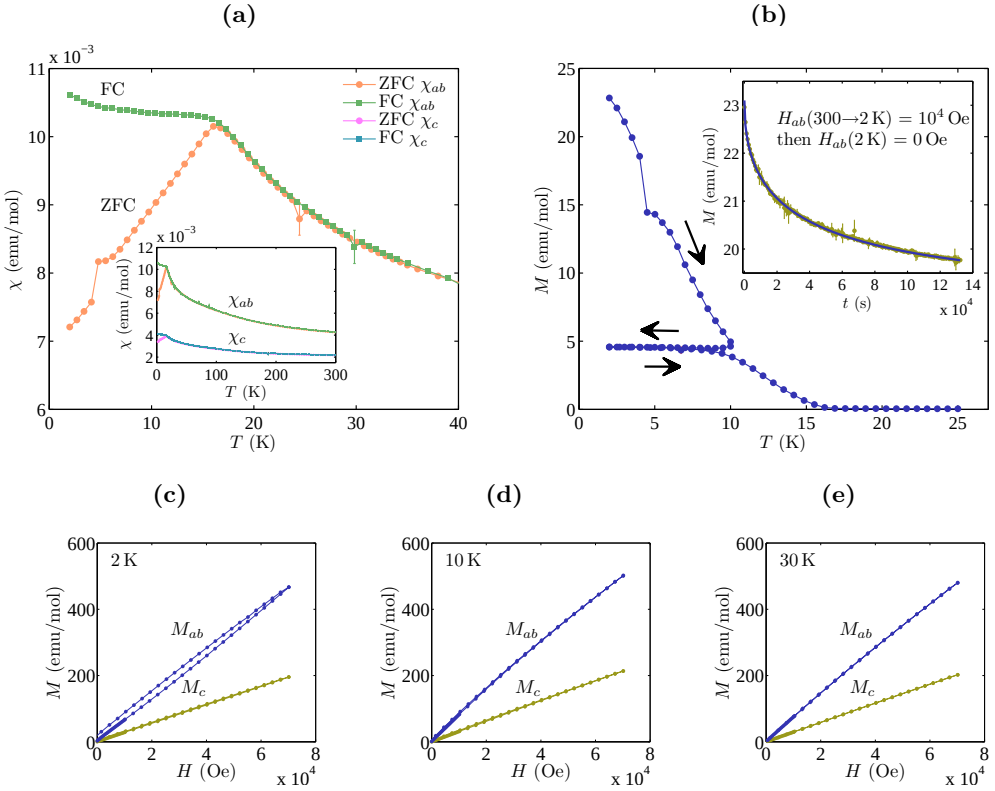

Figure 4.1: Temperature dependence of magnetisation in $La_{5/3}Sr_{1/3}CoO_4$ (a) Magnetic susceptibility ($\chi \equiv M/H$) in ZFC and FC protocols in a measuring field of 1000 Oe. Measurements were performed with the magnetic field in the *ab*-plane and parallel to the *c* axis. (b) Thermo-remnant magnetisation signal was found by cooling the sample to 2 K in an applied field of 10^4 Oe in the *ab*-plane. At 2 K, the field was turned off and the resultant magnetisation measured as a function of temperature and time (the inset shows a line of best fit to a stretched exponential). (c)–(e) The hysteresis measurements on $La_{5/3}Sr_{1/3}CoO_4$ single crystal at 2, 10 and 30 K, the magnetic field was swept from 0 Oe to 7×10^4 Oe before returning to 0 Oe.

4.3 Bulk properties measurements

The spin states of Co^{2+} and Co^{3+} ions in $La_{2-x}Sr_xCoO_4$ has been studied using a variety of techniques such as neutron diffraction [89], magnetic susceptibility [86, 114], soft x-ray absorption spectroscopy [87] and neutron spectroscopy [85, 88, 98]. The surrounding oxygen environment creates an axially-distorted octahedral crystal field which the Co ions experience. An understanding of the electronic structure of the $3d$ levels is required in order to understand the Co^{2+}/Co^{3+} mixed valence phases in cobaltates [115]. For the Co^{2+} ions (electronic configuration $3d^7$), the crystal field strongly favours the high spin (HS, $S = 3/2$) state (Fig. 4.2), and this has been confirmed experimentally. For Co^{3+} ions ($3d^6$) in this crystal field, however, there are three spin states with similar energy: low spin (LS, $S = 0$), intermediate spin (IS, $S = 1$) and high spin (HS, $S = 2$), shown in Fig. 4.2. The LS

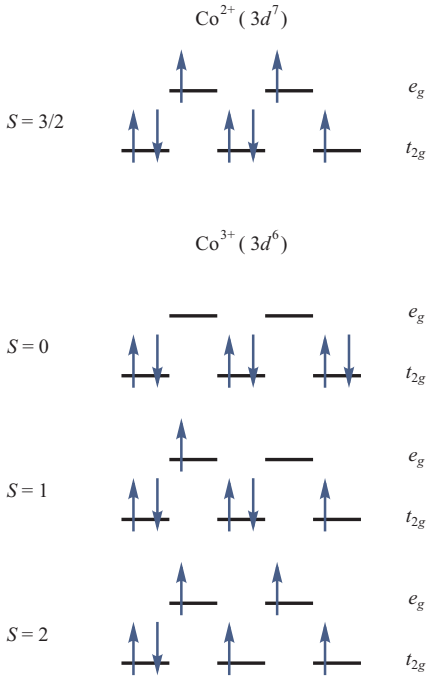

Figure 4.2: Filling of the electronic levels in $La_{5/3}Sr_{1/3}CoO_4$. In an octahedral crystal field environment surrounding Co atoms the levels are split into a lower t_{2g} triplet and an e_g doublet. In the Co^{2+} valence state a HS ($S = 3/2$) spin state is adopted. Possible spin states for Co^{3+} are shown in the LS ($S = 0$), IS ($S = 1$) and HS ($S = 2$) configurations.

Co^{3+} state is non-magnetic apart from a possible small exchange-induced van Vleck contribution. Which of these spin states is lowest in energy depends on a delicate balance between the intra-atomic exchange energy and the crystal field interaction. Measurements of the magnetic susceptibility led strong support that the Co^{3+} ions in $La_{5/3}Sr_{1/3}CoO_4$ are in the LS state [86, 116].

Magnetisation measurements to characterise $La_{5/3}Sr_{1/3}CoO_4$ have been carried out using a SQUID magnetometer. A crystal of 69 mg was cut from one of the batches used for the neutron scattering experiments (§ 4.4 and 4.5). The sample quality and alignment were verified using x-ray Laue diffraction. The sample was mounted in a plastic straw, from which background contamination is negligible. The magnetisation data presented here was collected using direct current and reciprocating sample methods. The crystal axes were aligned relative to the applied field to within $\sim 10°$. The protocols for measuring the magnetic susceptibility were: (i) cooling and measuring on warming the $La_{5/3}Sr_{1/3}CoO_4$ crystal in an applied field of 1000 Oe (Field Cool or FC) or (ii) cooling in a zero field and measuring on warming in a field of 1000 Oe (Zero Field Cool or ZFC). The magnetic susceptibility tensor χ relates the response of the magnetisation $\boldsymbol{M}$ to an applied magnetic field $\boldsymbol{H}$. In a linear, homogenous, isotropic medium it relates $\boldsymbol{M}$ and $\boldsymbol{H}$ as $\boldsymbol{M} = \chi\boldsymbol{H}$. In a tetragonal crystal structures, the susceptibility tensor reduces to the in-plane (χ_{ab})

and out-of-plane (χ_c) components as,

$$\chi = \begin{pmatrix} \chi_{ab} & 0 & 0 \\ 0 & \chi_{ab} & 0 \\ 0 & 0 & \chi_c \end{pmatrix}. \tag{4.1}$$

Magnetic susceptibility measurements of $La_{5/3}Sr_{1/3}CoO_4$ along mutually perpendicular axes did not show any sign of secondary grains and the in-plane components were consistent to within 4%, as expected for a tetragonal crystal.

The high temperature ($T > 100\,\mathrm{K}$) evolution of the paramagnetic susceptibility in Fig. 4.1(a) follows approximately a Curie-Weiss law, slowly increasing with decreasing temperature. In this regime, the susceptibility could be described by the Curie-Weiss law: $\chi = C/(T - T_\mathrm{C})$, where C ($\propto \mu_\mathrm{eff}^2$) is the Curie constant and T_C is the Curie temperature. The effective magnetic moments were calculated to be $\mu_{\mathrm{eff}\,ab} \approx 4.73\,\mu_\mathrm{B}$ and $\mu_{\mathrm{eff}\,c} \approx 4.16\,\mu_\mathrm{B}$ per Co site. This is slightly larger than values reported for $La_{2-x}Sr_xCoO_4$ at $x = 0.4$ and $x = 0.5$ doping [114]. However, the susceptibility measurements for $0.4 \leqslant x \leqslant 1.0$ reported follow the Curie-Weiss law much better over $100 < T < 300\,\mathrm{K}$ temperature range than was found for $La_{5/3}Sr_{1/3}CoO_4$.

At 16 K, a cusp is observed in the ZFC protocol in χ_{ab} and χ_c, and on further cooling, there is a rapid divergence between FC and ZFC scans indicating a possible glassy groundstate. The ZFC sweep shows a small kink at around 5 K, whilst below the same temperature FC shows an small increase in susceptibility. This unfortunately is an artifact of a background signal present in the instrument.

Hollmann *et al.* [86] have demonstrated that the anisotropy in the magnetic susceptibility of $La_{2-x}Sr_xCoO_4$ is very sensitive to the spin state of Co^{3+}. The anisotropy of the susceptibility of $La_{5/3}Sr_{1/3}CoO_4$ [Fig. 4.1(a)] closely resembles temperature dependence of $La_{2-x}Sr_xCoO_4$ samples for $x \geqslant 0.4$ reported and therefore we can draw some analogies in the analysis of systems of similar doping [86]. Using full atomic multiplet model Hollmann *et al.* [86] calculated the in-plane (χ_{ab}) and out-of-plane (χ_c) susceptibilities of HS Co^{2+} and of HS and IS Co^{3+}. The HS Co^{2+} state was found to give a strong planar (XY-like) anisotropy ($\chi_{ab} > \chi_c$), whereas HS and IS Co^{3+} both produce anisotropy in the opposite sense ($\chi_c > \chi_{ab}$). From analysis of susceptibility data on samples of $0.3 \leqslant x \leqslant 0.8$, Hollmann *et al.* [86] concluded that the Co^{3+} ion is in the LS state for $x \geqslant 0.4$. Their conclusions are supported experimentally for the case of $x = 0.5$ [87, 98]. It is therefore a reasonable assumption that Co^{3+} is also found in the LS state ($S = 0$) in $La_{5/3}Sr_{1/3}CoO_4$.

Isothermal hysteresis loops [Figs. 4.1(c)–(e)] show that there is irreversibility when an applied magnetic field is swept from 0 to 7×10^4 Oe and back to 0 Oe. The greatest deviation from linear relation between M and H is observed for measurements at $T = 2\,\mathrm{K}$ for the in-plane magnetisation component, M_{ab}. The hysteresis loops obtained when the magnetic field applied along c shows little change over the 2 to 30 K temperature range remaining nearly linear. Analogously to the susceptibility measurements, strong anisotropy in the magnetisation is found to be about

two times greater for M_{ab} than M_c at all temperatures and fields measured.

The ZFC-FC susceptibility splitting is indicative of spin-glass and spin-freezing behaviour. This suggests that the low temperature state is not in thermodynamic equilibrium and relaxation may occur on the time scale of experimental measurements. To investigate this, the sample was cooled in a magnetic field of 10^4 Oe applied in the ab plane and turned off on reaching 2 K. The remnant magnetisation shown in inset of Fig. 4.1(b) was measured as a function of time after the field was switched off. The signal is most pronounced with field applied along the ab plane, being almost a factor of ten times greater than with the field applied along c. The response of the decay with c axis parallel to the applied field has the same lineshape and is likely to be due to a slight misalignment such that there is a small ab plane contribution. This result further shows that the system is strongly anisotropic and spins are more easily manipulated by fields parallel to the CoO_2 layers. The remnant magnetisation was sufficiently well fitted by a stretched exponential of the form, $M(t) = M_0 \exp\left(-\alpha t^{(1-n)}\right) + M_{\text{bg}}$, with $n = 0.521(8)$. For comparison, n is expected to be 2/3 based on the hypothesis that there exist small local excitations that drive the system through large number of metastable states to eventually reach equilibrium that minimises the total energy [117]. Similar memory effect are seen in $La_{5/3}Sr_{1/3}NiO_4$, however two different relaxation rates were found to dominate at early and late times [118]. The decay at 2 K is much more rapid in the nickelate – decreasing by 40% on a timescale of 2 hours, whereas in $La_{5/3}Sr_{1/3}CoO_4$ a decrease of only 15% is observed in 36 hours of measurement.

Let us now consider the memory effect shown in thermo-remnant magnetisation data in Fig. 4.1(b). The sample was aligned with the field in the ab plane of magnitude of 10^4 Oe and cooled from room temperature to 2 K. At this temperature, the field was switched off and temperature was swept initially from 2 to 10 K after which a cooling-reheating loop was made to 2 K and back to 25 K. A decrease in magnetisation at 5 K corresponds background signal of the instrument recorded in the susceptibility [Fig. 4.1(a)]. The loop back to 2 K returns to the same thermo-remnant magnetisation curve at 10 K. The state at 10 K appears to be frozen in, however above this temperature, the thermal fluctuations allow the system to reach new states and thereby relax. Above the spin magnetic ordering temperature of 16 K, the remnant magnetisation decreases to about 0.05 emu/mol and continues to decay slowly with increasing temperature.

Measurements of heat capacity of the $La_{5/3}Sr_{1/3}CoO_4$ sample were made to look at any possible phase transitions below 20 K. The system was well described by the usual Debye and electronic terms. The application of a $\mu_0 H = 5$ T field parallel to c axis did not induce any phase transitions that could be seen in the heat capacity. Attempts were made to measure resistivity of the sample using the four wire method, but the sample appeared to be an extremely good insulator with a resistance exceeding the sensitivity of the PPMS instrument.

4.4 Elastic neutron scattering measurements

Coupling between charge and magnetic degrees of freedom in layered cuprates [78] and in nicklates [79, 80, 119] has attracted a lot of interest due to its possibility pivotal role in high-temperature superconductors. Doping of holes into the parent isostructural compounds of La_2NiO_4 or La_2CuO_4 suppresses commensurate antiferromagnetism and causes an incommensurately modulated magnetic structure to appear which depends on the doping concentration. Approximately 12% Sr doping is required to drive the magnetism in La_2NiO_4 to become stripe ordered [79, 80, 82, 119]. In the cuprates $La_{2-x}Sr_xCuO_4$, commensurate order is lost above nominal $x = 0.02$ doping which has been interpreted in the same stripe order picture [120]. However, when the hole doping becomes too high $x > 0.055$, the cuprate samples become metallic and superconductivity emerges [121].

The interest in $La_{2-x}Sr_xCoO_4$ is due to the fact that it shares the same tetragonal crystal structure as the Ni- and Cu- based systems and it shows similar spin-charge stripe phases. Unlike in the much studied nicklates, Co^{3+} is in the low-spin state over a wide range of carrier doping [86] and so does not contribute to the magnetic interactions. Cobaltates are therefore intriguing system to study in order to gain a clearer insight into the stripe order. Evidence for a stripe phase in $La_{2-x}Sr_xCoO_4$ has already been examined [85]. Incommensurate magnetic order was found for samples of $x \geqslant 0.4$, whilst commensurate order is found for Sr doping of $x \leqslant 0.3$. This section will deal with the particular case of $x = 1/3$ doped compound which has not been previously examined. At this hole concentration, Coulomb repulsion between Co^{2+} and Co^{3+} ions dominates. At sufficiently low temperatures a nematic charge order phase is established as Co^{3+} form domain walls separating Co^{2+} ions. This unidirectional charge modulation along $[1, 1, 0]$ is the charge ordered stripe phase. Magnetic interactions are a second order effect and the groundstate spin structure is formed by adjacent antiferromagnetically aligned pairs of moments on Co^{2+} sitting between non-magnetic ($S = 0$) Co^{3+} ions.

4.4.1 Experimental setup

The neutron diffraction experiment was performed on two $La_{5/3}Sr_{1/3}CoO_4$ single crystals of mass of 3.6 g and 11.5 g which within the experimental uncertainty had the same characteristics. Measurements were made using two triple-axis spectrometers: IN3 and IN8 at Institut Laue-Langevin. The samples were aligned to gain access to $(h, k, 0)$ and (h, h, l) reflections. The reciprocal lattice space was indexed by $I4/mmm$ crystal structure whose cell parameters were refined to be $a = b = 3.86$ Å and $c = 12.59$ Å. No realignment of the crystal was necessary throughout the temperature range studied (2–300 K) as $La_{5/3}Sr_{1/3}CoO_4$ did not show any structural phase transitions to within the experimental precision.

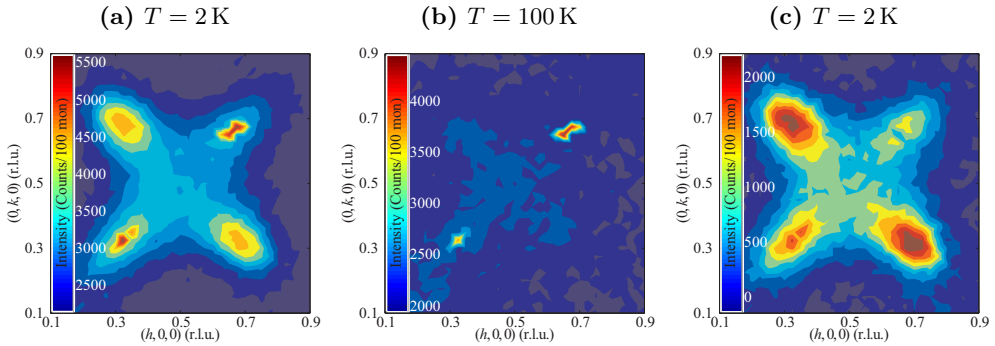

Figure 4.3: Incommensurate magnetic order in $La_{5/3}Sr_{1/3}CoO_4$. (a) and (b) Elastic neutron scattering measurements in the $(h, k, 0)$ scattering plane at 2 and 100 K showing broad magnetic peaks. The dark reds represent large number of counts, blue conversely represents low number of counts. (c) Shows the plane at 2 K with background measured at 100 K subtracted.

4.4.2 Evidence for stripe order

Diagonally modulated charge and spin density wave order present at low temperatures in $La_{5/3}Sr_{1/3}CoO_4$ gives rise to magnetic diffraction peaks at wavevectors $\boldsymbol{q}_\mathrm{m} = \boldsymbol{Q}_\mathrm{AF} \pm (\varepsilon, \varepsilon, 0)$ where $2\varepsilon = 1/3$ and equivalent positions in reciprocal space (Fig 4.3), where $\boldsymbol{Q}_\mathrm{AF} = (h + 0.5, k + 0.5, l)$ is the antiferromagnetic wavevector and h, k and l are integers. The antiferromagnetic order can equally well be modulated along the other diagonal giving peaks at $\boldsymbol{q}_\mathrm{m} = \boldsymbol{Q}_\mathrm{AF} \pm (\varepsilon, -\varepsilon, 0)$. In reality, peaks from both orthogonal domains are present in equal proportion.

Figure 4.3(a) shows a map of the $(h, k, 0)$ plane in reciprocal space. The elastic scattering contains four magnetic peaks centred on the $\boldsymbol{q}_\mathrm{m}$ positions. Sharp peaks are found at $\boldsymbol{Q} = (1/3, 1/3, 0)$ and $(2/3, 2/3, 0)$ which persist at 100 K [Fig. 4.3(b)] – at a temperature above which magnetic order should disappear. From this we associate these peaks as due to higher-order neutron harmonics such as $\lambda/3$ Bragg reflections from the $(1, 1, 0)$ and $(2, 2, 0)$ planes, rather than corresponding to any magnetic property of the crystal. The data corrected for this background contribution is shown in Fig. 4.3(c).

The magnetic peaks are significantly broader than the instrumental resolution and are elongated in the direction perpendicular to the stripes. From the measured half-widths, the correlation lengths are found to be $\xi_\parallel \approx 10\,\text{Å}$ and $\xi_\perp \approx 6.5\,\text{Å}$ parallel and perpendicular to the stripes, respectively. This demonstrates that the system does not possess long-range magnetic order but is rather disordered.

The intensity of the magnetic peaks is modulated in the out-of-plane direction. This is shown in Fig. 4.4(a), which displays a wavevector scan parallel to $(0, 0, l)$ passing through a point close to $(1/3, 1/3, 0)$. Measurements were made slightly away from from $(1/3, 1/3, 0)$ in order not to pick up third-order scattering $(\lambda/3)$ from the $(1, 1, l)$ structural Bragg peaks (when l is even integer). The scan shows a periodic modulation with l which peaks at odd integers of l, consistent with the

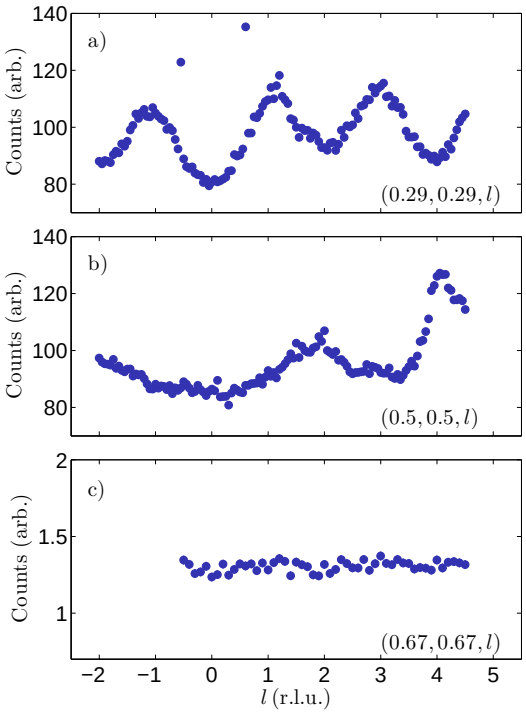

Figure 4.4: Out-of-plane magnetic and superstructure correlations in $La_{5/3}Sr_{1/3}CoO_4$. The scans displayed in each of the panels are parallel to the $(0, 0, l)$ direction and were recorded at a temperature of 2 K. (a) Elastic magnetic scattering. The scan is displaced slightly from the maximum in-plane magnetic signal to avoid third-order scattering from the $(1, 1, l)$ structural Bragg peaks, shown in Fig. 4.3(b). (b) Elastic nuclear scattering from the superstructure originating from the tilting CoO_6 octahedra. (c) Inelastic magnetic scattering at an energy transfer of $E = 5$ meV.

expected stacking of period-3 stripes [122]. Scans along l are broader and magnetic order is very short-ranged [Fig. 4.4(a)], parameterised by correlation length of just $\xi_c \approx 3\,\text{Å}$. This highlights the quasi-two dimensional ordering of moments due to strong in-plane exchange interactions and very weak out-of-plane coupling. The magnetism in the related $x = 0.5$ Sr-doped compound is found be better correlated, with correlation lengths of $\xi_{ab} \approx 52\,\text{Å}$ and $\xi_c \approx 12\,\text{Å}$ [98].

Figure 4.4(b) shows a similar $(0, 0, l)$ scan, this time passing through $(0.5, 0.5, 0)$. In this scan the intensity peaks at l = even integer, consistent with the $\sqrt{2} \times \sqrt{2}$ superstructure formed by the tilts of the CoO_6 octahedra in the low-temperature orthorhombic and low-temperature tetragonal phases of La_2CoO_4 (see § 3). The superstructure peaks are very broad in the out-of-plane direction, indicating very weak inter-layer correlations.

The broad nature of the magnetic and superstructure peaks, which overlap, makes it impossible to obtain reliable integrated intensities and thereby deduce the precise magnetic structure. Unlike in $La_{3/2}Sr_{1/2}CoO_4$ [98], no appreciable signature of charge order was found. Let us consider collinear spins lying in the $z = 0$ plane as depicted in Fig. 4.8(c). Assuming collinear order, the spins $\boldsymbol{\mu}(\boldsymbol{r})$ at position $\boldsymbol{r}$ can be related to those displaced by $\boldsymbol{\tau}$, $\boldsymbol{\mu}(\boldsymbol{r} + \boldsymbol{\tau})$ using,

$$\boldsymbol{\mu}(\boldsymbol{r}) = \lambda \boldsymbol{\mu}(\boldsymbol{r} + \boldsymbol{\tau}), \tag{4.2}$$

where $\lambda = \pm 1$ dictates whether moments translated by $\boldsymbol{\tau}$ are antiferromagnetically or ferromagnetically aligned. Under these assumptions, there are 6 possible spin arrangements for $La_{5/3}Sr_{1/3}CoO_4$. The model where $\boldsymbol{\tau} = (0.5, -0.5, 0.5)$ and $\lambda = -1$ gives allowed reflections for $(1/3, 1/3, l)$ where l is odd as expected from the experiment. However, spin structures $\boldsymbol{\tau} = (0.5, 0.5, 0.5)$ and $\boldsymbol{\tau} = (-0.5, -0.5, 0.5)$ for $\lambda = 1$ show that the structure factor gives the correct modulation with maxima at $(1/3, 1/3, l)$ when l is odd but also predict non-zero intensity at $(1/3, 1/3, l)$ when l is even. A large amount of disorder could well mask the presence of weaker peaks at even l positions. Based on the neutron scattering data collected for $La_{5/3}Sr_{1/3}CoO_4$ it is not possible to determine which of the three spin arrangements is correct. The spin structure where the spins are allowed to rotate by 90° from $z = 0$ to $z = 0.5$ layers can reproduce the correct periodicity found in the l scans [Fig. 4.4(a)], but the ratios of adjacent peaks tends to unity whilst the absolute magnitude of the structure factor decreases rapidly on increasing l, not observed in our data.

The temperature dependence of scans along $(h, h, 3)$ and $(0.325, 0.325, l)$ directions in reciprocal space through the $(1/3, 1/3, 3)$ magnetic peak are shown in Fig. 4.5. The integrated intensity [Fig. 4.5(c)] of the magnetic Bragg peak increases smoothly with decreasing temperature below about 100 K deduced from in-plane scans. The transition to the magnetic order is very broad in temperature, indicating a gradual build-up of magnetic correlations in the time window of 10^{-12} s of fluctuations probed by neutron diffraction. This is consistent with a high degree of disorder, as also indicated by large width of the magnetic peaks and glassy magnetic susceptibility data shown in Fig. 4.1(a). Bulk magnetisation measurements using

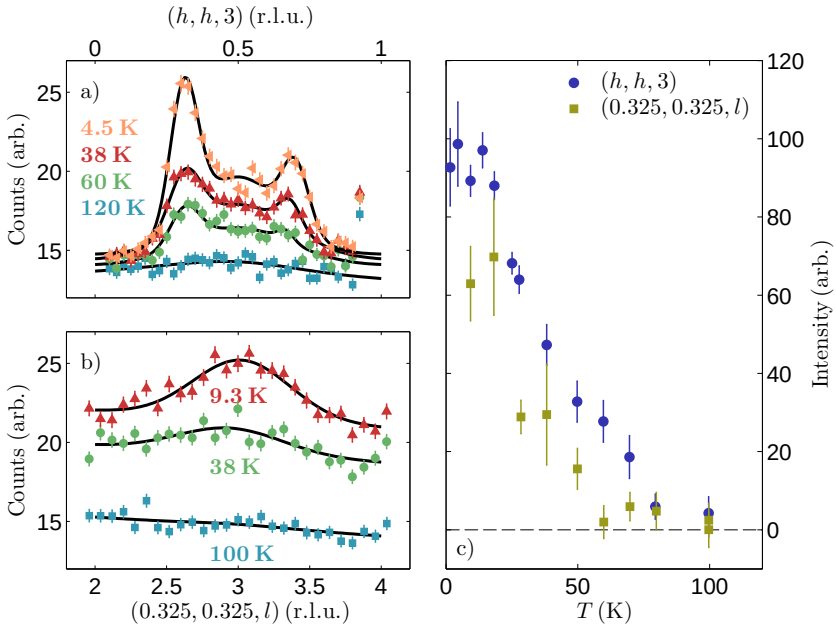

Figure 4.5: Temperature dependence of the magnetic diffraction intensity. Panels (a) and (b) show cuts through the magnetic peaks along $(h, h, 3)$ and $(0.325, 0.325, l)$ directions in reciprocal space, respectively. Measurements for the former scans were made at 4.5, 38, 60 and 120 K, whilst the l-scans were recorded at 9.3, 38 and 100 K. The black lines show Gaussian lineshapes as guides to the eye. (c) Integrated intensities as a function of temperature of the $(1/3, 1/3, 3)$ magnetic Bragg peak deduced from cuts along $(h, h, 0)$ and $(0, 0, l)$ directions. The intensity was obtained by fitting constant-$\boldsymbol{Q}$ cuts using a Gaussian function.

SQUID magnetometer probe correlations in the sample on a much longer timescale of 10^{-3} s and due to the glassy nature of the system a transition indicative of magnetic order is found at much lower temperature of 16 K. Such spin-freezing behaviour has been found in many other spin-glass material through combination of bulk properties measurements and elastic neutron diffraction [123–125].

Surprisingly, the correlation lengths were not observed to change within the measurement accuracy and temperature range measured in contrast to what was observed in the nickelates [82, 122]. However, correlations appear to evolve differently along c than in ab plane. From Fig. 4.5(b), we can see that at around 40 K, the scan along l shows very weak peak whereas in Fig. 4.5(a) at the same temperature strong incommensurate magnetic peaks are present at $\boldsymbol{Q} = (1/3, 1/3, 3)$ and $(2/3, 2/3, 3)$ in the in-plane scans. Measurements along $(h, h, 3)$ show that there is still measurable Bragg peaks up to temperatures of around 100 K indicating spin order in the CoO_2 planes is present. In contrast, scans along c at 70 K show no sign of magnetic order. This would suggest that the magnetic correlations in the CoO_2 planes are nearly completely decoupled in the 70 to 100 K temperature range.

4.5 Hourglass dispersion

We next consider the dynamic properties of $La_{5/3}Sr_{1/3}CoO_4$ and its unusual relation to hole-doped layered copper oxide compounds which exhibit superconductivity. The precise origin of the superconductive phenomena in cuprates is still not understood. However, these materials exhibit a richness of electronic behaviour not found in conventional superconductors. Doping with charge carriers into antiferromagnetically-ordered CuO_2 layers destroys magnetic order, but strong spin fluctuations persist throughout the superconducting phase. Inelastic neutron scattering experiments of hole-doped cuprates have revealed an unusual 'hourglass' feature in the momentum-resolved magnetic spectrum in a wide range of superconducting and non-superconducting materials [126–135]. No conclusive explanation for this feature has so far been found but the similarity in the magnetic excitation spectra would suggest that this may be universal in the cuprates [129, 136]. Experiments on $La_{1.875}Ba_{0.125}CuO_4$ lend support to the notion that this comes about due to charge and spin stripe order [135]. However, an equally valid argument has been put forward which explains the shape of the dispersion in terms of a weakly interacting gas of itinerant electrons [137].

In this section I shall discuss the recent experimental and theoretical evidence that the hourglass spectrum is indeed inherently due to stripe-order in the isostructural but non-superconducting $La_{5/3}Sr_{1/3}CoO_4$ [116]. The 'hourglass' is a term describing the nature of the magnetic spectrum as a function of wavevector $\boldsymbol{Q}$ and energy transfer E. At low energies, there is a four-fold pattern of incommensurate peaks centred on the antiferromagnetic wavevector ($\boldsymbol{Q}_{\mathrm{AF}}$) of the parent (undoped) CuO_2 square lattice. On increasing the energy transfer, the peaks disperse inwards before coalescing at $\boldsymbol{Q}_{\mathrm{AF}}$ and then dispersing outwards again. A square-shaped intensity distribution is observed at energies above the meeting point but appears rotated by 45° with respect to the pattern below the meeting point. Such shape is common to nearly all layered copper-oxides, especially in the underdoped compositions. The 'hourglass' is observed regardless whether the low-energy incommensurate peaks are parallel to the CuO_2 bonds or at 45° to them [132]. However, superconductivity also plays an important role in its influence on the spin fluctuations and thereby the magnetic spectrum of unconventional superconductors. For optimally doped cuprates and many other non-copper-based superconductors, a drastic change in the magnetic scattering is found in the superconducting phase characterised by the opening of a spin gap. This is a redistribution of the spectral weight from below to above the gap and the gap size is proportional to the critical temperature [138]. The spin dynamics of $La_{2-x}Sr_xCoO_4$ do not exhibit this as the material is insulating over a wide range of Sr-doping.

4.5.1 Introduction

The preceding section has already discussed the neutron diffraction evidence that stripe order is very likely to be present in $La_{5/3}Sr_{1/3}CoO_4$. The magnetism in

$La_{5/3}Sr_{1/3}CoO_4$ is controlled to a large extent by a the self-organisation of holes (Co^{3+}) into arrays of charge stripes which create antiphase domain walls in the antiferromagnetic order. The period-3 arrangement contains Co^{2+} ions which carry a magnetic moment, as discussed with reference to the diffraction measurements in § 4.4.

Figure 4.4(c) shows an out-of-plane scan through $(2/3, 2/3, 0)$ magnetic wavevector recorded at an energy transfer of 5 meV. The magnetic modulations in the corresponding elastic scan [Fig. 4.4(a)] are absent from the inelastic scan, to within the precision of the measurement. We can therefore conclude that the inter-layer magnetic correlations are vanishingly small for energy transfers above 5 meV. This justifies the assumption that the system is two-dimensional to analyse and interpret the magnetic spectrum of $La_{5/3}Sr_{1/3}CoO_4$.

4.5.2 Data analysis

Inelastic neutron scattering measurements were carried out using the IN8 triple-axis spectrometer at Institut Laue-Langevin to study a single crystal of $La_{5/3}Sr_{1/3}CoO_4$. A fixed final energy of either 14.7 meV or 34.8 meV, was set by Bragg reflection from a graphite analyser. The incident energy was selected by Bragg reflection from a silicon ($E < 35$ meV) or copper ($E \geq 35$ meV) monochromator. A graphite filter was placed after the sample to suppress contamination from higher orders. No collimation was used. The sample was mounted in a helium cryostat and aligned with the a and b axes in the horizontal scattering plane.

Figure 4.6 is a composite image of the measured magnetic spectrum for the wavevectors in the $(h, k, 0)$ plane in reciprocal space. At the base of the spectrum is a map of the background-corrected elastic scattering intensity discussed in § 4.4. The excitation spectrum appears to evolve from the incommensurate $\boldsymbol{q}_{\mathrm{m}}$ positions and disperse inwards with increasing energy. A small spin-gap is formed at low energy of approximately 3.5 meV, this is more clearly observed in the data of $La_{3/2}Sr_{1/2}CoO_4$, where a clear gap of 3 meV was found [98]. Going up in energy, the two branches meet at approximately 14 meV. The distribution of intensity in the $(h, k, 0)$ plane at 14 meV decreases monotonically with distance away from $\boldsymbol{Q}_{\mathrm{AF}}$. The peak at $\boldsymbol{Q} = \boldsymbol{Q}_{\mathrm{AF}}$ is broad and has anisotropic cross-section with lines of scattering extending along the diagonals of the reciprocal lattice. Intensity remains peaked at $\boldsymbol{Q}_{\mathrm{AF}}$ for energy transfers of up to about 20 meV, where it begins to disperse outwards again. The scattering intensity pattern above 20 meV retains the four-fold symmetry but is rotated by 45° with respect to scattering observed below 14 meV, as demonstrated by the 25 meV cut in Fig. 4.6.

Further details of the magnetic dispersion can be seen in Fig. 4.7 and 4.10(a)–(d). The constant-energy scans in Fig. 4.7(a) show that the inward dispersion is not accompanied by outward dispersion as would be expected for usual cone-like dispersion of spin-waves, such as in La_2CoO_4 in § 3.7. For energy transfers in the range of 14 to 20 meV, the dispersion is centred on $\boldsymbol{Q}_{\mathrm{AF}}$. Above 20 meV, Fig. 4.7(a) and (b) show the maximum intensity disperses away from $\boldsymbol{Q}_{\mathrm{AF}}$. The peak positions

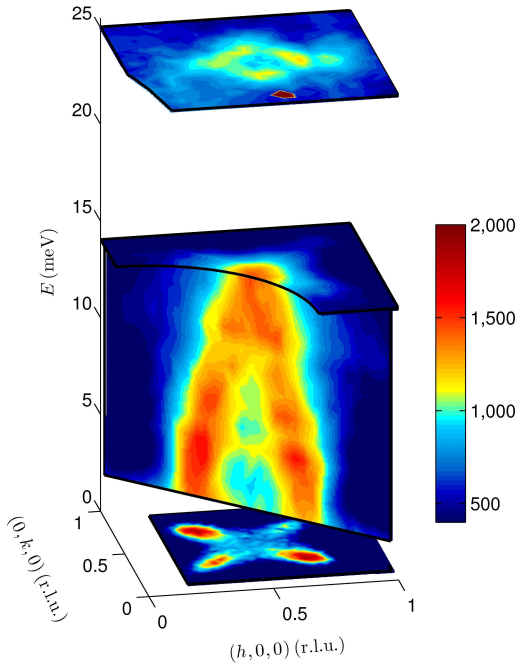

Figure 4.6: Neutron scattering intensity maps of the magnetic excitation spectrum of $La_{5/3}Sr_{1/3}CoO_4$. The constant-energy transfer scans in the $(h,k,0)$ scattering plane at $E = 0$ and 14 meV were centred at $\boldsymbol{Q} = (0.5, 0.5, 0)$; map collected at $E = 25$ meV was centred at $\boldsymbol{Q} = (1.5, 0.5, 0)$. The wavevector-energy map was constructed from a series of constant-energy scans made at 1 meV intervals through $(0.5, 0.5, 0)$ in the $(\varepsilon, -\varepsilon, 0)$ direction. All measurements were made at 2 K, but a background recorded at 100 K was subtracted from the elastic map. The colour scale shows neutron counts for the 14 meV and diagonal $\boldsymbol{Q}$-E maps. The elastic and 25 meV maps were scaled to facilitate comparison on the same colour scale. The sharp peak near $(1.5, 0, 0)$ is spurious. Reprinted by permission from Macmillan Publishers Ltd: Nature, Boothroyd *et al.*, Nature **471**, 341 (2011) [116], Copyright (2011).

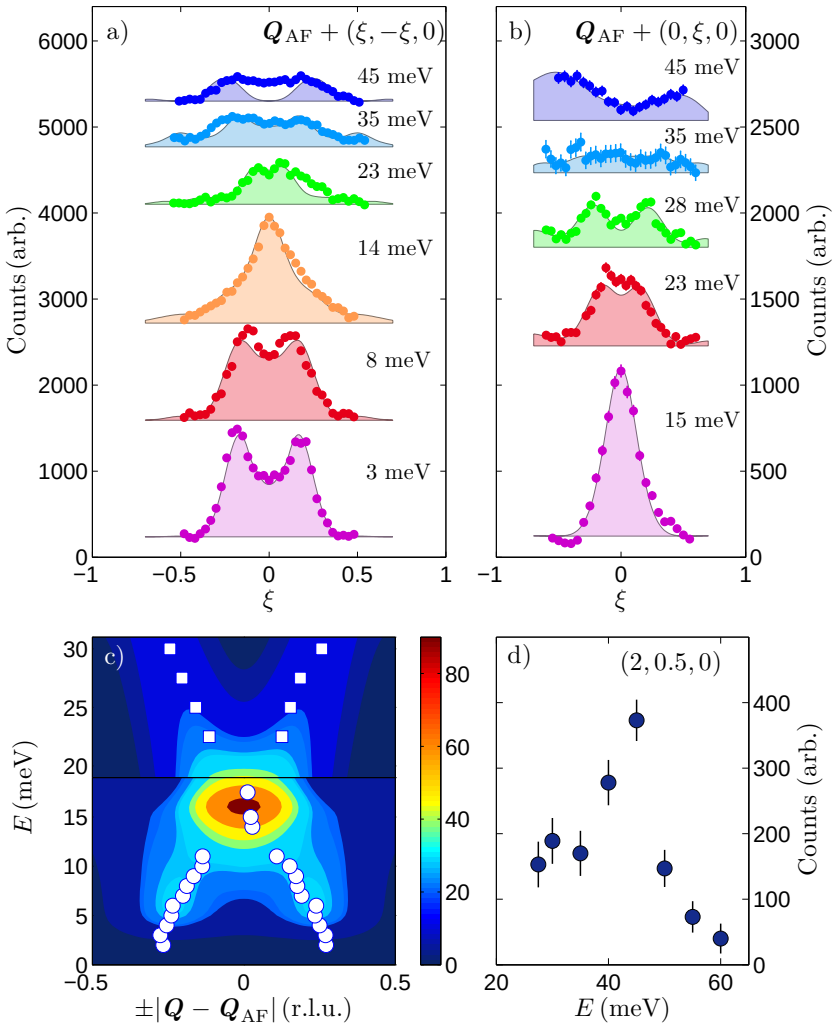

Figure 4.7: Dispersion of the magnetic excitation spectrum. (a) and (b) The variation in the scattered intensity with wavevector in diagonal and vertical scans through $\boldsymbol{Q}_{\mathrm{AF}}$ for a series of different excitation energies. To close the scattering triangle, scans for energy transfer less that 15 meV were centred on $(0.5, 0.5, 0)$; above 15 meV the scans pass through equivalent point in reciprocal space at $(1.5, 0.5, 0)$. Successive scans have been displaced vertically for clarity, and the intensities at 35 meV and 45 meV have been scaled to facilitate comparison with the lower-energy data. (c) Dispersion of the intensity in the magnetic spectrum. The symbols represent the centres of Gaussian or Lorentzian peaks fitted to those constant-energy scans which show either two clearly resolved peaks or a single central peak, circles from scans parallel to $(\xi, -\xi, 0)$ and squares from scans parallel to $(0, \xi, 0)$. The colour map is a simulation from the spin-wave model (§ 4.5.3), colour-coded in arbitrary units. (d) Energy dependence of the magnetic intensity at the magnetic Brillioun zone edge $(2, 0.5, 0)$. A background measured at $(2, 0, 0)$ has been subtracted. The strong peak at ∼45 meV corresponds to the top of the magnetic spectrum. All measurements were made at a temperature of 2 K. Reprinted by permission from Macmillan Publishers Ltd: Nature, Boothroyd *et al.*, Nature **471**, 341 (2011) [116], Copyright (2011).

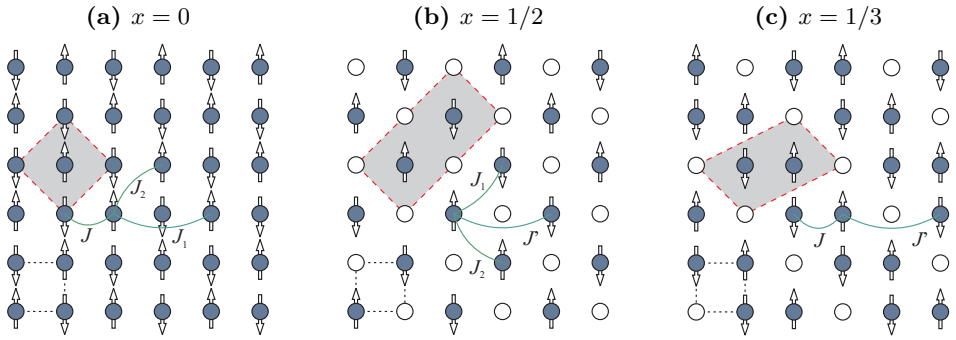

Figure 4.8: Models for the magnetic groundstate of $La_{2-x}Sr_xCoO_4$. Proposed spin structures of (a) La_2CoO_4, (b) $La_{3/2}Sr_{1/2}CoO_4$ and (c) $La_{5/3}Sr_{1/3}CoO_4$ in the CoO_2 plane. Empty circles represent the non-magnetic Co^{3+} sites and the arrows indicate the magnetic moments on the Co^{2+} sites. Red dashed lines show the magnetic unit cell whilst the dashed black outline shows the crystallographic unit cell. The dominant exchange interactions and their paths are connected by green lines.

are plotted in Fig. 4.7(c) and show the characteristic hourglass spectrum. As the modes disperse outwards above 30 meV, they eventually reach the antiferromagnetic zone boundary, as is evident in the enhancement of spectral weight at ∼45 meV from constant-$\boldsymbol{Q}$ measurement plotted in Fig. 4.7(d).

The dispersion of $La_{5/3}Sr_{1/3}CoO_4$ clearly displays the same features as the magnetic spectra of hole-doped cuprates. The shape of the dispersion acquires the same hourglass-like shape, there is no outward dispersion emerging from $\boldsymbol{Q}_{\mathrm{AF}}$ as would be expected for spin-waves and the pattern of spectral weight rotates by 45° above and below the meeting point.

4.5.3 Simulation of the dispersion using a spin-wave model

Since $La_{5/3}Sr_{1/3}CoO_4$ is an insulator, it can be treated as a local-moment system. As already discussed, magnetism in $La_{5/3}Sr_{1/3}CoO_4$ can be thought of as two-dimensional as the inter-layer coupling is weak. A many-level spin-wave model as used to describe the closely related La_2CoO_4 [88] and $La_{3/2}Sr_{1/2}CoO_4$ [98] compositions can be applied to try to understand the dynamics in $La_{5/3}Sr_{1/3}CoO_4$. The magnetic order in the La_2CoO_4 and $La_{3/2}Sr_{1/2}CoO_4$ compounds is well correlated and spin-wave theory provides an excellent description of their magnetic spectra. Figure 4.8 shows the magnetic structures in the $z = 0$ plane for $La_{2-x}Sr_xCoO_4$ in the parent ($x = 0$) and Sr-doped $x = 1/2$ and $x = 1/3$ phases. As was demonstrated in § 3, the nearest-neighbour exchange interaction $J = 9.69(2)$ meV is dominant over the next-nearest and next-next-nearest interactions which are over an order of magnitude weaker, see Fig. 4.8(a). Analysis of the excitation spectrum by Helme *et al.* [98] has shown that doping with Sr in a manner as to produce equal Co^{2+} and Co^{3+} valencies, the strongest interaction is the one which relates spins separated by a hole along the CoO_2 bond direction [Fig. 4.8(b)], whose magnitude was calcu-

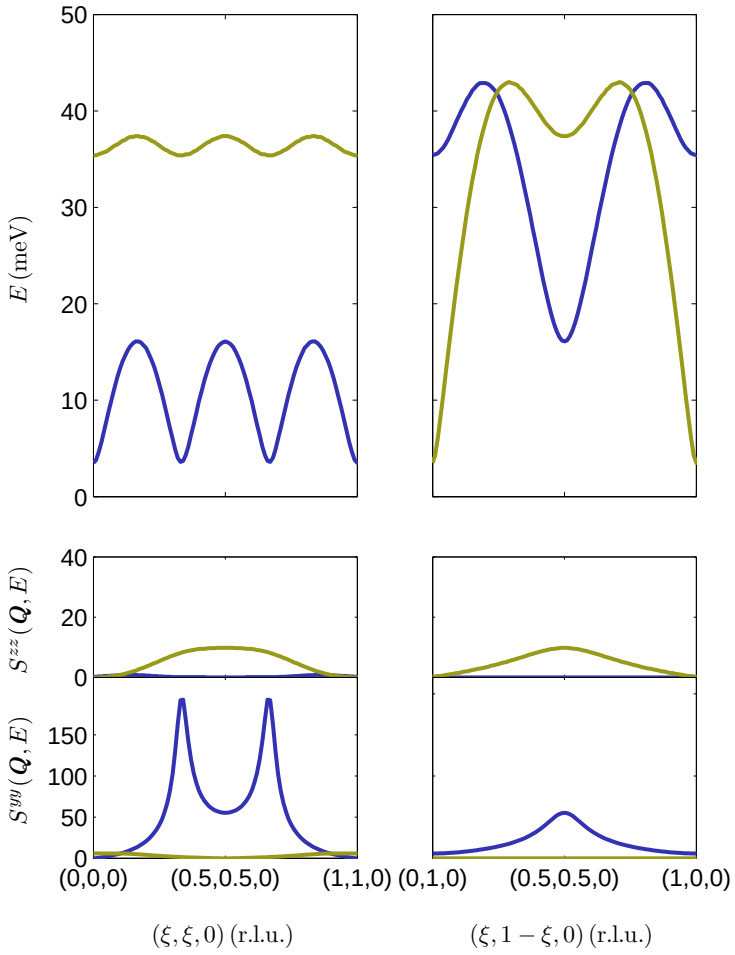

Figure 4.9: Calculated spin-wave spectrum for ideal period-3 stripe. Panels to show the calculations of the dispersion and partial cross-sections employing best-fit parameters $J = 11.5\,\text{meV}$ and $J' = 0.55\,\text{meV}$. The upper panels show the dispersion of the lowest two modes perpendicular (left) and parallel (right) to the stripe direction. The lower panels show the response functions $S^{yy}(\boldsymbol{Q}, E)$ and $S^{zz}(\boldsymbol{Q}, E)$ for the same two modes illustrated in the upper panels as calculated using Eq. 4.4. The correlations are calculated for coordinate system in which x lies along the ordered moment direction and z is parallel to the crystallographic c axis.

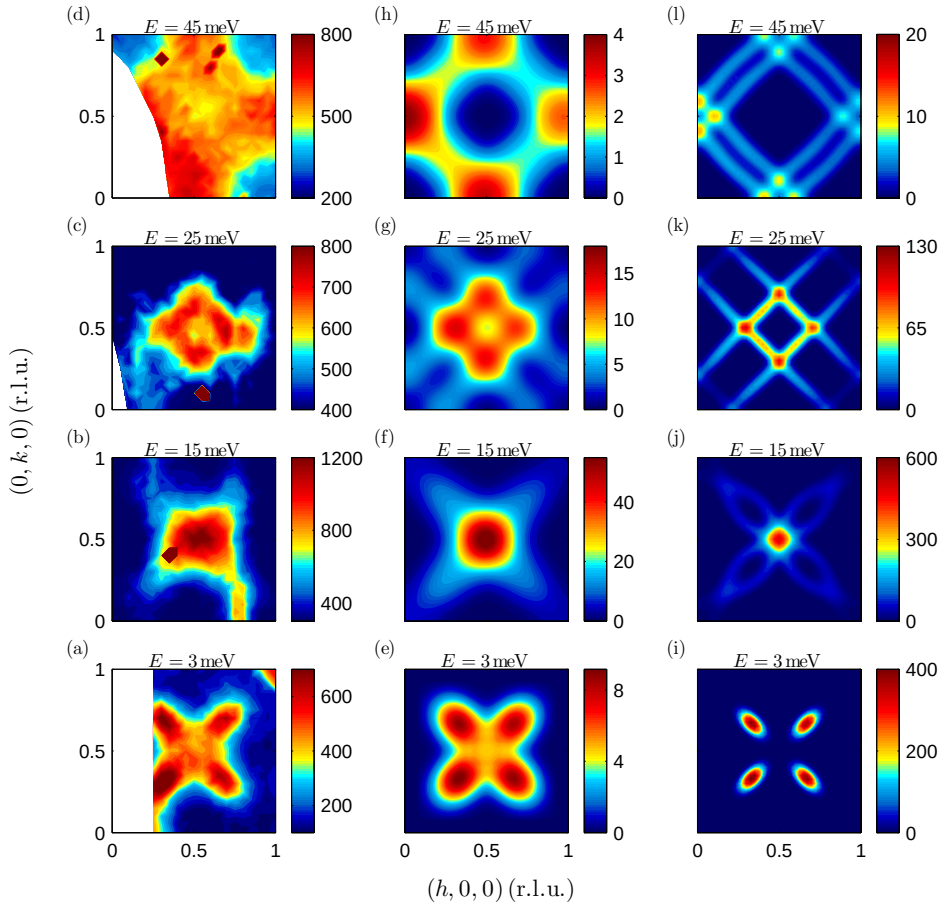

Figure 4.10: Simulations of the magnetic spectrum of $La_{5/3}Sr_{1/3}CoO_4$. (a)–(d) Constant-energy slices in the $(h, k, 0)$ plane through the inelastic neutron scattering data at energies in the 3 to 45 meV range. The colour scales show neutron counts, but different counting times were used for each map. Sharp spots at $E = 15$, 25 and 45 meV are due to spurious scattering. All measurements were made at 2 K. (e)–(l) The corresponding simulations from the spin-wave model. The exchange parameters were set to $J = 11.5$ meV and $J' = 0.55$ meV. To simulate the instrumental resolution a Gaussian broadening was applied with a standard deviation of 1 meV in energy. The spectrum was further broadening by convolution with two-dimensional Gaussian in reciprocal space with standard deviations of $\sigma_{\parallel}$ and $\sigma_{\perp}$ parallel and perpendicular to stripes, respectively. The panels (e)–(h) were broadened by $\sigma_{\parallel} = 0.06$ r.l.u. and $\sigma_{\perp} = 0.09$ r.l.u. whereas panels (i)–(j) show the same initial spectrum broadened by $\sigma_{\parallel} = 0.007$ r.l.u. and $\sigma_{\perp} = 0.014$ r.l.u. instead. The model includes the $\boldsymbol{Q}$ variation of the dipole magnetic form factor of Co^{2+}. A common intensity scale given in arbitrary units is used for (e)–(l), indicated by colour coding.

lated to be $J' = 1.4\,\text{meV}$. In $La_{3/2}Sr_{1/2}CoO_4$, interactions J_1 and J_2 were found to negligible and the dispersion can be well described assuming no magnetic degrees of freedom on the Co^{3+} ions [98].

Therefore, we can try to extend the same treatment of the spin fluctuations to $La_{5/3}Sr_{1/3}CoO_4$. Neutron diffraction analysis appears to agree well with a stripe-ordered magnetic groundstate as depicted in Fig. 4.8(c). We can therefore model the system by considering just the exchange interactions J and J' with starting values for the parameters determined for La_2CoO_4 and $La_{3/2}Sr_{1/2}CoO_4$, respectively. The symmetry of the crystal structure allows for four equivalent domains to be present. Two wavevector domains allow the stripe modulations to be either along $(\xi, \xi, 0)$ or $(\xi, -\xi, 0)$ directions and two spin domains which allow the ordered spins to align either along x or y axes. The simulations presented here have been averaged over an equal population of all four domains.

The model Hamiltonian has the form,

$$\mathcal{H} = \sum_{\langle jk \rangle} J_{jk} \boldsymbol{S}_j \cdot \boldsymbol{S}_k + \sum_j \left[\sum_{l,m} B_l^m O_l^m(\boldsymbol{L}_j) + \lambda \boldsymbol{L}_j \cdot \boldsymbol{S}_j \right]. \tag{4.3}$$

where J and J' are the principal exchange parameters as defined in Fig. 4.8(c). The strong planar single-ion anisotropy of Co^{2+} is included in the model by the last two terms. In analogy with § 3.7.4, the ligand field interaction is described by Stevens operators O_l^m and B_l^m are the corresponding parameters. Only three O_l^m operators are required to describe the tetragonal ligand field acting on Co^{2+} site. The values used for the non-zero parameters were $B_4^0 = 1.35\,\text{meV}$, $B_4^4 = 8.00\,\text{meV}$ and $B_2^0 = 13.5\,\text{meV}$. The magnetic spectrum is not very sensitive to the first two of these, and they are fixed to values established for La_2CoO_4 and $La_{3/2}Sr_{1/2}CoO_4$ as explained in Refs. [88, 98]. The B_2^0 parameter does affect the magnetic spectrum, through its control of the degree of planar magnetocrystalline anisotropy. However, since the values of B_2^0 determined from the spectra of La_2CoO_4 and $La_{3/2}Sr_{1/2}CoO_4$ were not very different we can take an average of these weighted by the doping levels. The the ligand field parameters were not adjusted in the analysis presented here. The strength of the spin-orbit coupling was taken to be $\lambda = -18.7\,\text{meV}$, as determined from optical data for CoO [103].

The procedure for diagonalising the Hamiltonian[1] in Eq. 4.3 is described in detail in Ref. [98] and is the same one used in § 3.7.4 for La_2CoO_4. In order to describe the spin fluctuations in Figs. 4.7 and 4.10 it is necessary to adjust the values of J and J'. A good fit to the hourglass spectrum is obtained when $J = 11.5\,\text{meV}$ and $J' = 0.55\,\text{meV}$. The partial response function $S^{\alpha\alpha}$ (per $La_{5/3}Sr_{1/3}CoO_4$ f.u.) can be calculated using,

$$S^{\alpha\alpha}(\boldsymbol{Q}, \omega) = \sum_j |\langle j | M^\alpha(\boldsymbol{Q}) | 0 \rangle|^2 \delta[\omega - \omega_j(\boldsymbol{Q})]. \tag{4.4}$$

[1] The diagonalisation of the Eq. 4.3 was carried out using ExcitonQ program written by A.T. Boothroyd.

where the spin and orbital magnetisation $\boldsymbol{M} = -(\boldsymbol{L} + 2\boldsymbol{S})$ is evaluated for a transition from the groundstate to an excited mode j. Figure 4.9 shows the dispersion and partial response functions as a function of in-plane wavevector parallel and perpendicular to the stripes. The spectrum is shown for a single domain with stripe modulation along $(\xi, \xi, 0)$ direction as shown in Fig. 4.8(c). The low energy spectrum contains two modes at each $\boldsymbol{Q}$. The low-energy gap of approximately 4 meV is well reproduced in our model. This arises due to single-ion anisotropy in the Hamiltonian. The B_4^4 term in the crystal field describes a Coulomb potential which has a four-fold symmetry in the ab plane, therefore there are four potential minima in this plane. This affects the spatial distribution of the electrons and in turn the spin direction via the spin-orbit coupling. Thus there is a preferred spin direction in the plane and this creates a gap in the excitation spectrum corresponding to the energy required to rotate the spins out of the potential minimum.

Strong single-ion anisotropy splits the magnon modes producing a gap of about 35 meV at magnetic zone centres. Slices along $(\xi, \xi, 0)$ and $(\xi, 1-\xi, 0)$ show that a saddle point is formed at $\boldsymbol{Q} = (0.5, 0.5, 0)$ at around 17 meV as the maximum in the inter-stripe dispersion reaches the minimum in the intra-stripe dispersion. The intensity close to $\boldsymbol{Q}_{\mathrm{AF}}$ is the strongest. Hence as the incommensurate branches below saddle point disperse, the intensity distribution is such that the spectral weight shifts towards the zone centre. The upper half of the dispersion is formed by magnon modes, rotated by 45°, dispersing away from $\boldsymbol{Q}_{\mathrm{AF}}$.

This effect is illustrated in Fig. 4.10(i)–(j). Here the wavevector broadening has been reduced significantly in order to help identify distinct features of the dispersion. The magnetic dispersion at low energies (< 15 meV) is cone-like. However, the difference between J and J' causes the elliptical shape. By the saddle point the intensity is strongly peaked close to the antiferromagnetic ordering wavevector [Fig. 4.10(f) and (j)], the protrusions along $(\xi, \xi, 0)$ and $(\xi, -\xi, 0)$ are formed from the finite scattering cross-section of the remaining spin-wave cones. Above the saddle point a more complicated four-fold pattern is observed as the cone-like dispersions originating from $\boldsymbol{q}_{\mathrm{m}}$ interfere. Disorder in the system ensures that the finer details of the magnetic excitations are lost resulting in the pattern in Figs. 4.10(e)–(h).

Comparison of measured and calculated intensity maps in Fig. 4.10 at different energies demonstrates that within the experimental limitations the agreement is generally very good. The 3, 15 and 25 meV maps clearly show the houglass spectrum and the twist of 45° in the intensity distribution above and below the saddle point. All the prominent features of the data are reproduced by the simulations. The enhancement of the intensity near the top of the spectrum is due to the planar anisotropy in $La_{5/3}Sr_{1/3}CoO_4$ which creates a nearly flat dispersion at the highest energies.

A more quantitative comparison between model and data is found in Fig. 4.7. The constant-energy cuts along high-symmetry directions shown in panels (a) and (b) show how the simulated spectrum compares to the data. The amplitude of the calculated cuts has been scaled to match the data and a linear background added.

Figure. 4.7(c) the fitted peak positions are superposed on the best-fit model to highlight the agreement between the data and model throughout the entire spectrum.

4.5.4 Discussion

In modelling the hourglass dispersion in $La_{5/3}Sr_{1/3}CoO_4$ using a spin-wave model, an assumption was made in that the magnetic order is static. However, the results should be relevant for slowly fluctuating order too, as is likely for $La_{5/3}Sr_{1/3}CoO_4$ given the short magnetic correlation. In the neutron scattering process, a neutron will be insensitive to fluctuations on a timescale lower than about $\hbar/\Delta E$, where $\Delta E \sim 1\,\text{meV}$ is the energy resolution. Therefore, a magnetic order parameter which fluctuates slower than this will have nearly the same spectrum as one in which correlations are static.

The analysis presented in this section has shown that in order to fit the experimental observation of an intensity peak localised at $\boldsymbol{Q}_{\text{AF}}$ and approximately 15 meV, it is necessary to adjust the exchange interaction parameters J and J' from those obtained for La_2CoO_4 and $La_{3/2}Sr_{1/2}CoO_4$. The dominant exchange interaction J agrees to within about 10% with La_2CoO_4 but J' differs by more than a factor of 2 from $La_{3/2}Sr_{1/2}CoO_4$. These findings are strong evidence that the basis of the model, the groundstate, and the important interactions are indeed correct. Using the values determined independently from the inelastic neutron scattering data for $La_{5/3}Sr_{1/3}CoO_4$ results in the model predicting the same hourglass shaped dispersion but with a saddle point located at higher energies of around 20–25 meV, as opposed to the observed 15–20 meV. The renormalisation of the exchange parameters is likely to be caused by the breakdown of the linear spin-wave theory at low energies as magnetic correlations extend over a few unit cells rather than being long-ranged as assumed in the linear spin-wave theory. Thus, the fitted parameters should be regarded as effective exchange parameters in the model rather than the true reflection of the coupling strengths. Recent Monte-Carlo simulations have confirmed that a disordered spin-glass phase can lead to an hourglass dispersion in $La_{5/3}Sr_{1/3}CoO_4$ [139]. The bulk magnetometry measurements presented in § 4.3 are consistent with the disordered stripe phase groundstate on which this model is based.

The work presented in this section can be used to explain the absence of an hourglass feature in the magnetic spectrum of the closely related $La_{2-x}Sr_xNiO_4$ family of layered nickelates which also have charge and spin stripe phase similar to $La_{2-x}Sr_xCoO_4$. The main difference arises due to differing J/J' ratios in the two systems. In $La_{5/3}Sr_{1/3}NiO_4$ the ratio $J/J' \approx 2$ [84, 140], whereas in $La_{5/3}Sr_{1/3}CoO_4$ $J/J' \approx 7$ or 30 depending on whether the estimated or fitted exchange parameter values are taken. The relative magnitudes of J and J' determine the spin-wave spectrum such that when $J/J' \approx 2$, the maximum of the inter-stripe dispersion is found at the top of the spectrum. When $J/J' > 2$, a saddle point is formed and its position in energy decreases relative to the magnon bandwidth with increasing J/J'. In the cuprates the saddle point is typically observed around 30–40 meV with

a band width in the range of 300 meV. Therefore, by comparison this would imply a much larger J/J' ratio for the cuprates.

In addition to coupling of charges and magnetic moments in the cuprates, nickelates and cobaltates, the orbital degrees of freedom play a part in the manganites. Comprehensive neutron diffraction experiments have ascribed stripe-like arrangement of the magnetic and electronic order in the manganites [141]. More recent work has emerged showing an hourglass dispersion reminiscent of that of $La_{5/3}Sr_{1/3}CoO_4$ in single-layered manganites, $Sr_{1.67}Nd_{0.33}MnO_4$ and $Ca_{1.67}Pr_{0.33}MnO_4$ [142]. Inelastic neutron scattering measurements to map out the spin fluctuations in the $Ca_{1.67}Pr_{0.33}MnO_4$ compound have demonstrated the importance of disorder in the formation of the hourglass spectrum. The outward dispersing branch from the zone centre of excitations at low-energies from the incommensurate wavevector positions are suppressed upon heating. At low temperatures the magnetic order is long-ranged but on warming the correlations lengths decrease to an order of the distance between charge stripes and concomitantly the dispersion develops the full hourglass shape.

4.6 Conclusions

In summary, the neutron scattering measurements on insulating $La_{5/3}Sr_{1/3}CoO_4$ provide evidence that the system forms a stripe-ordered phase at low temperatures. The non-magnetic Co^{3+} arrange periodically to act as antiphase domain walls between antiferromagnetically ordered Co^{2+} ions. The material is found to exhibit an hourglass spin fluctuation spectrum which is strikingly similar to that observed in hole-doped layered cuprates. This similarity lends support to the explanation of the hourglass spectrum in cuprates as arising from dynamical stripes [143]. From analysis of $La_{5/3}Sr_{1/3}CoO_4$ two key ingredients are necessary to form an hourglass magnetic spectrum, namely (i) unidirectionally modulated antiferromagnetic correlations and (ii) a large ratio of magnetic couplings parallel and perpendicular to the stripes. A large degree of broadening is also required in order to smear out the spin-wave-like dispersion cones. Although spins may well be correlated in copper oxides at low energies, experiments indicate that the spectrum can appear broadened with increasing energy [129].

The local-moment picture used here to describe $La_{5/3}Sr_{1/3}CoO_4$ may not necessarily apply to the copper oxide superconductors, since the later are metals. However, the results of $La_{5/3}Sr_{1/3}CoO_4$ impose tight constraints on any possible future models and are support interpretation of the hourglass dispersion based on disordered stripe order.

Chapter 5

Interplay of magnetism and superconductivity in $Fe_ySe_xTe_{1-x}$

Contents

5.1 Introduction

Research into high-temperature superconductivity has experienced an upheaval in recent years after the discovery of iron-pnictide superconductors [24, 25]. Ever since, research into these and related materials has been intense. Several families of Fe-based superconductors have been discovered typified by LaFeAsO (1111) [24, 25], $SrFe_2As_2$ (122) [144–147], LiFeAs (111) [148–153], Sr_2PO_3FePn (21311) [154, 155] and $Fe_ySe_xTe_{1-x}$ (11) [156–161]. The numbers in the parenthesis are derived from the elemental ratios in the chemical formula of the parent compound. In most compounds the superconducting transition temperatures are relatively low with the record set by $Gd_{1-x}Th_xFeAsO$ with $T_c = 56.3\,K$ [162]. All share a tetragonal crystal structure at room temperature [24, 152, 163, 164]. These systems raise interesting questions about the physical origin of superconductivity and their relationship to the cuprate superconductors. In both Cu- and Fe-based systems, superconductivity is found in close proximity to a magnetically ordered parent phase. This suggests that magnetic fluctuations are profoundly linked with superconductivity in these two families. The superconductivity in the Fe-based family is subject of debate, but appears to arise from suppression of a semi-metallic [1] magnetic ground state rather than from doping an antiferromagnetic Mott insulator [158].

The work presented in this section will focus on the $Fe_ySe_xTe_{1-x}$ system. Although amongst the five types of Fe-based superconductors the maximum T_c of the 11 system is the lowest [165], it is nevertheless of great interest to study. This is because:

(i) Its crystal structure is simple, meaning it is easier to analyse and model.

(ii) The system does not contain As and is therefore safer to grow and handle. The only other Fe-based superconductors without As are the phosphides LaFePO and LaNiPO.

(iii) Importantly, large single-crystal samples can be grown relatively easily over a wide range of doping.

The availability of large single-crystals is particularly important for neutron scattering experiments. In this chapter I will discuss the progress that has been made in the investigation of $Fe_ySe_xTe_{1-x}$ in the magnetic and superconducting phases. A useful strategy for tackling this problem is combining neutron scattering and muon-spin rotation (μSR) measurements on one and the same sample. Neutron scattering provides information on magnetic correlations and on the nature of the magnetic excitations, while μSR can determine whether static magnetic order and/or bulk superconductivity exists. The μSR and magnetisation measurements work presented here has been the result of the collaboration with M. Bendele and R. Khasanov at Paul Scherrer Institut, culminating in Refs. [160, 166–168].

[1] This is the term given to a material in which the conduction and valance bands overlap slightly in energy but are displaced in crystal momentum space, in analogy to a indirect band gap semiconductors.

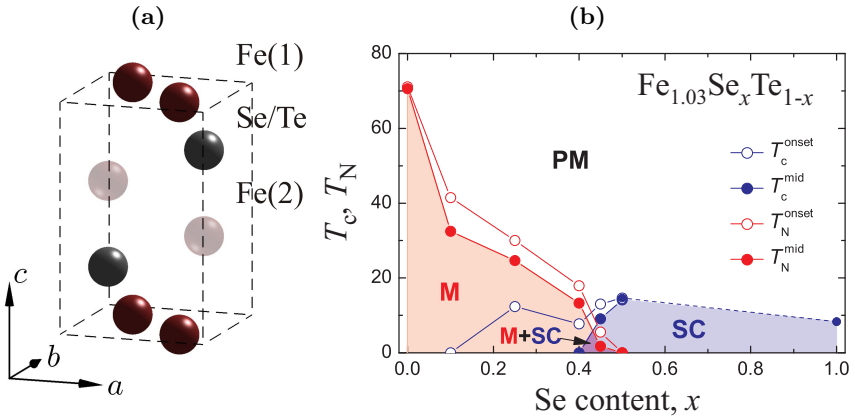

Figure 5.1: Crystal structure and phase diagram of $Fe_ySe_xTe_{1-x}$. (a) Crystal structure of $Fe_ySe_xTe_{1-x}$ described by the $P4/nmm$ space group showing the Fe(1) layers separated by Se/Te atoms along c axis. The faded red atoms denote the interstitial $(y-1)$ atoms which can also occupy sites between the Fe(1) layers. (b) Phase diagram showing the temperature dependence of the magnetic (M), paramagnetic (PM) and superconducting (SC) states in $Fe_ySe_xTe_{1-x}$ as a function of doping with Se. The region (M+SC) identifies the phase in which magnetism and partial superconductivity coexist. Reprinted figure with permission from Khasanov *et al.*, Phys. Rev. B **80**, 140511(R) (2009) [160]. Copyright © (2009) by the American Physical Society.

5.2 Tuning the magnetism and superconductivity in $Fe_ySe_xTe_{1-x}$

The crystal structure of $Fe_ySe_xTe_{1-x}$ is of anti-PbO-type and is shown in Fig. 5.1(a). The tetragonal structure belongs to the $P4/nmm$ space group with Fe(1) atoms in the square basal plane forming a layered structure. Depending on doping, Se or Te act to separate the Fe(1) planes. High-resolution single-crystal structure refinements of $FeSe_{0.44}Te_{0.56}$ suggest that due to differing sizes of Te and Se atoms they are located at different positions along c in the unit cell despite being crystallographically equivalent [169]. Interstitial Fe(2) atoms are often required to stabilise the crystal growth and these also occupy positions in between the Fe(1) layers. The minimum amount of excess interstitial Fe(2) (amounting to $y-1$) required decreases with increasing x [27]. As will be demonstrated in this chapter, the excess Fe atoms also influence the phase diagram of $Fe_ySe_xTe_{1-x}$ by tuning the delicate balance between magnetism and superconductivity. It must be noted that most of the $Fe_ySe_xTe_{1-x}$ compounds tend to have significant nonstoichiometry, disorder and clustering problems [27]. This results in broad superconducting phase transitions. Although large single-crystals show bulk superconductivity, careful examination of the sample compositions have shown that usually they are highly inhomogeneous [158, 170].

The pure FeSe compound is a superconductor with a transition temperature of $T_c \approx 8\,\mathrm{K}$ [156]. The T_c can be increased by partial substitution of Te for Se

such that $T_c \approx 14\,K$ for $0.4 \lesssim x \lesssim 0.8$ and $y \approx 0$ [160, 161]. The application of pressure has also been found to raise T_c, with values as high as 37 K observed for FeSe [171–174]. Compounds with $x \lesssim 0.4$ do not exhibit bulk superconductivity but order magnetically below a temperature which has a maximum of 67 K at $x = 0$ and which decreases with x and vanishes at $x \approx 0.4$, as illustrated in Fig. 5.1(b). Recently, evidence was found for coexistence of incommensurate magnetic order and partial superconductivity for $x \sim 0.25$ [160], shown in Fig. 5.1(b). Similar phase diagrams were obtained and are reported in Refs. [175, 176]. However, the doping region $0.1 \lesssim x \lesssim 0.3$ is characterised by only partial superconductivity and a spin-glass regime. The question arises as to whether the magnetism and superconductivity are truly coexisting or if there is macroscopic phase separation where magnetism and superconductivity are mutually exclusive [177]. Long-range antiferromagnetic order ceases for $x \gtrsim 0.1$ and structural studies indicate that the low-temperature structural distortion also disappears at the same x. The phase diagram shown in Fig. 5.1(b), where superconductivity emerges after the destruction of long-range antiferromagnetic order, is qualitatively similar to observations in layered cuprate high-T_c superconductors. This would perhaps suggest a common electronic or magnetic origin of superconductivity. However, the (semi-)metallic and insulating parent phases are a significant discriminating feature between the two classes of superconductors.

5.2.1 Electronic band structure

It is well known that when transition metal ions are in a electronegative environment, the Coulomb interaction will tend to lift the single-ion d-orbital degeneracy producing energy levels e_g and t_{2g}, as in the case of cobaltates already discussed in § 3 and 4. For the cobaltates the split d-orbitals form energetically distinct bands, whereas for the Fe-based compounds the d bands overlap strongly. The electronic density of states at the Fermi energy is dominated by the Fe $3d$ orbital contribution rather than Te $5p$ orbitals [27, 178]. The main metallic conduction mechanism is believed to be due to electrons hopping between Fe atoms, without intermediate Se/Te atoms along the path. It is widely believed that the superconductivity in the Fe-based superconductors originates from the electrons of the d-orbitals of Fe [179]. The nature of the electronic band structure at the Fermi surface plays a key role in determining the magnetic properties in the $Fe_ySe_xTe_{1-x}$ systems. In the cuprates, the situation is quite different. Only one Cu $3d$-orbital contributes and the strong antiferromagnetic exchange interactions are mediated along the Cu–O–Cu bonds, with O $2p$ orbital contributing to the density of states at Fermi energy.

Density functional calculations have found that the Fermi surfaces of $Fe_ySe_xTe_{1-x}$ compounds are broadly similar to the 122 and 1111-type compounds [180]. ARPES studies of the magnetic and superconducting single-crystals of $Fe_ySe_xTe_{1-x}$ reveal in each case a metallic character at the Fermi energy with a Fermi-surface structure which is typical of most iron-based superconductors [181, 182]. In $Fe_{1+y}Te$, the hole pockets are located at $(0, 0, 0)$ and elliptical electron pockets centred on $(0.5, 0.5, 0)$

[181]. The number of electrons and holes are found to be the same, as would be expected for a semi-metal material. The nesting wavevector $(0.5, 0.5, 0)$ connects the hole and electron pockets. This is usually considered to be favourable for spin density wave nesting, found in essentially all FeAs-superconductors and has two serious implications on the understanding of $Fe_ySe_xTe_{1-x}$. Firstly, experimentally the antiferromagnetic propagation wavevector is found close to $(0.5, 0, 0.5)$ below the magnetic ordering temperature. This would suggest that the antiferromagnetic order is not driven by Fermi surface nesting of itinerant electrons/holes but by some alternate mechanism of which a number have been proposed in Refs. [183–185]. The nature of the magnetic order of $Fe_ySe_xTe_{1-x}$ will be discussed in more detail in § 5.3. Secondly, the existence of electron and hole pockets allows for a new type of superconductivity, known as $s^{\pm}$ electron pairing [26]. This form of pairing relies on the semi-metallic Fermi surface such that a pairing interaction between holes and electrons pockets connected by the nesting wavevector can occur provided the superconducting order parameter has opposite signs on the hole and electron pockets. The superconducting order parameter can be probed using inelastic neutron scattering, as will be discussed later in § 5.6.

5.3 Static magnetic order in $Fe_ySe_xTe_{1-x}$

Band structure calculations [178] have shown that the ground state of the parent FeTe phase is a collinear antiferromagnet with large local magnetic moments of approximately $2.5\mu_B$. The collinear antiferromagnetic order is formed from lines of spins aligned ferromagnetically along one diagonal and antiferromagnetically along the other diagonal direction in the Fe-Fe square lattice. The composition formed from FeSe is predicted to form a simple collinear antiferromagnetic groundstate [178]. The low-temperature magnetic structure of $Fe_{1.125}Te$ was solved nearly four decades ago [186]. The propagation wavevector was found to be $\boldsymbol{q}_m = (0.5, 0, 0.5)$ with a large ordered magnetic moment of $2.07\ \mu_B$ [186], more recent studies on similarly doped compounds have further indicated that the moment is mainly orientated along the crystallographic b-axis [187–189].

Magnetism probed by bulk magnetisation measurements and μSR provides valuable clues to the nature of magnetic correlations in the system. However, neutron scattering is the technique best suited to study magnetism in single-crystals when large, good quality samples are available. This section will describe the efforts in trying to understand the static magnetic order in $Fe_ySe_xTe_{1-x}$ when either the Se:Te ratio is varied. Further in § 5.5.3 I shall describe what happens when interstitial Fe is added or removed.

5.3.1 Experimental details

Single-crystal measurements on several compositions of $Fe_ySe_xTe_{1-x}$ were carried out on the triple-axis spectrometer TASP at the SINQ spallation source (Paul Scherrer Institut, Switzerland) [95, 96]. In addition, polarised neutron scattering was

employed using the MuPAD device [76] in order to conclusive ascribe reflections to be of magnetic origin. In unpolarised neutron scattering measurements, Bragg reflections from a pyrolytic graphite PG(002) monochromator and analyser were used at a fixed final wavevector of 2.66 $Å^{-1}$. The polarised neutron diffraction measurements were carried out using $k_f = 1.97\,Å^{-1}$. A PG filter was used in unpolarised neutron scattering measurements, placed after the sample to reduce contamination from higher-order harmonics in the beam and the instrument was set up in the open–open–open–open collimation with the analyser focusing in the horizontal plane. The crystal masses were typically in the 2–6 g range. Two scattering geometries were employed to access $(h, k, 0)$ and $(h, 0, l)$ planes in reciprocal space. Here we index the reciprocal space with respect to the tetragonal unit cell described by the $P4/nmm$ space group with unit cell parameters $a \approx 3.8$ Å and $c \approx 6.1$ Å along the lines joining the nearest neighbour Fe atoms.

Zero-field-cooled magnetisation measurements were performed on a Quantum Design MPMS magnetometer with a measuring field $\mu_0 H = 0.3$ mT using the direct current method. To reduce the effects of demagnetisation, thin plate-like pieces of $Fe_ySe_xTe_{1-x}$, cleaved from the main single crystals, were oriented with the flat surface (ab plane) parallel to the applied field. Zero-field (ZF) and transverse-field (TF) muon-spin rotation (μSR) experiments were performed on the πM3 beam line at SμS (Paul Scherrer Institut, Switzerland). In TF experiments a magnetic field of 11.8 mT was applied parallel to the crystallographic ab plane of the crystal and perpendicular to the muon-spin polarisation. The magnetisation and μSR measurements were performed by M. Bendele and R. Khasanov.

5.3.2 Crystal growth

Single crystals of $Fe_ySe_xTe_{1-x}$ the results of which are presented in this chapter were grown by a modified Bridgman method similar to that reported by Ref. [158]. The samples were prepared by E. Pomjakushina and K. Conder at Paul Scherrer Institut, Switzerland. Powders of Fe, Se and Te of minimum purity 99.99% were mixed in the appropriate ratios, pressed into a rod 7 mm in diameter, and placed into an evacuated, double-walled quartz ampule. The rod was first melted and homogenised at 1200°C for 4 hours and then cooled in a temperature gradient 8°C/cm at a rate of 4°C/hr down to 750°C followed by 50°C/hr cooling. The crystals had mirror like surface and were easily cleaved parallel to the ab planes. Some of the samples were ground into a powder and analysed using neutron powder diffraction. The main constituent of the $P4/nmm$ structure was found to occupy more than 94% of the volume of the crystals analysed. A small amount of impurity was found of the hexagonal Fe(Se,Te) which has a structure of the $P6_3/mmc$ space group.

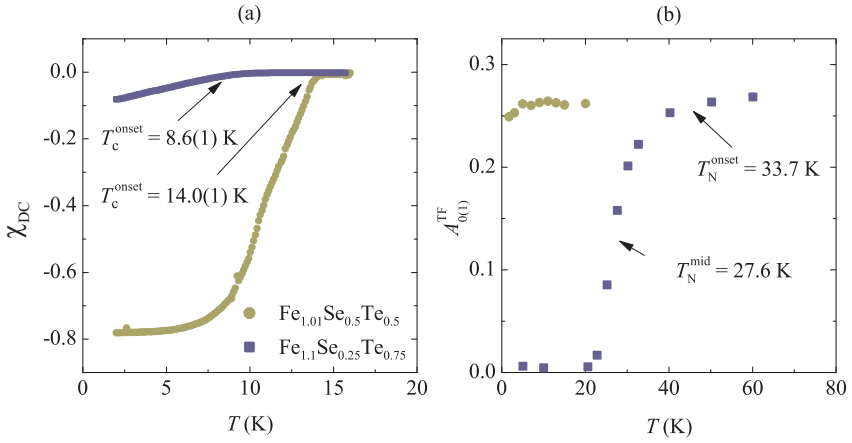

Figure 5.2: Temperature dependence of magnetic and superconducting phase transitions in $Fe_{1.01}Se_{0.50}Te_{0.50}$ and $Fe_{1.10}Se_{0.25}Te_{0.75}$. (a) Temperature dependence of the zero-field-cooled magnetisation of $Fe_{1.01}Se_{0.50}Te_{0.50}$ and $Fe_{1.10}Se_{0.25}Te_{0.75}$ normalised to the ideal $1/4\pi$ value. The onset T_c^{onset} of the superconducting transition is determined from the intersection of straight lines fit to the data above and below the transition. (b) Temperature-dependent initial TF asymmetry of the slow relaxing component [A_0^{TF} and A_1^{TF}] for single crystals of $Fe_{1.01}Se_{0.50}Te_{0.50}$ and $Fe_{1.10}Se_{0.25}Te_{0.75}$. The onset ($T_N^{onset}$) and the mid-point ($T_N^{mid}$) of the magnetic transition are determined from the intersection of straight lines fit to the data above and below the transition and as the point where the asymmetry decreases by a factor of 2 from its maximum value, respectively.

5.3.3 Magnetisation and μSR measurements

Zero-field-cooled magnetisation data normalised to the ideal $1/4\pi$ value (χ_{DC}) are shown in Fig. 5.2(a). The $Fe_{1.01}Se_{0.50}Te_{0.50}$ sample is a bulk superconductor with the onset of the transition found at $T_c^{onset} \simeq 14.0\,K$ and $\chi_{DC} \simeq -0.8$ at $T \simeq 2\,K$. A value of -1 is expected for an ideal diamagnet. The $Fe_{1.10}Se_{0.25}Te_{0.75}$ sample also exhibits superconductivity ($T_c^{onset} \simeq 8.6\,K$) but has a small superconducting fraction of order 10% at low temperature.

The evolution of the μ^+ spin polarisation is sensitive to the spatial distribution and dynamical fluctuations of μ^+ magnetic environment. If the μ^+ is in a static magnetic field which varies slightly at different μ^+ sites, μ^+ will precess at slightly different frequencies. This results in oscillations of the ensemble becoming dephased and damping of spin polarisation with time is observed [190]. Should the changes in field from site to site be large, the oscillations will be heavily damped. This can also be caused by fluctuating internal fields, intrinsic sample properties or μ^+ diffusion [190, 191]. Application of an external magnetic field, such as one perpendicular to the incident μ^+ beam axis (TF-μSR), allows us to distinguish between dynamic and static internal field distributions [190].

ZF-μSR measurements on the $x = 0.5$ sample show that the spectra are unchanged at $T = 1.7\,K$ and $20\,K$ and therefore the magnetic state is the same above and below the superconducting phase transition [166]. The μSR measurements were

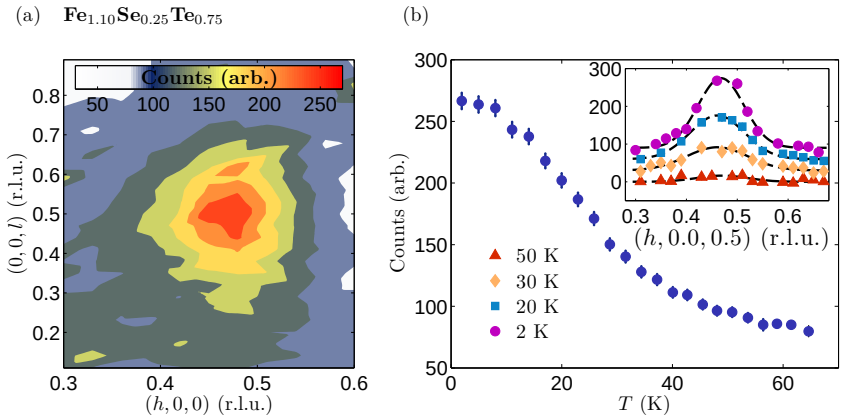

Figure 5.3: Elastic neutron measurements of $Fe_{1.10}Se_{0.25}Te_{0.75}$ at the fundamental reflection $\boldsymbol{q} = (0.47, 0, 0.5)$. (a) Map showing the incommensurate peak at $\boldsymbol{q}$ in the $(h, 0, l)$ plane at 2 K. (b) Temperature dependence of the magnetic peak centered on $\boldsymbol{q}$ upon transition through the magnetic ordering temperature. Inset shows scans along $(h, 0, 0.5)$ measured at 2, 20, 30 and 50 K. A sloping background function has been subtracted from the data and the dashed lines show a Gaussian fit through the peaks. For clarity, the scans have been displaced vertically.

consistent with dilute Fe moments as observed in $FeSe_{1-x}$ [192]. At higher temperatures an anomalous change in the polarisation is found around 130 K. The origin of this is uncertain but it could be a Verwey transition like that in Fe_3O_4 [193] and/or due to impurity phase of Fe_7Se_8 which is known to undergo a spin-axis transition below 130 K [194–196].

Static (within the μSR time window) magnetism in $Fe_{1.10}Se_{0.25}Te_{0.75}$ is signalled by a fast drop of both ZF and TF asymmetries within the first 100 ns. The TF spectrum was found to be well described by two components governing slow and fast relaxation of the signal. The temperature evolution of A_1^{TF}, shown in Fig. 5.2(b), reveals that below 20 K magnetism occupies more than 95% of the whole sample volume. The corresponding values of the onset and the mid-point of the magnetic transitions, determined as shown in the figure, are $T_{\mathrm{N}}^{\mathrm{onset}} \simeq 33.7\,\mathrm{K}$ and $T_{\mathrm{N}}^{\mathrm{mid}} \simeq 27.6\,\mathrm{K}$.

5.3.4 Elastic neutron scattering

Elastic neutron scattering measurements on $Fe_{1.10}Se_{0.25}Te_{0.75}$ in the $(h, 0, l)$ scattering plane at 2 K, as shown in Fig. 5.3(a), reveal a diffuse magnetic peak centred on $(0.5 - \delta, 0, 0.5)$ with $\delta \approx 0.03$. The incommensurate peak is much broader than the resolution of the instrument. From $\boldsymbol{Q}$ scans through the peak we obtain correlation lengths along a and c axes of 13.8(8) Å and 7.5(4) Å respectively at 2 K. Figure 5.3(b) shows that the magnetic peak develops gradually below $T_{\mathrm{N}} \approx 50\,\mathrm{K}$. The correlation lengths did not change measurably upon warming through the T_{N}, see Fig. 5.3(b): inset.

Our polarised neutron scattering measurements to study the closely related com-

position $Fe_{1.03}Se_{0.25}Te_{0.75}$ revealed that the peak found at $\boldsymbol{Q} = (0.5 - \delta, 0, 0.5)$ is indeed magnetic [160]. Measurements at equivalent positions in reciprocal space showed that the propagation vector is described by $\boldsymbol{q}_{\mathrm{m}} = (0.5 - \delta, 0, \pm 0.5)$. The peaks appear on only one side of the antiferromagnetic wavevector. This was explained as due to an imbalance of ferromagnetic/antiferromagnetic correlations between nearest-neighbour spins [197]. Our results are consistent with measurements on $Fe_{1.07}Se_{0.25}Te_{0.75}$ for which the incommensurability is found to be $\delta \approx 0.04$ but the correlation lengths are smaller – 6.1(1) Å and 4.9(1) Å along a and c axes, respectively [197].

5.3.5 Discussion

The main difference between the $Fe_{1.01}Se_{0.50}Te_{0.50}$ and $Fe_{1.10}Se_{0.25}Te_{0.75}$ samples is that the $x = 0.25$ sample exhibits short-range static magnetic order with a characteristic wavevector $\boldsymbol{q}_{\mathrm{m}} = (0.5 - \delta, 0, \pm 0.5)$, $\delta \approx 0.03$, whereas according to the μSR data collected on a crystal from the same batch there is no static magnetic order in the bulk superconductor. The magnetic ordering wavevector $\boldsymbol{q}_{\mathrm{m}}$ found at $x = 0.25$ is the same as that in the parent phase $Fe_{1+y}Te$. The slight incommensurability is thought to be caused by the small excess of Fe accommodated in interstitial sites in the crystal structure [178, 187, 198].

It is also worth commenting on the fact that in the $x = 0.25$ sample elastic magnetic peaks are observed below $T \approx 50\,\mathrm{K}$ by neutron scattering but static magnetic order is only detected below $T \approx 35\,\mathrm{K}$ by μSR. These observations can be reconciled by the difference in the fluctuation rates observable by muons (GHz) and neutrons (THz) below which spin freezing is measured. We infer from this that the characteristic fluctuations of the spin system lie in the GHz to THz range for $35\,\mathrm{K} \lesssim T \lesssim 50\,\mathrm{K}$. Such a gradual slowing down of the fluctuations could be a consequence of the quasi-two-dimensional nature of the spin system, which is also indicated by the persistence of spin correlations to temperatures well above the ordered phase. It is also interesting that the size of the magnetically ordered domains does not significantly increase with decreasing temperature, which suggests that the short-range order is never truly static but fluctuates down to the lowest temperature investigated. This picture is consistent with the observation of spin-glass behaviour in $Fe_ySe_xTe_{1-x}$ for $0.1 < x < 0.3$ where $y \approx 0$ [175].

5.4 Excitation spectrum in $Fe_ySe_xTe_{1-x}$

Many inelastic neutron scattering experiments on Fe-based superconductors have focused on finding the spin resonance mode which appears below T_{c} and is common to hole-doped cuprate and heavy-fermion systems. We shall now turn to the low-energy excitation spectrum of $Fe_{1.01}Se_{0.50}Te_{0.50}$ and $Fe_{1.10}Se_{0.25}Te_{0.75}$ probed using unpolarised inelastic neutron scattering which reveals stark differences in the superconducting and magnetic phases. The inelastic magnetic neutron scattering cross-section is directly proportional to the magnetic response function $S(\boldsymbol{Q}, E)$ –

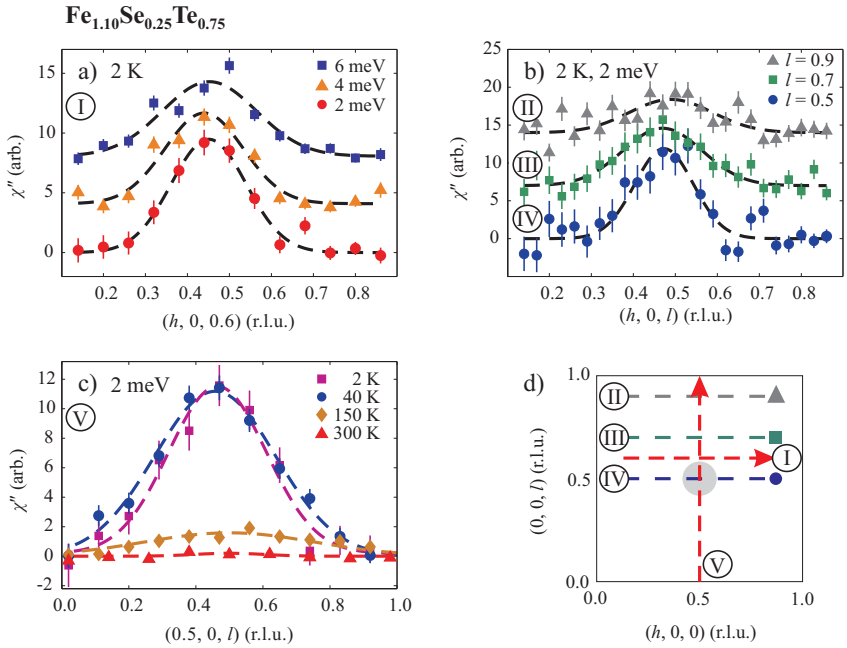

Figure 5.4: Inelastic neutron scattering measurements on $Fe_{1.10}Se_{0.25}Te_{0.75}$ to show dispersion at q_m. (a) Constant energy scans collected at 2, 4 and 6 meV and 2 K along $(h, 0, 0.6)$. The data has been shifted in $\chi''(\boldsymbol{Q}, E)$ by arbitrary amounts for clarity. (b) Constant energy scans collected at 2 meV and temperature of 2 K showing $\chi''(\boldsymbol{Q}, E)$ along $(h, 0, 0.5)$, $(h, 0, 0.7)$ and $(h, 0, 0.9)$. The plots have been displaced and the dashed lines show Gaussian peaks through the spectra. (c) Temperature dependence of excitation mode as measured along $(0.5, 0, l)$. Note that a linear background has been subtracted in all scans. (d) Diagram of the $(h, 0, l)$ plane to show scan directions denoted by roman numerals. Reprinted from Babkevich *et al.*, J. Phys.: Condens. Matter **22**, 142202 (2010), Copyright (2010) by Institute of Physics Publishing Ltd.

the Fourier transform of the space- and time-dependent spin–spin correlation function. According to the fluctuation–dissipation theorem (see § 2.2.2.2), the dynamical part of the response function, $\tilde{S}(\boldsymbol{Q}, E)$, is in turn related to the imaginary part of the dynamical susceptibility $\chi''(\boldsymbol{Q}, E)$ by [46]

$$\tilde{S}(\boldsymbol{Q}, E) = \frac{1}{\pi} \left[n(E, T) + 1 \right] \chi''(\boldsymbol{Q}, E). \tag{5.1}$$

The Bose–Einstein population factor $n(E, T) = [\exp(E/k_B T) - 1]^{-1}$ takes into account the increase in scattering from bosonic excitations due to thermal population at temperatures $T > 0$. Correction for this factor allows the temperature dependence of $\chi''(\boldsymbol{Q}, E)$ to be studied.

5.4.1 Results of inelastic neutron scattering experiments

Figure 5.4(a) shows background corrected scans along the $(h, 0, 0.6)$ direction at energy transfers of 2, 4 and 6 meV for the $Fe_{1.10}Se_{0.25}Te_{0.75}$ crystal. A peak at the

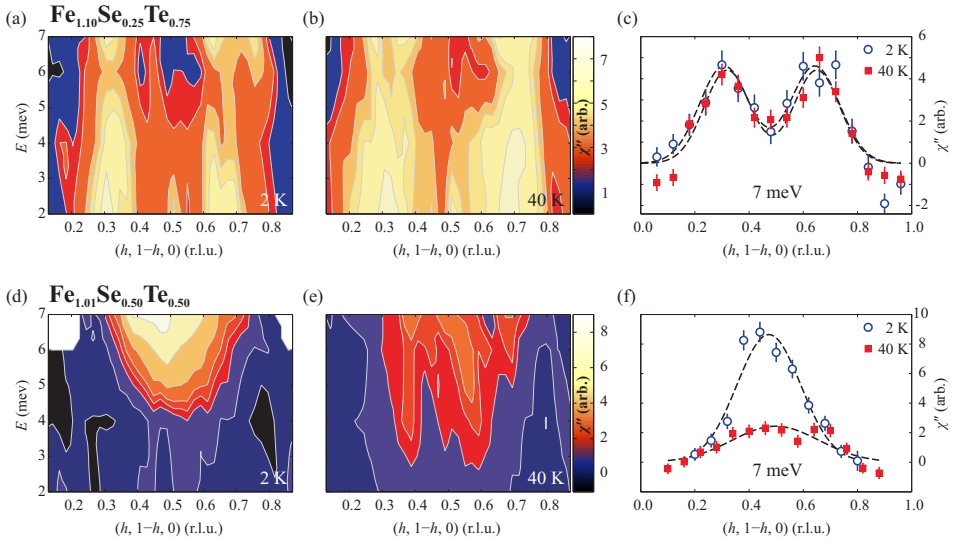

Figure 5.5: Low-energy spin excitation spectra of $Fe_{1.01}Se_{0.50}Te_{0.50}$ and $Fe_{1.10}Se_{0.25}Te_{0.75}$ compositions. Maps show the variation in $\chi''(\boldsymbol{Q}, E)$ along the $(h, 1-h, 0)$ direction for energies between 2 meV and 7 meV at temperatures of 2 and 40 K. Data in (a)–(c) are from $Fe_{1.10}Se_{0.25}Te_{0.75}$ and in (d)–(f) are from $Fe_{1.01}Se_{0.50}Te_{0.50}$. Constant energy cuts at 7 meV along $(h, 1-h, 0)$, measured at 2 and 40 K for $Fe_{1.10}Se_{0.25}Te_{0.75}$ and $Fe_{1.01}Se_{0.50}Te_{0.50}$ are shown in (c) and (f) respectively. A flat background has been subtracted in all scans and dashed lines through the data are fits with a Gaussian lineshape. Reprinted from Babkevich *et al.*, J. Phys.: Condens. Matter **22**, 142202 (2010), Copyright (2010) by Institute of Physics Publishing Ltd.

same position in reciprocal space [i.e. at $\boldsymbol{Q} = \boldsymbol{q}_{\rm m}$, where $\boldsymbol{q}_{\rm m} = (0.47, 0, 0.5)$] is present in each scan, indicating a steeply rising excitation. The broadening of the dispersion in $\boldsymbol{Q}$ may be due to unresolvable splitting of the mode into two excitations at higher energies. The measured magnetic response at 2 meV parallel to $(1, 0, 0)$ for $l = 0.5$, 0.7 and 0.9, as shown in Fig. 5.4(b), reveals considerable broadening of $\chi''(\boldsymbol{Q}, E)$ in the out-of-plane direction. Such broadening is characteristic of a quasi-two-dimensional system with weak interactions along the crystallographic c axis. Figure 5.4(c) shows that spin fluctuations persist up to at least 150 K, well into the paramagnetic state. At 40 K, i.e. close to the magnetic ordering temperature, $\chi''(\boldsymbol{Q}, E)$ is almost the same as at 2 K.

The low-energy excitation spectrum in the vicinity of the antiferromagnetic wavevector $\boldsymbol{Q}_{\rm AF} = (0.5, 0.5, 0)$ is shown in Fig. 5.5. This is the wavevector which is associated with the connection of the hole-electron pockets on the Fermi surface. The observation of a resonance at this position provides information related to the pairing symmetry. Figures 5.5(a) and (b) show maps of $\chi''(\boldsymbol{Q}, E)$ measured along $(h, 1-h, 0)$ for $Fe_{1.10}Se_{0.25}Te_{0.75}$ at 2 and 40 K. The fluctuations measured at 2 K are consistent with the magnetic excitation spectrum at higher energies reported for $Fe_{1.03}Se_{0.27}Te_{0.73}$ [199]. The excitation spectrum at 2 K is characterised by steep incommensurate branches arising from $(0.5 \pm \varepsilon, 0.5 \mp \varepsilon, 0)$ where $\varepsilon \approx 0.18$. The incommensurate excitations are still present at 40 K. The scans shown in Fig. 5.5(c)

reveal that at $E = 7\,\text{meV}$, the system response is nearly the same at 2 K as at 40 K. The background corrected $\chi''(\boldsymbol{Q}, E)$ for the $Fe_{1.10}Se_{0.25}Te_{0.75}$ sample does not appear to change for energies in the 2 to 7 meV range measured at these temperatures. This is also the case for measurements along $(0.5, 0, l)$ in Fig. 5.5(c) that show $\chi''(\boldsymbol{Q}, E)$ data at 2 meV to be similar at 2 and 40 K.

The results obtained for $Fe_{1.01}Se_{0.50}Te_{0.50}$ greatly differ to those of the non-superconducting $Fe_{1.10}Se_{0.25}Te_{0.75}$ sample just described. Figures 5.5(d) and (e) show maps of the dispersion spectrum as a function of wavevector along $(h, 1-h, 0)$ for energies between 2 meV and 7 meV at 2 and 40 K. At 2 K we find a strong signal in $\chi''(\boldsymbol{Q}, E)$ centred on $\boldsymbol{Q} = (0.5, 0.5, 0)$ and $E \approx 7\,\text{meV}$. This feature corresponds to the spin resonance reported previously in superconducting $FeSe_{0.4}Te_{0.6}$ [200], $FeSe_{0.46}Te_{0.54}$ [201] and $FeSe_{0.5}Te_{0.5}$ [202]. However, unlike all FeAs-superconductors, the spin resonance and magnetic order occur at different wavevectors. At higher energies, the excitations have been found to disperse away from $(0.5, 0.5, 0)$ along $(1, -1, 0)$ [201]. However, it is the low energy response of the system which shows the most dramatic change on transition into the superconducting state, as may be seen in Fig. 5.5(f). As the sample is cooled from 40 K to 2 K, the integrated intensity of the peak at 7 meV increases by more than a factor of 2 and decreases in width along $(1, -1, 0)$ by about 30%. Fluctuations continue to be observed well above T_c.

5.4.2 Discussion

The results presented here establish that the low-energy excitations of $Fe_ySe_xTe_{1-x}$ vary strongly with x. The magnetic spectra of the magnetically-ordered compound ($x = 0.25$) and the bulk superconductor ($x = 0.5$) both contain low-energy magnetic fluctuations in the vicinity of the antiferromagnetic wavevector $(0.5, 0.5, 0)$. However, at $x = 0.25$ the fluctuations are incommensurate with wavevector $(0.5 \pm \varepsilon, 0.5 \mp \varepsilon, 0)$, $\varepsilon \approx 0.18$, whereas at $x = 0.5$ the strongest magnetic signal is commensurate. Moreover, at $x = 0.5$ the magnetic spectrum has a gap of almost 6 meV and the size of the signal just above the gap increases strongly at low temperatures. This behaviour is consistent with the superconductivity-induced spin resonance reported recently in bulk superconducting samples of $Fe_ySe_xTe_{1-x}$ of similar composition to ours [200–203], and also in other FeAs-superconductors [188, 204–207].

The elastic and inelastic neutron scattering results suggest that there are two distinct magnetic ordering tendencies at $x = 0.25$, one with wavevector $(0.5 - \delta, 0, \pm 0.5)$ and the other with wavevector $(0.5 \pm \varepsilon, 0.5 \mp \varepsilon, 0)$. The μSR data indicate that the volume fraction of magnetically ordered phase is close to 100%, but we cannot say whether the two characteristic magnetic correlations coexist on an atomic scale or whether the sample is magnetically inhomogeneous.

5.5 Coexistence of magnetism and superconductivity

As demonstrated in § 5.4, the magnetic order and excitation spectra of magnetic and superconducting samples of $Fe_ySe_xTe_{1-x}$ are quite different. In the non-superconducting $Fe_{1.10}Se_{0.25}Te_{0.75}$ sample, magnetic order is observed characterised by a magnetic Bragg peak in the vicinity of $\boldsymbol{Q} = \boldsymbol{q}_{\rm m} = (0.5 - \delta, 0, 0.5)$. A steep magnetic dispersion is found to originate from this position in reciprocal space. Incommensurate spin fluctuations are found in scans transverse to $\boldsymbol{Q}_{\rm AF} = (0.5, 0.5, 0)$ in the *ab* plane. No static magnetic order is observed in the superconducting $Fe_{1.01}Se_{0.50}Te_{0.50}$. The magnetic spectrum contains a spin resonance centred on $\boldsymbol{Q}_{\rm AF}$ and $E \approx 6.5\,\text{meV}$ which disappears as the temperature is raised above $T_{\rm c}$. It is therefore of interest to investigate the cross-over from the systems displaying superconductivity to those that do not.

In this section I will deal with the systematic study of $Fe_ySe_{0.25}Te_{0.75}$ when the amount of interstitial Fe is varied but Se:Te doping is fixed. The excess Fe turns out to play an important role in the physical properties of the system. This is especially significant as it is easier to grow large single crystals of $Fe_ySe_{0.25}Te_{0.75}$ when $y > 1$ and these have been examined the most – usually without regard to the possible effect of the excess Fe content.

5.5.1 Dimensionality of the magnetic excitations

Inelastic neutron scattering measurements on the Fe_yTe compounds reveal the onset of incommensurate magnetic order is concomitant with the vanishing spin gap at the position of the magnetic Bragg peak [208]. The commensurately ordered phase of Fe_yTe possesses spin fluctuations which are three-dimensional in momentum transfer.

One common feature in the phenomenology of both the Fe-based and cuprate superconductors is a sharp peak in the magnetic spectrum localised in wavevector and energy which increases in intensity on cooling below $T_{\rm c}$ (spin resonance) [200]. In superconducting $Fe_ySe_xTe_{1-x}$ a spin resonance is observed to develop below $T_{\rm c} = 14\,\text{K}$ at an energy of 6.5 meV, centered on the wavevector $\boldsymbol{Q}_{\rm AF}$. The position of the resonance peak in momentum space carries information about the symmetry of the superconducting gap $\Delta(\boldsymbol{Q})$. For singlet pairing, the BCS coherence factor enhances the neutron response function when the superconducting gap changes sign between the points on the Fermi surface connected by $\boldsymbol{Q}_{\rm AF}$ [209]. The FeSe- and FeAs-based superconducting compounds share a similar crystallographic structure and have a Fermi surface composed of quasi-two-dimensional electron and hole pockets at Brillouin zone corner and center points, respectively. This would suggest that the pairing mechanism is also related in these materials [180].

The spin resonance in $FeSe_{0.4}Te_{0.6}$ is believed to be of nearly two-dimensional character with very weak change in energy along $\boldsymbol{c}^*$ [200]. This is a widely accepted view which has not been challenged in this family of compounds. The work by Pratt *et al.* [210] demonstrates that the resonance in optimally doped $BaFe_2As_2$ has

very weak out-of-plane dispersion and no static antiferromagnetic ordering. However, the under-doped compound was found to have both a significant spin resonance dispersion along $\boldsymbol{c}^*$ and antiferromagnetic ordering in the ab-plane. This would indicate that interlayer interactions become important in the under-doped $BaFe_2As_2$ in the presence of antiferromagnetic order. Our preliminary measurements on bulk superconducting $FeSe_{0.4}Te_{0.6}$ have indicated that there is very little if any dispersion of the resonance along $\boldsymbol{c}^*$. In addition, elastic neutron measurements on bulk superconducting $Fe_{1.01}Se_{0.50}Te_{0.50}$ sample do not show magnetic order, whilst samples that are underdoped have finite intensity close to $(0.5, 0, 0.5)$ [167, 177]. Therefore within a region of the phase diagram, there is coexistence of incommensurate magnetic order and superconductivity. These properties would strongly suggest that in such compounds, as in under-doped $BaFe_2As_2$, the magnetic fluctuations may exhibit three-dimensional character or other unique behaviour.

5.5.2 Experimental setup

The $Fe_ySe_{0.25}Te_{0.75}$ samples were prepared with a wide range of nominal Fe content, over the $0.9 < y < 1.1$ range using the modified Bridgman growth method described in § 5.3.2. The Se-doping was fixed such that $x \approx 0.25$, the samples are therefore close to the spin-glass phase, shown in Fig. 5.1(b). The single-crystal samples were prepared in form of rods with masses of approximately 4–7 g for use in the neutron scattering experiments.

The crystal structure and stoichiometry was examined using single-crystal x-ray diffraction at room temperature [167]. All samples were found to possess a tetragonal lattice (space group $P4/nmm$) with lattice parameters $a \approx 3.8$ Å and $c \approx 6.2$ Å and site occupancy in good agreement with the nominal values.

The magnetic susceptibility of $Fe_ySe_{0.25}Te_{0.75}$ samples was measured using a Quantum Design (MPMS-XL7) magnetometer. A small measuring field of 3 Oe was applied to the samples along the ab-plane. This orientation was used as the crystal cleaves easily perpendicular to the crystallographic c axis and therefore thin, plate-like samples can be measured in the magnetometer. This experimental setup geometry was chosen to minimise the effect of diamagnetic shielding – the shielding currents generated at the sample surface screening the applied field.

To investigate the change in the magnetic correlations with Fe content, elastic and inelastic neutron scattering measurements were performed on the TASP triple-axis spectrometer at SINQ [95, 96]. In order to probe the static magnetic order, the samples were orientated in the $(h, 0, l)$ plane and reoriented to access $(h, k, 0)$ to probe spin fluctuations close to $\boldsymbol{Q}_{\mathrm{AF}} = (0.5, 0.5, 0)$. To examine the dispersion of excitations along $\boldsymbol{c}^*$, the (h, h, l) scattering plane was also explored. Each sample was aligned on nuclear Bragg reflections to an accuracy better than 0.008 r.l.u. at 1.5 K.

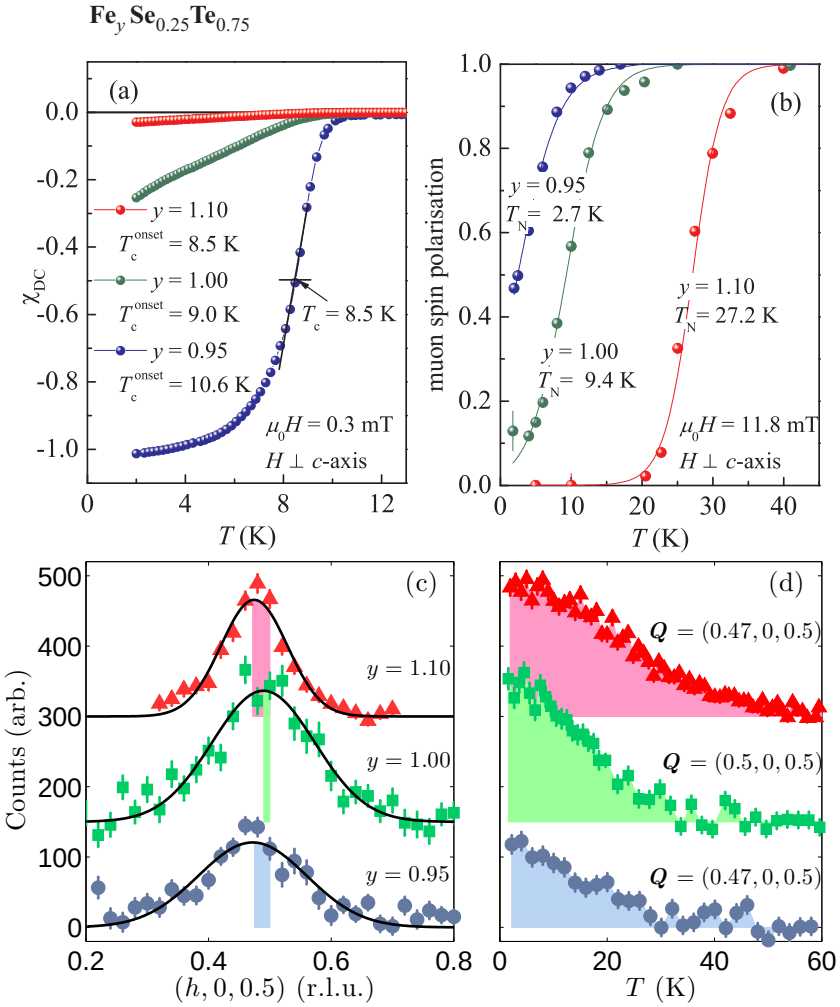

Figure 5.6: Nature of the magnetic order in Fe$_y$Se$_{0.25}$Te$_{0.75}$ probed using magnetometery, μSR and neutron diffraction. (a) Temperature dependence of the volume susceptibility χ_{DC} of representative compositions (y = 0.95, 1.00, and 1.10) of single-crystal Fe$_y$Se$_{0.25}$Te$_{0.75}$. The onset of the superconducting transition T_c^{onset} and the midpoint corresponding to $\chi_{DC} = -0.5$ are indicated. (b) Temperature dependence of the muon-spin polarisation of the slow relaxing component. The magnetic transition T_N is determined from a fit to a Fermi-type function. Neutron diffraction from Fe$_y$Se$_{0.25}$Te$_{0.75}$ samples are shown in panels (c) and (d). In both panels the $y = 1.00$ and $y = 1.10$ data are displaced vertically for clarity. (c) Profiles along the $(h, 0, 0.5)$ direction at $T = 2$ K after subtraction of a background signal measured at $T \approx 50$ K. The solid line shows a fit to a Lorentzian function convoluted with the resolution function of the instrument using ResLib [71]. The shading represents the displacement of the peak from the commensurate position. (d) Temperature dependence of the magnetic reflections centred on $\boldsymbol{Q}$. Reprinted figure with permission from Bendele *et al.*, Phys. Rev. B **82**, 212504 (2010) [167]. Copyright © (2010) by the American Physical Society.

5.5.3 Static magnetic order

Measurements of the magnetic susceptibility of $Fe_ySe_{0.25}Te_{0.75}$ samples for $y = 0.95$, 1.00 and 1.10 are shown in Fig. 5.6(a). We found that bulk superconductivity develops in the samples with nominal Fe content of 0.90 to 0.98, as indicated by $\chi_{DC} \approx -1$ found at low temperatures. The onset of superconductivity for these crystals is found to be typically around 10 K. Conversely, samples with nominal compositions greater than $y \approx 1$, show only traces of superconductivity with volume fraction of less than 30% at low temperatures. The superconducting volume fraction decreases with increasing Fe content up to $y \approx 1.1$.

The magnetic ordering temperature was investigated using TF-μSR in a similar fashion to the measurements described in § 5.3. A fast drop of muon polarisation on incidence with the sample is attributed to the development of magnetism. More than 60% of the bulk superconducting samples ($y = 0.9$ and 0.95) were found to be magnetically ordered at 1.6 K. Increasing the nominal Fe content to more than 0.98 was shown to lead to samples becoming 100% magnetically ordered. The development of the magnetic order probed by μSR is shown in Fig. 5.6(b). The ordering temperature T_N is found to increase sharply as the interstitial Fe content is increased from $y = 0.98$ to 1.03. The transition temperature T_N becomes largely invariant above the $y \approx 1.03$ composition.

The magnetic order was further examined using neutron diffraction. Scans in the $(h, 0, l)$ scattering plane through the fundamental magnetic Bragg peaks at 1.5 K are shown in Fig. 5.6(c). A background recorded at around 50 K (above the magnetic ordering temperature) was subtracted in order to isolate the magnetic contribution to the scattering at 1.5 K. Diffuse incommensurate magnetic peaks centered at $\boldsymbol{Q} = (0.5 - \delta, 0, 0.5)$, with $\delta \approx 0.03$, are observed in all three samples. These results show that samples in the entire range $0.95 < y < 1.10$ have incommensurate magnetic order. A possible reduction in incommensurability δ is found for the $y = 1.00$ sample, however due to the broad nature of the peak, this shift may not be related to the sample. As can be seen from Fig. 5.6(c), the magnetic peaks along $(h, 0, 0.5)$ appear to become broader with reduced Fe-content with correlation lengths along a deduced to be 7.1(5) Å, 8.4(6) Å and 13.8(8) Å for $y = 0.95$, 1.00 and 1.10 respectively. This would suggest that the magnetic order becomes more disordered on lowering the Fe content, with magnetic correlations becoming more short-ranged.

The temperature at which magnetic order sets in appears also to be dependent on y in $Fe_ySe_{0.25}Te_{0.75}$ as shown in Fig. 5.6(d). In the $y = 1.10$ sample, magnetic order is found to develop below about 50 K. However, for $y = 1.00$ and $y = 0.95$, the transition temperature is lowered to nearly 30 K. These results are in good agreement with the change in T_N with doping observed using μSR but due to the difference in fluctuation rates sampled by neutrons and muons, the temperatures at which spin freezing occurs are not the same. The spin-glass nature of the order and different time scales of the microscopy probes (muons and neutrons) ensures that the ordering temperatures deduced from neutron diffraction and μSR differ, as already discussed in § 5.3.5.

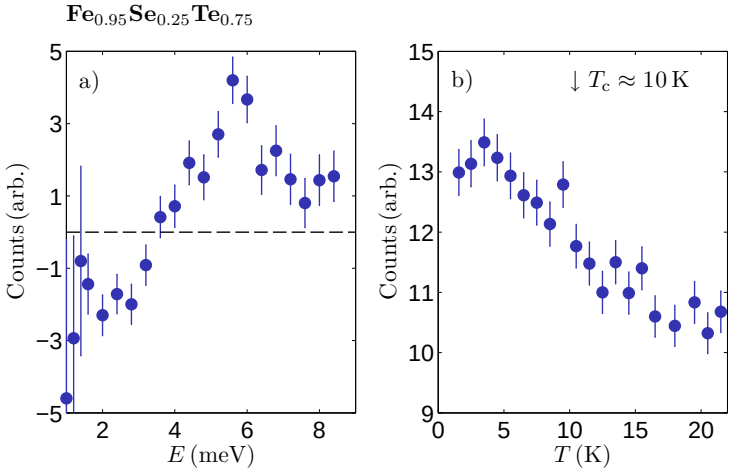

Figure 5.7: Spin resonance in $Fe_{0.95}Se_{0.25}Te_{0.75}$ measured by inelastic neutron scattering. (a) Constant-$\boldsymbol{Q}$ cut at $\boldsymbol{Q}_{\mathrm{AF}}$ position in reciprocal space. Data was obtained from measurements at 2 and 20 K and then subtracted to reveal a spin resonance centred at $E \approx 5.8$ meV. The dashed line shows the spectrum at which the number of counts at 2 K is equal to those at the same position in $(\boldsymbol{Q}, E)$ at 20 K. (b) Temperature dependence of the intensity of the spin resonance measured at $\boldsymbol{Q}_{\mathrm{AF}}$ and $E = 5.8$ meV.

5.5.4 Spin fluctuations in $Fe_ySe_{0.25}Te_{0.75}$

In § 5.4.1 we have dealt with two systems which provide us with contrasting pictures of what the excitation spectra of superconducting and non-superconducting samples of $Fe_ySe_xTe_{1-x}$ look like. The evidence found in § 5.5.3 shows that incommensurate magnetic order and superconductivity can coexist in the $Fe_ySe_{0.25}Te_{0.75}$ systems. Moreover, the physical properties change drastically with small amount of Fe content variation. Using unpolarised inelastic neutron scattering we have analysed the same systems to look at what happens when superconductivity and magnetism coexist in $Fe_ySe_{0.25}Te_{0.75}$.

Let us first examine the experimental results of $Fe_{0.95}Se_{0.25}Te_{0.75}$ which is a bulk superconducting sample with $T_c \approx 10$ K [Fig. 5.6(a)]. A peak corresponding to incommensurate magnetic order was found at $\boldsymbol{Q} = (0.46, 0, 0.5)$. Inelastic neutron scattering measurements in the $(h, 0, l)$ scattering plane have found that, as in the $Fe_{1.10}Se_{0.25}Te_{0.75}$ composition, strongly dispersive excitations arise from this position in reciprocal space at the low-energies studied (2–6 meV). These were identical to measurements on $Fe_{1.10}Se_{0.25}Te_{0.75}$, shown in Fig. 5.4(a). However, interestingly the constant-$\boldsymbol{Q}$ scans at the $\boldsymbol{Q}_{\mathrm{AF}}$ position demonstrate a magnetic spin resonance. That is, an increase in spectral weight at $\boldsymbol{Q}_{\mathrm{AF}}$ and $E \approx 5.8$ meV. Figure 5.7(a) shows the change in spectral weight between 2 and 20 K for $Fe_{0.95}Se_{0.25}Te_{0.75}$. Intensity below around 4 meV is reduced, whereas an enhancement of the signal is observed between 4 and 8 meV. This is very much similar to the optimally doped $Fe_{1.01}Se_{0.50}Te_{0.50}$ compound whose magnetic excitation spectrum is shown in Fig. 5.5(f). No static magnetic order was found in the elastic scans close to $\boldsymbol{Q}_{\mathrm{AF}}$.

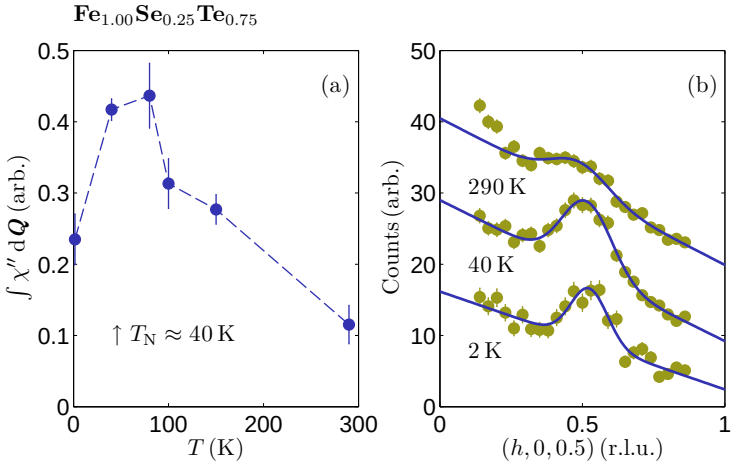

Figure 5.8: Temperature dependence of magnetic fluctuations in $Fe_{1.00}Se_{0.25}Te_{0.75}$. (a) Plot to show the variation of the $\boldsymbol{Q}$-integrated χ'' of fluctuations measured at 2 meV as a function of temperature. (b) Constant energy scans at 2 meV along $(h, 0, 0.5)$ direction in reciprocal space collected at 2, 40 and 290 K. Solid lines show Gaussian lineshapes as guides to the eye.

The temperature dependence of the resonance peak is depicted in Fig. 5.7(b). The peak appears to grow at a transition temperature close to the T_c. This measurement was made at a fixed position of $\boldsymbol{Q}_{AF}$ and E. Although it may be possible that softening of the mode occurs, it was not possible to examine this in detail. Such scenario is unlikely as inelastic neutron scattering studies of bulk superconducting $Fe_ySe_xTe_{1-x}$ compounds showed no signs of resonance mode changing position in $(\boldsymbol{Q}, E)$ space with temperature close to T_c [168, 200].

The non-superconducting $y = 1.10$ sample at the other end of the $Fe_ySe_{0.25}Te_{0.75}$ phase diagram has already been discussed in § 5.4.1. The dynamic susceptibility was found to be unchanged between 2 and 40 K [Fig. 5.5(c)]. In order to obtain a better understanding of the cross-over in the dynamics between $y = 0.95$ and 1.10, we have examined the stoichiometric Fe sample, $Fe_{1.00}Se_{0.25}Te_{0.75}$, shown in Fig. 5.9. Magnetisation and μSR measurements show that superconductive volume fraction is approximately 30% with $T_c \approx 9$ K but static magnetic order occupies the bulk of the sample. The build up of magnetic correlations is found from neutron diffraction to occur below $T_N \approx 40$ K.

Orientating the sample to access $(h, 0, l)$ reflection plane reveals a magnetic Bragg peak below the ordering temperature. A strongly dispersive excitation is found at this position in $\boldsymbol{Q}$ at energies below 6 meV, as also found in $Fe_{1.10}Se_{0.25}Te_{0.75}$ and $Fe_{0.95}Se_{0.25}Te_{0.75}$. Due to the broad nature in $\boldsymbol{Q}$ of the spin fluctuations, it is not possible to say whether they are centred at precisely the commensurate $(0.5, 0, 0.5)$ position. Strong neutron scattering is expected to occur from magnetic fluctuations near the critical temperature of a continuous magnetic phase transition [211]. The $\boldsymbol{Q}$-integrated dynamic susceptibility χ'' appears to peak at a temperature close to the magnetic ordering phase transition, shown in Fig. 5.8(a), could be tentatively a

sign of a criticality at T_N. The resolution of the instrument in the setup used is better than 1 meV and therefore the scattering cannot be attributed to leakage of the elastic signal into the inelastic channel. Magnetic excitations persist well above the ordering temperature and appear at the maximum temperature of approximately $290\,\mathrm{K} \approx 7T_N$, shown in Fig. 5.8(b). Such paramagnetic excitations have been previously observed in itinerant electron systems such as Fe and Ni [212–214], although their precise origin is still unresolved.

Figures 5.9(a) and (b) show low-energy inelastic maps measured transverse to $\boldsymbol{Q}_{\mathrm{AF}}$ collected at 2 and 20 K, respectively. A flat background was subtracted from the raw data and the counts were corrected for the Bose-Einstein thermal population factor defined in Eq. 5.1 to deduce $\chi''(\boldsymbol{Q}, E)$. The inelastic spectra shows at first little change between these two temperatures. The dispersion is dominated by steeply rising incommensurate excitations, as found in $Fe_{1.10}Se_{0.25}Te_{0.75}$. Figure 5.9(d) shows the two columns of excitations more clearly when measured at 6 meV. One of the peaks at $h \approx 0.4$ appears to dominate in terms of spectral weight. The reason for this is unclear but may be due to a slight misalignment in the *ab*-plane. Nevertheless, a change with temperature is found above and below T_c. The difference between $\chi''(\boldsymbol{Q}, E)$ measured at 2 and 20 K is shown in Fig. 5.9(c). Comparing this to Fig. 5.5(d), the resulting spectrum seems to show similar enhancement of signal above approximately 4 meV and diminishing intensity below it.

This is illustrated more clearly in Fig. 5.9(e) where a cut along $(h, 1-h, 0)$ at 6 meV is plotted. The counts measured at 20 K have been subtracted from the 2 K data in this scan. A single peak centred on $\boldsymbol{Q} = (0.5, 0.5, 0)$ is then revealed. Longitudinal constant energy scans show no other excitation modes, just a single broad peak at $(0.5, 0.5, 0)$. No static magnetic order was detected close to the $\boldsymbol{Q}_{\mathrm{AF}}$ position. Constant-$\boldsymbol{Q}$ scans at $(0.5, 0.5, 0)$ (not shown here) confirm that spectral weight is enhanced at 6.2 meV below 12 K. As expected from the low superconducting volume fraction the spin resonance signal is weak but its position in $(\boldsymbol{Q}, E)$ and temperature dependence suggest this feature is indeed the spin resonance.

5.5.5 Discussion

Using complementary set of experimental techniques, we find evidence that the magnetic and superconducting properties of $Fe_ySe_xTe_{1-x}$ system are sensitive to Fe-content. This is an important result which must be considered in future studies into this and related systems. The systematic investigation of $Fe_ySe_xTe_{1-x}$ with differing nominal Fe content shows that samples where $y < 1$ are found to be bulk superconductors with coexisting magnetic order that sets in at temperature below T_c. Stoichiometric samples ($y \approx 1$) show filamentary superconductivity and magnetic order. Fe-rich samples $y > 1$ are almost purely magnetic with only traces of superconductivity. The magnetic order was found to be incommensurate over the range of dopings examined although correlation length increases with increasing y. The results presented here indicate that the interstitial Fe content is also important

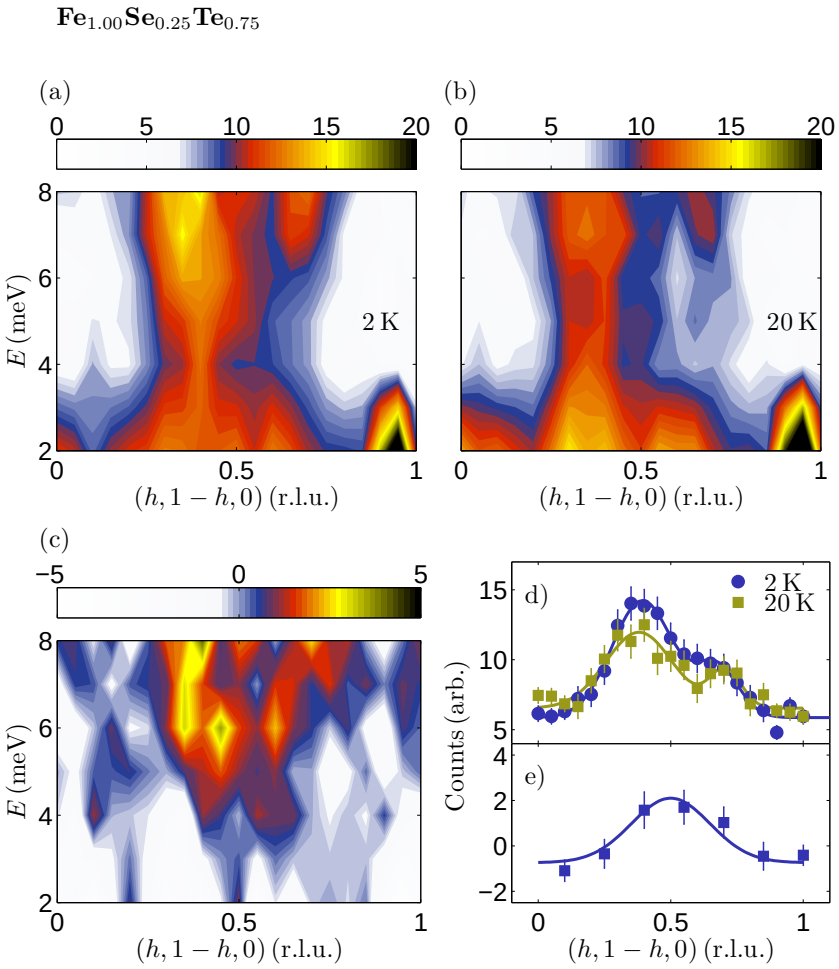

Figure 5.9: Low energy magnetic excitation spectrum of $Fe_{1.00}Se_{0.25}Te_{0.75}$ in the $(h, k, 0)$ plane. (a) and (b) Panels showing the steeply rising excitations of $Fe_{1.00}Se_{0.25}Te_{0.75}$ close to $\boldsymbol{Q}_{AF}$ measured using inelastic neutron scattering at 2 and 20 K. (c) The variation of $\chi''(\boldsymbol{Q}, E)$ calculated from the difference between scans measured at 2 and 20 K, shown in (a) and (b) , respectively. Constant energy cuts through the dispersion at $E = 6$ meV measured at 2 and 20 K are shown in panel (d). The change in the magnetic scattering at 6 meV is shown in panel (e). Gaussian lineshapes serve as guides to the eye.

to consider when examining the phase diagram of $Fe_ySe_xTe_{1-x}$. The systematic study examining Fe(2) content variation presented here is consistent with studies on similar compositions [208, 215, 216].

The inelastic neutron scattering experiments allow for a comparison between the measured samples of $Fe_ySe_{0.25}Te_{0.75}$ for different Fe content. The results appear to suggest that the spin resonance, which emerges below T_c, reflects the order parameter which disappears when either temperature is raised above T_c or doping by Fe is such that suppresses superconductivity. Despite attempts with long counting times, no measurable spin-resonance dispersion along $\boldsymbol{c}^*$ was observed in measurements on $Fe_{1.00}Se_{0.25}Te_{0.75}$. This could simply be due to the weak signal of the spin resonance being overwhelmed by the incommensurate excitations nearby and we cannot rule out that the resonance does not disperse. However, as will be demonstrated in the next section, the spin fluctuations in the FeSe- and FeAs-systems of superconductors differ greatly.

5.6 Spin anisotropy of the resonance peak in superconducting $FeSe_{0.5}Te_{0.5}$

In common with the cuprates, the phase diagram of the Fe-based superconductors shows a suppression of static magnetic order and the emergence of superconductivity with doping. Also like the cuprates, a spin resonance develops below T_c in the magnetic spectrum of the Fe-based superconductors as measured by inelastic neutron scattering [166, 200–202, 204–207, 217, 218]. The existence of a superconductivity-induced spin resonance peak has been shown to relate to the superconducting pairing state and gap symmetry [219, 220].

Inelastic neutron scattering experiments on $Fe_ySe_xTe_{1-x}$ have shown that the spin fluctuations extend up to 250 meV [199]. A spin resonance is observed to develop below T_c in $Fe_ySe_xTe_{1-x}$ at an energy of 6.5 meV, centered on wave vectors of the form $\boldsymbol{Q}_{AF} = (0.5, 0.5, l)$ [166, 200–202, 221]. The resonance peak is quasi-two-dimensional, as discussed in § 5.5.1, which means that it varies only weakly with the out-of-plane wavevector component l [200]. The position of the resonance peak in momentum space carries information about the symmetry of the superconducting state. For example, for singlet pairing, the BCS coherence factor enhances the neutron response function when the superconducting gap changes sign between the points on the Fermi surface connected by $\boldsymbol{Q}_{AF}$ [209]. In Fe-based superconductors, the singlet $s^{\pm}$ pairing state [26] is consistent with many experimental results including the existence of a spin resonance at $\boldsymbol{Q}_{AF}$ [204]. However, a spin resonance at $\boldsymbol{Q}_{AF}$ is not particular to $s^{\pm}$. It is also predicted, for example, for certain triplet p-wave states [220].

Until now, inelastic neutron scattering measurements on $Fe_ySe_xTe_{1-x}$ were performed with an unpolarised neutron beam. However, certain superconducting gap functions can result in anisotropic spin susceptibilities at the resonance energy [220, 222]. In this section, I shall present the results of polarised-neutron inelastic scattering measurements on $FeSe_{0.5}Te_{0.5}$ which determine the anisotropy of the imaginary part of the dynamical susceptibility $\chi''(\boldsymbol{Q}, E)$.

5.6.1 Experimental setup

The single crystal sample of $FeSe_{0.5}Te_{0.5}$ was grown by the modified Bridgman method [158, 167]. Analysis of pulverised crystals from the same batch by x-ray powder diffraction revealed a composition $Fe_{1.045}Se_{0.406}Te_{0.594}$ with traces of Fe_7Se_8 (5% volume fraction) and Fe ($\leq 1\%$) as impurity phases [167]. The magnetometry measurements on a piece of the same crystal found bulk superconductivity below $T_c = 14$ K. The neutron scattering sample was rod-shaped and had a mass of approximately 5 g. The mosaic spread in the ab-plane was found to be 1.5° (full-width at half-maximum). The same sample was used in unpolarised inelastic neutron scattering experiments described in § 5.4.

The inelastic neutron scattering measurements were carried out on the IN22 triple-axis spectrometer at the Institut Laue-Langevin, France. The crystal was

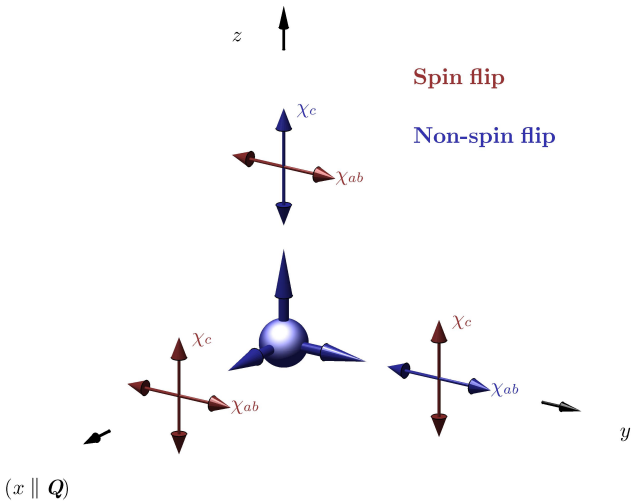

Figure 5.10: Schematic diagram representing the axis convention used in the polarised neutron scattering experiment. The scattering vector $\boldsymbol{Q}$ defines the x-axis, which in scattering geometry employed is always parallel to the ab plane. Only the magnetic fluctuations perpendicular to $\boldsymbol{Q}$ are observed. The incident polarisation vector $\boldsymbol{P}_\mathrm{i} = (P_x, P_y, P_z)$ is spin-flipped by the magnetic fluctuation component perpendicular to both $\boldsymbol{Q}$ and $\boldsymbol{P}_\mathrm{i}$ (red double arrows). Components of the magnetic fluctuations which are perpendicular to $\boldsymbol{Q}$ but not $\boldsymbol{P}_\mathrm{i}$ appear in the non-spin-flip channel (blue double-arrows). Hence, a separation of the in-plane and out-of-plane susceptibilities $\chi''_{ab}(\boldsymbol{Q}, E)$ and $\chi''_c(\boldsymbol{Q}, E)$ can be achieved.

aligned with the c axis perpendicular to the scattering plane and mounted in an ILL-type orange cryostat. The spectrometer was operated with a fixed final wavevector of $k_\mathrm{f} = 2.66\,\mathrm{\AA}^{-1}$ and without collimation. A graphite filter was installed in the scattered beam to suppress contamination by higher-order wavelengths. The analyser was horizontally-focused to increase intensity. The corresponding energy resolution with this setup is approximately 0.8 meV at the elastic position.

Longitudinal polarisation analysis was performed with the CryoPAD device [74]. CryoPAD is designed such that the sample is in a zero magnetic-field environment, and the incident and final neutron polarisation states are controlled with nutation and precession fields which are decoupled by superconducting Nb shielding. With a Heusler monochromator and analyser the effective flipping ratio was about 10 as measured on the (110) structural Bragg peak. No corrections were made to compensate for the non-ideal polarisation.

In total, six neutron cross-sections were measured, denoted by $\sigma(x, \pm x)$, $\sigma(y, \pm y)$ and $\sigma(z, \pm z)$. The coordinate x is taken along the scattering vector $\boldsymbol{Q}$, z is perpendicular to the scattering plane (here $z \parallel c$) and y completes the right-handed Cartesian system – Fig. 5.10. The two indices in σ refer to the direction of the neutron polarisation before and after the sample, respectively.

The crystal structure of $FeSe_{0.5}Te_{0.5}$ is tetragonal and so in general $\chi''_{ab}(\boldsymbol{Q}, E)$ can be different from $\chi''_c(\boldsymbol{Q}, E)$. Longitudinal polarisation analysis allows a com-

plete separation of $\chi''_{ab}(\boldsymbol{Q}, E)$ and $\chi''_c(\boldsymbol{Q}, E)$ because of two properties of the magnetic scattering cross-section: (i) neutrons only scatter from spin fluctuations perpendicular to $\boldsymbol{Q}$, and (ii) spin fluctuations perpendicular to the incident neutron polarisation $\boldsymbol{P}_\mathrm{i}$ scatter in the spin-flip (SF) channel, while spin fluctuations parallel to $\boldsymbol{P}_\mathrm{i}$ scatter in the non-spin-flip (NSF) channel. With the geometry chosen for the present measurements the SF cross-sections are given by [44]

$$\begin{aligned} \sigma(x,-x) &\propto \chi''_{ab} + \chi''_c + b_\mathrm{SF} \\ \sigma(y,-y) &\propto \chi''_c + b_\mathrm{SF} \\ \sigma(z,-z) &\propto \chi''_{ab} + b_\mathrm{SF}, \end{aligned} \tag{5.2}$$

and the NSF cross-sections

$$\begin{aligned} \sigma(x,x) &\propto N^2 + b_\mathrm{NSF} \\ \sigma(y,y) &\propto \chi''_{ab} + N^2 + b_\mathrm{NSF} \\ \sigma(z,z) &\propto \chi''_c + N^2 + b_\mathrm{NSF}, \end{aligned} \tag{5.3}$$

where N^2 refers to the coherent nuclear cross-section, and b_SF and b_NSF are the SF and NSF backgrounds, respectively. To make the notation more clear, the explicit dependence of $\chi''(\boldsymbol{Q}, E)$ on $\boldsymbol{Q}$ and E, will be omitted from now on. These scattering processes are represented in Fig. 5.10. The background was found to be independent of the polarisation in the SF cross-sections to within experimental error from measurements at $\boldsymbol{Q} \approx (0.1, 0.9, 0)$ and $E \approx 6\,\mathrm{meV}$.

5.6.2 Results

Figure 5.11(a) shows energy scans performed at $\boldsymbol{Q}_\mathrm{AF} = (0.5, 0.5, 0)$ in the three spin-flip channels and in the $\sigma(x,x)$ non-spin-flip channel. The intensity in the $\sigma(x,x)$ channel is significant, highlighting the importance of using polarised neutron scattering to separate the nuclear contribution from the magnetic signal. From Eq. 5.2, the $\sigma(x,-x)$ cross-section contains the total magnetic scattering. The scattering in this channel contains a peak at $\hbar\omega_0 \approx 6.5\,\mathrm{meV}$, corresponding to the spin resonance previously reported by unpolarised inelastic neutron scattering measurements in compounds of similar composition [166, 200–202, 221] and shown in Fig. 5.5. Figure 5.11(b) shows the $\sigma(x,-x)$ cross-section in wavevector scans along $(h, 1-h, 0)$ at selected energies. At 3 meV only a flat background is evident. Above the resonance energy, steeply-rising incommensurate magnetic excitations are observed. The results are consistent with independent unpolarised neutron scattering measurements on similar compositions of $Fe_ySe_xTe_{1-x}$ [201, 202].

The $\sigma(y,-y)$ and $\sigma(z,-z)$ spin-flip channels, shown in Fig. 5.11(a), contain the magnetic scattering from out-of-plane and in-plane fluctuations, respectively as described by Eq. 5.2. The signal in these channels is very similar throughout the energy range measured, both channels having a peak at the resonance energy. A small but statistically significant difference is observed between $\sigma(y,-y)$ and $\sigma(z,-z)$ on

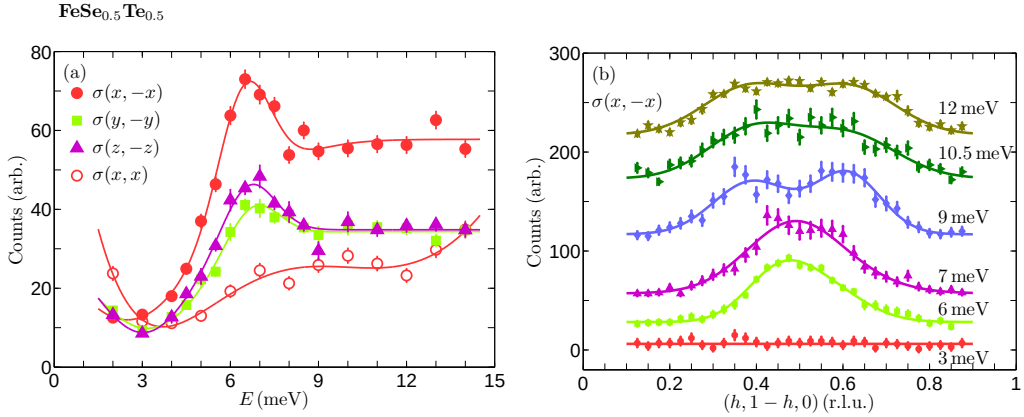

Figure 5.11: Constant energy and wavevector cuts through the spin fluctuations in the superconducting state of $FeSe_{0.5}Te_{0.5}$. (a) Energy scans at $\boldsymbol{Q}_{\mathrm{AF}} = (0.5, 0.5, 0)$ showing the SF channels which contain the magnetic scattering and the $\sigma(x, x)$ NSF channel which contains non-magnetic scattering. Lines are visual guides. (b) Wavevector scans along $(h, 1-h, 0)$ at energies of 3 to 12 meV (displaced vertically) showing the $\sigma(x, -x)$ SF scattering. Solid lines show least-squares fits to the spectra assuming a Gaussian lineshape. Data in both (a) and (b) were recorded at a temperature of 2 K. Reprinted figure with permission from Babkevich *et al.*, Phys. Rev. B **83**, 180506(R) (2011) [168]. Copyright © (2011) by the American Physical Society.

the resonance peak itself. Using Eq. 5.2 we can eliminate the background contribution and separate the in-plane and out-of-plane components of magnetic scattering: $\chi''_{ab} \propto \sigma(x, -x) - \sigma(y, -y)$ and $\chi''_c \propto \sigma(x, -x) - \sigma(z, -z)$. Figure 5.12(a) shows the result of this procedure. The resonance peak appears at the same energy to within an experimental error of 1 meV in both χ''_{ab} and χ''_c. The peak is slightly larger in χ''_{ab}. Either side of the spin resonance energy the intensity is approximately the same for both channels.

The similarity between the χ''_{ab} and χ''_c components is emphasised in the color maps shown in Fig. 5.12(b) and (c), which show the intensity distribution as a function of energy and wavevector along $(h, 1-h, 0)$. The data plotted in these maps are the $\sigma(y, -y)$ and $\sigma(z, -z)$ cross-sections, which contain the χ''_c and χ''_{ab} fluctuations, respectively. The overall conclusion from all the $T = 2$ K data is that the low-energy spin fluctuations in $FeSe_{0.5}Te_{0.5}$ are isotropic ($\chi''_{ab} \approx \chi''_c$) to within experimental error, except on the resonance peak itself where χ''_{ab} is approximately 20% larger than χ''_c.

Figure 5.13 presents the results of measurements of the temperature dependence of the magnetic fluctuations at $\boldsymbol{Q}_{\mathrm{AF}} = (0.5, 0.5, 0)$ in $FeSe_{0.5}Te_{0.5}$. The measurements at 2 K, shown in Fig. 5.12, have demonstrated that $\chi''_{ab}(\boldsymbol{Q}_{\mathrm{AF}}, E) \approx \chi''_c(\boldsymbol{Q}_{\mathrm{AF}}, E)$ and therefore from Eq. 5.2, we can study the temperature dependence of $\sigma(x, -x)$ cross-section. From Eq. 5.1, the measured intensity is proportional to $\chi''(\boldsymbol{Q}_{\mathrm{AF}}, E)/[1-\exp(-E/k_{\mathrm{B}}T)]$ and therefore multiplying the intensity by $1 - \exp(-E/k_{\mathrm{B}}T)$ we can compare susceptibilities at different temperatures. The

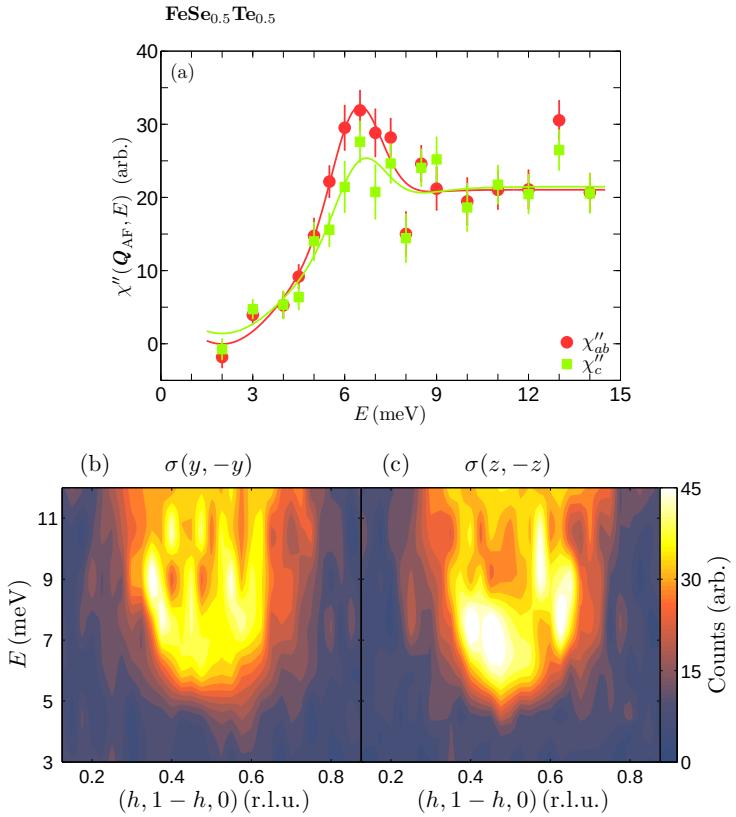

Figure 5.12: Spin resonance anisotropy. (a) Comparison of the scattering from in-plane (χ''_{ab}) and out-of-plane (χ''_c) magnetic fluctuations in $FeSe_{0.5}Te_{0.5}$. Solid lines through the data points are guides to the eye. (b) and (c) Intensity maps showing the cross-sections $\sigma(y,-y)$ and $\sigma(z,-z)$, which contain χ''_c and χ''_{ab}, respectively. All the data in this figure were recorded at $T = 2\,\mathrm{K}$. Reprinted figure with permission from Babkevich *et al.*, Phys. Rev. B **83**, 180506(R) (2011) [168]. Copyright © (2011) by the American Physical Society.

resonance peak disappears above $T_c = 14\,\mathrm{K}$, while at higher energies the susceptibility remains essentially unchanged. An increase in the response below the spin gap is found on warming to 16 K.

The temperature evolution of $\sigma(x,-x)$ cross-section for temperatures from 2 to 13 K is shown in Fig. 5.13(b). A scan measured at 16 K (above T_c) was subtracted to isolate the spin resonance contribution to the spectral weight. Upon warming, the intensity of the spin resonance shows little change up to 9 K. When the temperature approaches T_c, the spectral weight diminishes and the spin-gap is gradually filled. Another notable feature is that the spin resonance does not shift to lower energies with increasing temperature [Fig. 5.13(c)], as one might expect if the spin resonance were simply caused by a gap which closes at T_c with temperature. From our measurements we conclude that the position and the energy width of the spin resonance are temperature independent up to at least $\sim 0.8T_c$. The lack of softening of the resonance energy with increasing temperature has also been found in inelas-

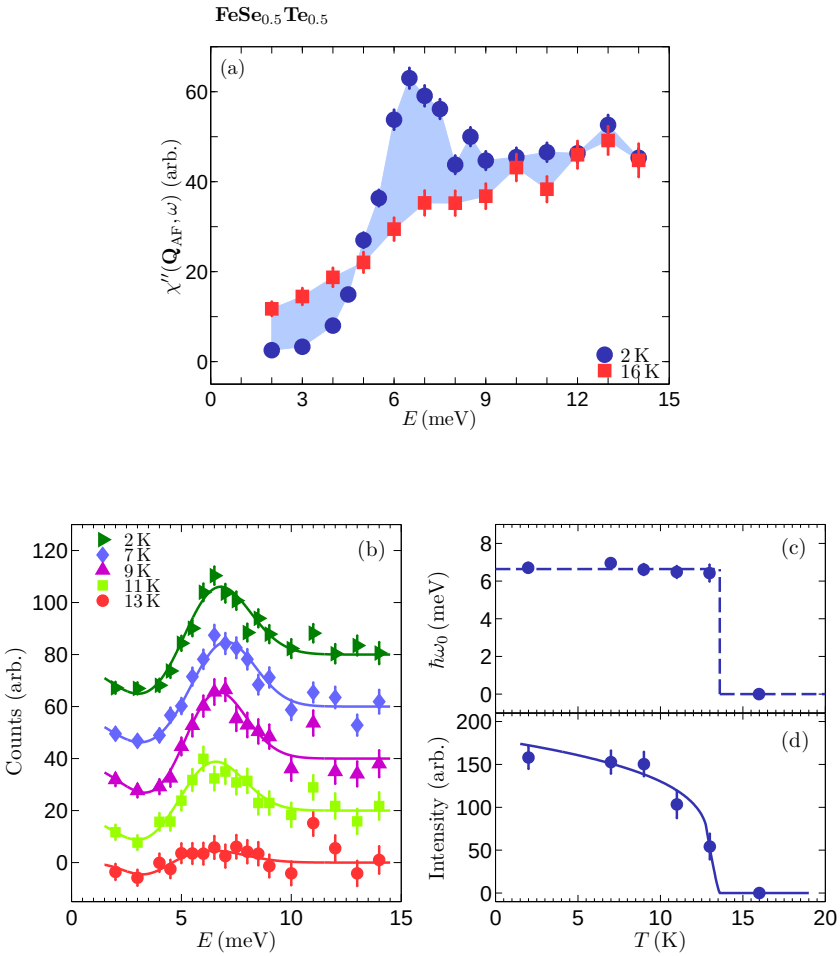

Figure 5.13: Temperature dependence of the spin resonance in $FeSe_{0.5}Te_{0.5}$. (a) Energy scans at $\boldsymbol{Q}_{\mathrm{AF}} = (0.5, 0.5, 0)$ showing $\chi'' = \chi''_{ab} + \chi''_c$ at 2 K and 16 K. The shaded region highlights the change in the spectrum with temperature. (b) Energy scans at $\boldsymbol{Q}_{\mathrm{AF}}$ for a series of temperatures from 2 to 13 K. The scans are displaced vertically. (c) Position of the resonance energy as a function of temperature as determined from fits show in panel (b). The datum at 16 K represents that the resonance has been lost. (d) Integrated intensity of the resonance peak as a function of temperature. Data recorded at 16 K have been subtracted in panels (b)–(d). Solid dashed lines are guides to the eye. Reprinted figure with permission from Babkevich *et al.*, Phys. Rev. B **83**, 180506(R) (2011) [168]. Copyright © (2011) by the American Physical Society.

$s^{\pm}$	$\chi''_{ab} = \chi''_c$
s^{-}	no peak
p_x	$\chi''_{ab} \ll \chi''_c$
p_{2x}	$\chi''_{ab} \gg \chi''_c$
$p_x + ip_y$	no peak

Table 5.1: Theoretical predictions of χ''_{ab} and χ''_c at the resonance position based on different superconducting gap symmetries. Adapted from Ref. [220].

tic neutron scattering measurements of $FeSe_{0.4}Te_{0.6}$ [200, 223]. Although Andreev reflection measurements on a similar composition appear to contradict this and suggest instead that the superconducting gap energy gradually closes on transition from superconducting to normal state [224].

Figure 5.13(d) shows the evolution of the integrated intensity of the spin resonance which behaves as an order parameter of the superconducting phase. In the vicinity of T_c measurements with higher precision are needed to obtain a more quantitative estimate of the renormalisation of the inelastic intensity than is available from the present experiment.

5.6.3 Discussion

The polarised neutron data presented in this section go beyond what is possible with unpolarised neutron scattering and provide new insights into the magnetic excitations of $FeSe_{0.5}Te_{0.5}$. A superconducting wavefunction with purely $s^{\pm}$ pairing state would result in an isotropic spin resonance peak [220]. The experimental results suggest a small anisotropy, in the sense $\chi''_{ab} > \chi''_c$. This small anisotropy cannot readily be explained by the usual anisotropic terms in the spin Hamiltonian since the magnetic scattering is isotropic above and below the resonance peak. This would indicate that the spin anisotropy is connected with the superconducting pairing state. It is possible, therefore, that the superconducting pairing function contains a minority component with a different symmetry, this is shown in Table 5.1 for a selection of gap function symmetries. For example, a spin-triplet with sign-reversed p-wave gap is predicted to give a resonance in χ''_{ab}, but not in χ''_c [220]. It is perhaps possible that a small macroscopic region of the sample possesses a superconducting state with a gap symmetry which is different to $s^{\pm}$.

The relatively small anisotropy in the spin resonance of $FeSe_{0.5}Te_{0.5}$ is in stark contrast to the results of a study on $BaFe_{1.9}Ni_{0.1}As_2$, which revealed a highly anisotropic spin resonance with only the χ''_{ab} component non-zero [225]. The results also differ from the spin-ladder system $Sr_{14}Cu_{24}O_{41}$, which also has a resonance-like coherent singlet–triplet excitation [226]. Firstly, the anisotropy is in the opposite sense (in $Sr_{14}Cu_{24}O_{41}$ the out-of-plane fluctuations are stronger than the in-plane fluctuations), and second, the anisotropy in $Sr_{14}Cu_{24}O_{41}$ is observed over a range of energies not just on the peak [227].

Recently, polarised-neutron scattering measurements have been performed on

$YBa_2Cu_3O_{6+x}$ [228]. The spin resonance in $YBa_2Cu_3O_{6.9}$ at 40 meV, corresponding to the odd-parity mode, was found to be quasi-isotropic to within the precision of the measurements. This implies that the resonance peak is predominantly a singlet–triplet excitation in both $FeSe_{0.5}Te_{0.5}$ and $YBa_2Cu_3O_{6+x}$. Furthermore, the resonance peaks in these materials do not soften appreciably as the temperature is increased towards T_c (see Fig. 5.13 and Ref. [229]). These similarities suggest that the superconducting states in the cuprates and Fe-based superconductors have some general features in common.

If a spin resonance is associated with a singlet-triplet excitation [230], then applying a sufficient large magnetic field should result in a Zeeman splitting of the mode. An externally applied magnetic field has been shown to have an effect on the superconducting state in the well-known $YBa_2Cu_3O_{6.6}$ and $La_{1.82}Sr_{0.18}CuO_4$ [231, 232]. Experimental studies of the magnetic field dependence of the resonance in $Fe_ySe_xTe_{1-x}$ have observed a suppression of the signal at the resonance position in fields up to 16 T [221, 233]. However, an expected change in the resonance energy or resonance peak broadening has not been found so far. In contrast Zhao *et al.* [234] have shown that in $BaFe_{1.9}Ni_{0.1}As_2$ the magnetic spin gap closes with magnetic field. Furthermore, in zero-field measurements of $BaFe_{2-x}Co_xAs_2$, the resonance softens on increasing the temperature to T_c [207]. The temperature and field dependence of the resonance energy provides compelling evidence that in the $BaFe_2As_2$-type systems the resonance is indeed related to the superconducting gap. Although the spin resonance in $Fe_ySe_xTe_{1-x}$ is also likely to be associated with the superconducting state, it is less clear why the temperature dependence of the pairing state would be so different to the $BaFe_2As_2$ systems.

The magnetic excitations in $FeSe_{0.5}Te_{0.5}$ are found to be nearly isotropic $\chi''_{ab} \approx \chi''_c$, both in terms of amplitude of the response and position in energy. Conversely, polarised inelastic neutron scattering studies of magnetic excitations in non-superconducting $BaFe_2As_2$ compound reveal that there is strong in-plane anisotropy below T_N [235]. The pronounced anisotropy suggests orbital degrees of freedom are important in FeAs-systems [235] and corroborates with the anisotropy of the resonance in the superconducting $BaFe_{1.9}Ni_{0.1}As_2$ [225].

One of the most intriguing itinerant antiferromagnets is Cr in which steeply rising incommensurate dispersion is similar to that observed in the non-superconducting $Fe_{1.10}Se_{0.25}Te_{0.75}$ crystal and above the spin resonance energy in superconducting $Fe_{1.01}Se_{0.50}Te_{0.50}$. Polarisation analysis of inelastically scattered neutrons in Cr reveals that the modes at $(1 \pm \delta, 0, 0)$ in fact consist of longitudinal and transverse spin density waves [236]. Any anisotropy in the incommensurate spin fluctuations are important to determine because it could also be relevant to the mechanism of unconventional pairing. For example, strong anisotropy $\chi''_c \gg \chi''_{ab}$ in the incommensurate spin fluctuations of Sr_2RuO_4 have been suggested to lead to triplet pairing [28]. The fact that this is not found in $Fe_{1.01}Se_{0.50}Te_{0.50}$ compared to $BaFe_{1.9}Ni_{0.1}As_2$ and Sr_2RuO_4 would perhaps suggest that anisotropy of spin fluctuations is not crucial to the superconducting pairing mechanism in $Fe_ySe_xTe_{1-x}$.

5.7 Conclusions

We have observed a resonance-like peak at the antiferromagnetic nesting wavevector $(0.5, 0.5, 0)$ in the low-energy magnetic spectrum of $Fe_{1.01}Se_{0.50}Te_{0.50}$, and shown that this feature is absent from the magnetic spectrum of $Fe_{1.10}Se_{0.25}Te_{0.75}$ which instead shows incommensurate peaks flanking $(0.5, 0.5, 0)$. The results reveal a clear distinction between the magnetic excitation spectra of $Fe_ySe_xTe_{1-x}$ samples which are magnetically ordered and those which are bulk superconductors. Therefore, the existence of a resonance peak at the commensurate antiferromagnetic wavevector is a characteristic of bulk superconductivity in $Fe_ySe_xTe_{1-x}$.

In order to understand the spin fluctuations better, we have studied compositions of $Fe_ySe_xTe_{1-x}$ which are on the brink of bulk superconductivity. Using μSR and neutron scattering techniques we find that interstitial Fe content is also important in determining the physical properties of the system. In the Fe-deficient samples $y \lesssim 1$, bulk superconductivity and incommensurate magnetic order coexist. The magnetic excitation spectrum close to the nesting wavevector is incommensurate with branches either side of the $\boldsymbol{Q}_{\mathrm{AF}}$ position in transverse wavevector scans. On doping with Fe, the magnetic order becomes correlated over a longer range and abruptly superconductivity vanishes at around $y \approx 1$. A spin resonance emerges as superconductivity develops in the material.

Finally, using polarised inelastic neutron scattering, we find that the resonance in the optimally doped $Fe_{1.01}Se_{0.50}Te_{0.50}$ sample is predominantly isotropic. This indicates that there is a uniform superconducting gap and provides support for the $s^{\pm}$ pairing symmetry in which the superconducting order parameter changes sign between electron and hole pockets. The small anisotropy observed at the resonance cannot be readily accounted for in the $s^{\pm}$ theory or by orbital degree of freedom in the system.

Chapter 6

Multiferroicity in CuO

Contents

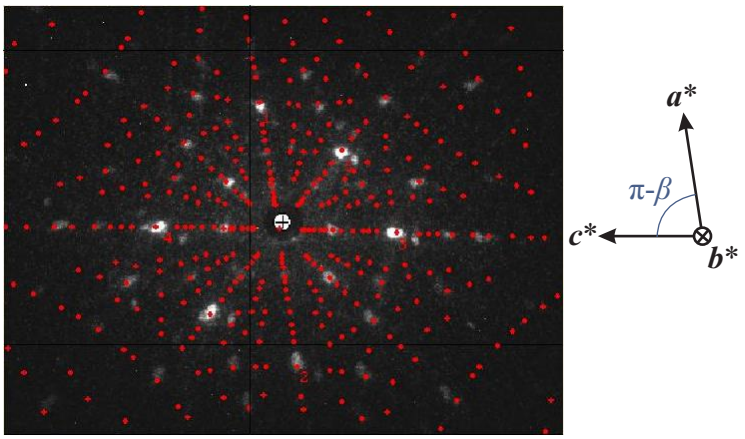

Figure 6.1: Sample quality check and alignment. Neutron Laue pattern of CuO sample together with the indexation (red dots) to deduce the orientation of the crystal. The schematic shows the reciprocal lattice vectors which can be found from the pattern.

6.1 Introduction

Materials in which electric and magnetic order parameters couple are of great interest in the application to spintronic devices. Such materials are termed magnetoelectric multiferroics and have been actively studied in recent years. Of particular interest are the type-II multiferroics in which magnetic order is directly and strongly coupled to the electric polarisation. The strong coupling is often associated with non-collinear magnetic structures which originate from competition and frustration in the magnetic interactions. Most of the strongly coupled multiferroics exhibit these unusual properties at low temperatures (typically $< 40\,\mathrm{K}$). A notable exception is cupric oxide which develops multiferroic coupling below 230 K [42].

6.2 Sample preparation

The single crystal samples of CuO were prepared in Oxford by D. Prabhakaran from high-purity powder (99.995%) of CuO using the optical floating-zone furnace (Crystal System Inc.). The growth process has previously been optimised and reported in Ref. [237]. The oxygen content was analysed using thermogravimetric analysis (TGA) on a grounded piece of CuO – pieces from the same initial rod were used in the experiments described in this chapter. The polycrystalline sample was then heated in a 5% H_2 - 95% N_2 atmosphere to break CuO into the constituting Cu and O elements. The weight of the powder was recorded as a function of temperature. A breakdown of CuO is found at around 800°C with just Cu remaining above this temperature. The mass before and after the breakdown is related to the ratio of Cu to O. The calculated excess O in $CuO_{1+\delta}$ was found to be approximately $\delta \approx -0.03(1)$ which is very close to stoichiometry.

A piece of CuO was checked using x-ray and neutron Laue. The neutron Laue

probes the bulk of the sample and is therefore useful in gaining insight into the quality of the sample as well as its orientation. The neutron Laue measurements were carried out using OrientExpress instrument at ILL [238]. Figure 6.1 shows a typical Laue pattern in the backscattering geometry with the $\boldsymbol{b}^*$ axis aligned parallel to the neutron beam. To be sure of the orientation, the Bragg peaks were indexed using the OrientExpress program [239]. The crystal was then aligned on an x-ray Laue and cut into several pieces. Two flat, rectangular pieces were found to be of good quality and size and were subsequently coated in 8-10 nm of Cr and 40-50 nm of Au on opposite sides to act as electrodes in order to apply an electric potential difference across the sample. A thin layer of Cr is required in order to avoid Au stripping off too easily from the surface. Care was taken in using a mask to avoid any short circuits along the sides of the crystals.

6.3 Magnetic susceptibility of CuO

Magnetisation measurements were made using a Superconducting Quantum Interference Device (SQUID) magnetometer MPMS (Quantum Design). A 0.175 g piece of CuO was cut from the the same initial rod as examined in § 6.2. The same sample was used in the electric polarisation measurements described further in § 6.4. The Cr/Au coating is considered to give negligible contribution to the signal due to the thinness of the layers. The sample was wrapped in teflon tape to avoid damaging the Au electrodes and mounted inside a plastic straw with crystal orientation having been determined previously using neutron diffraction. The magnetisation was measured in the following protocols along all the reciprocal lattice axes $\{\boldsymbol{a}^*, \boldsymbol{b}^*, \boldsymbol{c}^*\}$:

Zero-field-cool (ZFC) The sample was cooled from the paramagnetic phase in zero applied field to a specific temperature. Measurements in an applied field of 1000 Oe were made on warming.

Field-cool (FC) The sample was cooled in a field H from the paramagnetic phase. Measurements were made in the same field on warming.

Furthermore, to study any possible hysteretic behaviour, magnetic field sweeps were made at constant temperature. In order to avoid any remnant field contribution coming from the instrument, the shielding was degaussed and magnet reset prior to taking measurements. The degauss procedure involves oscillating the magnetic field rapidly whilst continuously decreasing the magnetic field. The reset is followed by heating the superconducting magnet above critical temperature to expel any trapped flux.

Figure 6.2 shows temperature sweeps of magnetic susceptibility recorded along reciprocal lattice vectors $\{\boldsymbol{a}^*, \boldsymbol{b}^*, \boldsymbol{c}^*\}$. A sharp discontinuous transition is observed in all directions at T_{N1}. Above T_{N1}, the susceptibility increases linearly with temperature up to $T_{\mathrm{N2}} \approx 230$ K at which a change of slope is found. The data collected are in excellent agreement with previously reported results by Kimura *et al.* [42].

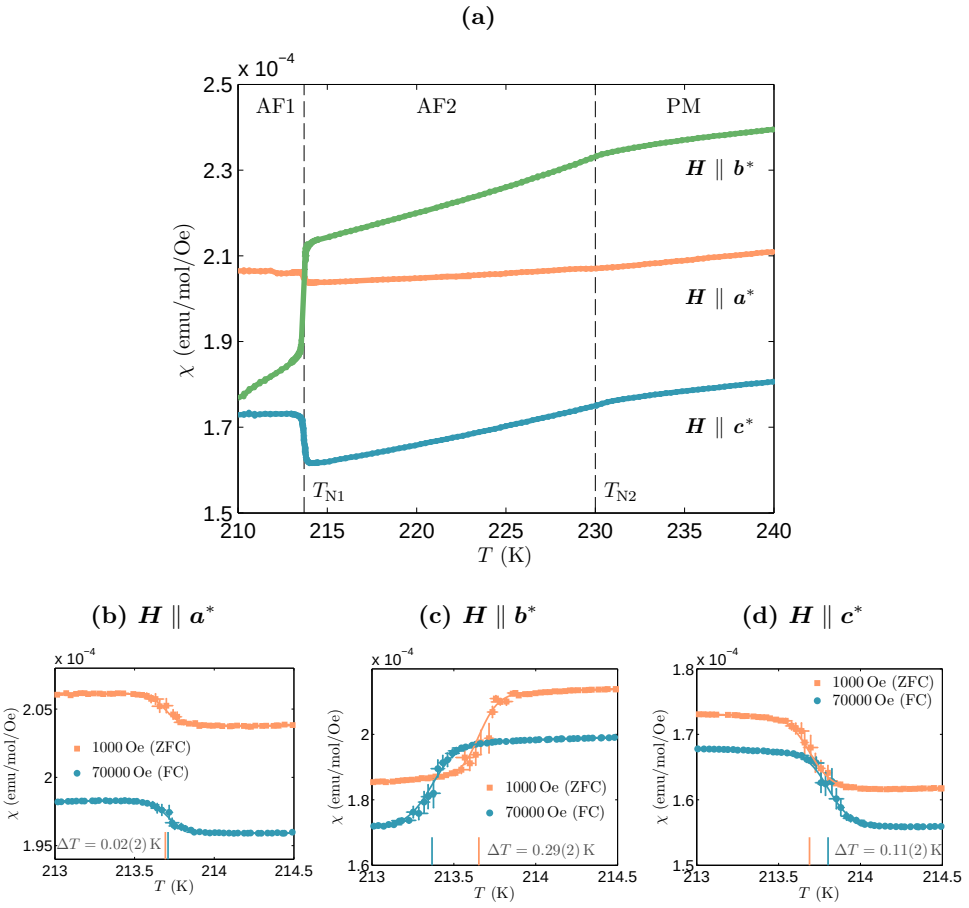

Figure 6.2: Magnetic susceptibility measurements on CuO. (a) ZFC data along reciprocal lattice vectors $\{\boldsymbol{a}^*, \boldsymbol{b}^*, \boldsymbol{c}^*\}$. Panels (b)-(d) show the temperature scans through the T_{N1} transition for applied magnetic field $\boldsymbol{H}$ along the reciprocal lattice axes $\{\boldsymbol{a}^*, \boldsymbol{b}^*, \boldsymbol{c}^*\}$ as measured in the ZFC and FC protocols with applied fields of 1000 Oe and 70000 Oe respectively. Lines plotted through the data points are a guide to the eye.

The susceptibility obeys a Curie-Weiss law with a paramagnetic temperature of 458 K above 700 K [240]. A broad maximum in susceptibility is found around 540 K whose origin was proposed to be due to thermal excitations of the triplet molecular Cu-Cu antiferromagnetism [240, 241]. However, an alternative and more prominent view is that the paramagnetic susceptibility behaviour is due to low-dimensional magnetism with strong correlations along certain directions above Néel temperature [242, 243]. The low-dimensionality explains other unusual properties of CuO, i) the large superexchange coupling J which is an order of magnitude larger than expected from value of T_{N} [243]; ii) spin moment of $0.65\,\mu_{\mathrm{B}}$ [244, 245] rather than $1\,\mu_{\mathrm{B}}$ expected for a Cu^{2+} ion, although this could also be affected by covalency; iii) spin correlations along $[1, 0, \bar{1}]$ direction are far stronger than approximately perpendicular to it along $[1, 0, 1]$ suggesting CuO behaves as a low-dimensional antiferromagnet [246, 247]. Therefore, a quasi-one-dimensional antiferromagnet, in a system which is chemically three-dimensional, seems to consistently explain a lot of experimental results. From the Anderson model for superexchange interactions, the antiferromagnetic coupling is strongest for largest bond angle [248]. In CuO, this is found along the $[1, 0, \bar{1}]$ direction with Cu–O–Cu angle of 146°.

The first-order transition at T_{N1} was studied by making slow scans in temperature on warming in the ZFC and FC protocols. The corresponding data is shown in Fig. 6.2(b)-(d). In ZFC runs, the phase transition appears at $T_{\mathrm{N1}} = 213.7\,\mathrm{K}$ along each direction measured with field along $\{\boldsymbol{a}^*, \boldsymbol{b}^*, \boldsymbol{c}^*\}$. However, cooling from the paramagnetic phase in a 70000 Oe field, the transition appears to shift in temperature. For the case of the field applied along $\boldsymbol{a}^*$ in Fig. 6.2(b), no change is recorded. The largest change in T_{N1} comes when the $\boldsymbol{b}^*$ axis is aligned with the field, such that the midpoint of the transition is displaced to lower temperature by 0.29(2) K, see Fig. 6.2(c). Somewhat surprisingly a change in the temperature of the transition is also found with field along $\boldsymbol{c}^*$. However, the FC procedure seems to displace T_{N1} to a higher temperature albeit by a smaller magnitude of 0.11(2) K. Checks were made to establish the validity of these results. Measurements along $\boldsymbol{b}^*$ were repeated using the same protocol and the change in temperature was found to be reproducible. Since, a very slow heating rate of 0.01 K/min was employed, it would seem unlikely that thermal lag of the actual sample temperature could be responsible. In any case, the measurements were made on warming and for the $\boldsymbol{H}$ parallel to $\boldsymbol{b}^*$ measurements, the phase transition appears at a lower temperature. Similar results have been reported from specific-heat capacity measurements in magnetic fields of up to 6 T and were explained in terms of two-component Landau theory [249].

Isothermal measurements of the magnetic response to a magnetic field applied along the b-axis at 205, 215 and 220 and 240 K are summarised in Fig. 6.3. These measurements probe the magnetisation in the three magnetic phases of CuO: in the collinearly ordered AF1 phase (205 K), in the multiferroic AF2 phase (215 and 220 K) and above the magnetic ordering phase transition temperature (240 K). For each measurement, the sample was cooled from the paramagnetic state in zero applied field. Once the required temperature has been reached and stabilised, field

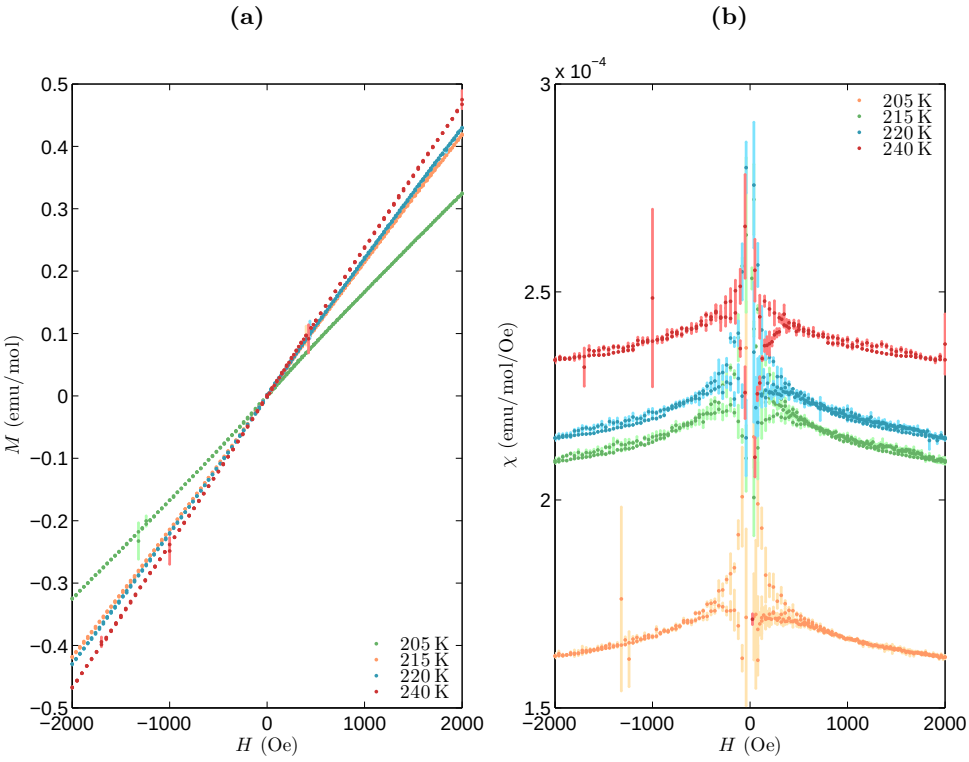

Figure 6.3: Hysteresis loops. Magnetic field sweeps at constant temperature of 205, 215 and 220 K in the antiferromagnetic phase such that $\boldsymbol{H} \parallel \boldsymbol{b}^*$. The magnetic response M to an applied field H is shown in panel (a). Panel (b) shows the same data as in panel (a) but with magnetisation normalised by the magnetic field, $\chi = M/H$ as a function of magnetic field.

was swept from 0 to 2000 Oe to measure the virgin curve. Measurements were then made from 2000 Oe to −2000 Oe and back to 2000 Oe in steps of 20 Oe. The resulting plots are shown in Fig. 6.3(a) of magnetisation against magnetic field. The magnetisation response appears to be proportional to the applied magnetic field with no hysteretic behaviour. The response is in excellent agreement with previous measurements of CuO [237, 250].

However, further examination of the magnetic field loops reveal there is very small hysteresis at fields less that 500 Oe. Figure 6.3(b) shows magnetisation weighted by the applied magnetic field as a function of applied field. Below ±500 Oe, a splitting appears between field-sweep-up and field-sweep-down at each temperature. The irreversibility in magnetisation would posit the existence of a small ferromagnetic moment which may be due to small quantity of impurities in the sample. The expected behaviour of an antiferromagnet would be that the macroscopic magnetisation tends to vanish in the low field limit. The figure also shows that the magnetisation is not exactly linear with an applied field, as we would then expect the data to fall on a horizontal line. The progressive lack of a response to the applied

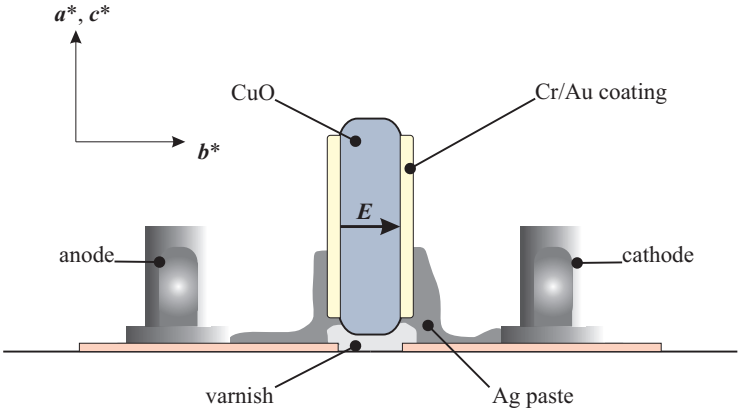

Figure 6.4: Pyrocurrent measurement setup. Schematic diagram of the setup used to measure pyroelectric current in CuO with the electric field applied parallel to $\boldsymbol{b}$ direction. The sample is placed on a puck insert for the PPMS (Quantum Design). A silver paste was applied to the gold coated surfaces of the sample to attach electrodes.

field can also be seen in the temperature scans shown in Fig. 6.2(b)-(d) wherein the magnetic response at $\mu_0 H = 7\,\mathrm{T}$ lies somewhat below the ZFC scans. The presence of the hysteretic behaviour for $|H| < 500\,\mathrm{Oe}$ in the paramagnetic phase would imply that it has no relation to the successive magnetic phase transitions in CuO.

Measurements of the field sweeps at constant temperature were made up to $\mu_0 H = 7\,\mathrm{T}$ applied along $\boldsymbol{b}^*$ and reveal no deviation from a (nearly) linear relation between M and H. This was also found in the study of polycrystalline CuO sample reported by Wang *et al.* (Ref. [250]) with a field applied up to 13 T. The authors concluded that weak coupling between ferroelectricity and magnetic order results in a negligible magnetoelectric effect. Indeed in $MnWO_4$, whose phase diagram closely resembles that of CuO, a spin flop transition was induced by a magnetic field applied along the ferroelectric axis [251]. This is due to the relatively weak anisotropy in $MnWO_4$ which is of order 2 T [252] and therefore moderately weak magnetic fields can be applied to manipulate the magnetic spin structure and thereby the ferroelectricity. Our and reported [250] magnetometery data for CuO do not show any anomalies which could be associated with a spin flop. This is consistent with a larger anisotropic interaction, which from theoretical models [253], gives a magnetic field of approximately 37 T that would be required to overcome the anisotropy. Therefore, the magnetic structure is effectively too stable to be perturbed by magnetic fields of 13 T.

6.4 Electric polarisation measurements

A piece of the same initial crystal rod as that used in the polarised neutron scattering measurements described in § 6.6 was used in the measurements of the pyroelectric current. The parallel faces have a surface area of 10.0 mm^3 perpendicular to $\boldsymbol{b}$ and

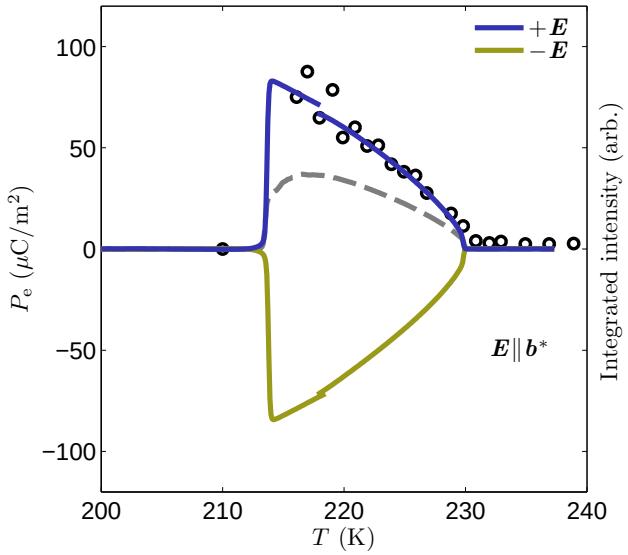

Figure 6.5: Measurements of the electric polarisation in CuO. Electric poling field of 106 V/mm was applied along $\boldsymbol{b}$ axis and pyroelectric current measured through the T_{N1} and T_{N2} phase transitions. The reversal of the electric polarisation is shown when poling field in the opposing direction is applied. The dashed grey line corresponds to electric polarisation measurements on warming after the sample was field cooled to 200 K. The circular data points show integrated intensity as a function of temperature of the incommensurate Bragg peak using unpolarised neutron scattering, from Ref. [244].

a thickness of 1.7 mm. The sample was mounted vertically between the electrodes. Electrical contact with the sample's Cr/Au thin-film coating was made using Ag epoxy. A similar setup using Cu wires to make the contacts was found to give significant background contribution to the signal, most likely due to an induction of a small thermoelectric current. A custom setup for measuring pyroelectric current was used inside a PPMS (Quantum Design) acting only as a cryostat. The sample insert was connected to a high-voltage power supply such that an electric field of 106 V/mm was applied along $\boldsymbol{b}$. The experimental setup of these measurements is illustrated in Fig. 6.4 and is discussed in greater detail in § 2.5.2.

The multiferroic phase in CuO exists within a narrow range of temperature, namely between T_{N1} and T_{N2} as found using magnetometery data described in § 6.3. To infer the electric polarisation P_e in this phase, measurements were carried out using the following protocol. The sample was cooled in an applied electric field $\boldsymbol{E}$ from the paraelectic phase at 250 K to the multiferroic phase at 220 K. At the settling point, the electric field was removed from the sample. However, it is important to remove any effects due to the surface charge built up on the Au plates. The plates were therefore allowed to discharge through the power supply for a period of approximately 30 min. Following this, the sample was connected to an electrometer to measure the pyroelectric current.

Measurements showing the ferroelectric response in CuO are shown in Fig. 6.5.

A correction was made for a small background current which had a linear dependence on temperature. On cooling from the paraelectric phase, a sharp increase in the polarisation at 230 K is observed. The polarisation then increases almost linearly up to 213 K. A very sharp discontinuous transition is observed close to 213 K below which no electric polarisation signal is measured. The pyroelectric current measurements were repeated with a poling field applied in the reverse bias. The electric polarisation was found to be switchable when electric field in the opposite direction was applied. The transition temperatures at which the ferroelectric response was measured were found to closely agree with the magnetic phase transitions measured, as shown in Fig. 6.2. The trend of the polarisation closely follows that of the neutron scattering integrated intensity when measured at $\boldsymbol{Q} = \boldsymbol{q}_{\mathrm{icm}}$, the incommensurate Bragg peak [244]. This is as expected for a multiferroic where the onset of ferroelectricity is coupled to the magnetic order and therefore the electric polarisation should scale as the square of the magnetisation, $P_{\mathrm{e}} \propto |M|^2$ and hence proportionally to the intensity. This relationship has been found in other magnetically ordered incommensurate systems [254–256].

The maximum electric polarisation attained was $P_{\mathrm{e}} \approx 90\,\mu\mathrm{C/m^2}$. The pyroelectric current measurements were reproducible but did not exceed this electric polarisation value. This is comparable to the previously reported electric polarisation measurements with a maximum approximately $150\,\mu\mathrm{C/m^2}$ [42]. The discrepancy may be due to incomplete coating of the sample to make electrical contact. If not all of the surface is coated by Cr/Au film, the edges of the crystal will experience a lower electric field.

First principle density functional theory calculations of CuO reproduce the experimentally obtained value of P_{e} using the Berry phase method, showing that the electronic contribution to the polarisation is an order of magnitude greater than the lattice effects [253]. However, similar microscopic calculation performed by Jin *et al.* [257] find that the electronic and ionic contributions are comparable.

Intriguingly, CuO was found to display a form of memory effect. The sample was first field cooled from well above T_{N2} (250 K) to well below T_{N1} (200 K). At 200 K, the field was removed and the pyroelectric current measured on warming back to 250 K. For a truly paralectric AF1 phase below T_{N1}, one would expect there to be no response. However, as shown in Fig. 6.5, we instead recover approximately half of the electric polarisation response in the multiferroic AF2 phase. The crystal therefore memorises the electric polarisation which was previously induced. Such behaviour has been reported for CuO [258] but is also found in other multiferroic non-collinear magnets such as $TbMnO_3$ [259], $MnWO_4$ [260] and $CuFe_{1-x}Ga_xO_2$ [261]. The origin of the memory effect in CuO has been studied in detail using soft x-ray diffraction by Wu *et al.* [258]. The measurements show that a finite component of magnetisation in the *ac*-plane exists in the collinearly ordered phase below T_{N1}. Such nanoregions occupy a small fraction of the total volume of the sample compared to the purely collinear regions and hence are not detected in neutron scattering experiments or in the electric polarisation measurements. The spin-flip is energetically unfavourable and the electric polarisation remains unchanged. The

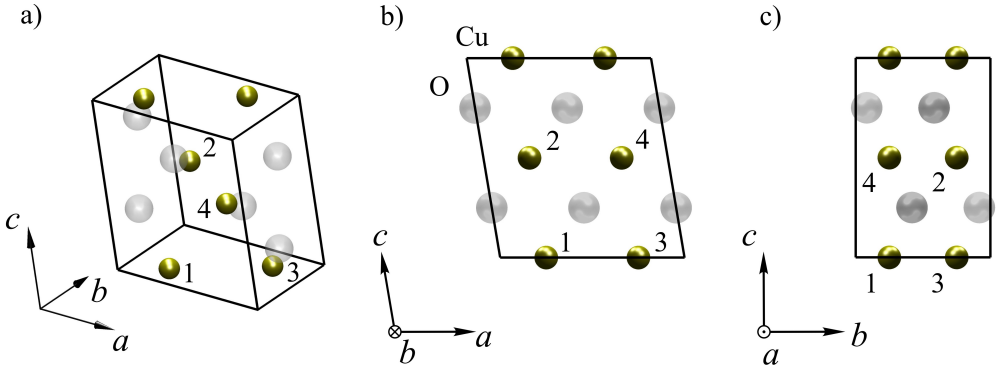

Figure 6.6: Crystallographic structure of CuO. The crystal structure is shown in (a) three-dimensions and viewed in the (b) *ac*- and (c) *bc*-plane. The black outline represents the conventional unit cell within which the Cu atoms are situated at 1. $(0.25, 0.25, 0)$, 2. $(0.25, 0.75, 0.5)$, 3. $(0.75, 0.75, 0)$ and 4. $(0.75, 0.25, 0.5)$.

helicoidally ordered spin moments in the multiferroic nanoregions provide a preference in the domains when the sample is warmed above T_{N1}. This process appears to be analogous to polar nanoregions observed in relaxor ferroelectrics [262].

6.5 Representation analysis of magnetic structures in CuO

The symmetry of the space group constrains the possible magnetic structures of a system. I have previously discussed the methods in applying representation analysis to find the basis vectors in § 2.3. In this section I shall apply the representation analysis to find possible magnetic structures of CuO. In order to do so, we require knowledge of the magnetic propagation wavevector $\boldsymbol{\kappa}$, the crystallographic space group and the atomic coordinates of the magnetic atoms in the paramagnetic state. From previous studies of CuO, it has been well established that the propagation wavevector has the form, $\boldsymbol{\kappa} = (\kappa_x, 0, \kappa_z)$ in the commensurate and incommensurate magnetic phases [244, 245, 263–266].

The crystal structure of CuO can be described using the monoclinic space group $C2/c$ with setting of a unique axis along $\boldsymbol{b}$, see Fig. 6.6. High-resolution x-ray diffraction measurements over a temperature range from 100 to 1000 K have shown that below 300 K the crystal retains the $C2/c$ space group [267]. The Cu^{2+} and O^{2-} ions occupy the symmetry sites 4(c): $(0.25, 0.25, 0)$ and 4(e): $(0, y, 0.25)$ where $y = 0.4184$ respectively. Each Cu atom is connected to four (nearly) equidistant O atoms which mediate the superexchange. Within the conventional unit cell, there are four Cu and four O atoms. Since only Cu atoms carry a magnetic moment, our discussion will therefore focus on irreducible representational analysis (IR) of the Cu site.

The symmetry elements g_n of $C2/c$ space group forming group G_0 are shown in Table 6.1. The symmetry can be described by a combination of a unitary transfor-

Element g_n	Symbol	Rotation matrix R	IT notation $g_n = \{R \mid \boldsymbol{\tau}\}$	Jones symbol
g_1	E	$\begin{pmatrix} 1 & 0 & 0 \\ 0 & 1 & 0 \\ 0 & 0 & 1 \end{pmatrix}$	$\{E\|0,0,0\}$	x, y, z
g_2	C_{2y}	$\begin{pmatrix} \bar{1} & 0 & 0 \\ 0 & 1 & 0 \\ 0 & 0 & \bar{1} \end{pmatrix}$	$\{C_{2y}\|0,0,0.5\}$	$-x, y, -z+\frac{1}{2}$
g_3	I	$\begin{pmatrix} \bar{1} & 0 & 0 \\ 0 & \bar{1} & 0 \\ 0 & 0 & \bar{1} \end{pmatrix}$	$\{I\|0,0,0\}$	$-x, -y, -z$
g_4	σ_y	$\begin{pmatrix} 1 & 0 & 0 \\ 0 & \bar{1} & 0 \\ 0 & 0 & 1 \end{pmatrix}$	$\{\sigma_y\|0,0,0.5\}$	$x, -y, z+\frac{1}{2}$

Table 6.1: Symmetry operators for the space group $C2/c$ (G_0). The notation using the International Tables is separated into the R rotational and $\boldsymbol{\tau}$ translational parts, from Ref. [66].

(a)

C_h	g_1	g_4
Γ_1 (A_g)	1	1
Γ_2 (A_u)	1	$\bar{1}$

(b)

$G_{\boldsymbol{\kappa}}$	g_1	g_4
Γ_1	1	φ
Γ_2	1	$\bar{\varphi}$

Table 6.2: (a) Character table showing the irreducible representations of the C_h point group. (b) Irreducible representations of space group $C2/c$ where the phasing due to the translational $\boldsymbol{\tau}$ part of g_4 symmetry element is $\varphi = \exp(\mathrm{i}\boldsymbol{\kappa} \cdot \boldsymbol{\tau})$.

mation matrix R and a translation $\boldsymbol{\tau}$, such that the position $\boldsymbol{x}$ can be related to $\boldsymbol{x}'$ by $\boldsymbol{x}' = \{R|\boldsymbol{\tau}\}\boldsymbol{x} = R\boldsymbol{x} + \boldsymbol{\tau}$. Although the conventional unit cell, shown in Fig. 6.6, contains four Cu and O atoms, it is possible to relate atoms 1 and 2 to 3 and 4 by a translation of $\boldsymbol{\tau}_c = (0.5, 0.5, 0)$. The primitive unit cell can therefore be used in the representation analysis which contains just two Cu atoms. The magnetic moments on sites 3 and 4 can then be related to those on sites 1 and 2 by a phase factor of $\boldsymbol{\kappa} \cdot \boldsymbol{\tau}_c$ to obtain the magnetic structure within the conventional unit cell.

The little group $G_{\boldsymbol{\kappa}}$ contains the symmetry elements of G_0 which leave the propagation vector invariant under operation R. From Table 6.1, the little group for both the commensurate and incommensurate magnetic structures contains elements g_1 and g_4. The irreducible representations of $G_{\boldsymbol{\kappa}}$ will therefore be of C_h point group modified by a phase factor φ, shown in Table 6.2. There must be two one-dimensional representations corresponding to g_1 and g_4 and hence the two irreducible representations, Γ_1 and Γ_2. The g_4 symmetry operation corresponds to

g_n	Γ_{perm}	χ_{perm}	Γ_{axial}	χ_{axial}	χ_{mag}
g_1	$\begin{pmatrix}1&0&0&0\\0&1&0&0\\0&0&1&0\\0&0&0&1\end{pmatrix}$	4	$\begin{pmatrix}1&0&0\\0&1&0\\0&0&1\end{pmatrix}$	3	12
g_2	$\begin{pmatrix}0&1&0&0\\1&0&0&0\\0&0&0&1\\0&0&1&0\end{pmatrix}$	0	$\begin{pmatrix}1&0&0\\0&\bar{1}&0\\0&0&1\end{pmatrix}$	1	0
g_3	$\begin{pmatrix}0&0&1&0\\0&0&0&\bar{b}\\1&0&0&0\\0&\bar{b}&0&0\end{pmatrix}$	0	$\begin{pmatrix}1&0&0\\0&1&0\\0&0&1\end{pmatrix}$	3	0
g_4	$\begin{pmatrix}0&0&0&1\\0&0&b&0\\0&1&0&0\\b&0&0&0\end{pmatrix}$	0	$\begin{pmatrix}\bar{1}&0&0\\0&1&0\\0&0&\bar{1}\end{pmatrix}$	-1	0

Table 6.3: Table showing the permutation and axial vector representation together with the corresponding character of the representations of symmetry operations of G_0. The action of operation g_4 takes atoms at $(-0.25, 0.25, 0.5)$ and $(0.25, -0.25, 0.5)$ out of the zeroth cell by $(0, 0, 1)$. The phase change is then such that $b = \exp(2\pi \mathrm{i}\kappa_z)$, where κ_z is the z-component of the propagation vector $\boldsymbol{\kappa}$.

a glide plane which is composed of a mirror plane perpendicular to $\boldsymbol{b}$ and a translation of $(0, 0, 0.5)$. The translation part of the symmetry operation results in the additional phase of $\exp(\mathrm{i}\boldsymbol{\kappa} \cdot \boldsymbol{\tau})$ which is included in Table 6.2(b).

The magnetic representation Γ_{mag} is the result of the symmetry operations on magnetic (axial) and position (polar) vectors. The two effects are independent and can be treated separately. The matrix which identifies the permutation of atom labels and a phase change is the permutation representation Γ_{perm}. The general case of swapping atom labels to find the permutation representation for the G_0 group is shown in Table 6.3. However, in order to deduce the magnetic representation, we need to consider just the interchange of atoms generated by g_1 and g_4 symmetry operations whose permutation representation is found in Table 6.4.

The axial representation Γ_{axial} relates how the moment vector is altered by the symmetry operations and is a 3×3 matrix. The character of permutation and axial vector representations is simply given by the trace of the respective representations and these results are shown in Table 6.3. The magnetic representation of CuO structure can then be found by using Eq. 2.46 and details given in Tables 6.2 and 6.4 to be,

$$\Gamma_{\text{mag}} = 3\Gamma_1 + 3\Gamma_2. \tag{6.1}$$

For each representation there are three distinct basis vectors. The basis vectors

$G_{\boldsymbol{\kappa}}$	$\boldsymbol{\Gamma}_{\mathbf{perm}}$	$\boldsymbol{\chi}_{\mathbf{perm}}$	$\boldsymbol{\chi}_{\mathbf{axial}}$	$\boldsymbol{\chi}_{\mathbf{mag}}$
g_1	$\begin{pmatrix}1 & 0\\ 0 & 1\end{pmatrix}$	2	3	6
g_4	$\begin{pmatrix}0 & 1\\ b & 0\end{pmatrix}$	0	-1	0

Table 6.4: Character table of the little group $G_{\boldsymbol{\kappa}}$.

	$\boldsymbol{g_1}$	$\boldsymbol{g_4}$		$\boldsymbol{g_1}$	$\boldsymbol{g_4}$
Γ_1	1	φ	Γ_2	1	$-\varphi$
$\chi_1^*\Gamma_{\text{axial}}$	$\begin{pmatrix}1 & 0 & 0\\ 0 & 1 & 0\\ 0 & 0 & 1\end{pmatrix}$	$\varphi^*\begin{pmatrix}1 & 0 & 0\\ 0 & \bar{1} & 0\\ 0 & 0 & 1\end{pmatrix}$	$\chi_2^*\Gamma_{\text{axial}}$	$\begin{pmatrix}1 & 0 & 0\\ 0 & 1 & 0\\ 0 & 0 & 1\end{pmatrix}$	$\varphi^*\begin{pmatrix}\bar{1} & 0 & 0\\ 0 & 1 & 0\\ 0 & 0 & \bar{1}\end{pmatrix}$
$\boldsymbol{\psi}_1$	$(1,0,0)$	$(\varphi^*,0,0)$	$\boldsymbol{\psi}_1$	$(1,0,0)$	$-(\varphi^*,0,0)$
$\boldsymbol{\psi}_2$	$(0,1,0)$	$-(0,\varphi^*,0)$	$\boldsymbol{\psi}_2$	$(0,1,0)$	$(0,\varphi^*,0)$
$\boldsymbol{\psi}_3$	$(0,0,1)$	$(0,0,\varphi^*)$	$\boldsymbol{\psi}_3$	$(0,0,1)$	$-(0,0,\varphi^*)$

Table 6.5: Table to show the calculation of the basis vectors for atomic positions (x,y,z) and $(x,-y,z+1/2)$ related by symmetry operators g_1 and g_4 respectively. The basis vectors ψ are calculated for irreducible representations Γ_1 and Γ_2 and projected onto the crystallographic axes $\{\boldsymbol{a},\boldsymbol{b},\boldsymbol{c}\}$. The phasing is given by $\varphi = e^{\mathrm{i}\boldsymbol{\kappa}\cdot(g_1-g_4)\boldsymbol{x}}$, where Cu atom position is $\boldsymbol{x} = (0.25, 0.25, 0)$.

can be found using the standard method of projection operator technique. The projection operator is defined as an operator which transforms one basis vector into another basis vector of the same irreducible representation Γ_ν. To do this we can use trial functions along crystallographic axes $\boldsymbol{m}_a = (1,0,0)$, $\boldsymbol{m}_b = (0,1,0)$ and $\boldsymbol{m}_c = (0,0,1)$. The projection operator formula to find the basis vector $\boldsymbol{\psi}$ for magnetic representation Γ_ν is given as,

$$\boldsymbol{\psi}_{\alpha\nu} = \sum_{g\in G_{\boldsymbol{\kappa}}} \chi_\nu^*(g) \sum_n \delta_{n,g_n} \Gamma_{\text{axial}}(g)\boldsymbol{m}_\alpha \tag{6.2}$$

where $\chi(g)$ is the character of the little group $G_{\boldsymbol{\kappa}}$ defined in Table 6.2(b).

The derivation of the basis vectors of CuO magnetic structure is found in Table 6.5. We find that the basis vectors in the mirror plane (which is perpendicular to $\boldsymbol{b}$) transform in the same way, whereas the magnetic moment perpendicular to the mirror plane (along $\boldsymbol{b}$) will transform in the opposite sense. As expected from the relation in Eq. 6.1, there are three basis vectors per irreducible representation. Any linear combination of the basis vectors will have the symmetry of the irreducible representation. The analysis shows that the moment can in general be orientated along any direction. We find that the basis vectors can in general be complex, whereas magnetic moments must be real vectors. If we consider the sum of the linear basis vectors and their respective complex conjugates, the moment distribution

$\boldsymbol{M}_j$ of the jth atom can be written as,

$$\boldsymbol{M}_j = \sum_{\alpha} \left(C_\alpha \boldsymbol{\psi}_\alpha e^{-\mathrm{i}\boldsymbol{\kappa}\cdot\boldsymbol{\tau}} + C_\alpha^* \boldsymbol{\psi}_\alpha^* e^{\mathrm{i}\boldsymbol{\kappa}\cdot\boldsymbol{\tau}} \right), \tag{6.3}$$

which is equivalent to,

$$\boldsymbol{M}_j = 2 \sum_{\alpha} |C_\alpha| \hat{\boldsymbol{v}}_\alpha \cos\left(\boldsymbol{\kappa}\cdot\boldsymbol{\tau} + \omega_\alpha + \theta_\alpha\right), \tag{6.4}$$

where the basis vectors in a direction $\hat{\boldsymbol{v}}$ can be expressed as $\boldsymbol{\psi} = e^{-\mathrm{i}\omega}\hat{\boldsymbol{v}}$ and the complex coefficient as $C = |C|e^{-\mathrm{i}\theta}$. The phase contribution ω is restricted by the symmetry of the space group whereas θ is a free parameter.

6.5.1 Application of irreducible representation to CuO

The irreducible representations can be applied to magnetic order in the AF1 and AF2 phases of CuO as described in § 6.5. The magnetic representation analysis does not significantly constrain the possible magnetic structures as the spin direction on Cu site can be orientated in an arbitrary direction. Possible collinear, helicoidal and cycloidal arrangements are in principle allowed. However, the relative phases between Cu sites are fixed and this information together with some experimental results will be shown to provide a unique solution to the AF1 and AF2 magnetic structures of CuO. Neutron diffraction experiments described in Refs. [264, 265] show that the commensurate phase below T_{N1} is characterised by a propagation vector $\boldsymbol{q}_{\mathrm{cm}} = (0.5, 0, -0.5)$ and Cu moments lie parallel to the $\boldsymbol{b}$ direction. Helical order is observed in the AF2 phase with magnetic order modulated by $\boldsymbol{q}_{\mathrm{icm}} = (0.506, 0, -0.483)$ propagation vector and moments rotating in the plane containing the real space vectors $\hat{\boldsymbol{b}}$ and $0.48\hat{\boldsymbol{a}} + 0.96\hat{\boldsymbol{c}}$ [265].

From Table 6.5, the phase factor in both the commensurate and incommensurate magnetic structures is given by $\varphi^* = e^{-\mathrm{i}\kappa_z\pi}$. Combining the experimental observations together with magnetic irreducible representation analysis, leads to the possible magnetic structure defined in Table 6.6 projected onto the $\boldsymbol{b}$ and ac-plane containing the moments. The application of the rotational part of the g_4 symmetry operation on the structure in Table 6.6 gives as expected, $R\boldsymbol{\psi} = \pm\varphi\boldsymbol{\psi}$, where the $+$ $(-)$ sign corresponds to the Γ_1 (Γ_2) representation and the translational part of g_4 determines the phase factor φ.

The following analysis is limited to the special case where each basis vector can only have a particular symmetry, i.e. magnetisation component along b or in the ac-plane has either Γ_1 or Γ_2 irreducible representation but not a mixture of Γ_1 and Γ_2 for the same basis vector. The condition that the moments on each of the Cu ions are the same imposes the constraint that the common phase $\theta_b = \pi/4$ for the AF1 magnetic structure.

To correctly describe the AF2 spin structure we set $\theta_b = 0$ and $\theta_{ac} = \pi/2$ so that the spins rotate with a circular envelope, as observed experimentally. For each Cu

	j	$\boldsymbol{M_b}$	$\boldsymbol{M_{ac}}$
Γ_1	1.	$2C\cos(2\pi\boldsymbol{\kappa}\cdot\boldsymbol{\tau}+\theta_b)$	$2C\cos(2\pi\boldsymbol{\kappa}\cdot\boldsymbol{\tau}+\theta_{ac})$
	2.	$2C\cos(2\pi\boldsymbol{\kappa}\cdot\boldsymbol{\tau}+\kappa_z\pi+\theta_b)$	$-2C\cos(2\pi\boldsymbol{\kappa}\cdot\boldsymbol{\tau}+\kappa_z\pi+\theta_{ac})$
	3.	$2C\cos(2\pi\boldsymbol{\kappa}\cdot\boldsymbol{\tau}+\kappa_x\pi+\theta_b)$	$2C\cos(2\pi\boldsymbol{\kappa}\cdot\boldsymbol{\tau}+\kappa_x\pi+\theta_{ac})$
	4.	$2C\cos(2\pi\boldsymbol{\kappa}\cdot\boldsymbol{\tau}+\kappa_x\pi+\kappa_z\pi+\theta_b)$	$-2C\cos(2\pi\boldsymbol{\kappa}\cdot\boldsymbol{\tau}+\kappa_x\pi+\kappa_z\pi+\theta_{ac})$
Γ_2	1.	$2C\cos(2\pi\boldsymbol{\kappa}\cdot\boldsymbol{\tau}+\theta_b)$	$2C\cos(2\pi\boldsymbol{\kappa}\cdot\boldsymbol{\tau}+\theta_{ac})$
	2.	$-2C\cos(2\pi\boldsymbol{\kappa}\cdot\boldsymbol{\tau}+\kappa_z\pi+\theta_b)$	$2C\cos(2\pi\boldsymbol{\kappa}\cdot\boldsymbol{\tau}+\kappa_z\pi+\theta_{ac})$
	3.	$2C\cos(2\pi\boldsymbol{\kappa}\cdot\boldsymbol{\tau}+\kappa_x\pi+\theta_b)$	$2C\cos(2\pi\boldsymbol{\kappa}\cdot\boldsymbol{\tau}+\kappa_x\pi+\theta_{ac})$
	4.	$-2C\cos(2\pi\boldsymbol{\kappa}\cdot\boldsymbol{\tau}+\kappa_x\pi+\kappa_z\pi+\theta_b)$	$2C\cos(2\pi\boldsymbol{\kappa}\cdot\boldsymbol{\tau}+\kappa_x\pi+\kappa_z\pi+\theta_{ac})$

Table 6.6: The magnetic irreducible representations result in the possible magnetic structure for CuO as shown in the table. The helical structure can be resolved into magnetisation along $\boldsymbol{b}$ (M_b) and in the $\boldsymbol{a}$-$\boldsymbol{c}$ (M_{ac}) plane. The moments of atoms outside of the primitive unit cell is found using the C-centering $\boldsymbol{\tau}_c = (0.5, 0.5, 0)$ translation, resulting in an additional phase of $\boldsymbol{\kappa}\cdot\boldsymbol{\tau}_c$ for atoms 3 and 4. The jth atomic positions are 1. $(0.25, 0.25, 0)$, 2. $(0.25, 0.75, 0.5)$, 3. $(0.75, 0.75, 0)$ and 4. $(0.75, 0.25, 0.5)$. The constant factor of $2C$ defines the magnitude of the magnetisation in a given direction whose precise value is not important in the context discussed. The phase factors are set as $\theta_b = \pi/4$ in the AF1 and $\theta_b = 0$ and $\theta_{ac} = \pi/2$ in the AF2 magnetic phases.

site, the magnetic moment along b or in ac-plane can have either Γ_1 or Γ_2 symmetry. This leads to 4 possible magnetic spin structures, as shown in Fig. 6.7. Taking the basis vectors from the same irreducible representation, $M_b^{(1)} \circ M_{ac}^{(1)}$ or $M_b^{(2)} \circ M_{ac}^{(2)}$ is shown schematically in Fig. 6.7. It is therefore evident that in such cases there will be effectively two helical chains, originating from either Cu(1) or Cu(2) inequivalent sites, with opposing senses of rotation. This results in zero net electric polarisation in the unit cell assuming the magnetoelectric coupling depends on the spin current $\boldsymbol{S}_i \times \boldsymbol{S}_j$. The system is 'antiferroelectric' in analogy to antiferromagnetism and no macroscopic electric polarisation is possible for such mixing of basis vectors in CuO.

A polar state is allowed if we consider the $\boldsymbol{b}$-component of the magnetisation to be of Γ_1 and at the same site the ac-component to be of Γ_2 symmetry, or vice versa. In such mixing all the moments in the unit cell will rotate in the same sense. A ferroelectric response will then, in principle, exist. As will be demonstrated in the following sections, only the $M_b^{(1)} \circ M_{ac}^{(2)}$ mixing of basis vectors produces a magnetic structure consistent with the experimental results.

6.5.2 Fourier transform of the magnetisation density

The magnetisation $\boldsymbol{M}$ in unit cell $\boldsymbol{\tau}$ can in general be described by the relation,

$$\boldsymbol{M}(\boldsymbol{r}+\boldsymbol{\tau}) = \boldsymbol{A}(\boldsymbol{r})\cos(\boldsymbol{\kappa}\cdot\boldsymbol{\tau}+\theta(\boldsymbol{r})) + \boldsymbol{B}(\boldsymbol{r})\sin(\boldsymbol{\kappa}\cdot\boldsymbol{\tau}+\theta(\boldsymbol{r})), \tag{6.5}$$

for the case of a single propagation vector $\boldsymbol{\kappa}$ and moments $\boldsymbol{A}(\boldsymbol{r})$ and $\boldsymbol{B}(\boldsymbol{r})$ are along orthogonal directions at positions within the unit cell $\boldsymbol{r}$. In addition there may be a phase dependence accounted for by $\theta(\boldsymbol{r})$. Equivalently, the magnetisation density

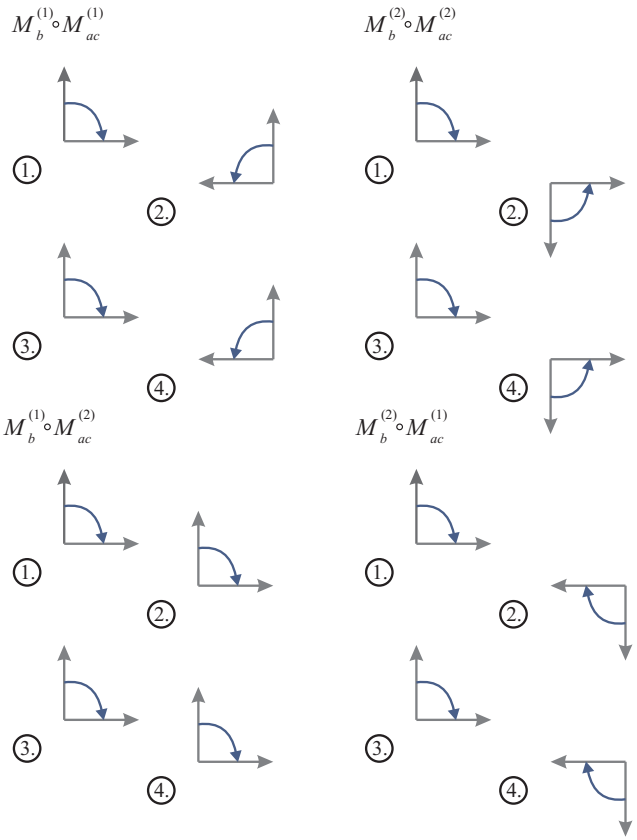

Figure 6.7: Possible magnetic structure of CuO from mixing of irreducible representations. Figure shows schematically the possible magnetic structure of the 4 Cu atoms in the conventional unit cell described by irreducible representations in Table 6.6. The superscript of $M_b^{(i)}$ ($M_{ac}^{(i)}$) defines the Γ_i to which the the $\boldsymbol{b}$ ($\boldsymbol{a}$-$\boldsymbol{c}$) component of helix belongs to. The blue arrows indicate a sense of the rotation of the structure on each Cu site when propagating the magnetic structure into an adjacent unit cell.

can be expressed as

$$\boldsymbol{M}(\boldsymbol{r}+\boldsymbol{\tau}) = \frac{1}{2}\left[\boldsymbol{A}(\boldsymbol{r}) + \mathrm{i}\boldsymbol{B}(\boldsymbol{r})\right] e^{-\mathrm{i}\boldsymbol{\kappa}\cdot\boldsymbol{\tau}-\mathrm{i}\theta(\boldsymbol{r})} + \frac{1}{2}\left[\boldsymbol{A}(\boldsymbol{r}) - \mathrm{i}\boldsymbol{B}(\boldsymbol{r})\right] e^{\mathrm{i}\boldsymbol{\kappa}\cdot\boldsymbol{\tau}+\mathrm{i}\theta(\boldsymbol{r})}, \quad (6.6)$$

which is equivalent to Eq. 6.3 defined previously, hence collecting all the $\boldsymbol{r}$-dependent terms, $\boldsymbol{\Psi}(\boldsymbol{r}) = \frac{1}{2}[\boldsymbol{A}(\boldsymbol{r}) + \mathrm{i}\boldsymbol{B}(\boldsymbol{r})]e^{-\mathrm{i}\theta(\boldsymbol{r})}$, we obtain the relation equivalent to Eq. 2.49,

$$\boldsymbol{M}(\boldsymbol{r}+\boldsymbol{\tau}) = \boldsymbol{\Psi}(\boldsymbol{r})e^{-\mathrm{i}\boldsymbol{\kappa}\cdot\boldsymbol{\tau}} + \boldsymbol{\Psi}^*(\boldsymbol{r})e^{\mathrm{i}\boldsymbol{\kappa}\cdot\boldsymbol{\tau}}. \quad (6.7)$$

The Fourier transform of the magnetisation can then be calculated from $\boldsymbol{M}(\pm\boldsymbol{Q}) = \sum_{\boldsymbol{r}} \boldsymbol{M}(\boldsymbol{r}+\boldsymbol{\tau})e^{\pm\mathrm{i}\boldsymbol{Q}\cdot(\boldsymbol{r}+\boldsymbol{\tau})}$, where the argument of $\boldsymbol{M}$ refers to the sign in the expo-

nential term in the summation,

$$\boldsymbol{M}(-\boldsymbol{Q}) = \left(\sum_{\boldsymbol{r}} \boldsymbol{\Psi}(\boldsymbol{r}) e^{-\mathrm{i}\boldsymbol{Q}\cdot\boldsymbol{r}}\right) \delta(\boldsymbol{G}+\boldsymbol{Q}+\boldsymbol{\kappa}) + \left(\sum_{\boldsymbol{r}} \boldsymbol{\Psi}^*(\boldsymbol{r}) e^{-\mathrm{i}\boldsymbol{Q}\cdot\boldsymbol{r}}\right) \delta(\boldsymbol{G}+\boldsymbol{Q}-\boldsymbol{\kappa}) \tag{6.8}$$

$$\boldsymbol{M}(\boldsymbol{Q}) = \left(\sum_{\boldsymbol{r}} \boldsymbol{\Psi}(\boldsymbol{r}) e^{\mathrm{i}\boldsymbol{Q}\cdot\boldsymbol{r}}\right) \delta(\boldsymbol{G}-\boldsymbol{Q}+\boldsymbol{\kappa}) + \left(\sum_{\boldsymbol{r}} \boldsymbol{\Psi}^*(\boldsymbol{r}) e^{\mathrm{i}\boldsymbol{Q}\cdot\boldsymbol{r}}\right) \delta(\boldsymbol{G}-\boldsymbol{Q}-\boldsymbol{\kappa}) \tag{6.9}$$

where $\boldsymbol{G}$ is the reciprocal lattice vector and has the property $\boldsymbol{\tau}\cdot\boldsymbol{G} = 2\pi$. From these relations, it is trivial to show that when $\boldsymbol{Q} = \boldsymbol{G} - \boldsymbol{\kappa}$, $\boldsymbol{M}(-\boldsymbol{Q}) = \boldsymbol{M}^*(\boldsymbol{Q})$ or that in general $\boldsymbol{M}(-\boldsymbol{Q}) \neq \boldsymbol{M}(\boldsymbol{Q})$. For the case when reflections from the wavevector pair $(\boldsymbol{\kappa}, -\boldsymbol{\kappa})$ superpose $\boldsymbol{Q} = \boldsymbol{Q}'$ where $\boldsymbol{G} - \boldsymbol{\kappa} = \boldsymbol{G}' + \boldsymbol{\kappa}$,

$$\boldsymbol{M}(-\boldsymbol{Q}) = \sum_{\boldsymbol{r}} \left[\boldsymbol{A}(\boldsymbol{r}) \cos\theta(\boldsymbol{r}) + \boldsymbol{B}(\boldsymbol{r}) \sin\theta(\boldsymbol{r})\right] e^{-\mathrm{i}\boldsymbol{Q}\cdot\boldsymbol{r}}. \tag{6.10}$$

6.5.3 Comparison to previous work on determination of the magnetic structure

One of the first neutron diffraction studies of CuO was carried out by Brockhouse [263] on a polycrystalline sample was able to identify only the fundamental reflection which was indexed as $(0.5, 0, -0.5)$. Detailed single crystal neutron scattering measurements reported by Forsyth *et al.* [245] and Yang *et al.* [244] were able to identify the low-temperature $T < T_{\mathrm{N1}}$ (AF1), intermediate-temperature $T_{\mathrm{N1}} < T < T_{\mathrm{N2}}$ (AF2) and paramagnetic $T > T_{\mathrm{N2}}$ (PM) phases in CuO. Strong spin-lattice coupling is observed through changes in the lattice parameters at magnetic phase transitions T_{N1} and T_{N2} [267]. The AF1 and AF2 phases were found to correspond to commensurate and incommensurate phases, respectively. The ordered moment in the AF1 phase was initially constrained to the lower limit of $0.5\,\mu_{\mathrm{B}}$ [263], however further measurements set the moment to be close to $0.69\,\mu_{\mathrm{B}}$ [244, 245] and orientated along $\boldsymbol{b}$.

A detailed analysis of the CuO magnetic structure derived from minimisation of the Hamiltonian and group theory by Aïn *et al.* [265] concluded that the magnetic moments in cell $\boldsymbol{\tau}$ are arranged as given in Table 6.7(a). In the AF2 phase the *ac*-plane component of the magnetisation derives from the same irreducible representation as the component along $\boldsymbol{b}$. From Eq. 6.9 the magnetisation at scattering wavevector $\boldsymbol{Q} = \boldsymbol{\kappa}$ can then be simplified to,

$$\boldsymbol{M}(\boldsymbol{\kappa}) = \sum_{r} \frac{1}{2} \left[\boldsymbol{A}(\boldsymbol{r}) + \mathrm{i}\boldsymbol{B}(\boldsymbol{r})\right] e^{\mathrm{i}\boldsymbol{\kappa}\cdot\boldsymbol{r} - \mathrm{i}\theta(\boldsymbol{r})}. \tag{6.11}$$

Therefore, taking the sum over $\boldsymbol{r}$ in Eq. 6.11 and assuming a spherically symmetric magnetic form factor, the Aïn model predicts zero intensity. This is inconsistent with neutron diffraction measurements. Furthermore, this magnetic structure cannot generate an electric polarisation according to symmetry arguments outlined in § 6.5.1.

(a) Aïn *et al.* model

j	$\boldsymbol{r}_j$	M_b	M_{ac}	θ_j	$\boldsymbol{\kappa}\cdot\boldsymbol{r}_j$
1	$\left(\frac{1}{4},\frac{1}{4},0\right)$	S_0	$-S_0$	0	$\frac{1}{2}\pi\kappa_x$
2	$\left(\frac{1}{4},\bar{\frac{1}{4}},\frac{1}{2}\right)$	$-S_0$	$-S_0$	$\pi\kappa_z$	$\frac{1}{2}\pi\kappa_x+\pi\kappa_z$
3	$\left(\frac{3}{4},\frac{3}{4},0\right)$	$-S_0$	S_0	$\pi\kappa_x$	$\frac{3}{2}\pi\kappa_x$
4	$\left(\frac{3}{4},\frac{1}{4},\frac{1}{2}\right)$	S_0	S_0	$\pi(\kappa_x+\kappa_z)$	$\frac{3}{2}\pi\kappa_x+\pi\kappa_z$

(b) $M_b^{(1)}\circ M_{ac}^{(2)}$

j	$M_b^{(1)}$	$M_{ac}^{(2)}$	θ_j
1	$2C$	$-2C$	0
2	$2C$	$-2C$	$\pi\kappa_z$
3	$2C$	$-2C$	$\pi\kappa_x$
4	$2C$	$-2C$	$\pi(\kappa_x+\kappa_z)$

(c) $M_b^{(2)}\circ M_{ac}^{(1)}$

j	$M_b^{(2)}$	$M_{ac}^{(1)}$	$\theta(\boldsymbol{r}_j)$
1	$2C$	$-2C$	0
2	$-2C$	$2C$	$\pi\kappa_z$
3	$2C$	$-2C$	$\pi\kappa_x$
4	$-2C$	$2C$	$\pi(\kappa_x+\kappa_z)$

Table 6.7: (a) Magnetic structure of CuO in the incommensurate phase according to symmetry analysis by Aïn *et. al* [265]. The helix is defined to lie in the $(\boldsymbol{p},\boldsymbol{q})$ plane, where $\boldsymbol{p}=\hat{\boldsymbol{b}}$ and $\boldsymbol{q}=0.48\hat{\boldsymbol{a}}+0.96\hat{\boldsymbol{c}}$ which corresponds to $\hat{\boldsymbol{p}}\cdot\hat{\boldsymbol{q}}=0$. Panels (b) and (c) show the magnetic structure of CuO in the AF2 phase according to symmetry analysis described in § 6.5.1. The magnetic moment component along $\boldsymbol{b}$ and in the ac-plane are described through mixing of irreducible representations Γ_1 and Γ_2 denoted by $M^{(1)}$ and $M^{(2)}$, respectively. The jth moment is given by, $\boldsymbol{M}_j=M_b^{(n)}(\boldsymbol{r}_j)\boldsymbol{p}\cos(2\pi\boldsymbol{\kappa}\cdot\boldsymbol{\tau}+\theta_j)+M_{ac}^{(m)}(\boldsymbol{r}_j)\boldsymbol{q}\sin(2\pi\boldsymbol{\kappa}\cdot\boldsymbol{\tau}+\theta_j)$.

6.6 Polarised neutron scattering measurements

To examine the effect of an externally applied electric field along the ferroelectric axis, a CuO single-crystal sample of mass 0.175 g was employed. The sample was prepared as described in § 6.2. The CuO piece used was cut to minimise the thickness along $\boldsymbol{b}$ to allow large electric fields to be applied and maximised in surface area normal to $\boldsymbol{b}$, thereby increasing sample volume probed by the neutrons. The surface perpendicular to $\boldsymbol{b}$ was 20.9 mm^2 with thickness of 0.9 mm. In order to examine the crystal using spherical neutron polarimetry the sample has to be very precisely aligned to better than 0.5 °. Initial analysis of the crystal on ORION diffractometer at SINQ, PSI [95] revealed that the sample quality was very high with a secondary grain constituting approximately 3% of the volume fraction present and sufficiently far away in the rocking scans not to pose any problems. The sample was orientated to allow for the inspection of the $\boldsymbol{a}^*$-$\boldsymbol{c}^*$ scattering plane and attached to an Al spacer with Ag apoxy which was attached to a non-magnetic goniometer, as

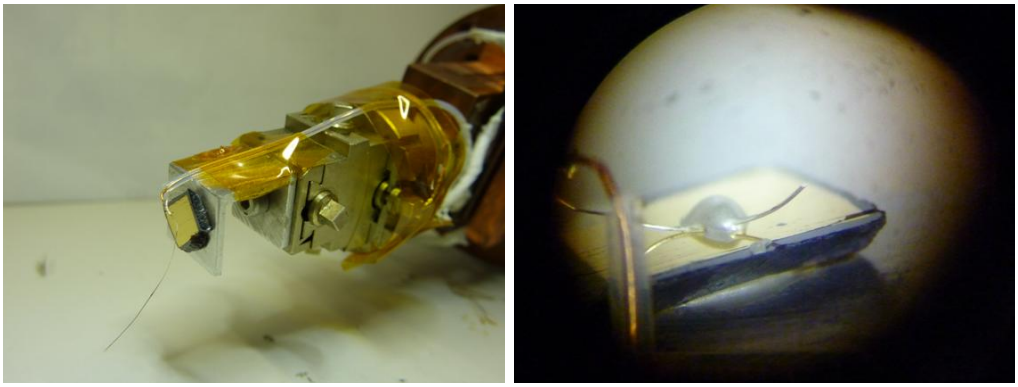

Figure 6.8: Sample setup for spherical neutron polarimetry measurements on MuPAD/TASP. The left panel shows the sample mounted on a goniometer and attached to the sample stick. The right panel is a view of the electrode attached to the surface of the sample by Ag epoxy.

shown in Fig. 6.8. An electrode was attached to the Au surface using Ag epoxy. The entire apparatus was then sealed with In inside an Al vacuum can, which was evacuated. A layer of Cd was wrapped around the outside of the can and held in place by Al to shield the goniometer from the neutron beam and reduce background.

Spherical neutron polarimetry allows us to examine the complete polarisation matrix. Polarisation analysis of CuO was carried out using the MuPAD [76] instrument mounted on TASP, SINQ, PSI [95, 96] with incident neutron wavevector of $1.97\,\text{Å}^{-1}$. We employ the convention where the scattering wavevector is defined as $\boldsymbol{Q} = \boldsymbol{k}_\text{i} - \boldsymbol{k}_\text{f}$. The scattering geometry and theoretical modelling employ the standard coordinate system wherein the x component is defined along the wavevector $\boldsymbol{Q}$, z is perpendicular to the scattering plane (therefore along $\boldsymbol{b}^*$) and y completes the right-handed coordinate system.

The sample was aligned using $(2,0,0)$ and $(0,0,2)$ nuclear Bragg peaks. The lattice parameters were found to be $a = 4.72(2)$ Å and $c = 5.18(1)$ Å with $\beta = 99.54°$ at 218 K. The parameters are in good agreement with the values reported [267] and the small difference could be attributed to not taking the resolution function into consideration. The flipping ratio $R = I_{\alpha\alpha}/I_{\alpha\bar{\alpha}}$, where $I_{\alpha\bar{\alpha}}$ ($I_{\alpha\alpha}$) is the intensity in the (non)-spin-flip channel, was measured on the nuclear reflections and found to be approximately 17, corresponding to 94% beam polarisation efficiency. The polarimetry data presented hereafter has not been corrected for the non-ideal beam polarisation but the models take this effect into account. The background signal in different polarisation channels was measured at positions away from the Bragg peaks and found to be negligible. The signal-to-background ratio in the vicinity of a magnetic peak was found to be of around 200 using unpolarised neutron beam. This gives us confidence that the measured results are of very high quality and corrections for the background are not necessary.

6.6.1 Lessons learned from initial study using polarised neutron analysis

Initial study of the electric field dependence of the domains in the AF2 phase of CuO was attempted at SINQ [95] using polarised neutron analysis setup of MuPAD/TASP [76, 96]. A single crystal CuO sample was attached to a sapphire plate in an alignment to access $(h, 0, l)$ scattering plane. Electrodes were also attached to the sapphire plate above and below the sample but crucially did not make direct contact with the surface of the CuO. An electric potential difference could then be applied across the gap containing CuO and parallel to the $\boldsymbol{b}$-axis. Sapphire was chosen as it is a poor electric conductor but a relatively good thermal conductor. The arrangement was then placed inside a vacuum Al can and evacuated to avoid dissociation of He gas and thereby allow the application of large electric fields. The inherent disadvantage of this experimental setup is that exchange gas is at a low pressure inside the Al can and therefore cooling and warming rates are very slow as thermal coupling to the cryostat is low.

The chiral term P_{xy} was monitored during different heating and cooling scans. Large changes in P_{xy} were observed, however, they did not appear to be correlated with the direction or magnitude of the applied electric field. The domain population appeared to vary randomly on each entry into the incommensurate phase.

The absence of electric field switching was rather puzzling as the applied electric field was sufficiently large for the effect to be observed according to published results [42]. The likely explanation for the failure of the experiment was due to presence of free electrons in CuO. The potential difference across the sample created surface charges which effectively screened the bulk of the sample from the electric field. This problem was overcome by applying the electrodes directly to the surface of the sample such that the charge on the surface could be removed. The results of the experiment using this sample environment are discussed § 6.6.4.

6.6.2 Polarisation matrix determination

Using the group theory analysis outlined in § 6.5, we can therefore describe the magnetic structure and compare it to experimental results. To begin with an account of the means of calculating the polarisation matrix is given which forms the basis for analysis of polarimetry data in the AF1 and AF2 magnetic phases. All the measurements on MuPAD have been carried out looking at the $\boldsymbol{q}_{\text{icm}}$ or $\boldsymbol{q}_{\text{cm}}$ position in reciprocal space. Taking the expression defined in Eq. 6.9 for $\boldsymbol{Q} = \boldsymbol{\kappa}$, we find the Fourier transform of the magnetisation $\boldsymbol{M}(\boldsymbol{Q})$ as,

$$\boldsymbol{M}(\boldsymbol{Q}) = \frac{1}{2}\sum_{\boldsymbol{r}} \left[\boldsymbol{A}(\boldsymbol{r}) + \mathrm{i}\boldsymbol{B}(\boldsymbol{r})\right] e^{\mathrm{i}\boldsymbol{Q}\cdot\boldsymbol{r} - \mathrm{i}\theta(\boldsymbol{r})} = \boldsymbol{A}(\boldsymbol{Q}) + \mathrm{i}\boldsymbol{B}(\boldsymbol{Q}), \tag{6.12}$$

where $\boldsymbol{A}(\boldsymbol{r})$ and $\boldsymbol{B}(\boldsymbol{r})$ are orthogonal components with phase $\theta(\boldsymbol{r})$ of magnetic moment at position $\boldsymbol{r}$ within the unit cell. Equivalently, the magnetisation can be resolved into Fourier terms $\boldsymbol{A}(\boldsymbol{Q})$ and $\boldsymbol{B}(\boldsymbol{Q})$ which in general are complex. The

magnetic interaction vector $\boldsymbol{M}_\perp$ is the component of $\boldsymbol{M}(\boldsymbol{Q})$ perpendicular to the scattering wavevector $\boldsymbol{Q}$, given by $\boldsymbol{M}_\perp(\boldsymbol{Q}) = \hat{\boldsymbol{Q}} \times \boldsymbol{M}(\boldsymbol{Q}) \times \hat{\boldsymbol{Q}}$, and related to $\boldsymbol{A}(\boldsymbol{Q})$ and $\boldsymbol{B}(\boldsymbol{Q})$ as,

$$\boldsymbol{M}_\perp(\boldsymbol{Q}) = \boldsymbol{A}_\perp(\boldsymbol{Q}) + \mathrm{i}\boldsymbol{B}_\perp(\boldsymbol{Q}), \tag{6.13}$$

where in the scattering geometry employed in the polarised neutron experiment, $\boldsymbol{A}_\perp(\boldsymbol{Q})$ is the projection of the $\boldsymbol{A}(\boldsymbol{Q})$ Fourier term onto $\hat{z}$, which is perpendicular to $\boldsymbol{Q}$ and parallel to the $\boldsymbol{b}^*$-axis. The $\boldsymbol{B}_\perp(\boldsymbol{Q})$ component is defined to be projected onto the $\hat{y}$ axis and is both perpendicular to $\boldsymbol{Q}$ and in the scattering plane.

The Pauli spin matrices are defined for a spin-1/2 particle to be,

$$\sigma_x = \begin{pmatrix} 0 & 1 \\ 1 & 0 \end{pmatrix}, \qquad \sigma_y = \begin{pmatrix} 0 & -\mathrm{i} \\ \mathrm{i} & 0 \end{pmatrix}, \qquad \sigma_z = \begin{pmatrix} 1 & 0 \\ 0 & -1 \end{pmatrix}, \tag{6.14}$$

where the eigenstates of σ_z are $|\uparrow_z\rangle = (1,0)$ and $|\downarrow_z\rangle = (0,1)$ in the spinor representation and correspond to spins pointing either parallel or antiparallel to z, the corresponding eigenstates for x, y and z are listed below,

$$\begin{aligned} |\uparrow_x\rangle &= \frac{1}{\sqrt{2}}\begin{pmatrix} 1 \\ 1 \end{pmatrix}, & |\uparrow_y\rangle &= \frac{1}{\sqrt{2}}\begin{pmatrix} 1 \\ \mathrm{i} \end{pmatrix}, & |\uparrow_z\rangle &= \begin{pmatrix} 1 \\ 0 \end{pmatrix}, \\ |\downarrow_x\rangle &= \frac{1}{\sqrt{2}}\begin{pmatrix} 1 \\ -1 \end{pmatrix}, & |\downarrow_y\rangle &= \frac{1}{\sqrt{2}}\begin{pmatrix} 1 \\ -\mathrm{i} \end{pmatrix}, & |\downarrow_z\rangle &= \begin{pmatrix} 0 \\ 1 \end{pmatrix}. \end{aligned} \tag{6.15}$$

A general state is the linear combination of spin-up and spin-down states along z. An incident neutron can be considered to be a dipolar moment which experiences a magnetic field inside the sample. The Fourier transform of this interaction potential is $V(\boldsymbol{Q}) \propto \boldsymbol{\sigma} \cdot \boldsymbol{M}_\perp(\boldsymbol{Q})$, where the neutron only senses the perpendicular component of the magnetisation inside the sample. Therefore, using the convention previously defined, the interaction potential may be expressed as,

$$\boldsymbol{\sigma} \cdot \boldsymbol{M}_\perp(\boldsymbol{Q}) = \begin{pmatrix} A_\perp & B_\perp \\ -B_\perp & -A_\perp \end{pmatrix}. \tag{6.16}$$

Finally, the polarisation matrix $P_{\alpha\beta}$ where a neutron with initial spin state $|\beta\rangle$ (or spin-flip state $|\bar{\beta}\rangle$) given in Eq. 6.15 scatters from the interacting potential defined in Eq. 6.16 into a final state $|\alpha\rangle$ is found as,

$$P_{\alpha\beta} = \frac{|\langle\alpha|\boldsymbol{\sigma} \cdot \boldsymbol{M}_\perp|\beta\rangle|^2 - |\langle\alpha|\boldsymbol{\sigma} \cdot \boldsymbol{M}_\perp|\bar{\beta}\rangle|^2}{|\langle\alpha|\boldsymbol{\sigma} \cdot \boldsymbol{M}_\perp|\beta\rangle|^2 + |\langle\alpha|\boldsymbol{\sigma} \cdot \boldsymbol{M}_\perp|\bar{\beta}\rangle|^2}, \tag{6.17}$$

where the cross-section $I_{\alpha\beta} = |\langle\alpha|\boldsymbol{\sigma}\cdot\boldsymbol{M}_\perp|\beta\rangle|^2$ can be measured in a polarised neutron scattering experiment and the weighted difference between non-spin-flip and spin-flip channels compared to magnetic structure models. Using this nomenclature the polarisation matrix in the absence of nuclear interference and the special case of a

single domain is,

$$P = \begin{pmatrix} -1 & 0 & 0 \\ H & -K & L \\ H & L & K \end{pmatrix} \tag{6.18}$$

$$\begin{aligned} HD &= A_\perp^* B_\perp + A_\perp B_\perp^*, \\ KD &= A_\perp^2 - B_\perp^2, \\ LD &= \mathrm{i}\left(A_\perp^* B_\perp - A_\perp B_\perp^*\right), \\ D &= A_\perp^2 + B_\perp^2. \end{aligned} \tag{6.19}$$

The precession of the neutron moment about an internal magnetic field generates a spin-flip state resulting in $P_{xx} = -1$ when measured on a magnetic Bragg peak. The existence of a non-zero 'chiral' term H in the polarisation matrix implies a non-collinear magnetic structure that is, by definition, constructed from orthogonal, out-of-phase components, such as a helix or cycloid. Therefore, $H = 0$ in the collinear AF1 structure of CuO, and in the AF2 phase, left- and right-handed chiral domains will give $H < 0$ and $H > 0$, respectively. Equivalently, if we measure the P_{yx} and P_{zx} elements on a magnetic reflection we can determine the relative proportions of the two chiral domains.

The parameters H and K can be calculated from Eqs. 6.19 for a general helicoidal magnetic structure. For the particular case when the spins rotate with a circular envelope in a plane perpendicular to $\boldsymbol{\kappa}$, the values for the reflection $\boldsymbol{Q} = \boldsymbol{\kappa}$ are $H = \pm 1$ and $K = 0$. In the AF2 phase of CuO, the propagation vector $\boldsymbol{q}_{\mathrm{icm}}$ is not perpendicular to the plane of rotation of the spins, but rather lies at an angle of 107° to it. For $\boldsymbol{Q} = \boldsymbol{\kappa}$ this results in a small but non-zero value of K, and a magnitude of H which is slightly less than 1 for a single chiral domain.

It is not possible to extract the absolute magnitude of the magnetic moment on a Cu ion. Therefore, without a loss in generality it is possible to transform $A_\perp = \cos(\psi)e^{\mathrm{i}\phi_A}$ and $B_\perp = \sin(\psi)e^{\mathrm{i}\phi_B}$ such that the projected magnetisation $\boldsymbol{M}(\boldsymbol{Q})$ lies at an angle ψ in the yz plane and there is a phase difference $\phi_A - \phi_B$ between components along y and z. The elements in the matrix can be understood in terms of these relations such that Eq. 6.18 becomes,

$$\begin{aligned} H &= \cos(\phi_A - \phi_B)\sin 2\psi, \\ K &= \cos 2\psi, \\ L &= \sin(\phi_A - \phi_B)\sin 2\psi. \end{aligned} \tag{6.20}$$

In general, the relation,

$$H^2 + K^2 + L^2 = 1, \tag{6.21}$$

will hold for a magnetic reflection of a single domain. The presence of domains will however generate an additional source for depolarisation. In the case of domains in CuO related to each other by a spatial inversion, the H and L terms in the matrix

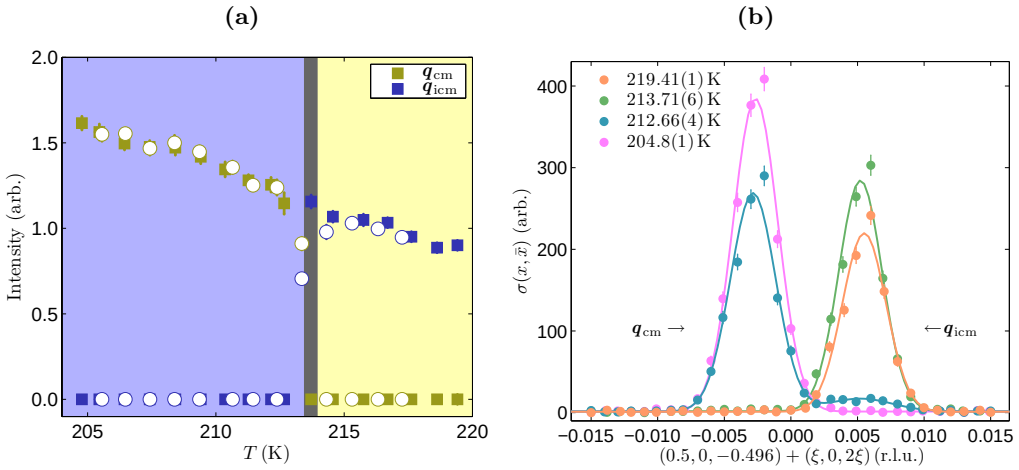

Figure 6.9: Temperature evolution of magnetism close to $T_{\rm N1}$. (a) Temperature dependence of the $\boldsymbol{Q}$-integrated intensity of the magnetic Bragg peaks at commensurate ($\boldsymbol{Q} = \boldsymbol{q}_{\rm cm}$) and incommensurate ($\boldsymbol{Q} = \boldsymbol{q}_{\rm icm}$) positions. The full symbols (□) denote the measurements carried out on cooling, conversely the open symbols (○) are measurements done on warming. The grey line shows the sharp change in slope at $T_{\rm N1}$ as found from magnetic susceptibility measurements. (b) Typical $\boldsymbol{Q}$ scans in the $x\bar{x}$ channel used to construct panel (a) close to $T_{\rm N1}$. The cut through reciprocal space was made along wavevector $\boldsymbol{Q} \approx \boldsymbol{q}_{\rm cm} + \xi(\boldsymbol{q}_{\rm icm} - \boldsymbol{q}_{\rm cm})$. Solid lines show Gaussian lineshapes acting as a guide to the eye.

will vanish.

The neutron-nucleus interaction potential does not contain operators which act on the neutron spin and therefore the spin state will be preserved. The polarisation matrix for purely nuclear scattering is then $P_{\alpha\beta} = \delta_{\alpha\beta}$. This property allows for polarised neutron scattering to unambiguously separate the coherent nuclear and magnetic contributions to the scattering cross-section. [1] Tuning of the relative values of magnetisation and nuclear scattering amplitudes makes the production of polarised neutrons possible by reflections from single-crystals [56]. In addition, experimentally it is never possible to achieve 100% neutron beam polarisation incident on a sample and analogously maintain the beam after scattering with the sample due to stray magnetic fields. However, by measuring reflections which are known to be of purely magnetic or nuclear origin it is possible to make corrections for this effect for each polarisation channel. This is quantified by a flipping ratio, defined for a nuclear Bragg peak as the ratio of the scattering intensity measured in the non-spin-flip to spin-flip channel, $R = I_{\alpha\alpha}/I_{\alpha\bar{\alpha}}$.

6.6.3 Experimental results

After the initial setup of sample alignment, we checked the positions of the magnetic reflections in the $x\bar{x}$-channel which contains purely magnetic contribution to

[1] Nuclear spin incoherent scattering is negligible in the measurements performed on CuO.

the signal. The magnetic peak at 200 K, in the AF1 phase, was found to be centred on $\boldsymbol{Q} = (0.497(2), 0, -0.5041(1))$. Upon warming into the multiferroic phase (AF2) at 215 K, the structure becomes modulated by wavevector corresponding to $\boldsymbol{Q} = (0.5075(3), 0, -0.4865(2))$. The coordinates in reciprocal space are indexed with respect to the real space lattice belonging to $C2/c$ space group with lattice parameters measured at 218 K. The peak positions closely match the previously reported values for propagation vectors $\boldsymbol{q}_{\mathrm{cm}} = (0.5, 0, -0.5)$ (AF1) and $\boldsymbol{q}_{\mathrm{icm}} = (0.506, 0, -0.483)$ (AF2) [264, 265]. No magnetic order was observed above 230 K in the paramagnetic phase (PM).

Figure 6.9 shows the temperature evolution of the magnetic order close to the AF1-AF2 phase transition. The scans were recorded along the line in reciprocal space connecting wavevectors associated with magnetic order in the AF1 and AF2 phases, $\boldsymbol{Q} = \boldsymbol{q}_{\mathrm{cm}}$ and $\boldsymbol{Q} = \boldsymbol{q}_{\mathrm{icm}}$ in the $x\bar{x}$ channel. Only a magnetic signal can contribute to this polarisation channel. The magnetic phase transition at $T_{\mathrm{N1}} = 213.7$ K, found from bulk magnetisation measurements in § 6.3, closely coincides with the abrupt change in the magnetic structure. The integrated intensity of the peaks is found to slowly increase with decreasing temperature as the size of the ordered magnetic moment increases – Fig. 6.9(a). The trend is very similar to analogous scans already reported [244, 245]. However, Yang *et al.* [244] also found significant hysteresis around the T_{N1} transition – the phase transition was shifted by ~ 5 K to a lower temperature during measurements on cooling compared to those on warming. This would be expected from a first-order transition and was attributed so by the authors. We do not find the same behaviour in our neutron data. The transition seems to appear at the same temperature on warming and cooling runs. Careful measurements of this effect were confirmed by SQUID magnetometery with a measuring field of 1000 Oe. Using very slow heating and cooling rates of 0.01 K/min, the transition was found to be the same to within 0.1 K. The particularly sharp nature of the transition is evident in Fig. 6.9(b) where the commensurate magnetic peak at $\boldsymbol{Q} = \boldsymbol{q}_{\mathrm{cm}}$ becomes incommensurate $\boldsymbol{Q} = \boldsymbol{q}_{\mathrm{icm}}$ within a very small temperature range. This demonstrates the first-order nature of T_{N1} phase transition. Measurements at higher and lower temperatures show that there is no noticeable change in peak positions in the temperature range of interest in the experiment.

6.6.3.1 Commensurate magnetic structure, AF1

Commensurate, antiferromagnetic AF1 magnetic phase observed below T_{N1} contains moments along $\boldsymbol{b}$ with no magnetic moment in the ac-plane. Indeed, polarised neutron scattering measurements constrain the moment in the ac-plane to be less than 5% of the ordered moment along $\boldsymbol{b}$ [264]. According to representation analysis of magnetic structure of CuO, there are 2 possible structures corresponding to Γ_1 and Γ_2 as shown in Table 6.6. The inversion operation in the group G_0 changes the propagation vector $\boldsymbol{q}_{\mathrm{cm}}$. This results in a $\boldsymbol{\kappa}$-domain described by propagation wavevector $-\boldsymbol{q}_{\mathrm{cm}}$ which is energetically equivalent but distinguishable from the

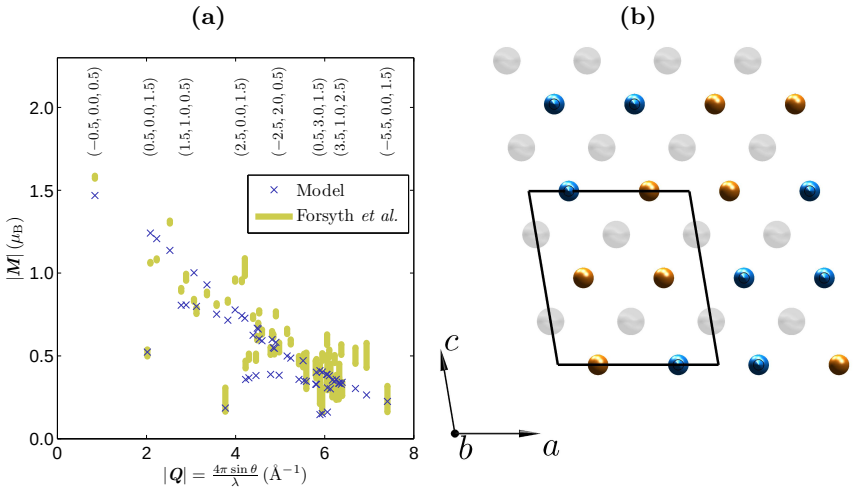

Figure 6.10: Magnetic structure in the commensurate magnetic phase AF1. (a) The calculation corresponds to the Γ_1 irreducible representation with moments along $\boldsymbol{b}$. A spherically symmetric magnetic form factor for Cu^{2+} is assumed together with a moment of $0.76\,\mu_B$ per Cu site. The measured single-crystal data were recorded by Forsyth *et al.* [245]. (b) Proposed magnetic and nuclear structure of CuO in the $\boldsymbol{a}$-$\boldsymbol{c}$ plane. The black outline shows the conventional unit cell and the colors denote the orientation of the moments on Cu sites. The O atoms are plotted in grey.

symmetry of the lattice.

Calculation of the magnetic structure factor based on Γ_1 irreducible representation is shown in Fig. 6.10. In order to compare the theoretical model with the experimental data recorded for 59 magnetic reflections by Forsyth *et al.* [245], one has to make assumptions about the magnetic form factor and magnetic moment size. Previous measurements in the commensurate phase find in agreement a value of the magnetic moment on each Cu site of $0.69\,\mu_B$ [244, 245]. The lowest order approximation to the form factor is spherically symmetric, based on this, the model predicts the structure factors plotted in Fig. 6.10(a). The poor goodness of fit ($\chi^2_\nu = 119$) is in fact comparable to fit obtained by Forsyth *et al.* [245] ($\chi^2_\nu = 139$) under the same assumptions. A slight improvement in the quality of fit ($\chi^2_\nu = 88$) is possible by setting the moment to be $0.76\,\mu_B$ on each Cu ion. Extinction and self absorption effects will also be important but it is not clear from Ref. [245] to what extent this was taken into account. The projection of the magnetisation by the same authors shows that the moment on Cu is not spherically symmetric, but extends in the $[1, 0, 0]$ direction. A small amount of the magnetic moment is found to reside on the O^{2-} sites. Taking the moment distribution into account has been shown to give a significant improvement to the goodness of the fit ($\chi^2_\nu = 9$) [245]. However, this was done ad hoc by adding many different components of the spherical harmonics to obtain a fit. A more realistic model is to consider the $3d$ electron density of Cu^{2+} in a $d_{x^2-y^2}$ orbital whose Fourier transform will exhibit considerable anisotropy resulting in a magnetic form factor dependence on direction as well

magnitude of $\boldsymbol{Q}$. The plane of the orbital has four-fold symmetry and these lobes extend along orthogonal directions connecting Cu to the nearest and next-nearest O atoms. Surprisingly, however, no improvement in the fit quality was achieved under these assumptions compared to the spherically symmetric form factor.

Polarised neutron diffraction partly overcomes this difficulty as by taking the ratio of intensities, we lose information of channel independent multiplication factors in the magnetic structure factor. Measurements of the full polarisation matrix at 200 K,

$$P_{\text{measured}} = \begin{pmatrix} -0.839(9) & -0.048(17) & 0.105(17) \\ 0.075(18) & -0.848(9) & -0.034(17) \\ 0.033(17) & -0.036(17) & 0.854(9) \end{pmatrix},$$

show that only the diagonal terms are non-zero within experimental error and the polarisation in the z channel is not spin-flipped. It is unclear what the origin of the anomalously large P_{xz} term is but could be due to slight misalignment of the crystal. The matrix is representative of measurements at other temperatures in the AF1 phase that were obtained in our measurements. Previous polarised neutron scattering experiments have shown that the polarisation matrices in the AF1 phase in the $\boldsymbol{a}^*$-$\boldsymbol{c}^*$ scattering plane appear to be the same, that is in the ac-plane the magnetic structure looks the same [264]. Hence, these measurements place an upper bound on the possible moment in the ac-plane to 3% of the total moment. Using Γ_1 irreducible representation presented in Table 6.6 for M_b, one can simulate the polarisation matrix at $\boldsymbol{Q} = \boldsymbol{q}_{\text{cm}}$,

$$P_{\text{model}} = \begin{pmatrix} -0.846 & 0.000 & 0.000 \\ 0.000 & -0.846 & 0.000 \\ 0.000 & 0.000 & 0.846 \end{pmatrix}.$$

A correction is made for the loss of the beam polarisation due to external sources assuming a spin-flip ratio of 12, corresponding to 92% beam polarisation efficiency. The symmetry analysis produces a magnetic structure consisting of three Cu atoms with an identical direction and magnitude and a forth Cu atom with a moment of the same magnitude but in the opposite direction within the conventional unit cell, as shown in Fig. 6.10(b). This forms a stripe-like periodic arrangement of moments where spins at the same position in $\boldsymbol{b}$ are antiferromagnetically arranged along the Cu–O–Cu chain direction $[1, 0, \bar{1}]$. Previous neutron diffraction studies of single-crystal and powder samples of CuO come to the same conclusion based on their experimental evidence [244, 245, 266].

Turning to the Γ_2 representation, we find that neither the unpolarised diffraction [245] nor the polarimetry data [264] can be fitted. Hence, only the Γ_1 representation appears to describe our data.

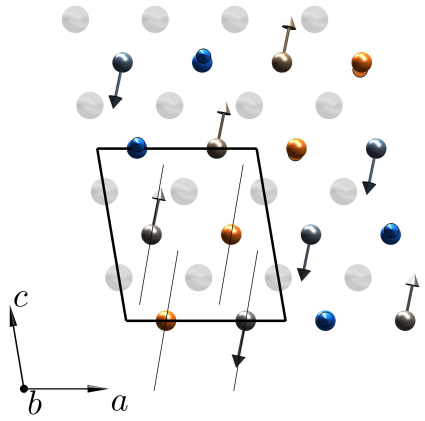

Figure 6.11: Helical magnetic order in the AF2 phase. Magnetic moment arrangement shown in the *ac*-plane in the incommensurate phase. The structure is based on the $M_b^{(1)} \circ M_{ac}^{(2)}$ representation wherein the magnetisation components along $\boldsymbol{b}$ and in *ac*-plane are derived from Γ_1 and Γ_2 irreducible representations, respectively. The O atoms are shown in grey and the Cu atoms are coloured such that to represent component of magnetisation along $\boldsymbol{b}$. The moments lie in the planes indicated by the lines going through the atoms, which contain the $\hat{\boldsymbol{b}}$ and $0.48\hat{\boldsymbol{a}} + 0.96\hat{\boldsymbol{c}}$ vectors. The AF2 structure has two domains of opposite handedness. The left-handed domain is shown here.

6.6.3.2 Incommensurate magnetic structure, AF2

In trying to model the incommensurate AF2 phase using the group theory approach, we must consider the two possible magnetic structures obtained from irreducible representations in Table 6.6 which allow for a polar state to develop. The magnetic structure deduced from mixing of the irreducible representations is shown in Table 6.7(b) and 6.7(c) with magnetic moment projected along axes defining the plane of the rotation. Assuming the M_b and M_{ac} components can each be described by a single irreducible representation, Γ_1 or Γ_2, there are four possible magnetic structures which we denote by $M_b^{(n)} \circ M_{ac}^{(m)}$. These structures are chiral, so each has two domains of opposite handedness related by spatial inversion. When the b and ac magnetic components belong to the same irreducible representation, i.e. $M_b^{(1)} \circ M_{ac}^{(1)}$ or $M_b^{(2)} \circ M_{ac}^{(2)}$, this corresponds to a spin arrangement in which the spins on sites 1 and 3 rotate in the opposite sense along the a axis to those on sites 2 and 4. This results in zero net electric polarisation in the unit cell assuming the magnetoelectric coupling depends on the spin current $\boldsymbol{S}_1 \times \boldsymbol{S}_2$. The two magnetic structures with different symmetry for the b and ac magnetic components ($M_b^{(1)} \circ M_{ac}^{(2)}$ or $M_b^{(2)} \circ M_{ac}^{(1)}$) do have a net electric polarisation in the spin current model.

Further evidence against a magnetic structure originating from the same irreducible representation for M_b and M_{ac} comes from the polarimetry data recorded in the incommensurate phase by Brown *et al.* [264] for 7 magnetic Bragg peaks. The structure $M_b^{(1)} \circ M_{ac}^{(1)}$ produces a fit whose goodness of fit is $\chi^2_\nu \approx 180$ whilst basis vectors corresponding to the Γ_2 representation give $\chi^2_\nu \approx 870$. On comparison,

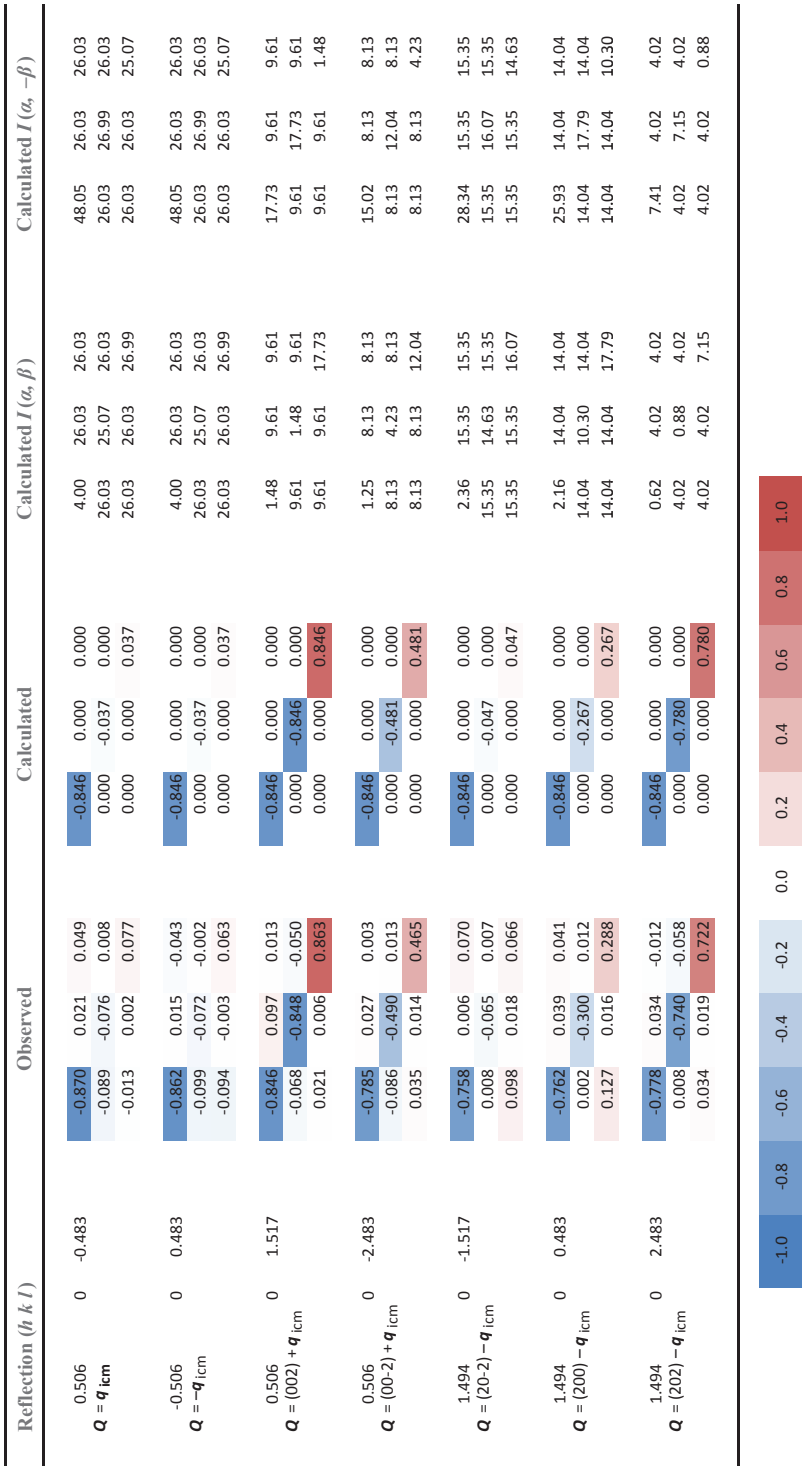

Table 6.8: Table to show the comparison between the measured polarisation matrices recorded by Brown *et al.* [264] and calculation based on the $M_b^{(1)} \circ M_{ac}^{(2)}$ model. The model fits the data with a goodness-of-fit of $\chi^2_\nu = 5.4$. The calculated intensity I in the spin-flip (α, β) and non-spin-flip $(\alpha, -\beta)$ channel is given in units of barns. The colour scale denotes the magnitude of the $P(\alpha, \beta)$ components, ranging from -1 to $+1$.

the $M_b^{(1)} \circ M_{ac}^{(2)}$ structure gives excellent agreement to the polarisation matrices as shown in Table 6.8. The simulation includes the depolarisation effect by the domains which are weighted equally, hence the terms H (from Eq. 6.18) are equal to zero for all reflections. Measurements of the polarisation matrix at $\boldsymbol{Q} = (002) + \boldsymbol{q}_{\text{icm}}$ contain only non-zero terms along the diagonal. The components $P_{xx} = P_{yy} \approx -0.85$ and $P_{zz} = 0.85$ indicate that only magnetisation along $\boldsymbol{b}^*$ (equivalently z) is causing a spin flip. The magnitude of $P_{\alpha\alpha}$ is not ± 1 due to non-ideal beam polarisation and is taken account in the model by assuming a flipping ratio of 12. From this matrix, we can therefore ascertain that the rotation plane must lie very close to the plane defined by reciprocal space wavevectors $(002) + \boldsymbol{\kappa}$ and $\boldsymbol{b}^*$. The experimental polarisation matrices are found to have a decreasing component P_{xx} with larger $\boldsymbol{Q}$ which cannot be accounted for by the model. This was attributed to significant unpolarised background which affects weaker reflections [264]. Measurements of the polarisation matrix at $\boldsymbol{Q} = \boldsymbol{q}_{\text{icm}}$, which is nearly perpendicular to the rotation plane of the moments, shows that only the P_{xx} contains the full polarisation. The small values of P_{yy} and P_{zz} are related to the fact that magnetisation along y and z axes are almost equal. A non-zero value is expected as the projection of $\boldsymbol{B}$ on z is such that $B_\perp / A_\perp = 0.96$. Further refinement of the magnetic structure is possible by allowing the domain population to vary slightly and lift the restriction of a circular envelope of moment rotation as proposed by Brown *et al.* [264]. However, the improvement in the fit quality in such case is negligible and therefore to a good approximation, a circular envelope is sufficient to describe the magnetic structure. Under these assumptions, the magnetic structure $M_b^{(1)} \circ M_{ac}^{(2)}$ gives a fit of $\chi^2_\nu = 5.4$.

Therefore, we obtain a magnetic structure illustrated in Fig. 6.11 for a left-handed domain whose propagation wavevector is given by $\boldsymbol{q}_{\text{icm}}$. Neglecting the small incommensurate component of the magnetic structure, we find stripes of magnetic moments. The moments along $[1, 0, 1]$ are found parallel to one another. The structure is modulated antiferromagnetically along $[1, 0, \bar{1}]$, with moments on different stripes related by a displacement of $[0, 0.5, 0.5]$, found almost orthogonal to each other. This is precisely the magnetic spin configuration predicted by *ab initio* calculations for the AF2 phase in CuO and predict the emergence of ferroelectricity in the AF2 phase [253, 257]. The antiferromagnetic exchange interaction along $[1, 0, \bar{1}]$ path is predicted to be around 5 times larger than any other competing interactions. In both studies, the magnetic structure is found to be stabilised by the inverse Dzyaloshinskii-Moriya interaction. Rather surprisingly, the small incommensurability in the AF2 phase is not important to the emergence of the ferroelectricity, whereas non-collinearity plays a crucial role.

6.6.4 Electric field control of domains in CuO

The preceding sections demonstrate that the group theoretical approach to deriving a magnetic structure of CuO in the AF1 and AF2 phases provides magnetic structures in excellent agreement with the reported experimental results. This gives us confidence in applying these models to look at the switching of the chiral domain

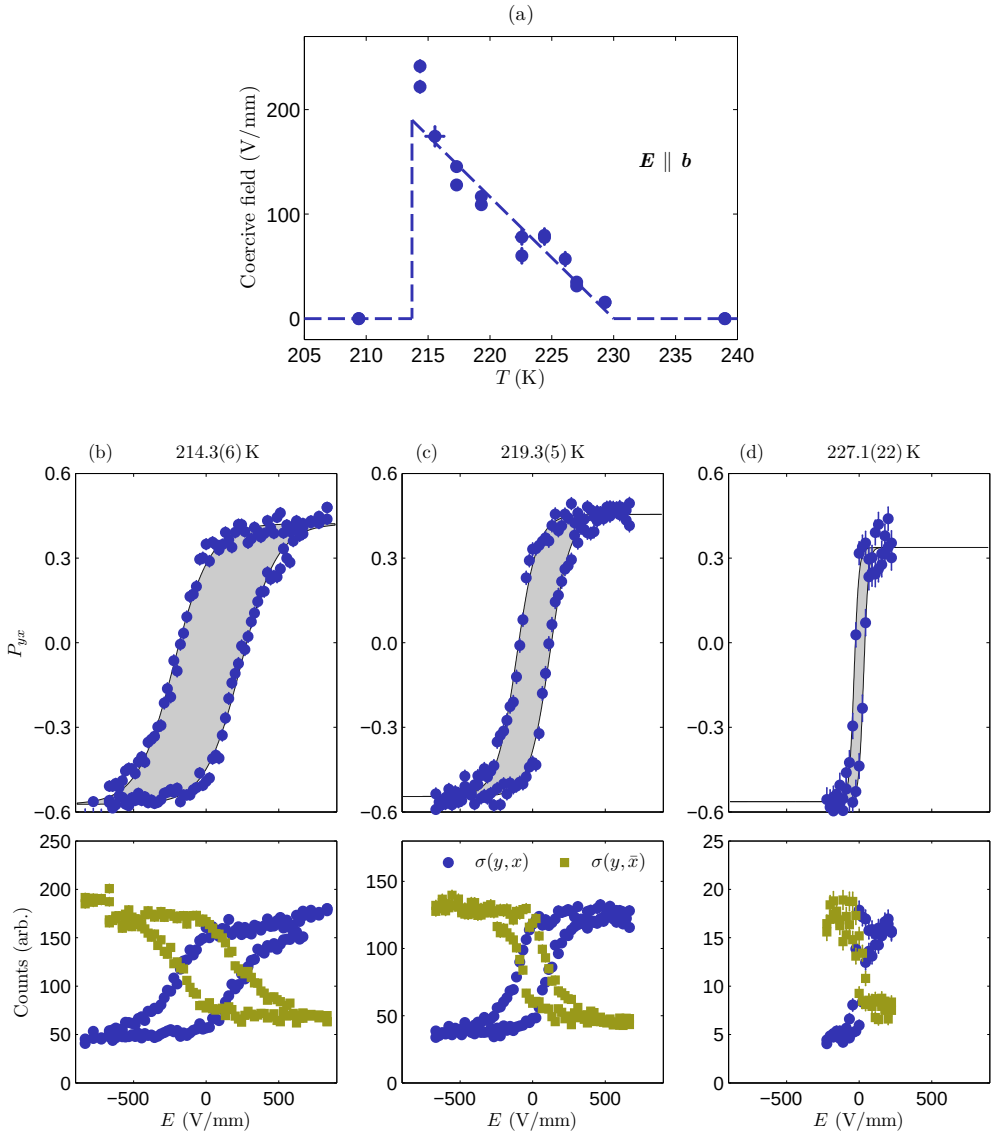

Figure 6.12: Electric field dependence of the chiral P_{yx} polarisation matrix term. Panel (a) shows the temperature dependence of the coercive field measured by neutron polarimetry. Electric field sweeps at fixed temperatures of (a) 214.3(6) K, (b) 219.3(6) K and (c) 227.1(22) K. Upper panels show the variation in the P_{yx} component as a function of applied electric field E swept from +830 V/mm to −830 V/mm and back to +850 V/mm. The lower panels correspond to normalised counts at $\boldsymbol{Q} = \boldsymbol{q}_{\text{icm}}$ of the yx scattering cross-section σ (●) and its complimentary spin-flip component $y\bar{x}$ (■) as a function of applied field.

population in CuO when an *in situ* electric field is applied. The symmetry of the space group only allows two chiral domains related to each other by an inversion. For consistency, domain D1 is defined as having a propagation vector $+\boldsymbol{q}_{\mathrm{icm}}$ and domain D2 a propagation vector of $-\boldsymbol{q}_{\mathrm{icm}}$. In the cycloidal scenario, proposed by Kimura *et al.* [42], D1 corresponds to a clockwise propagating cycloid whose propagation wavevector is $\boldsymbol{q}_{\mathrm{icm}} - \boldsymbol{q}_{\mathrm{cm}}$. The second domain D2 consists of spins rotating in the opposite sense to D1. As discussed previously in § 6.6.2, neutron polarimetry can be used to determine the relative proportions of the chiral domains in CuO. Any changes in domain population induced by an applied electric field will affect the P_{yx} and P_{zx} elements in the polarisation matrix while leaving the other elements unchanged.

The change in P_{yx} when an electric field is applied is shown in Fig. 6.12(b)-(d) in the multiferroic AF2 phase. A hysteresis is found to develop when the sample is cooled below $T_{\mathrm{N2}} \approx 230\,\mathrm{K}$, shown in Fig. 6.12(d). The component P_{yx} was measured as a function of the electric field at 214.3(6), 219.3(5) and 227.1(22) K. We find that by sweeping the electric field, which is in the opposite direction to the crystallographic $\boldsymbol{b}$ direction, from $+830\,\mathrm{V/mm}$ to $-830\,\mathrm{V/mm}$ and back to $+830\,\mathrm{V/mm}$ we observe a change in sign and magnitude of P_{yx}. It follows that the electric field must be coupled to the chiral magnetic domains. The magnitude of P_{yx} in the AF2 phase never reaches the maximal value of around ± 1 as expected for the case of a single magnetic domain. Even at large electric fields a significant depolarisation is observed such that $|P_{yx}| < 0.6$. To verify that the electric field switching of the magnetic domains exists only in the incommensurate AF2 phase, hysteresis loops were also made at 240 K (centred on $\boldsymbol{q}_{\mathrm{icm}}$) and 210 K (centred on $\boldsymbol{q}_{\mathrm{icm}}$ and $\boldsymbol{q}_{\mathrm{cm}}$). These measurements showed field-independent behaviour of P_{yx}, confirming that these phases do not possess a magnetoelectric coupling.

The coercive field, defined as the electric field at which the chiral domains are equally populated is shown in Fig. 6.12(a). This is proportional to the width of the hysteresis loops shown in Figs. 6.12(b)-(d). The coercive field in CuO is found to increase with decreasing temperature – a larger field is required to switch the domain population at lower temperature. The system becomes softer at higher temperatures and therefore the electric field required to balance the domain population is reduced up to the point of the phase transition at 230 K. No hysteresis and hence no coercive field is found in the collinear AF1 or paramagnetic phases.

The P_{yx} component of the polarisation matrix is related to the number of counts in the non-spin-flip $\sigma(y,x)$ and spin-flip $\sigma(y,\bar{x})$ channels from Eq. 6.17 as $P_{yx} = [\sigma(y,x) - \sigma(y,\bar{x})]/[\sigma(y,x) + \sigma(y,\bar{x})]$. The lower panels of Fig. 6.12 show the normalised counts of the scattering measured in $\sigma(y,x)$ and $\sigma(y,\bar{x})$ channels as a function of electric field and temperature. When the domains are equally populated, the signal observed in the non-spin-flip and spin-flip channels will be the same. As will be demonstrated later, D1 contributes to a large extent to the $\sigma(y,x)$ cross-section, such that $\sigma(y,x) \gg \sigma(y,\bar{x})$. The reverse is true when D2 dominates. As the temperature decreases, the ordered magnetic moment increases, hence the signal in $\sigma(y,x)$ and $\sigma(y,\bar{x})$ becomes greater.

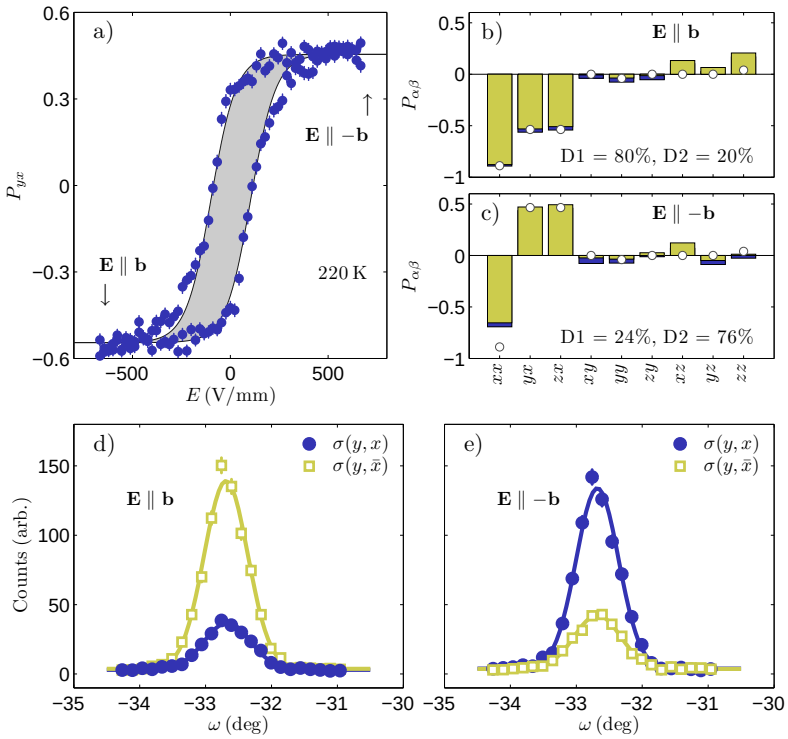

Figure 6.13: Spherical neutron polarimetry data for CuO with an applied electric field at 220 K. Panel (a) shows the P_{yx} component of the polarisation matrix during an electric field sweep at a fixed temperature of 220 K. Panels (b) and (c) represent the complete polarisation matrix at $\boldsymbol{q}_{\text{icm}} = (0.506, 0, -0.483)$ with applied field E of -670 V/mm and $+670$ V/mm, respectively. The colour bars are the measurements, and the symbols (○) are calculated assuming the $M_b^{(1)} \circ M_v^{(2)}$ AF2 magnetic structure and taking into account the non-ideal neutron beam polarisation. The fitted populations of the two chiral magnetic domains are indicated. Panels (d) and (e) show rocking scans through the magnetic peak as measured in the yx and $y\overline{x}$ polarisation channels. Measurements were made at constant applied electric field of -670 V/mm (panel d) and $+670$ V/mm (panel e). Reprinted figure with permission from Babkevich *et al.*, Phys. Rev. B **85**, 134428 (2012) [268]. Copyright © (2012) by the American Physical Society.

Figure 6.13 shows the polarimetry data recorded at 220 K. Even at large electric fields a significant depolarisation is observed such that a saturation value of $P_{yx} \approx \pm 0.5$ is reached at around ± 500 V/mm, as shown in Fig. 6.13(a). The coercive field at this temperature is found to be approximately 90 V/mm. Reported results [42] for the electric polarisation dependence on the electric field at this temperature find instead that the coercive field is closer to 55 V/mm. The difference could be slight differences in the temperatures at which the loops were made.

To examine what happens at the saturating fields we performed rocking scans through the Bragg peak at $\boldsymbol{q}_{\text{icm}}$. Figure 6.13(a) and (b) show the number of counts in the spin-flip and non-spin-flip yx polarisation channels at the extrema of the hysteresis loop. We would expect the left-handed helical domain (i.e. that shown in

Fig. 6.11) to scatter mainly into the $y\bar{x}$ channel. Taking into account the non-ideal beam polarisation in the experiment, we calculate the ratio of $\sigma(y,x)/\sigma(y,\bar{x})$ to be 15 for a single magnetic domain. However, from Fig. 6.13(d) this ratio is closer to 3.4.

The significant depolarisation of the P_{yx} term can be attributed to the following, not mutually exclusive factors:

(i) There exists an imbalance of chiral domain population even at saturation field.

(ii) The assumed magnetic structure for the AF2 phase is incorrect. However, the envelope of the rotation plane has been tightly constrained by Aïn *et al.* [265], Brown *et al.* [264] and our own measurements with all studies concluding that the non-collinear structure is helicoidal with a (nearly) circular envelope.

(iii) There is a phase difference between $\boldsymbol{A}_{\perp}(\boldsymbol{Q})$ and $\boldsymbol{B}_{\perp}(\boldsymbol{Q})$. The effect of this can be found from relations defined in Eqs. 6.20. This also seems unlikely as group theory shows that the phases are tightly constrained. However, even if irreducible representation analysis is not considered, we find no evidence of a finite P_{yz} and P_{zy} polarisation matrix elements which are also sensitive to the phase differences.

We can therefore conclude that the most adequate explanation for the depolarisation is that complete switching from one domain into another cannot be achieved.

Complete polarisation matrices $P_{\alpha\beta}$ measured with an applied external electric field of $\pm 670\,\mathrm{V/mm}$, at 220 K, are shown in Figs. 6.13(b) and (c). The data clearly shows a reversal in the sign of P_{yx} and P_{zx}. A decrease in the xx component is anomalous. Its origin is unclear but may be due to a small misalignment of the crystal with respect to the polarisation axes which also causes the P_{xz} term to be non-zero. It can be shown from Eq. 6.21 that $P_{yx}^2 + P_{yy}^2 + P_{yz}^2 = 1$ for a single domain of any magnetic structure. This relation is not satisfied by our data and therefore this adds weight to the notion that the presence of domains is responsible for the reduced values of P_{yx} and P_{zx}.

To quantify our data, we have the model for the AF2 magnetic structure where the basis vectors along $\boldsymbol{b}$ correspond to Γ_1 representation and the basis vectors in the ac-plane to Γ_2. A correction was made to the simulations to account for the non-ideal beam polarisation assuming beam polarisation efficiency of 94% (based on a flipping ratio of 17). The polarisation matrices were fitted allowing just the domain fraction to vary. The domains D1 and D2 correspond to left- and right-handed spin structure, respectively. The electric field switches between the domains, with a large positive electric field yielding a predominantly left-handed domain and conversely a large negative field promoting the right-handed domain. The switching by applied electric fields has been observed in several materials with non-collinear magnetic ordering such as $Ni_3V_2O_8$, $MnWO_4$, $LuCu_2O_2$ and $TbMnO_3$ [269–272].

We find that typically, in the AF2 phase, at electric fields approaching saturation in P_{yx}, the magnetic domains are populated in approximately 80:20 proportion. We

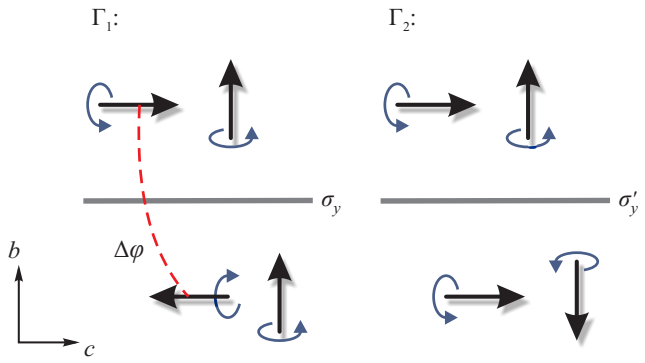

Figure 6.14: Symmetry operation effect on the magnetic structure. Diagram to show the how the magnetic moments on Cu atoms are related to each other by the $\{\sigma_y|0,0,0.5\}$ symmetry of the space group. The moments in the mirror $\boldsymbol{a}$-$\boldsymbol{c}$ plane are transformed in the opposite sense to the moments along $\boldsymbol{b}$ when the mirror plane (σ_y) or mirror plane together with a time reversal (σ'_y) is applied. The translational part of the symmetry operation $\boldsymbol{\tau}$ adds an additional phase change $\Delta\varphi = \boldsymbol{\kappa}\cdot\boldsymbol{\tau}$.

have observed, therefore, that the electric field does not induce a single magnetic domain. Possible reasons for this are, (i) crystal defects acting to pin the magnetic structure and prevent full domain reversal, (ii) the high-temperature of the multiferroic phase causing thermal relaxation of the domain population in the time frame of the experiment, (iii) a reduced electric field strength near the edges of the crystal caused by the incomplete coating of the surfaces with the gold electrodes, or (iv) leakage currents could be responsible for partially screening the ferroelectric state.

6.6.5 Discussion

The measurements collected for CuO using polarised neutron scattering show that an electric field applied along the ferroelectric axis is able to switch the magnetic domains in the multiferroic AF2 phase. The results unambiguously demonstrate that the magnetic and ferroelectric degrees of freedom are strongly coupled as predicted by theoretical models [253, 257, 273]. The magnitude of $\boldsymbol{P}_\mathrm{e}$ predicted is consistent with the experimental bulk value of approximately $90\,\mu\mathrm{C/m^2}$. Furthermore, we observe that the direction of $\boldsymbol{P}_\mathrm{e}$ is along $+\boldsymbol{b}$ for the left-handed domain.

The AF2 structure which can produce a net ferroelectric polarisation requires the mixing of basis vectors symmetries. This can be understood qualitatively from Fig. 6.14. The symmetry operation $\{\sigma_y|0,0,0.5\}$ acts on Cu site 1 to generate Cu at site 2. Meanwhile, the magnetic structure transforms according to character Table 6.2(b). From Table 6.6, we find that in the Γ_1 representation, the b-component of the magnetic moment is parallel for sites 1 and 2 but the ac-component reverses direction. Conversely, in the Γ_1 representation, the ac-component is unchanged whereas the b-component is. This is qualitatively described in Fig. 6.14. The magnetic moments are axial vectors and therefore the mirror plane σ_y in the Γ_1 symmetry, leaves moments along $\boldsymbol{b}$ unchanged but flips the magnetic moment in the ac-plane. The Γ_2 symmetry can be composed of a mirror plane as well as

time inversion, this will cause the spins in the *ac*-plane to be unaltered but the moment along $\boldsymbol{b}$ will be reversed. Therefore, the moments on the two Cu sites in the primitive unit cell will always rotate in opposing senses if we take the basis vectors to belong to the same single irreducible representation. This results in zero net electric polarisation in the unit cell assuming the magnetoelectric coupling depends on the spin current $\boldsymbol{S}_i \times \boldsymbol{S}_j$. The mixing of basis vector symmetries ensures the spins rotate in the same sense and will generate a net ferroelectric response assuming this mechanism.

The magnetically-induced ferroelectric polarisation in CuO has been explained through a number of models, all of which are based upon the inverse Dzyaloshinskii-Moriya interaction between nearest-neighbour, non-collinear spins [35, 36]. This is a relativistic correction to the usual superexchange interaction whose Hamlitonian takes the form,

$$\mathcal{H}_{\mathrm{DM}} = \sum_{i,j} \boldsymbol{D}_{ij} \cdot (\boldsymbol{S}_i \times \boldsymbol{S}_j) \tag{6.22}$$

when acting between ith and jth spins separated by bond vector $\boldsymbol{r}_{ij}$. It is evident from this relation that the interaction favours non-collinear spins. The Dzyaloshinskii vector $\boldsymbol{D}_{ij}$ is material specific and in general can be decomposed into components parallel and perpendicular to $\boldsymbol{r}_{ij}$ as $\boldsymbol{D}_{ij} = \sigma_{ij}\boldsymbol{r}_{ij} + \boldsymbol{P}_{ij} \times \boldsymbol{r}_{ij}$, respectively [274]. The quantities $\boldsymbol{P}_{ij}$ and σ_{ij} are a polar vector and pseudoscalar [2] , respectively. In CuO, $\boldsymbol{P}_{ij}$ is proportional to a local electric polarisation and σ_{ij} is related to the magnetic chirality.

The cycloidal model ($\sigma_{ij} = 0$), where $\boldsymbol{P}_{\mathrm{e}} \propto \boldsymbol{q}_{\mathrm{c}} \times \boldsymbol{S}_i \times \boldsymbol{S}_j$ and $\boldsymbol{q}_{\mathrm{c}}$ is the propagation vector of the cycloid predicts that for high-symmetry cases the electric polarisation is perpendicular to the rotation plane of the spins and to the direction of propagation [37, 275]. This model can be extended for more complicated crystal structures with lower symmetry possessing general helicoidal magnetic moment arrangements. In such case, the electric polarisation and the propagation wavevector need not be perpendicular, nor the propagation vector should be restricted to the rotation plane. However, the electric polarisation will be constrained to lie in the plane containing the rotating moments [274]. This approach was used to explain the direction of the electric polarisation in the first study of multiferroic behaviour in CuO, by considering a cycloid propagating as modulated by $\boldsymbol{q}_{\mathrm{c}} = \boldsymbol{q}_{\mathrm{icm}} - \boldsymbol{q}_{\mathrm{cm}}$, which is almost parallel to the *ac* component of the rotation plane [42]. Such analysis does indeed predict a polarisation along $\boldsymbol{b}$ axis but relies on the fact that the magnetic structure is incommensurate in the AF2 phase. Subsequent theoretical models [253, 257, 273] find that the important magnetoelectric interaction is between approximately perpendicular spins on neighbouring chains of Cu atoms running along the $[1, 0, 1]$ direction and does not depend on the incommensurate modulation.

It has recently been shown that the chirality σ_{ij} of a magnetic structure can induce an electric polarisation through coupling to a unique structural rotation [274]. In $Cu_3Nb_2O_8$ the electric polarisation emerges perpendicular to the rotation

[2] A pseudoscalar is a scalar which changes sign under a spatial inversion.

plane and the mechanism involving coupling of the chirality to the crystal structure has been used to predict that $\boldsymbol{P}_{\mathrm{e}} \propto \sigma \boldsymbol{A}$, where $\boldsymbol{A}$ is an axial vector along the rotation axis [274]. Such coupling is limited to a small class of crystal structures which are termed ferroaxial [274]. CuO adopts the space group $C2/c$, a member of the ferroaxial crystal class, with a two-fold rotation axis parallel to the crystallographic b-axis. Coupling between the magnetic chirality and the crystal structure could therefore result in an electric polarisation parallel to the b-axis, as observed. It would be of interest to include this chiral term in future DFT calculations. However, as existing calculations predict an electric polarisation close to that observed in the experiments, its contribution may well be small.

A recent study of the bulk magnetoelectric properties of polycrystalline CuO showed that the application of a magnetic field has little effect on the ferroelectricity and concluded that the magnetoelectric coupling is very weak [250]. Our method of applying an electric field and measuring the effect on the magnetic structure shows that the magnetoelectric coupling is in fact strong. The difference between these experiments is that in our work we are probing the coupling between the macroscopic polarisation and a spatially-varying magnetisation, whereas in Ref. [250] the coupling is between the macroscopic polarisation and a uniform magnetisation. These studies are therefore complementary, not contradictory.

6.7 Conclusion

Spherical neutron polarimetry has been employed to study the high-temperature multiferroic phase of CuO. The application of an external electric field along the ferroelectric b axis has been found to be able to switch between chiral magnetic domains. These results demonstrate that the ferroelectric polarisation is directly coupled to the magnetic order. Magnetic representation analysis has been used to solve the magnetic structure in the multiferroic phase and was found to be consistent with experimental results. From symmetry considerations this magnetic structure allows for a ferroelectric polarisation to develop based on the spin current model. The microscopic origin of the ferroelectricity is consistent with models based on the inverse Dzyaloshinskii-Moriya mechanism [253, 257, 273].

Chapter 7

Concluding remarks and outlook

In this thesis a number of compounds have been investigated primarily using neutron scattering. The systems looked at can be classed into three distinct systems: (i) Mott insulating $La_{2-x}Sr_xCoO_4$ which share the same crystallographic structure as La_2CuO_4 based superconductors, (ii) $FeSe_xTe_{1-x}$, which belong to the newly discovered family of high-temperature superconductors and (iii) CuO which is a building block of La_2CuO_4 but exhibits multiferroicity at high temperatures.

The work on La_2CoO_4 has examined the magnetic structure and fluctuations. The magnetic fluctuations in the entire Brillouin zone were found to be well described by a two-dimensional XY-like model. An anomalous antiferromagnetic zone boundary dispersion was observed. This provides evidence of more distant interactions in the system beyond the nearest neighbour ones. Spherical neutron polarimetry was employed to try to refine the magnetic structure in the two antiferromagnetic phases in La_2CoO_4. The magnetic structure in the low-temperature orthorhombic phase was found to be identical to that of La_2NiO_4. The low-temperature tetragonal phase is less well understood. Our measurements do not provide a unique solution to the magnetic structure. However, more work could be envisaged in determining the magnetic structure in this phase. At low temperatures, the tilting of the O octahedra creates a lattice distortion whose modulation is concomitant with the antiferromagnetic order. This makes magnetic structure determination difficult. Although polarised neutrons allow for the separation of the nuclear and magnetic contributions to the signal, perhaps an alternative method could be used to verify these results. A possible candidate is x-ray diffraction. The presence of equivalent domains also makes magnetic structure determination complicated. One could try to break the symmetry in the low temperature phase in some way such by application of an in-plane magnetic field or uniaxial pressure.

An important result presented in this thesis is the observation of an hourglass dispersion in the stripe ordered $La_{5/3}Sr_{1/3}CoO_4$. The exchange interactions obtained from analysis of the magnetic fluctuations in La_2CoO_4 and $La_{3/2}Sr_{1/2}CoO_4$ [98] provide us with an excellent model of dynamics in $La_{5/3}Sr_{1/3}CoO_4$. A quantitative model of the dispersion is useful in guiding possible future experiments. The phase diagram of $La_{2-x}Sr_xCoO_4$ still requires some work and it would be useful to look at compounds with similar doping to $La_{5/3}Sr_{1/3}CoO_4$ to see how the incommensurate magnetic peaks evolve with doping and the effect on the dispersion. One of the key assumptions in the spin-wave model is the notion that the system becomes

charge ordered. However, this fact has not been verified directly in $La_{5/3}Sr_{1/3}CoO_4$. Since the material contains a mixture of Co valence states and these reside inside a crystal field environment, the difference in charge on Co would create slight distortion of the crystal structure. Periodic arrangement of charges should therefore lead to periodic structural distortion and this can be probed by x-ray diffraction. However, as the system is highly disordered and the distortion is likely to be small, this would present a formidable experiment challenge. An alternative would be to examine $La_{5/3}Sr_{1/3}CoO_4$, as well as other systems of $La_{2-x}Sr_xCoO_4$ using the μSR technique. The implanted muons carry positive charge and therefore would be more strongly repelled by the Co^{3+} than by Co^{2+}. Provided the stopping site can be found, it would serve to provide an alternative quantitative test of the Hamiltonian that we have considered.

Although some evidence exists that magnetic stripe order exists in cuprates, it is believed that the stripes run parallel to the Cu–O bonds, rather than along the diagonals as found in $La_{5/3}Sr_{1/3}CoO_4$, or similarly doped nickelates. It would therefore be interesting to look for insulators with vertical stripe order.

We have closely examined a range of compounds of the $FeSe_xTe_{1-x}$ type to look at the change in the low-energy magnetic fluctuations with temperature and doping. A localised mode in momentum and energy transfer appears below T_c in the superconducting samples. In contrast, strongly dispersive, incommensurate branches are found in the non-superconducting samples.

We have examined the resonance peak in $FeSe_{0.5}Te_{0.5}$ using polarised inelastic neutron scattering. One of the outstanding questions in the superconducting $FeSe_{0.5}Te_{0.5}$ sample is the appearance of a small anisotropy between the in-plane and out-of-plane components of spin fluctuations at the resonance position. This could serve as a motivation to look at the origin of this feature more closely using polarised neutron scattering. If the anisotropy is connected with some sort of orbital degree of freedom, it should change with wavevector. Therefore, measurements at inequivalent positions could be made in the $(h, k, 0)$ and (h, h, l) scattering planes for example. The behaviour could also be studied by examining non-superconducting samples to see if there is any change in the anisotropy of the magnetic fluctuations.

Recently, evidence has emerged that of an unconventional phonon broadening in the Raman spectrum of $FeSe_xTe_{1-x}$ which has been suggested to be a signature of the opening of spin-density-wave gap [276]. Neutron scattering is well suited to the study of lattice excitations and could be utilised in looking at how the phonon spectrum changes between the superconducting and non-superconducting samples. The effect is likely to be very weak and therefore high-energy resolution could be provided by using the spin-echo setup.

In comparison to the cuprates, the field of Fe-based superconductors, although hotly pursued, is still new and rapidly developing. A new compound, based on FeSe has emerged with a dramatically higher phase transition temperature of $T_c \approx 30\,\mathrm{K}$. This system has the form $A_xFe_2Se_2$, where A is an alkali metal ion. It possesses many unusual properties and the comparison between this compound and $FeSe_xTe_{1-x}$ could shed light on some new physics. It would seem very likely that

more Fe-based superconductors are yet to be discovered and this may well change the course of the field.

Our work on the multiferroic CuO has demonstrated that there is strong coupling between magnetism and ferroelectricity at high temperature. Many theoretical studies have been made using DFT to calculate the exchange interactions. However, there are considerable variations in the ab-initio values of the exchange parameters. These are important in trying to understand the high temperature at which the multiferroic phase occurs and the mechanism leading to ferroelectricity from the non-collinear magnetic structure. However, no complete map of the magnetic excitation spectrum has yet been reported for CuO. It would be an important step in characterising the dispersion and extracting the exchange interactions in CuO. The dominant interaction along the CuO chains with the largest Cu–O–Cu bond angle is already known to be antiferromagnetic and large. This strong interaction could exhibit some interesting one-dimensional-like properties such as spin-chains or spin-ladder. Such a study would also be important in the context of trying to relate how the interactions in CuO affect more complicated cuprate compounds.

Appendix A

Linear spin-wave theory

A.1 Introduction

In § 3.7.3 we have considered the linear spin-wave model to account for magnetic excitation spectrum of La_2CoO_4. In this Appendix, I shall further examine the key results of the linear spin-wave theory relating to antiferromagnets.

Figure A.1 shows how an antiferromagnet can be separated into two sublattices A and B. Within each sublattice the magnetic moments are ferromagnetically aligned and we shall consider a ferromagnetic interaction J^{F} between spins connected by $\boldsymbol{R}$. Antiferromagnetic coupling J^{A} exists between sublattices A and B. The sublattice A and B can be connected by an inter-lattice vector $\boldsymbol{r}$. The Hamiltonian $\mathcal{H}_m$ of mth magnetic unit cell is given in Eq. 3.3 as,

$$\begin{aligned}\mathcal{H}_m &= \sum_{\boldsymbol{r}} J_x^{\mathrm{A}} S_{\boldsymbol{m}}^x S_{\boldsymbol{m}+\boldsymbol{r}}^x + J_y^{\mathrm{A}} S_{\boldsymbol{m}}^y S_{\boldsymbol{m}+\boldsymbol{r}}^y + J_z^{\mathrm{A}} S_{\boldsymbol{m}}^z S_{\boldsymbol{m}+\boldsymbol{r}}^z \\ &\quad + \sum_{\boldsymbol{R}} J_x^{\mathrm{F}} S_{\boldsymbol{m}}^x S_{\boldsymbol{m}+\boldsymbol{R}}^x + J_y^{\mathrm{F}} S_{\boldsymbol{m}}^y S_{\boldsymbol{m}+\boldsymbol{R}}^y + J_z^{\mathrm{F}} S_{\boldsymbol{m}}^z S_{\boldsymbol{m}+\boldsymbol{R}}^z. \qquad \text{(A.1)}\end{aligned}$$

The spin operator components for the two sublattices can be represented using the Holstein-Primakoff transformation [10], defined exactly in natural units, for

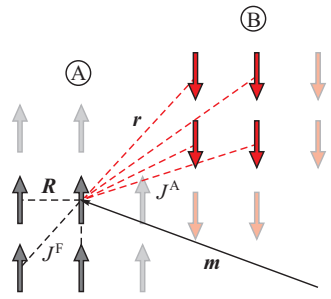

Figure A.1: Exchange interactions between sublattices A and B. The interactions within sublattice A or B are ferromagnetic and are denoted by an exchange interaction J^{F} with spins connected by vector $\boldsymbol{R}$. Sublattice A and B are antiferromagnetically arranged with exchange interaction J^{A} along the $\boldsymbol{r}$ bonds.

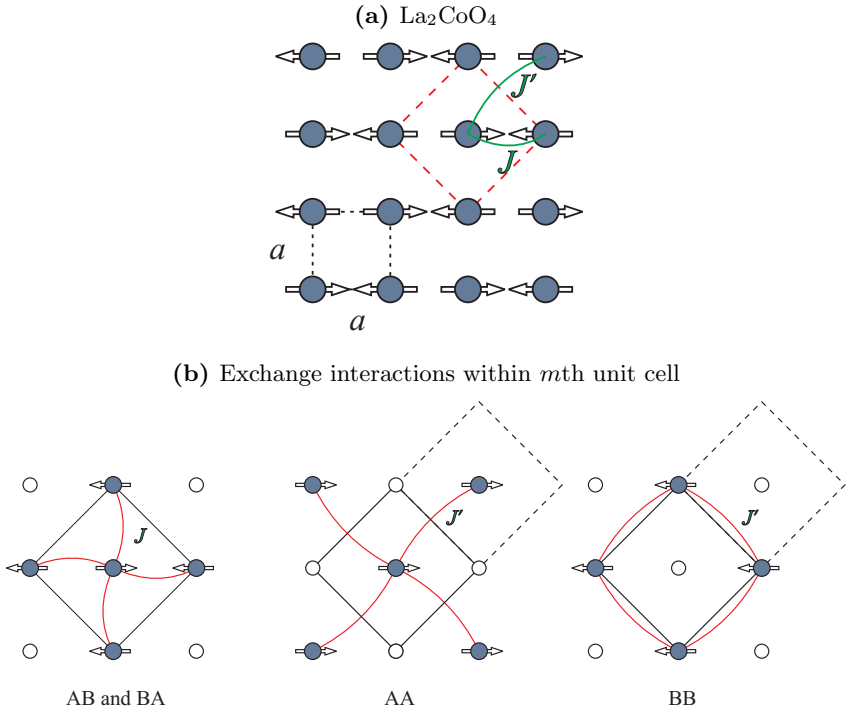

Figure A.2: Magnetic structure of La_2CoO_4 showing the dominant exchange interactions. (a) Groundstate spin structure of La_2CoO_4 with exchange interactions considered in the linear spin-wave model. The black outline shows the crystallographic unit cell, whilst the red represents the magnetic unit cell. (b) Exchange interactions between A and B sublattices, A and A: FM interactions and B and B: FM interactions to calculate the Hamiltonian. Black box is the magnetic unit cell, whilst the box in dashed outline represents the $(m+1)$th unit cell.

quantisation axis along x as,

$$\begin{aligned} S_i^x &= (S - a_i^\dagger a_i), \\ S_i^+ = S_i^y + \mathrm{i}S_i^z &= (2S - a_i^\dagger a_i)^{1/2} a_i, \\ S_i^- = S_i^y - \mathrm{i}S_i^z &= a_i^\dagger (2S - a_i^\dagger a_i)^{1/2}. \end{aligned} \tag{A.2}$$

The Bose operators obey $[a_i, a_j^\dagger] = \delta_{ij}$, while the spin operator commutes as $[S_i, S_j] = \mathrm{i}\varepsilon_{ijk} S_k$ as usual. The terms $a^\dagger a$ are introduced as magnon occupation number. A transformation using Dyson-Maleev transformations give the same results for the case of linear spin wave theory as Holstein-Primakoff version. However, the Holstein-Primakoff approach becomes reasonable in the quasi-classical limit of $S \gg 1$. This is of fundamental importance in the theory of antiferromagnetism [3]. In the approximation of $\langle a_i^\dagger a_i \rangle \ll S$,

$$(2S - a_i^\dagger a_i)^{1/2} \approx (2S)^{1/2} \left[1 - \frac{a_i^\dagger a_i}{4S} - \frac{(a_i^\dagger a_i)^2}{32S^2} - O\left(\frac{1}{S^3}\right) \right], \tag{A.3}$$

the expansion is in $1/S$ and is expected to converge rapidly for a large-spin system. For the case of two sublattices and keeping terms only bilinear in $\langle a_i^\dagger a_i \rangle$, the Holstein-Primakoff transformations are,

$$\begin{array}{ll} \textbf{Sublattice A} & \textbf{Sublattice B} \\ S_i^x = (S - a_i^\dagger a_i) & S_j^x = -(S - b_j^\dagger b_j) \\ S_i^y = \sqrt{S/2}(a_i + a_i^\dagger) & S_j^y = \sqrt{S/2}(b_j + b_j^\dagger) \\ S_i^z = -\mathrm{i}\sqrt{S/2}(a_i - a_i^\dagger) & S_j^z = \mathrm{i}\sqrt{S/2}(b_j - b_j^\dagger), \end{array} \tag{A.4}$$

where $a_i^\dagger (b_j^\dagger)$ creates a spin deviation on site $i(j)$ of sublattice A(B). The Hamiltonian defined in Eq. A.1 can then be suitably transformed into a form containing just the Bose operators. Following this, the Hamiltonian can be Fourier transformed, as described in § A.2. Keeping only the quadratic terms in the operators, gives a Hamiltonian in the form of Eq. 3.5,

$$\mathcal{H} = \mathcal{H}_0 + \frac{1}{2}\sum_{\boldsymbol{Q}} X_{\boldsymbol{Q}}^\dagger H_{\boldsymbol{Q}} X_{\boldsymbol{Q}}. \tag{A.5}$$

The solution to such a problem is known (Ref. [101]) and has already been described in § 3.7.3 by Eqs. 3.5–3.9. This methodology can be applied for the case of La_2CoO_4. For simplicity, I shall only consider nearest and next-nearest neighbour interactions, J and J'. The antiferromagnetic exchange J is taken to be anisotropic and the more distant J' we shall assume can be considered to be isotropic. Figure A.2 shows these exchange interactions. The interactions within and with neighbouring magnetic unit cells as shown in Fig. A.2(b) for the case of La_2CoO_4, the Hamiltonian for mth unit cell is $\mathcal{H}_m = \mathcal{H}_m^{\mathrm{AB}} + (\mathcal{H}_m^{\mathrm{AA}} + \mathcal{H}_m^{\mathrm{BB}})/2$. The factor of $1/2$ is due to the sharing of bonds between adjacent cells. The Hamiltonian defined in Eq. A.1 can be can be simplified for the case of isotropic and centrosymmetric and isotropic exchange interaction J', from derivation of Eqs. A.28 and A.29,

$$\begin{aligned} \mathcal{H}_m^{\mathrm{AB}} &= \sum_{\boldsymbol{r}} J_x \left(-S^2 + S a_{\boldsymbol{m}}^\dagger a_{\boldsymbol{m}} + S b_{\boldsymbol{m}+\boldsymbol{r}}^\dagger b_{\boldsymbol{m}+\boldsymbol{r}}\right) \\ &\quad + \frac{J_y S}{2}\left(a_{\boldsymbol{m}} b_{\boldsymbol{m}+\boldsymbol{r}} + a_{\boldsymbol{m}} b_{\boldsymbol{m}+\boldsymbol{r}}^\dagger + a_{\boldsymbol{m}}^\dagger b_{\boldsymbol{m}+\boldsymbol{r}} + a_{\boldsymbol{m}}^\dagger b_{\boldsymbol{m}+\boldsymbol{r}}^\dagger\right) \\ &\quad + \frac{J_z S}{2}\left(a_{\boldsymbol{m}} b_{\boldsymbol{m}+\boldsymbol{r}} - a_{\boldsymbol{m}} b_{\boldsymbol{m}+\boldsymbol{r}}^\dagger - a_{\boldsymbol{m}}^\dagger b_{\boldsymbol{m}+\boldsymbol{r}} + a_{\boldsymbol{m}}^\dagger b_{\boldsymbol{m}+\boldsymbol{r}}^\dagger\right) \end{aligned} \tag{A.6}$$

$$\begin{aligned} \mathcal{H}_m^{\mathrm{AA}} &= J' \sum_{\boldsymbol{R}} \left(S^2 - S a_{\boldsymbol{m}}^\dagger a_{\boldsymbol{m}} - S a_{\boldsymbol{m}+\boldsymbol{R}}^\dagger a_{\boldsymbol{m}+\boldsymbol{R}}\right) \\ &\quad + \frac{S}{2}\left(a_{\boldsymbol{m}} a_{\boldsymbol{m}+\boldsymbol{R}} + a_{\boldsymbol{m}} a_{\boldsymbol{m}+\boldsymbol{R}}^\dagger + a_{\boldsymbol{m}}^\dagger a_{\boldsymbol{m}+\boldsymbol{R}} + a_{\boldsymbol{m}}^\dagger a_{\boldsymbol{m}+\boldsymbol{R}}^\dagger\right) \\ &\quad - \frac{S}{2}\left(a_{\boldsymbol{m}} a_{\boldsymbol{m}+\boldsymbol{R}} - a_{\boldsymbol{m}} a_{\boldsymbol{m}+\boldsymbol{R}}^\dagger - a_{\boldsymbol{m}}^\dagger a_{\boldsymbol{m}+\boldsymbol{R}} + a_{\boldsymbol{m}}^\dagger a_{\boldsymbol{m}+\boldsymbol{R}}^\dagger\right) \end{aligned} \tag{A.7}$$

$$\begin{aligned}\mathcal{H}_m^{\mathrm{BB}} &= J'\sum_{\boldsymbol{R}}\left(S^2 - Sb_{\boldsymbol{m}}^\dagger b_{\boldsymbol{m}} - Sb_{\boldsymbol{m}+\boldsymbol{R}}^\dagger b_{\boldsymbol{m}+\boldsymbol{R}}\right)\\ &\quad+\frac{S}{2}\left(b_{\boldsymbol{m}}b_{\boldsymbol{m}+\boldsymbol{R}} + b_{\boldsymbol{m}}b_{\boldsymbol{m}+\boldsymbol{R}}^\dagger + b_{\boldsymbol{m}}^\dagger b_{\boldsymbol{m}+\boldsymbol{R}} + b_{\boldsymbol{m}}^\dagger b_{\boldsymbol{m}+\boldsymbol{R}}^\dagger\right)\\ &\quad-\frac{S}{2}\left(b_{\boldsymbol{m}}b_{\boldsymbol{m}+\boldsymbol{R}} - b_{\boldsymbol{m}}b_{\boldsymbol{m}+\boldsymbol{R}}^\dagger - b_{\boldsymbol{m}}^\dagger b_{\boldsymbol{m}+\boldsymbol{R}} + b_{\boldsymbol{m}}^\dagger b_{\boldsymbol{m}+\boldsymbol{R}}^\dagger\right)\end{aligned} \tag{A.8}$$

The Fourier transform of this Hamiltonian (see § A.2) is then,

$$\begin{aligned}\mathcal{H}_{\boldsymbol{Q}}^{\mathrm{AB}} &= -4NJ_x(\boldsymbol{0})S^2 + S\sum_{\boldsymbol{Q}} 4J_x(\boldsymbol{0})\left(a_{\boldsymbol{Q}}^\dagger a_{\boldsymbol{Q}} + b_{\boldsymbol{Q}}^\dagger b_{\boldsymbol{Q}}\right)\\ &\quad+\frac{1}{2}\left[J_y(\boldsymbol{Q}) + J_z(\boldsymbol{Q})\right]\left(a_{\boldsymbol{Q}}b_{-\boldsymbol{Q}} + a_{\boldsymbol{Q}}^\dagger b_{-\boldsymbol{Q}}^\dagger\right)\\ &\quad+\frac{1}{2}\left[J_y(\boldsymbol{Q}) - J_z(\boldsymbol{Q})\right]\left(a_{\boldsymbol{Q}}b_{\boldsymbol{Q}}^\dagger + a_{\boldsymbol{Q}}^\dagger b_{\boldsymbol{Q}}\right),\end{aligned} \tag{A.9}$$

$$\begin{aligned}\frac{1}{2}\left(\mathcal{H}_{\boldsymbol{Q}}^{\mathrm{AA}} + \mathcal{H}_{\boldsymbol{Q}}^{\mathrm{BB}}\right) &= 4NJ'(\boldsymbol{0})S^2 + S\sum_{\boldsymbol{Q}} -4J'(\boldsymbol{0})\left(a_{\boldsymbol{Q}}^\dagger a_{\boldsymbol{Q}} + b_{\boldsymbol{Q}}^\dagger b_{\boldsymbol{Q}}\right)\\ &\quad+J'(\boldsymbol{Q})\left(a_{\boldsymbol{Q}}^\dagger a_{\boldsymbol{Q}} + b_{\boldsymbol{Q}}^\dagger b_{\boldsymbol{Q}} + 1\right),\end{aligned} \tag{A.10}$$

The total Fourier-transformed Hamiltonian $H_{\boldsymbol{Q}}$ can be expressed in the form of Eq. A.5 by considering a set of operators defined in $X_{\boldsymbol{Q}}$

$$X_{\boldsymbol{Q}} = \begin{pmatrix} a_{\boldsymbol{Q}} \\ b_{\boldsymbol{Q}} \\ a_{-\boldsymbol{Q}}^\dagger \\ b_{-\boldsymbol{Q}}^\dagger \end{pmatrix} \qquad H_{\boldsymbol{Q}} = \begin{pmatrix} A_{\boldsymbol{Q}} & B_{\boldsymbol{Q}} & C_{\boldsymbol{Q}} & D_{\boldsymbol{Q}} \\ B_{\boldsymbol{Q}} & A_{\boldsymbol{Q}} & D_{\boldsymbol{Q}} & C_{\boldsymbol{Q}} \\ C_{\boldsymbol{Q}} & D_{\boldsymbol{Q}} & A_{\boldsymbol{Q}} & B_{\boldsymbol{Q}} \\ D_{\boldsymbol{Q}} & C_{\boldsymbol{Q}} & B_{\boldsymbol{Q}} & A_{\boldsymbol{Q}} \end{pmatrix} \tag{A.11}$$

where[1]

$$A_{\boldsymbol{Q}} = 4SJ_x(\boldsymbol{0}) - 4SJ'(\boldsymbol{0}) + SJ'(\boldsymbol{Q}) \tag{A.12}$$

$$B_{\boldsymbol{Q}} = \frac{1}{2}S\left[J_y(\boldsymbol{Q}) - J_z(\boldsymbol{Q})\right] \tag{A.13}$$

$$C_{\boldsymbol{Q}} = 0 \tag{A.14}$$

$$D_{\boldsymbol{Q}} = \frac{1}{2}S\left[J_y(\boldsymbol{Q}) + J_z(\boldsymbol{Q})\right] \tag{A.15}$$

The Hamiltonian can be diagonalised leading to expressions for the two modes with spin-wave dispersion relations given by,

$$E_+(\boldsymbol{Q}) = \left[\left(A_{\boldsymbol{Q}} + B_{\boldsymbol{Q}}\right)^2 - \left(C_{\boldsymbol{Q}} + D_{\boldsymbol{Q}}\right)^2\right]^{1/2} \tag{A.16}$$

$$E_-(\boldsymbol{Q}) = \left[\left(A_{\boldsymbol{Q}} - B_{\boldsymbol{Q}}\right)^2 - \left(C_{\boldsymbol{Q}} - D_{\boldsymbol{Q}}\right)^2\right]^{1/2} \tag{A.17}$$

[1]Note that in the derivation, we have assumed that exchange interactions are centrosymmetric ($J_{\boldsymbol{r}} = J_{-\boldsymbol{r}}$) and used the fact that independent operators commute, i.e. $[a_{\boldsymbol{Q}}^\dagger, b_{\boldsymbol{Q}}] = 0$.

The Fourier transforms of the exchange interactions are found to be,

$$J_\alpha(\boldsymbol{Q}) = 2J_i(\mathbf{0})\left(\cos\boldsymbol{Q}\cdot\boldsymbol{a}+\cos\boldsymbol{Q}\cdot\boldsymbol{b}\right) \tag{A.18}$$

$$J'(\boldsymbol{Q}) = 2J'(\mathbf{0})\left(\cos\boldsymbol{Q}\cdot(\boldsymbol{a}+\boldsymbol{b})+\cos\boldsymbol{Q}\cdot(\boldsymbol{a}-\boldsymbol{b})\right), \tag{A.19}$$

where the anisotropic nearest-neighbour exchange interaction J has components along $\alpha=\{x,y,z\}$.

A.2 Fourier transform of Hamiltonian

The Bose operators defined in Eq. A.4 can be expressed in terms of their Fourier transforms as,

$$a_j = \frac{1}{\sqrt{N}}\sum_{\boldsymbol{Q}} e^{\mathrm{i}\boldsymbol{Q}\cdot\boldsymbol{r}_j}a_{\boldsymbol{Q}} \qquad a_j^\dagger = \frac{1}{\sqrt{N}}\sum_{\boldsymbol{Q}} e^{-\mathrm{i}\boldsymbol{Q}\cdot\boldsymbol{r}_j}a_{\boldsymbol{Q}}^\dagger \tag{A.20}$$

$$b_j = \frac{1}{\sqrt{N}}\sum_{\boldsymbol{Q}} e^{\mathrm{i}\boldsymbol{Q}\cdot\boldsymbol{r}_j}b_{\boldsymbol{Q}} \qquad b_j^\dagger = \frac{1}{\sqrt{N}}\sum_{\boldsymbol{Q}} e^{-\mathrm{i}\boldsymbol{Q}\cdot\boldsymbol{r}_j}b_{\boldsymbol{Q}}^\dagger, \tag{A.21}$$

where N is the number of atoms on each sublattice and wavevector $\boldsymbol{Q}$ is defined in to the magnetic Brillioun zone. Must also define the Fourier transform of the δ-function as,

$$\delta_{\boldsymbol{q}+\boldsymbol{q}',0} = \frac{1}{N}\sum_{j=1}^{N} e^{\mathrm{i}(\boldsymbol{q}+\boldsymbol{q}')\cdot\boldsymbol{r}_j} = \begin{cases} 1 & \text{iff } \boldsymbol{q}+\boldsymbol{q}'=0 \\ 0 & \text{iff } \boldsymbol{q}+\boldsymbol{q}'\neq 0 \end{cases} \tag{A.22}$$

Applying these definitions to the spin-wave operators, yields identities such as,

$$a_{\boldsymbol{m}}^\dagger a_{\boldsymbol{m}} = \frac{1}{N}\sum_{\boldsymbol{Q}\boldsymbol{Q}'} e^{\mathrm{i}\boldsymbol{Q}\cdot\boldsymbol{m}}e^{-\mathrm{i}\boldsymbol{Q}'\cdot\boldsymbol{m}}a_{\boldsymbol{Q}}^\dagger a_{\boldsymbol{Q}'} \qquad \Rightarrow \sum_{\boldsymbol{m}} a_{\boldsymbol{m}}^\dagger a_{\boldsymbol{m}} = \sum_{\boldsymbol{Q}} a_{\boldsymbol{Q}}^\dagger a_{\boldsymbol{Q}}. \tag{A.23}$$

The completed list of Fourier transform identities is found in Table A.1. Applying these results to Eqs. A.6–A.8 and summing over all magnetic unit cells,

$$\begin{aligned}\sum_{\boldsymbol{m}}\mathcal{H}_m^{\mathrm{AB}} = &\sum_{\boldsymbol{m}}\sum_{\boldsymbol{r}} -J_x^{\mathrm{A}}S^2 \\ &+\sum_{\boldsymbol{Q}}\sum_{\boldsymbol{r}} J_x^{\mathrm{A}}\left(Sa_{\boldsymbol{Q}}^\dagger a_{\boldsymbol{Q}}+Sb_{\boldsymbol{Q}}^\dagger b_{\boldsymbol{Q}}\right) \\ &\quad+\frac{J_y^{\mathrm{A}}S}{2}\left(e^{-\mathrm{i}\boldsymbol{Q}\cdot\boldsymbol{r}}a_{\boldsymbol{Q}}b_{-\boldsymbol{Q}}+e^{-\mathrm{i}\boldsymbol{Q}\cdot\boldsymbol{r}}a_{\boldsymbol{Q}}b_{\boldsymbol{Q}}^\dagger+e^{\mathrm{i}\boldsymbol{Q}\cdot\boldsymbol{r}}a_{\boldsymbol{Q}}^\dagger b_{\boldsymbol{Q}}+e^{\mathrm{i}\boldsymbol{Q}\cdot\boldsymbol{r}}a_{\boldsymbol{Q}}^\dagger b_{-\boldsymbol{Q}}^\dagger\right) \\ &\quad+\frac{J_z^{\mathrm{A}}S}{2}\left(e^{-\mathrm{i}\boldsymbol{Q}\cdot\boldsymbol{r}}a_{\boldsymbol{Q}}b_{-\boldsymbol{Q}}-e^{-\mathrm{i}\boldsymbol{Q}\cdot\boldsymbol{r}}a_{\boldsymbol{Q}}b_{\boldsymbol{Q}}^\dagger-e^{\mathrm{i}\boldsymbol{Q}\cdot\boldsymbol{r}}a_{\boldsymbol{Q}}^\dagger b_{\boldsymbol{Q}}+e^{\mathrm{i}\boldsymbol{Q}\cdot\boldsymbol{r}}a_{\boldsymbol{Q}}^\dagger b_{-\boldsymbol{Q}}^\dagger\right).\end{aligned} \tag{A.24}$$

The above result can be simplified as the first summation is taken over all magnetic unit cells and all bonds connected by J_x^{A}. Furthermore, we define the Fourier

transform of the exchange interactions as, $J(\boldsymbol{Q}) = \sum_{\boldsymbol{r}} J_{\boldsymbol{r}} e^{\mathrm{i}\boldsymbol{Q}\cdot\boldsymbol{r}}$. Such that,

$$\begin{aligned}\sum_{\boldsymbol{m}} \mathcal{H}_m^{\mathrm{AB}} &= -N z_{\boldsymbol{r}} J_x^{\mathrm{A}}(\boldsymbol{0}) S^2 \\ &\quad + S \sum_{\boldsymbol{Q}} z_{\boldsymbol{r}} J_x^{\mathrm{A}}(\boldsymbol{0}) \left(a_{\boldsymbol{Q}}^\dagger a_{\boldsymbol{Q}} + b_{\boldsymbol{Q}}^\dagger b_{\boldsymbol{Q}} \right) \\ &\quad + \frac{1}{2}\left[J_y^{\mathrm{A}}(-\boldsymbol{Q}) + J_z^{\mathrm{A}}(-\boldsymbol{Q}) \right] a_{\boldsymbol{Q}} b_{-\boldsymbol{Q}} + \frac{1}{2}\left[J_y^{\mathrm{A}}(\boldsymbol{Q}) + J_z^{\mathrm{A}}(\boldsymbol{Q}) \right] a_{\boldsymbol{Q}}^\dagger b_{-\boldsymbol{Q}}^\dagger \\ &\quad + \frac{1}{2}\left[J_y^{\mathrm{A}}(-\boldsymbol{Q}) - J_z^{\mathrm{A}}(-\boldsymbol{Q}) \right] a_{\boldsymbol{Q}} b_{\boldsymbol{Q}}^\dagger + \frac{1}{2}\left[J_y^{\mathrm{A}}(\boldsymbol{Q}) - J_z^{\mathrm{A}}(\boldsymbol{Q}) \right] a_{\boldsymbol{Q}}^\dagger b_{\boldsymbol{Q}}, \end{aligned} \tag{A.25}$$

where $z_{\boldsymbol{r}}$ is the number of AFM spins connected by $\boldsymbol{r}$ and analogously, $z_{\boldsymbol{R}}$ is the number of FM exchange bonds. In the case of anisoptropic FM exchange interaction between spins on sublattices A and B, in the case of La_2CoO_4, Eqs. A.7 and A.8 can be generalised as

$$\begin{aligned}\mathcal{H}_m^{\mathrm{AA}} &= \sum_{\boldsymbol{R}} J_x^{\mathrm{F}} \left(S^2 - S a_{\boldsymbol{m}}^\dagger a_{\boldsymbol{m}} - S a_{\boldsymbol{m}+\boldsymbol{R}}^\dagger a_{\boldsymbol{m}+\boldsymbol{R}} \right) \\ &\quad + \frac{J_y^{\mathrm{F}} S}{2} \left(a_{\boldsymbol{m}} a_{\boldsymbol{m}+\boldsymbol{R}} + a_{\boldsymbol{m}} a_{\boldsymbol{m}+\boldsymbol{R}}^\dagger + a_{\boldsymbol{m}}^\dagger a_{\boldsymbol{m}+\boldsymbol{R}} + a_{\boldsymbol{m}}^\dagger a_{\boldsymbol{m}+\boldsymbol{R}}^\dagger \right) \\ &\quad - \frac{J_z^{\mathrm{F}} S}{2} \left(a_{\boldsymbol{m}} a_{\boldsymbol{m}+\boldsymbol{R}} - a_{\boldsymbol{m}} a_{\boldsymbol{m}+\boldsymbol{R}}^\dagger - a_{\boldsymbol{m}}^\dagger a_{\boldsymbol{m}+\boldsymbol{R}} + a_{\boldsymbol{m}}^\dagger a_{\boldsymbol{m}+\boldsymbol{R}}^\dagger \right) \end{aligned} \tag{A.26}$$

$$\begin{aligned}\mathcal{H}_m^{\mathrm{BB}} &= \sum_{\boldsymbol{R}} J_x^{\mathrm{F}} \left(S^2 - S b_{\boldsymbol{m}}^\dagger b_{\boldsymbol{m}} - S b_{\boldsymbol{m}+\boldsymbol{R}}^\dagger b_{\boldsymbol{m}+\boldsymbol{R}} \right) \\ &\quad + \frac{J_y^{\mathrm{F}} S}{2} \left(b_{\boldsymbol{m}} b_{\boldsymbol{m}+\boldsymbol{R}} + b_{\boldsymbol{m}} b_{\boldsymbol{m}+\boldsymbol{R}}^\dagger + b_{\boldsymbol{m}}^\dagger b_{\boldsymbol{m}+\boldsymbol{R}} + b_{\boldsymbol{m}}^\dagger b_{\boldsymbol{m}+\boldsymbol{R}}^\dagger \right) \\ &\quad - \frac{J_z^{\mathrm{F}} S}{2} \left(b_{\boldsymbol{m}} b_{\boldsymbol{m}+\boldsymbol{R}} - b_{\boldsymbol{m}} b_{\boldsymbol{m}+\boldsymbol{R}}^\dagger - b_{\boldsymbol{m}}^\dagger b_{\boldsymbol{m}+\boldsymbol{R}} + b_{\boldsymbol{m}}^\dagger b_{\boldsymbol{m}+\boldsymbol{R}}^\dagger \right) \end{aligned} \tag{A.27}$$

$$\begin{aligned}\sum_{\boldsymbol{m}} \mathcal{H}_m^{\mathrm{AA}} &= N z_{\boldsymbol{R}} J_x^{\mathrm{F}}(\boldsymbol{0}) S^2 \\ &\quad + S \sum_{\boldsymbol{Q}} -2 z_{\boldsymbol{R}} J_x^{\mathrm{F}}(\boldsymbol{0}) a_{\boldsymbol{Q}}^\dagger a_{\boldsymbol{Q}} \\ &\quad + \frac{1}{2}\left[J_y^{\mathrm{F}}(-\boldsymbol{Q}) - J_z^{\mathrm{F}}(-\boldsymbol{Q}) \right] a_{\boldsymbol{Q}} a_{-\boldsymbol{Q}} + \frac{1}{2}\left[J_y^{\mathrm{F}}(\boldsymbol{Q}) - J_z^{\mathrm{F}}(\boldsymbol{Q}) \right] a_{\boldsymbol{Q}}^\dagger a_{-\boldsymbol{Q}}^\dagger \\ &\quad + \frac{1}{2}\left[J_y^{\mathrm{F}}(-\boldsymbol{Q}) + J_z^{\mathrm{F}}(-\boldsymbol{Q}) \right] a_{\boldsymbol{Q}} a_{\boldsymbol{Q}}^\dagger + \frac{1}{2}\left[J_y^{\mathrm{F}}(\boldsymbol{Q}) + J_z^{\mathrm{F}}(\boldsymbol{Q}) \right] a_{\boldsymbol{Q}}^\dagger a_{\boldsymbol{Q}} \end{aligned} \tag{A.28}$$

$$\begin{aligned}\sum_{\boldsymbol{m}} \mathcal{H}_m^{\mathrm{BB}} &= N z_{\boldsymbol{R}} J_x^{\mathrm{F}}(\mathbf{0}) S^2 \\ &\quad + S \sum_{\boldsymbol{Q}} -2 z_{\boldsymbol{R}} J_x^{\mathrm{F}}(\mathbf{0}) b_{\boldsymbol{Q}}^\dagger b_{\boldsymbol{Q}} \\ &\qquad + \frac{1}{2}\left[J_y^{\mathrm{F}}(-\boldsymbol{Q}) - J_z^{\mathrm{F}}(-\boldsymbol{Q})\right] b_{\boldsymbol{Q}} b_{-\boldsymbol{Q}} + \frac{1}{2}\left[J_y^{\mathrm{F}}(\boldsymbol{Q}) - J_z^{\mathrm{F}}(\boldsymbol{Q})\right] b_{\boldsymbol{Q}}^\dagger b_{-\boldsymbol{Q}}^\dagger \\ &\qquad + \frac{1}{2}\left[J_y^{\mathrm{F}}(-\boldsymbol{Q}) + J_z^{\mathrm{F}}(-\boldsymbol{Q})\right] b_{\boldsymbol{Q}} b_{\boldsymbol{Q}}^\dagger + \frac{1}{2}\left[J_y^{\mathrm{F}}(\boldsymbol{Q}) + J_z^{\mathrm{F}}(\boldsymbol{Q})\right] b_{\boldsymbol{Q}}^\dagger b_{\boldsymbol{Q}}\end{aligned} \tag{A.29}$$

	$a_{\boldsymbol{m}}$	$a_{\boldsymbol{m}+\boldsymbol{r}}$	$a^\dagger_{\boldsymbol{m}}$	$a^\dagger_{\boldsymbol{m}+\boldsymbol{r}}$	$b_{\boldsymbol{m}}$	$b_{\boldsymbol{m}+\boldsymbol{r}}$	$b^\dagger_{\boldsymbol{m}}$	$b^\dagger_{\boldsymbol{m}+\boldsymbol{r}}$
$a_{\boldsymbol{m}}$	$a_{\boldsymbol{Q}}a_{-\boldsymbol{Q}}$	$e^{-\mathrm{i}\boldsymbol{Q}\cdot\boldsymbol{r}}a_{\boldsymbol{Q}}a_{-\boldsymbol{Q}}$	$a_{\boldsymbol{Q}}a^\dagger_{\boldsymbol{Q}}$	$e^{-\mathrm{i}\boldsymbol{Q}\cdot\boldsymbol{r}}a_{\boldsymbol{Q}}a^\dagger_{\boldsymbol{Q}}$	$a_{\boldsymbol{Q}}b_{-\boldsymbol{Q}}$	$e^{-\mathrm{i}\boldsymbol{Q}\cdot\boldsymbol{r}}a_{\boldsymbol{Q}}b_{-\boldsymbol{Q}}$	$a_{\boldsymbol{Q}}b^\dagger_{\boldsymbol{Q}}$	$e^{-\mathrm{i}\boldsymbol{Q}\cdot\boldsymbol{r}}a_{\boldsymbol{Q}}b^\dagger_{\boldsymbol{Q}}$
$a_{\boldsymbol{m}+\boldsymbol{r}}$	$e^{\mathrm{i}\boldsymbol{Q}\cdot\boldsymbol{r}}a_{\boldsymbol{Q}}a_{-\boldsymbol{Q}}$	$a_{\boldsymbol{Q}}a_{-\boldsymbol{Q}}$	$e^{\mathrm{i}\boldsymbol{Q}\cdot\boldsymbol{r}}a_{\boldsymbol{Q}}a^\dagger_{\boldsymbol{Q}}$	$a_{\boldsymbol{Q}}a^\dagger_{\boldsymbol{Q}}$	$e^{\mathrm{i}\boldsymbol{Q}\cdot\boldsymbol{r}}a_{\boldsymbol{Q}}b_{-\boldsymbol{Q}}$	$a_{\boldsymbol{Q}}b_{-\boldsymbol{Q}}$	$e^{\mathrm{i}\boldsymbol{Q}\cdot\boldsymbol{r}}a_{\boldsymbol{Q}}b^\dagger_{\boldsymbol{Q}}$	$a_{\boldsymbol{Q}}b^\dagger_{\boldsymbol{Q}}$
$a^\dagger_{\boldsymbol{m}}$	$a^\dagger_{\boldsymbol{Q}}a_{\boldsymbol{Q}}$	$e^{\mathrm{i}\boldsymbol{Q}\cdot\boldsymbol{r}}a^\dagger_{\boldsymbol{Q}}a_{\boldsymbol{Q}}$	$a^\dagger_{\boldsymbol{Q}}a^\dagger_{-\boldsymbol{Q}}$	$e^{\mathrm{i}\boldsymbol{Q}\cdot\boldsymbol{r}}a^\dagger_{\boldsymbol{Q}}a^\dagger_{-\boldsymbol{Q}}$	$a^\dagger_{\boldsymbol{Q}}b_{\boldsymbol{Q}}$	$e^{\mathrm{i}\boldsymbol{Q}\cdot\boldsymbol{r}}a^\dagger_{\boldsymbol{Q}}b_{\boldsymbol{Q}}$	$a^\dagger_{\boldsymbol{Q}}b^\dagger_{-\boldsymbol{Q}}$	$e^{\mathrm{i}\boldsymbol{Q}\cdot\boldsymbol{r}}a^\dagger_{\boldsymbol{Q}}b^\dagger_{-\boldsymbol{Q}}$
$a^\dagger_{\boldsymbol{m}+\boldsymbol{r}}$	$e^{-\mathrm{i}\boldsymbol{Q}\cdot\boldsymbol{r}}a^\dagger_{\boldsymbol{Q}}a_{\boldsymbol{Q}}$	$a^\dagger_{\boldsymbol{Q}}a_{\boldsymbol{Q}}$	$e^{-\mathrm{i}\boldsymbol{Q}\cdot\boldsymbol{r}}a^\dagger_{\boldsymbol{Q}}a^\dagger_{-\boldsymbol{Q}}$	$a^\dagger_{\boldsymbol{Q}}a^\dagger_{-\boldsymbol{Q}}$	$e^{-\mathrm{i}\boldsymbol{Q}\cdot\boldsymbol{r}}a^\dagger_{\boldsymbol{Q}}b_{\boldsymbol{Q}}$	$a^\dagger_{\boldsymbol{Q}}b_{\boldsymbol{Q}}$	$e^{-\mathrm{i}\boldsymbol{Q}\cdot\boldsymbol{r}}a^\dagger_{\boldsymbol{Q}}b^\dagger_{-\boldsymbol{Q}}$	$a^\dagger_{\boldsymbol{Q}}b^\dagger_{-\boldsymbol{Q}}$
$b_{\boldsymbol{m}}$	$b_{\boldsymbol{Q}}a_{-\boldsymbol{Q}}$	$e^{-\mathrm{i}\boldsymbol{Q}\cdot\boldsymbol{r}}b_{\boldsymbol{Q}}a_{-\boldsymbol{Q}}$	$b_{\boldsymbol{Q}}a^\dagger_{\boldsymbol{Q}}$	$e^{-\mathrm{i}\boldsymbol{Q}\cdot\boldsymbol{r}}b_{\boldsymbol{Q}}a^\dagger_{\boldsymbol{Q}}$	$b_{\boldsymbol{Q}}b_{-\boldsymbol{Q}}$	$e^{-\mathrm{i}\boldsymbol{Q}\cdot\boldsymbol{r}}b_{\boldsymbol{Q}}b_{-\boldsymbol{Q}}$	$b_{\boldsymbol{Q}}b^\dagger_{\boldsymbol{Q}}$	$e^{-\mathrm{i}\boldsymbol{Q}\cdot\boldsymbol{r}}b_{\boldsymbol{Q}}b^\dagger_{\boldsymbol{Q}}$
$b_{\boldsymbol{m}+\boldsymbol{r}}$	$e^{\mathrm{i}\boldsymbol{Q}\cdot\boldsymbol{r}}b_{\boldsymbol{Q}}a_{-\boldsymbol{Q}}$	$b_{\boldsymbol{Q}}a_{-\boldsymbol{Q}}$	$e^{\mathrm{i}\boldsymbol{Q}\cdot\boldsymbol{r}}b_{\boldsymbol{Q}}a^\dagger_{\boldsymbol{Q}}$	$b_{\boldsymbol{Q}}a^\dagger_{\boldsymbol{Q}}$	$e^{\mathrm{i}\boldsymbol{Q}\cdot\boldsymbol{r}}b_{\boldsymbol{Q}}b_{-\boldsymbol{Q}}$	$b_{\boldsymbol{Q}}b_{-\boldsymbol{Q}}$	$e^{\mathrm{i}\boldsymbol{Q}\cdot\boldsymbol{r}}b_{\boldsymbol{Q}}b^\dagger_{\boldsymbol{Q}}$	$b_{\boldsymbol{Q}}b^\dagger_{\boldsymbol{Q}}$
$b^\dagger_{\boldsymbol{m}}$	$b^\dagger_{\boldsymbol{Q}}a_{\boldsymbol{Q}}$	$e^{\mathrm{i}\boldsymbol{Q}\cdot\boldsymbol{r}}b^\dagger_{\boldsymbol{Q}}a_{\boldsymbol{Q}}$	$b^\dagger_{\boldsymbol{Q}}a^\dagger_{-\boldsymbol{Q}}$	$e^{\mathrm{i}\boldsymbol{Q}\cdot\boldsymbol{r}}b^\dagger_{\boldsymbol{Q}}a^\dagger_{-\boldsymbol{Q}}$	$b^\dagger_{\boldsymbol{Q}}b_{\boldsymbol{Q}}$	$e^{\mathrm{i}\boldsymbol{Q}\cdot\boldsymbol{r}}b^\dagger_{\boldsymbol{Q}}b_{\boldsymbol{Q}}$	$b^\dagger_{\boldsymbol{Q}}b^\dagger_{-\boldsymbol{Q}}$	$e^{\mathrm{i}\boldsymbol{Q}\cdot\boldsymbol{r}}b^\dagger_{\boldsymbol{Q}}b^\dagger_{-\boldsymbol{Q}}$
$b^\dagger_{\boldsymbol{m}+\boldsymbol{r}}$	$e^{-\mathrm{i}\boldsymbol{Q}\cdot\boldsymbol{r}}b^\dagger_{\boldsymbol{Q}}a_{\boldsymbol{Q}}$	$b^\dagger_{\boldsymbol{Q}}a_{\boldsymbol{Q}}$	$e^{-\mathrm{i}\boldsymbol{Q}\cdot\boldsymbol{r}}b^\dagger_{\boldsymbol{Q}}a^\dagger_{-\boldsymbol{Q}}$	$b^\dagger_{\boldsymbol{Q}}a^\dagger_{-\boldsymbol{Q}}$	$e^{-\mathrm{i}\boldsymbol{Q}\cdot\boldsymbol{r}}b^\dagger_{\boldsymbol{Q}}b_{\boldsymbol{Q}}$	$b^\dagger_{\boldsymbol{Q}}b_{\boldsymbol{Q}}$	$e^{-\mathrm{i}\boldsymbol{Q}\cdot\boldsymbol{r}}b^\dagger_{\boldsymbol{Q}}b^\dagger_{-\boldsymbol{Q}}$	$b^\dagger_{\boldsymbol{Q}}b^\dagger_{-\boldsymbol{Q}}$

Table A.1: Fourier transform identities of the form, $\sum_{\boldsymbol{m}} a_{\boldsymbol{m}}b_{\boldsymbol{m}} = \sum_{\boldsymbol{Q}} a_{\boldsymbol{Q}}b_{\boldsymbol{Q}}$.

Bibliography

[1] *Compass*. Encyclopaedia Britannica Online Academic Ed. Encyclopaedia Britannica Inc., 2012.

[2] S. J. Blundell. *Magnetism in condensed matter*. Oxford University Press, Oxford, 2001.

[3] P. Fazekas. *Lecture notes on electronc correlations and magnetism*. Series in Modern Condensed Matter Physics. World Scientific Publishing Co. Pte. Ltd., Singapore, 1999.

[4] J. B. Goodenough. *Phys. Rev.*, **100**(2):564, 1955.

[5] J. Kanamori. *J. Phys. Chem. Solid*, **10**:87, 1959.

[6] P. W. Anderson. Solid state physics. volume 14, page 99. Academic Press, New York and London, 1963.

[7] R. Skomski. *Simple models of magnetism*. Oxford University Press, New York, 2008.

[8] D. Feng and G. Jin. *Introduction to condensed matter physics*. World Scientific, Hackensack, N.J. ; London, 2005.

[9] H. Jahn and E. Teller. *Phys. Rev.*, **49**:874, 1936.

[10] T. Holstein and H. Primakoff. *Phys. Rev.*, **58**(12):1098, 1940.

[11] L. J. de Jongh and A. R. Miedema. *Adv. Phys.*, **23**:1, 1974.

[12] R. Coldea, R. A. Cowley, T. G. Perring, D. F. McMorrow, and B. Roessli. *Phys. Rev. B*, **57**(9):5281–5290, 1998.

[13] J. Bardeen, L. N. Cooper, and J. R. Schrieffer. *Phys. Rev.*, **106**(1):162–164, 1957.

[14] J. Bardeen, L. N. Cooper, and J. R. Schrieffer. *Phys. Rev.*, **108**(5):1175–1204, 1957.

[15] J. G. Bednorz and K. A. Müller. *Z. Phys. B*, **64**(2):189–193, 1986.

[16] S. N. Putilin, E. V. Antipov, O. Chmaissem, and M. Marezio. *Nature*, **362**(6417):226–228, 1993.

[17] A. Schilling, M. Cantoni, J. D. Guo, and H. R. Ott. *Nature*, **363**(6424):56–58, 1993.

[18] L. Gao, Y. Y. Xue, F. Chen, Q. Xiong, R. L. Meng, D. Ramirez, C. W. Chu, J. H. Eggert, and H. K. Mao. *Phys. Rev. B*, **50**(6):4260–4263, 1994.

[19] C. Varma. *Nature*, **468**(7321):184–185, 2010.

[20] N. M. Plakida. *High-temperature cuprate superconductors: experiment, theory, and applications*. Springer series in solid-state sciences. Springer-Verlag, Berlin; London, 2010.

[21] D. M. Broun. *Nature Phys.*, **4**(3):170–172, 2008.

[22] S. Sachdev. *Phys. Status Solidi B*, **247**(3):537–543, 2010.

[23] P. J. Hirschfeld, M. M. Korshunov, and I. I. Mazin. *Rep. Prog. Phys.*, **74**(12), 2011.

[24] Y. Kamihara, H. Hiramatsu, M. Hirano, R. Kawamura, H. Yanagi, T. Kamiya, and H. Hosono. *J. Am. Chem. Soc.*, **128**(31):10012–10013, 2006.

[25] Y. Kamihara, T. Watanabe, M. Hirano, and H. Hosono. *J. Am. Chem. Soc.*, **130**(11):3296, 2008.

[26] I. I. Mazin, D. J. Singh, M. D. Johannes, and M. H. Du. *Phys. Rev. Lett.*, **101**(5):057003, 2008.

[27] D. C. Johnston. *Adv. Phys.*, **59**(6):803 – 1061, 2010.

[28] M. Braden, P. Steffens, Y. Sidis, J. Kulda, P. Bourges, S. Hayden, N. Kikugawa, and Y. Maeno. *Phys. Rev. Lett.*, **92**(9):097402, 2004.

[29] J. B. Ketterson and S. N. Song. *Superconductivity*. Cambridge University Press, Cambridge, 1999.

[30] K. F. Wang, J. M. Liu, and Z. F. Ren. *Adv. Phys.*, **58**(4):321–448, 2009.

[31] M. Fiebig. *J. Phys. D: Appl. Phys.*, **38**(8):R123–R152, 2005.

[32] D. I. Khomskii. *Physics*, **2**:20, 2009.

[33] E. F. Bertaut. *J. Phys. Colloq.*, **C1**:462, 1971.

[34] S. W. Cheong and M. Mostovoy. *Nature Mater.*, **6**(1):13–20, 2007.

[35] I. Dzyaloshinskii. *Sov. Phys. JETP*, **19**:960–971, 1964.

[36] T. Moriya. *Phys. Rev.*, **120**:91–98, 1960.

[37] H. Katsura, N. Nagaosa, and A. V. Balatsky. *Phys. Rev. Lett.*, **95**(5):057205, 2005.

[38] C. D. Hu. *Phys. Rev. B*, **77**(17):174418, 2008.

[39] J. P. Hu. *Phys. Rev. Lett.*, **100**(7):077202, 2008.

[40] R. Coldea, D. A. Tennant, R. A. Cowley, D. F. McMorrow, B. Dorner, and Z. Tylczynski. *J. Phys.: Condens. Matter*, **8**(40):7473–7491, 1996.

[41] Y. J. Choi, H. T. Yi, S. Lee, Q. Huang, V. Kiryukhin, and S. W. Cheong. *Phys. Rev. Lett.*, **100**(4):047601, 2008.

[42] T. Kimura, Y. Sekio, H. Nakamura, T. Siegrist, and A. P. Ramirez. *Nature Mater.*, **7**(4):291–294, 2008.

[43] J. Chadwick. *Nature*, **129**:312, 1932.

[44] G. L. Squires. *Introduction to the theory of thermal neutron scattering*. Dover Publications, Mineola, N.Y., 1996.

[45] S. W. Lovesey. *Theory of neutron scattering from condensed matter*. Oxford science publications. Clarendon Press, Oxford, 1984.

[46] G. Shirane, S. M. Shapiro, and J. M. Tranquada. *Neutron scattering with a triple-axis spectrometer: basic techniques*. Cambridge University Press, New York, 2002.

[47] A. Furrer, J. Mesot, and T. Strässle. *Neutron Scattering in Condensed Matter Physics (Neutron Techniques and Applications)*. World Scientific Publishing Company, 2009.

[48] T. Chatterji. *Neutron scattering from magnetic materials*. Elsevier, Amsterdam; London, 2006.

[49] A. J. Dianoux and G. Lander. *Neutron Data Booklet*. Old City Publishing Inc, 2nd edition, 2003.

[50] I. A. Zaliznyak and S. H. Lee. *Magnetic neutron scattering*. Brookhaven National Laboratory, Upton, N.Y., 2004.

[51] A. Longmore, A. T. Boothroyd, C. Changkang, H. Yongle, M. P. Nutley, N. H. Andersen, H. Casalta, P. Schleger, and A. N. Christensen. *Phys. Rev. B*, **53**(14):9382–9395, 1996.

[52] J. Jensen and A. R. Mackintosh. *Rare earth magnetism : structures and excitations*. International series of monographs on physics. Clarendon Press, Oxford, 1991.

[53] F. Tasset. *Physica B*, **297**(1-4):1–8, 2001.

[54] M. Blume. *Phys. Rev.*, **130**(5):1670, 1963.

[55] Y. Izyumov and S. Maleyev. *Sov. Phys. JETP*, **14**:1168, 1962.

[56] B. Roessli and P. Böni. Polarised neutron scattering. volume 2, page 1242. Academic Press, London, 2001.

[57] Y.A. Izyumov, V.E. Naish, and R.P. Ozerov. *Neutron diffraction of magnetic materials*. Consultants Bureau, New York, 1991.

[58] E. F. Bertaut. *J. Appl. Phys.*, **33**(3):1138, 1962.

[59] E. F. Bertaut. *Acta Crystallogr.*, **A24**:217, 1968.

[60] E. F. Bertaut. *J. Magn. Magn. Mater.*, **24**(3):267–278, 1981.

[61] Y. A. Izyumov, V. Y. Naysh, S. B. Petrov, and V. N. Syromyatnikov. *Fiz. Metal. I*, **47**(2):231–246, 1979.

[62] Y. A. Izyumov and V. E. Naish. *J. Magn. Magn. Mater.*, **12**(3):239–248, 1979.

[63] Y. A. Izyumov, V. E. Naish, and V. N. Syromiatnikov. *J. Magn. Magn. Mater.*, **12**(3):249–261, 1979.

[64] Y. A. Izyumov, V. E. Naish, and S. B. Petrov. *J. Magn. Magn. Mater.*, **13**(3):267–274, 1979.

[65] Y. A. Izyumov, V. E. Naish, and S. B. Petrov. *J. Magn. Magn. Mater.*, **13**(3):275–282, 1979.

[66] A. S. Wills. *Physica B*, **276**:680–681, 2000.

[67] J. Rodriguez-Carvajal. *BasiReps*.

[68] A. S. Wills. *Phys. Rev. B*, **63**(6):064430, 2001.

[69] R. Rinaldi, L. Liang, and H. Schober. Neutron applications in earth, energy, and environmental sciences. Neutron Scattering Applications and Techniques. Springer US, 2009.

[70] D. C. Tennant. *Rev. Sci. Instrum.*, **59**(2):380–381, 1988.

[71] A. Zheludev. *ResLib 3.4c*. Oak Ridge National Laboratory, Oak Ridge, 2006.

[72] F. Tasset. *Physica B*, **156-157**:627–630, 1989.

[73] F. Tasset, E. Lelièvre-Berna, T. W. Roberts, E. Bourgeat-Lami, S. Pujol, and M. Thomas. *Physica B*, **241**:177–179, 1997.

[74] L. P. Regnault, B. Geffray, P. Fouilloux, B. Longuet, F. Mantegezza, F. Tasset, E. Lelièvre-Berna, E. Bourgeat-Lami, M. Thomas, and Y. Gibert. *Physica B*, **335**(1-4):255–258, 2003.

[75] L. P. Regnault, B. Geffray, P. Fouilloux, B. Longuet, F. Mantegazza, F. Tasset, E. Lelièvre-Berna, S. Pujol, E. Bourgeat-Lami, N. Kernavanois, M. Thomas, and Y. Gibert. *Physica B*, **350**(1-3):E811–E814, 2004.

[76] M. Janoschek, S. Klimko, R. Gähler, B. Roessli, and P. Böni. *Physica B*, **397**(1-2):125–130, 2007.

[77] F. Hippert, E. Geissler, J. L. Hodeau, E. Lelièvre-Berna, and J.-R. Regnard. *Neutron and X-ray Spectroscopy*. Springer, Dordrecht, 2006.

[78] J. M. Tranquada, B. J. Sternlieb, J. D. Axe, Y. Nakamura, and S. Uchida. *Nature*, **375**(6532):561–563, 1995.

[79] C. H. Chen, S. W. Cheong, and A. S. Cooper. *Phys. Rev. Lett.*, **71**(15):2461, 1993.

[80] J. M. Tranquada, D. J. Buttrey, V. Sachan, and J. E. Lorenzo. *Phys. Rev. Lett.*, **73**(7):1003, 1994.

[81] P. Wochner, J. M. Tranquada, D. J. Buttrey, and V. Sachan. *Phys. Rev. B*, **57**(2):1066, 1998.

[82] H. Yoshizawa, T. Kakeshita, R. Kajimoto, T. Tanabe, T. Katsufuji, and Y. Tokura. *Phys. Rev. B*, **61**(2):R854, 2000.

[83] A. T. Boothroyd, P. G. Freeman, D. Prabhakaran, A. Hiess, M. Enderle, J. Kulda, and F. Altorfer. *Phys. Rev. Lett.*, **91**(25):257201, 2003.

[84] A. T. Boothroyd, D. Prabhakaran, P. G. Freeman, S. J. S. Lister, M. Enderle, A. Hiess, and J. Kulda. *Phys. Rev. B*, **67**(10):100407, 2003.

[85] M. Cwik, M. Benomar, T. Finger, Y. Sidis, D. Senff, M. Reuther, T. Lorenz, and M. Braden. *Phys. Rev. Lett.*, **102**(5):057201–4, 2009.

[86] N. Hollmann, M. W. Haverkort, M. Cwik, M. Benomar, M. Reuther, A. Tanaka, and T. Lorenz. *New J. Phys.*, **10**(2):023018, 2008.

[87] C. F. Chang, Z. Hu, Hua Wu, T. Burnus, N. Hollmann, M. Benomar, T. Lorenz, A. Tanaka, H. J. Lin, H. H. Hsieh, C. T. Chen, and L. H. Tjeng. *Phys. Rev. Lett.*, **102**(11):116401–4, 2009.

[88] P. Babkevich, D. Prabhakaran, C. D. Frost, and A. T. Boothroyd. *Phys. Rev. B*, **82**(18):184425, 2010.

[89] K. Yamada, M. Matsuda, Y. Endoh, B. Keimer, R. J. Birgeneau, S. Onodera, J. Mizusaki, T. Matsuura, and G. Shirane. *Phys. Rev. B*, **39**(4):2336, 1989.

[90] J. T. Lewandowski, R. A. Beyerlein, J. M. Longo, and R. A. McCauley. *J. Am. Ceram. Soc.*, **69**(9):699–703, 1986.

[91] R. A. Mohan Ram, P. Ganguly, C. N. R. Rao, and J. M. Honig. *Mat. Res. Bull.*, **23**(4):501–506, 1988.

[92] T. Kajitani, S. Hosoya, K. Hiraga, and T. Fukuda. *J. Phys. Soc. Jpn.*, **59**(2):562–570, 1990.

[93] S. T. Bramwell and P. C. W. Holdsworth. *J. Phys. Condens. Matter*, **5**(4):L53–L59, 1993.

[94] F. Xiao, F. M. Woodward, C. P. Landee, M. M. Turnbull, C. Mielke, N. Harrison, T. Lancaster, S. J. Blundell, P. J. Baker, P. Babkevich, and F. L. Pratt. *Phys. Rev. B*, **79**(13):134412, 2009.

[95] W. E. Fischer. *Physica B*, **234**:1202–1208, 1997.

[96] F. Semadeni, B. Roessli, and P. Böni. *Physica B*, **297**(1-4):152–154, 2001.

[97] A. Poole and B. Roessli. *J. Phys.: Conf. Ser.*, **340**(1):012017, 2012.

[98] L. M. Helme, A. T. Boothroyd, R. Coldea, D. Prabhakaran, C. D. Frost, D. A. Keen, L. P. Regnault, P. G. Freeman, M. Enderle, and J. Kulda. *Phys. Rev. B*, **80**(13):134414, 2009.

[99] T. G. Perring and C. D. Frost. *Neutron News*, **15**(1):1 – 1, 2004.

[100] R. Coldea. *MSLICE: a data analysis programme for time-of-flight neutron spectrometers*, 2009.

[101] R. M. White, M. Sparks, and I. Ortenburger. *Phys. Rev.*, **139**(2A):A450, 1965.

[102] N. Metropolis, A. W. Rosenbluth, M. N. Rosenbluth, A. H. Teller, and E. Teller. *J. Chem. Phys.*, **21**(6):1087–1092, 1953.

[103] Ch. Kant, T. Rudolf, F. Schrettle, F. Mayr, J. Deisenhofer, P. Lunkenheimer, M. V. Eremin, and A. Loidl. *Phys. Rev. B*, **78**(24):245103, 2008.

[104] *Data from Neutron News*, **3**(3):29–37.

[105] A. C. Walters, T. G. Perring, J. S. Caux, A. T. Savici, G. D. Gu, C. C. Lee, W. Ku, and I. A. Zaliznyak. *Nature Phys.*, **5**(12):867–872, 2009.

[106] R. Coldea, S. M. Hayden, G. Aeppli, T. G. Perring, C. D. Frost, T. E. Mason, S. W. Cheong, and Z. Fisk. *Phys. Rev. Lett.*, **86**(23):5377, 2001.

[107] N. S. Headings, S. M. Hayden, R. Coldea, and T. G. Perring. *Phys. Rev. Lett.*, **105**(24):247001, 2010.

[108] Y. J. Kim, A. Aharony, R. J. Birgeneau, F. C. Chou, O. Entin-Wohlman, R. W. Erwin, M. Greven, A. B. Harris, M. A. Kastner, I. Y. Korenblit, Y. S. Lee, and G. Shirane. *Phys. Rev. Lett.*, **83**(4):852–855, 1999.

[109] H. M. Rønnow, D. F. McMorrow, R. Coldea, A. Harrison, I. D. Youngson, T. G. Perring, G. Aeppli, O. Syljuåsen, K. Lefmann, and C. Rischel. *Phys. Rev. Lett.*, **87**(3):037202, 2001.

[110] N. B. Christensen, H. M. Rønnow, D. F. McMorrow, A. Harrison, T. G. Perring, M. Enderle, R. Coldea, L. P. Regnault, and G. Aeppli. *PNAS*, **104**:15264–15269, 2007.

[111] T. Huberman, R. Coldea, R. A. Cowley, D. A. Tennant, R. L. Leheny, R. J. Christianson, and C. D. Frost. *Phys. Rev. B*, **72**(1):014413, 2005.

[112] N. Ichikawa, S. Uchida, J. M. Tranquada, T. Niemöller, P. M. Gehring, S. H. Lee, and J. R. Schneider. *Phys. Rev. Lett.*, **85**(8):1738, 2000.

[113] J. M. Tranquada, J. D. Axe, N. Ichikawa, A. R. Moodenbaugh, Y. Nakamura, and S. Uchida. *Phys. Rev. Lett.*, **78**(2):338–341, 1997.

[114] Y. Moritomo, K. Higashi, K. Matsuda, and A. Nakamura. *Phys. Rev. B*, **55**(22):R14725, 1997.

[115] I. A. Zaliznyak, J. M. Tranquada, R. Erwin, and Y. Moritomo. *Phys. Rev. B*, **64**(19):195117, 2001.

[116] A. T. Boothroyd, P. Babkevich, D. Prabhakaran, and P. G. Freeman. *Nature*, **471**(7338):341–344, 2011.

[117] I. A. Campbell. *Phys. Rev. B*, **37**(16):9800, 1988.

[118] P. G. Freeman, A. T. Boothroyd, D. Prabhakaran, and J. Lorenzana. *Phys. Rev. B*, **73**(1):014434–10, 2006.

[119] V. Sachan, D. J. Buttrey, J. M. Tranquada, J. E. Lorenzo, and G. Shirane. *Phys. Rev. B*, **51**(18):12742–12746, 1995.

[120] S. Wakimoto, R. J. Birgeneau, M. A. Kastner, Y. S. Lee, R. Erwin, P. M. Gehring, S. H. Lee, M. Fujita, K. Yamada, Y. Endoh, K. Hirota, and G. Shirane. *Phys. Rev. B*, **61**(5):3699, 2000.

[121] K. Yamada, C. H. Lee, K. Kurahashi, J. Wada, S. Wakimoto, S. Ueki, H. Kimura, Y. Endoh, S. Hosoya, G. Shirane, R. J. Birgeneau, M. Greven, M. A. Kastner, and Y. J. Kim. *Phys. Rev. B*, **57**(10):6165–6172, 1998.

[122] S. H. Lee, S. W. Cheong, K. Yamada, and C. F. Majkrzak. *Phys. Rev. B*, **63**(6):060405, 2001.

[123] S. Süllow, G. J. Nieuwenhuys, A. A. Menovsky, J. A. Mydosh, S. A. M. Mentink, T. E. Mason, and W. J. L. Buyers. *Phys. Rev. Lett.*, **78**(2):354–357, 1997.

[124] V. K. Anand, D. T. Adroja, A. D. Hillier, J. Taylor, and G. Andre. *Phys. Rev. B*, **84**(6):064440, 2011.

[125] A. Fukaya, A. Ito, K. Nakajima, and K. Kakurai. *J. Phys. Chem. Solids*, **60**(8-9):1245–1247, 1999.

[126] M. Arai, T. Nishijima, Y. Endoh, T. Egami, S. Tajima, K. Tomimoto, Y. Shiohara, M. Takahashi, A. Garrett, and S. M. Bennington. *Phys. Rev. Lett.*, **83**(3):608–611, 1999.

[127] P. Bourges, Y. Sidis, H. F. Fong, L. P. Regnault, J. Bossy, A. Ivanov, and B. Keimer. *Science*, **288**(5469):1234–1237, 2000.

[128] S. M. Hayden, H. A. Mook, P. Dai, T. G. Perring, and F. Dogan. *Nature*, **429**(6991):531–534, 2004.

[129] N. B. Christensen, D. F. McMorrow, H. M. Rønnow, B. Lake, S. M. Hayden, G. Aeppli, T. G. Perring, M. Mangkorntong, M. Nohara, and H. Takagi. *Phys. Rev. Lett.*, **93**(14), 2004.

[130] B. Vignolle, S. M. Hayden, D. F. McMorrow, H. M. Rønnow, B. Lake, C. D. Frost, and T. G. Perring. *Nature Phys.*, **3**(3):163–167, 2007.

[131] G. Y. Xu, G. D. Gu, M. Hucker, B. Fauque, T. G. Perring, L. P. Regnault, and J. M. Tranquada. *Nature Phys.*, **5**(9):642–646, 2009.

[132] M. Matsuda, M. Fujita, S. Wakimoto, J. A. Fernandez-Baca, J. M. Tranquada, and K. Yamada. *Phys. Rev. Lett.*, **101**(19), 2008.

[133] O. J. Lipscombe, B. Vignolle, T. G. Perring, C. D. Frost, and S. M. Hayden. *Phys. Rev. Lett.*, **102**(16), 2009.

[134] V. Hinkov, P. Bourges, S. Pailhes, Y. Sidis, A. Ivanov, C. D. Frost, T. G. Perring, C. T. Lin, D. P. Chen, and B. Keimer. *Nature Phys.*, **3**(11):780–785, 2007.

[135] J. M. Tranquada, H. Woo, T. G. Perring, H. Goka, G. D. Gu, G. Xu, M. Fujita, and K. Yamada. *Nature*, **429**(6991):534–538, 2004.

[136] J. M. Tranquada, H. Woo, T. G. Perring, H. Goka, G. D. Gu, G. Xu, M. Fujita, and K. Yamada. *J. Phys. Chem. Solids*, **67**(1-3):511–515, 2006.

[137] M. Eschrig. *Adv. Phys.*, **55**(1-2):47–183, 2006.

[138] J. M. Tranquada. Neutron scattering studies of antiferromagnetic correlations in cuprates handbook of high-temperature superconductivity. pages 257–298. Springer New York, 2007.

[139] E. C. Andrade and M. Vojta. *arXiv:1204.6323v1*, 2012.

[140] H. J. Woo, A. T. Boothroyd, K. Nakajima, T. G. Perring, C. D. Frost, P. G. Freeman, D. Prabhakaran, K. Yamada, and J. M. Tranquada. *Phys. Rev. B*, **72**(6):064437, 2005.

[141] H. Ulbrich, D. Senff, P. Steffens, O. J. Schumann, Y. Sidis, P. Reutler, A. Revcolevschi, and M. Braden. *Phys. Rev. Lett.*, **106**(15):157201, 2011.

[142] H. Ulbrich, P. Steffens, D. Lamago, Y. Sidis, and M. Braden. *arXiv:1112.1799v1*, 2011.

[143] S. A. Kivelson, I. P. Bindloss, E. Fradkin, V. Oganesyan, J. M. Tranquada, A. Kapitulnik, and C. Howald. *Rev. Mod. Phys.*, **75**(4):1201–1241, 2003.

[144] A. S. Sefat, R. Y. Jin, M. A. McGuire, B. C. Sales, D. J. Singh, and D. Mandrus. *Phys. Rev. Lett.*, **101**(11):117004, 2008.

[145] M. Rotter, M. Tegel, and D. Johrendt. *Phys. Rev. Lett.*, **101**(10):107006, 2008.

[146] G. F. Chen, Z. Li, G. Li, W. Z. Hu, J. Dong, J. Zhou, X. D. Zhang, P. Zheng, N. L. Wang, and J. L. Luo. *Chin. Phys. Lett.*, **25**(9):3403–3405, 2008.

[147] D. S. Inosov, A. Leineweber, X. P. Yang, J. T. Park, N. B. Christensen, R. Dinnebier, G. L. Sun, C. Niedermayer, D. Haug, P. W. Stephens, J. Stahn, O. Khvostikova, C. T. Lin, O. K. Andersen, B. Keimer, and V. Hinkov. *Phys. Rev. B*, **79**(22):224503, 2009.

[148] Z. Deng, X. C. Wang, Q. Q. Liu, S. J. Zhang, Y. X. Lv, J. L. Zhu, R. C. Yu, and C. Q. Jin. *Europhys. Lett.*, **87**(3), 2009.

[149] X. C. Wang, Q. Q. Liu, Y. X. Lv, W. B. Gao, L. X. Yang, R. C. Yu, F. Y. Li, and C. Q. Jin. *Solid State Commun.*, **148**(11-12):538–540, 2008.

[150] M. J. Pitcher, D. R. Parker, P. Adamson, S. J. C. Herkelrath, A. T. Boothroyd, R. M. Ibberson, M. Brunelli, and S. J. Clarke. *Chem. Commun.*, (45):5918–5920, 2008.

[151] C. W. Chu, F. Chen, M. Gooch, A. M. Guloy, B. Lorenz, B. Lv, K. Sasmal, Z. J. Tang, J. H. Tapp, and Y. Y. Xue. *Physica C*, **469**(9-12):326–331, 2009.

[152] J. H. Tapp, Z. J. Tang, B. Lv, K. Sasmal, B. Lorenz, P. C. W. Chu, and A. M. Guloy. *Phys. Rev. B*, **78**(6):060505, 2008.

[153] S. J. Zhang, X. C. Wang, Q. Q. Liu, Y. X. Lv, X. H. Yu, Z. J. Lin, Y. S. Zhao, L. Wang, Y. Ding, H. K. Mao, and C. Q. Jin. *Europhys. Lett.*, **88**(4):47008, 2009.

[154] X. Y. Zhu, F. Han, G. Mu, P. Cheng, B. Shen, B. Zeng, and H. H. Wen. *Phys. Rev. B*, **79**(22), 2009.

[155] H. Ogino, Y. Matsumura, Y. Katsura, K. Ushiyama, S. Horii, K. Kishio, and J. Shimoyama. *Supercond. Sci. Tech.*, **22**(7), 2009.

[156] F. C. Hsu, J. Y. Luo, K. W. Yeh, T. K. Chen, T. W. Huang, P. M. Wu, Y. C. Lee, Y. L. Huang, Y. Y. Chu, D. C. Yan, and M. K. Wu. *Proc. Natl. Acad. Sci. USA*, **105**(38):14262–14264, 2008.

[157] K. W. Yeh, T. W. Huang, Y. L. Huang, T. K. Chen, F. C. Hsu, P. M. Wu, Y. C. Lee, Y. Y. Chu, C. L. Chen, J. Y. Luo, D. C. Yan, and M. K. Wu. *Europhys. Lett.*, **84**(3), 2008.

[158] B. C. Sales, A. S. Sefat, M. A. McGuire, R. Y. Jin, D. Mandrus, and Y. Mozharivskyj. *Phys. Rev. B*, **79**(9), 2009.

[159] G. F. Chen, Z. G. Chen, J. Dong, W. Z. Hu, G. Li, X. D. Zhang, P. Zheng, J. L. Luo, and N. L. Wang. *Phys. Rev. B*, **79**(14):140509(R), 2009.

[160] R. Khasanov, M. Bendele, A. Amato, P. Babkevich, A. T. Boothroyd, A. Cervellino, K. Conder, S. N. Gvasaliya, H. Keller, H. H. Klauss, H. Luetkens, V. Pomjakushin, E. Pomjakushina, and B. Roessli. *Phys. Rev. B*, **80**(14):140511(R), 2009.

[161] M. H. Fang, H. M. Pham, B. Qian, T. J. Liu, E. K. Vehstedt, Y. Liu, L. Spinu, and Z. Q. Mao. *Phys. Rev. B*, **78**(22), 2008.

[162] C. Wang, L. J. Li, S. Chi, Z. W. Zhu, Z. Ren, Y. K. Li, Y. T. Wang, X. Lin, Y. K. Luo, S. A. Jiang, X. F. Xu, G. H. Cao, and Z. A. Xu. *Europhys. Lett.*, **83**(6), 2008.

[163] J. Zhao, Q. Huang, C. de la Cruz, J. W. Lynn, M. D. Lumsden, Z. A. Ren, J. Yang, X. L. Shen, X. L. Dong, Z. X. Zhao, and P. C. Dai. *Phys. Rev. B*, **78**(13), 2008.

[164] C. Lester, J. H. Chu, J. G. Analytis, S. C. Capelli, A. S. Erickson, C. L. Condron, M. F. Toney, I. R. Fisher, and S. M. Hayden. *Phys. Rev. B*, **80**(22), 2009.

[165] M. D. Lumsden and A. D. Christianson. *J. Phys.: Condens. Matter*, **22**(20):203203, 2010.

[166] P. Babkevich, M. Bendele, A. T. Boothroyd, K. Conder, S. N. Gvasaliya, R. Khasanov, E. Pomjakushina, and B. Roessli. *J. Phys.: Condens. Matter*, **22**(14):142202, 2010.

[167] M. Bendele, P. Babkevich, S. Katrych, S. N. Gvasaliya, E. Pomjakushina, K. Conder, B. Roessli, A. T. Boothroyd, R. Khasanov, and H. Keller. *Phys. Rev. B*, **82**(21):212504, 2010.

[168] P. Babkevich, B. Roessli, S. N. Gvasaliya, L. P. Regnault, P. G. Freeman, E. Pomjakushina, K. Conder, and A. T. Boothroyd. *Phys. Rev. B*, **83**(18):180506(R), 2011.

[169] M. Tegel, C. Löhnert, and D. Johrendt. *Solid State Commun.*, **150**(9-10):383–385, 2010.

[170] S. C. Speller, T. B. Britton, G. Hughes, S. Lozano-Perez, A. T. Boothroyd, E. Pomjakushina, K. Conder, and C. R. M. Grovenor. *Appl. Phys. Lett.*, **99**(19):192504, 2011.

[171] S. Margadonna, Y. Takabayashi, Y. Ohishi, Y. Mizuguchi, Y. Takano, T. Kagayama, T. Nakagawa, M. Takata, and K. Prassides. *Phys. Rev. B*, **80**(6):064506, 2009.

[172] Y. Mizuguchi, F. Tomioka, S. Tsuda, T. Yamaguchi, and Y. Takano. *Appl. Phys. Lett.*, **93**(15):152505–3, 2008.

[173] S. Medvedev, T. M. McQueen, I. A. Troyan, T. Palasyuk, M. I. Eremets, R. J. Cava, S. Naghavi, F. Casper, V. Ksenofontov, G. Wortmann, and C. Felser. *Nature Mater.*, **8**(8):630–633, 2009.

[174] G. Garbarino, A. Sow, P. Lejay, A. Sulpice, P. Toulemonde, M. Mezouar, and M. Nunez-Regueiro. *Europhys. Lett.*, **86**(2):27001, 2009.

[175] N. Katayama, S. D. Ji, D. Louca, S. Lee, M. Fujita, T. J. Sato, J. S. Wen, Z. J. Xu, G. D. Gu, G. Y. Xu, Z. W. Lin, M. Enoki, S. Chang, K. Yamada, and J. M. Tranquada. *J. Phys. Soc. Jpn.*, **79**(11), 2010.

[176] T. J. Liu, J. Hu, B. Qian, D. Fobes, Z. Q. Mao, W. Bao, M. Reehuis, S. A. J. Kimber, K. Prokes, S. Matas, D. N. Argyriou, A. Hiess, A. Rotaru, H. Pham, L. Spinu, Y. Qiu, V. Thampy, A. T. Savici, J. A. Rodriguez, and C. Broholm. *Nature Mater.*, **9**(9):716–720, 2010.

[177] Z. J. Xu, J. S. Wen, G. Y. Xu, Q. Jie, Z. W. Lin, Q. A. Li, S. X. Chi, D. K. Singh, G. D. Gu, and J. M. Tranquada. *Phys. Rev. B*, **82**(10):104525, 2010.

[178] F. Ma, W. Ji, J. Hu, Z.-Y. Lu, and T. Xiang. *Phys. Rev. Lett.*, **102**(17):177003–4, 2009.

[179] F. Wang and D. H. Lee. *Science*, **332**(6026):200–204, 2011.

[180] A. Subedi, L. Zhang, D. J. Singh, and M. H. Du. *Phys. Rev. B*, **78**(13):134514–6, 2008.

[181] Y. Xia, D. Qian, L. Wray, D. Hsieh, G. F. Chen, J. L. Luo, N. L. Wang, and M. Z. Hasan. *Phys. Rev. Lett.*, **103**(3):037002, 2009.

[182] A. Tamai, A. Y. Ganin, E. Rozbicki, J. Bacsa, W. Meevasana, P. D. C. King, M. Caffio, R. Schaub, S. Margadonna, K. Prassides, M. J. Rosseinsky, and F. Baumberger. *Phys. Rev. Lett.*, **104**(9):097002, 2010.

[183] M. D. Johannes and I. I. Mazin. *Phys. Rev. B*, **79**(22):220510, 2009.

[184] A. M. Turner, F. Wang, and A. Vishwanath. *Phys. Rev. B*, **80**(22):224504, 2009.

[185] M. J. Han and S. Y. Savrasov. *Phys. Rev. Lett.*, **103**(6):067001, 2009.

[186] D. Fruchart, P. Convert, P. Wolfers, R. Madar, J. P. Senateur, and R. Fruchart. *Mat. Res. Bull.*, **10**(3):169–174, 1975.

[187] W. Bao, Y. Qiu, Q. Huang, M. A. Green, P. Zajdel, M. R. Fitzsimmons, M. Zhernenkov, S. Chang, M. H. Fang, B. Qian, E. K. Vehstedt, J. H. Yang, H. M. Pham, L. Spinu, and Z. Q. Mao. *Phys. Rev. Lett.*, **102**(24):247001, 2009.

[188] S. Li, Y. Chen, S. Chang, J. W. Lynn, L. Li, Y. Luo, G. Cao, Z. Xu, and P. Dai. *Phys. Rev. B*, **79**(17):174527, 2009.

[189] A. Martinelli, A. Palenzona, M. Tropeano, C. Ferdeghini, M. Putti, M. R. Cimberle, T. D. Nguyen, M. Affronte, and C. Ritter. *Phys. Rev. B*, **81**(9):094115, 2010.

[190] S. J. Blundell. *Contemp. Phys.*, **40**(3):175–192, 1999.

[191] F. J. Litterst, M. Birke, B. Buchner, M. Hillberg, H. H. Klauss, W. Kopmann, H. Micklitz, and W. Wagener. *Aust. J. Phys.*, **51**(2):385–400, 1998.

[192] R. Khasanov, K. Conder, E. Pomjakushina, A. Amato, C. Baines, Z. Bukowski, J. Karpinski, S. Katrych, H. H. Klauss, H. Luetkens, A. Shengelaya, and N. D. Zhigadlo. *Phys. Rev. B*, **78**(22):220510, 2008.

[193] W. Tabiś, J. Kusz, N.-T. H. Kim-Ngan, Z. Tarnawski, F. Zontone, Z. Kakol, and A. Kozłowski. *Rad. Phys. Chem.*, **78**(10, Supplement):S93–S96, 2009.

[194] M. Bendele, S. Weyeneth, R. Puzniak, A. Maisuradze, E. Pomjakushina, K. Conder, V. Pomjakushin, H. Luetkens, S. Katrych, A. Wisniewski, R. Khasanov, and H. Keller. *Phys. Rev. B*, **81**(22):224520, 2010.

[195] A. F. Andresen and J. Leciejewicz. *J. Phys. France*, **25**(5):574–578, 1964.

[196] T. Kamimura. *J. Phys. Soc. Jpn.*, **43**(5):1594–1599, 1977.

[197] J. Wen, G. Xu, Z. Xu, Z. W. Lin, Q. Li, W. Ratcliff, G. Gu, and J. M. Tranquada. *Phys. Rev. B*, **80**(10):104506–4, 2009.

[198] C. Fang, B. A. Bernevig, and J. Hu. *Europhys. Lett.*, **86**(6):67005, 2009.

[199] M. D. Lumsden, A. D. Christianson, E. A. Goremychkin, S. E. Nagler, H. A. Mook, M. B. Stone, D. L. Abernathy, T. Guidi, G. J. MacDougall, C. de la Cruz, A. S. Sefat, M. A. McGuire, B. C. Sales, and D. Mandrus. *Nature Phys.*, **6**:182–6, 2010.

[200] Y. Qiu, W. Bao, Y. Zhao, C. Broholm, V. Stanev, Z. Tesanovic, Y. C. Gasparovic, S. Chang, Jin Hu, Bin Qian, M. H. Fang, and Z. Q. Mao. *Phys. Rev. Lett.*, **103**(6):067008–4, 2009.

[201] D. N. Argyriou, A. Hiess, A. Akbari, I. Eremin, M. M. Korshunov, J. Hu, B. Qian, Z Mao, Y. Qiu, C. Broholm, and W. Bao. *Phys. Rev. B*, **81**(22):220503, 2010.

[202] H. A. Mook, M. D. Lumsden, A. D. Christianson, S. E. Nagler, B. C. Sales, R. Jin, M. A. McGuire, A. S. Sefat, D. Mandrus, T. Egami, and C. dela Cruz. *Phys. Rev. Lett.*, **104**(18):187002, 2010.

[203] S. Iikubo, M. Fujita, S. Niitaka, and H. Takagi. *J. Phys. Soc. Jpn.*, **78**(10):103704, 2009.

[204] A. D. Christianson, E. A. Goremychkin, R. Osborn, S. Rosenkranz, M. D. Lumsden, C. D. Malliakas, I. S. Todorov, H. Claus, D. Y. Chung, M. G. Kanatzidis, R. I. Bewley, and T. Guidi. *Nature*, **456**(7224):930–932, 2008.

[205] M. D. Lumsden, A. D. Christianson, D. Parshall, M. B. Stone, S. E. Nagler, G. J. MacDougall, H. A. Mook, K. Lokshin, T. Egami, D. L. Abernathy, E. A. Goremychkin, R. Osborn, M. A. McGuire, A. S. Sefat, R. Jin, B. C. Sales, and D. Mandrus. *Phys. Rev. Lett.*, **102**(10):107005, 2009.

[206] S. Chi, A. Schneidewind, J. Zhao, L. W. Harriger, L. Li, Y. Luo, G. Cao, Z. Xu, M. Loewenhaupt, J. Hu, and P. Dai. *Phys. Rev. Lett.*, **102**(10):107006, 2009.

[207] D. S. Inosov, J. T. Park, P. Bourges, D. L. Sun, Y. Sidis, A. Schneidewind, K. Hradil, D. Haug, C. T. Lin, B. Keimer, and V. Hinkov. *Nature Phys.*, 2009.

[208] C. Stock, E. E. Rodriguez, M. A. Green, P. Zavalij, and J. A. Rodriguez-Rivera. *Phys. Rev. B*, **84**(4):045124, 2011.

[209] J. R. Schrieffer. *Theory of superconductivity.* Frontiers in physics a lecture note and reprint series. W.A. Benjamin, New York, 1964.

[210] D. K. Pratt, A. Kreyssig, S. Nandi, N. Ni, A. Thaler, M. D. Lumsden, W. Tian, J. L. Zarestky, S. L. Bud'ko, P. C. Canfield, A. I. Goldman, and R. J. McQueeney. *Phys. Rev. B*, **81**(14):140510(R), 2010.

[211] T. Chatterji. *Paramagnetic and critical scattering.* Neutron scattering from magnetic materials. Elsevier, Oxford, 2006.

[212] H. A. Mook, J. W. Lynn, and R. M. Nicklow. *Phys. Rev. Lett.*, **30**(12):556–559, 1973.

[213] J. W. Lynn and H. A. Mook. *Phys. Rev. B*, **23**(1):198–206, 1981.

[214] J. W. Lynn. *Phys. Rev. B*, **11**(7):2624–2637, 1975.

[215] E. E. Rodriguez, C. Stock, P. Y. Hsieh, N. P. Butch, J. Paglione, and M. A. Green. *Chem. Sci.*, **2**(9):1782–1787, 2011.

[216] N. Tsyrulin, R. Viennois, E. Giannini, M. Boehm, M. Jimenez-Ruiz, A. A. Omrami, B. Dalla Piazza, and H. M. Rønnow. *arXiv:1203.4974v1*, 2012.

[217] S. Shamoto, M. Ishikado, A. D. Christianson, M. D. Lumsden, S. Wakimoto, K. Kodama, A. Iyo, and M. Arai. *Phys. Rev. B*, **82**(17):172508, 2010.

[218] A. D. Christianson, M. D. Lumsden, S. E. Nagler, G. J. MacDougall, M. A. McGuire, A. S. Sefat, R. Jin, B. C. Sales, and D. Mandrus. *Phys. Rev. Lett.*, **103**(8):087002, 2009.

[219] M. M. Korshunov and I. Eremin. *Phys. Rev. B*, **78**(14):140509(R), 2008.

[220] T. A. Maier and D. J. Scalapino. *Phys. Rev. B*, **78**(2):020514(R), 2008.

[221] J. S. Wen, G. Y. Xu, Z. J. Xu, Z. W. Lin, Q. Li, Y. Chen, S. X. Chi, G. D. Gu, and J. M. Tranquada. *Phys. Rev. B*, **81**(10):100513(R), 2010.

[222] R. Joynt and T. M. Rice. *Phys. Rev. B*, **38**(4):2345–2353, 1988.

[223] L. W. Harriger, O. J. Lipscombe, C. Zhang, H. Luo, M. Wang, K. Marty, M. Lumsden, and P. Dai. *arXiv:1202.5015v1*, 2012.

[224] W. K. Park, C. R. Hunt, H. Z. Arham, Z. J. Xu, J. S. Wen, Z. W. Lin, Q. Li, G. D. Gu, and L. H. Greene. *arXiv:1005.0190v1*, 2010.

[225] O. J. Lipscombe, L. W. Harriger, P. G. Freeman, M. Enderle, C. Zhang, M. Wang, T. Egami, J. Hu, T. Xiang, M. R. Norman, and P. Dai. *Phys. Rev. B*, **82**(6):064515, 2010.

[226] J. E. Lorenzo, L. P. Regnault, C. Boullier, N. Martin, A. H. Moudden, S. Vanishri, C. Marin, and A. Revcolevschi. *Phys. Rev. Lett.*, **105**(9):097202, 2010.

[227] C. Boullier, L. P. Regnault, J. E. Lorenzo, H. M. Rønnow, U. Ammerahl, G. Dhalenne, and A. Revcolevschi. *Physica B*, **350**(1-3):40–44, 2004.

[228] N. S. Headings, S. M. Hayden, J. Kulda, N. H. Babu, and D. A. Cardwell. *Phys. Rev. B*, **84**(10):104513, 2011.

[229] H. F. Fong, B. Keimer, D. Reznik, D. L. Milius, and I. A. Aksay. *Phys. Rev. B*, **54**(9):6708–6720, 1996.

[230] E. Demler and S. C. Zhang. *Phys. Rev. Lett.*, **75**(22):4126–4129, 1995.

[231] P. C. Dai, H. A. Mook, G. Aeppli, S. M. Hayden, and F. Dogan. *Nature*, **406**(6799):965–968, 2000.

[232] J. M. Tranquada, C. H. Lee, K. Yamada, Y. S. Lee, L. P. Regnault, and H. M. Rønnow. *Phys. Rev. B*, **69**(17):174507, 2004.

[233] S. L. Li, X. Y. Lu, M. Wang, H. Q. Luo, M. Y. Wang, C. L. Zhang, E. Faulhaber, L. P. Regnault, D. Singh, and P. C. Dai. *Phys. Rev. B*, **84**(2):024518, 2011.

[234] J. Zhao, L.-P. Regnault, C. Zhang, M. Wang, Z. Li, F. Zhou, Z. Zhao, C. Fang, J. Hu, and P. Dai. *Phys. Rev. B*, **81**(18):180505, 2010.

[235] N. Qureshi, P. Steffens, S. Wurmehl, S. Aswartham, B. Büchner, and M. Braden. *arXiv:1201.2332v1*, 2012.

[236] P. Böni, B. J. Sternlieb, G. Shirane, B. Roessli, J. E. Lorenzo, and S. A. Werner. *Phys. Rev. B*, **57**(2):1057–1065, 1998.

[237] D. Prabhakaran and A. T. Boothroyd. *J. Cryst. Growth*, **250**(1-2):77–82, 2003.

[238] B. Ouladdiaf, J. Archer, G. J. McIntyre, A. W. Hewat, D. Brau, and S. York. *Physica B*, **385-86**:1052–1054, 2006.

[239] J. Laugier and A. Filhol. *J. Appl. Crystallogr.*, **16**:281, 1983.

[240] M. O'Keeffe and F. S. Stone. *J. Phys. Chem. Solids*, **23**(Mar):261, 1962.

[241] X. G. Zheng, C. N. Xu, E. Tanaka, Y. Tomokiyo, H. Yamada, Y. Soejima, Y. Yamamura, and T. Tsuji. *J. Phys. Soc. Jpn.*, **70**(4):1054–1063, 2001.

[242] V. N. Duginov, V. G. Grebinnik, K. I. Gritsaj, T. N. Mamedov, V. G. Olshevsky, V. Yu Pomjakushin, V. A. Zhukov, B. F. Kirillov, I. A. Krivosheev, A. V. Pirogov, and A. N. Ponomarev. *Hyperfine Interactions*, **85**(1):317–322, 1994.

[243] T. Shimizu, T. Matsumoto, A. Goto, T. V. C. Rao, K. Yoshimura, and K. Kosuge. *Phys. Rev. B*, **68**(22), 2003.

[244] B. X. Yang, T. R. Thurston, J. M. Tranquada, and G. Shirane. *Phys. Rev. B*, **39**(7):4343–4349, 1989.

[245] J. B. Forsyth, P. J. Brown, and B. M. Wanklyn. *J. Phys. C*, **21**(15):2917–2929, 1988.

[246] T. Chattopadhyay, G. J. Mcintyre, P. J. Brown, and J. B. Forsyth. *Physica C*, **170**(5-6):371–374, 1990.

[247] T. Chattopadhyay, G. J. Mcintyre, C. Vettier, P. J. Brown, and J. B. Forsyth. *Physica B*, **180**:420–422, 1992.

[248] P. W. Anderson. volume 1. Academic Press, New York, 1964.

[249] S. B. Ota and E. Gmelin. *Phys. Rev. B*, **46**(18):11632–11635, 1992.

[250] F. Wang, T. Zou, Y. Liu, L. Q. Yan, and Y. Sun. *J. Appl. Phys.*, **110**(5):054106, 2011.

[251] K. Taniguchi, N. Abe, T. Takenobu, Y. Iwasa, and T. Arima. *Phys. Rev. Lett.*, **97**(9):097203, 2006.

[252] F. Ye, R. S. Fishman, J. A. Fernandez-Baca, A. A. Podlesnyak, G. Ehlers, H. A. Mook, Y. Q. Wang, B. Lorenz, and C. W. Chu. *Phys. Rev. B*, **84**(17):179901, 2011.

[253] G. Giovannetti, S. Kumar, A. Stroppa, J. van den Brink, S. Picozzi, and J. Lorenzana. *Phys. Rev. Lett.*, **106**(2):026401, 2011.

[254] D. L. Fox, D. R. Tilley, J. F. Scott, and H. J. Guggenheim. *Phys. Rev. B*, **21**(7):2926–2936, 1980.

[255] Y. Yasui, Y. Naito, K. Sato, T. Moyoshi, M. Sato, and K. Kakurai. *J. Phys. Soc. Jpn.*, **77**(2):023712, 2008.

[256] M. Kenzelmann, G. Lawes, A. B. Harris, G. Gasparovic, C. Broholm, A. P. Ramirez, G. A. Jorge, M. Jaime, S. Park, Q. Huang, A. Y. Shapiro, and L. A. Demianets. *Phys. Rev. Lett.*, **98**(26):267205, 2007.

[257] G. Jin, K. Cao, G.-C. Guo, and L. He. *Phys. Rev. Lett.*, **108**(18):187205, 2012.

[258] W. B. Wu, D. J. Huang, J. Okamoto, S. W. Huang, Y. Sekio, T. Kimura, and C. T. Chen. *Phys. Rev. B*, **81**(17):172409, 2010.

[259] D. Senff, P. Link, N. Aliouane, D. N. Argyriou, and M. Braden. *Phys. Rev. B*, **77**(17):174419, 2008.

[260] K. Taniguchi, N. Abe, S. Ohtani, and T. Arima. *Phys. Rev. Lett.*, **102**(14):147201, 2009.

[261] S. Mitsuda, T. Nakajima, M. Yamano, K. Takahashi, H. Yamazaki, K. Masuda, Y. Kaneko, N. Terada, K. Prokes, and K. Kiefer. *Physica B*, **404**(17):2532–2534, 2009.

[262] G. Y. Xu, J. S. Wen, C. Stock, and P. M. Gehring. *Nature Mater.*, **7**(7):562–566, 2008.

[263] B. N. Brockhouse. *Phys. Rev.*, **94**(3):A781, 1954.

[264] P. J. Brown, T. Chattopadhyay, J. B. Forsyth, V. Nunez, and F. Tasset. *J. Phys.: Condens. Matter*, **3**(23):4281–4287, 1991.

[265] M. Aïn, A. Menelle, B. M. Wanklyn, and E. F. Bertaut. *J. Phys.: Condens. Matter*, **4**(23):5327–5337, 1992.

[266] B. X. Yang, J. M. Tranquada, and G. Shirane. *Phys. Rev. B*, **38**(1):174–178, 1988.

[267] H. Yamada, X. G. Zheng, Y. Soejima, and M. Kawaminami. *Phys. Rev. B*, **69**(10):104104, 2004.

[268] P. Babkevich, A. Poole, R. D. Johnson, B. Roessli, D. Prabhakaran, and A. T. Boothroyd. *Phys. Rev. B*, **85**(13):134428, 2012.

[269] I. Cabrera, M. Kenzelmann, G. Lawes, Y. Chen, W. C. Chen, R. Erwin, T. R. Gentile, J. B. Leao, J. W. Lynn, N. Rogado, R. J. Cava, and C. Broholm. *Phys. Rev. Lett.*, **103**(8):087201, 2009.

[270] A. Poole, P. J. Brown, and A. S. Wills. *J. Phys.: Conf. Ser.*, **145**, 2009.

[271] S. Seki, Y. Yamasaki, M. Soda, M. Matsuura, K. Hirota, and Y. Tokura. *Phys. Rev. Lett.*, **100**(12):127201, 2008.

[272] Y. Yamasaki, H. Sagayama, T. Goto, M. Matsuura, K. Hirota, T. Arima, and Y. Tokura. *Phys. Rev. Lett.*, **98**(21):147204, 2007.

[273] P. Toledano, N. Leo, D. D. Khalyavin, L. C. Chapon, T. Hoffmann, D. Meier, and M. Fiebig. *Phys. Rev. Lett.*, **106**(25), 2011.

[274] R. D. Johnson, Sunil Nair, L. C. Chapon, A. Bombardi, C. Vecchini, D. Prabhakaran, A. T. Boothroyd, and P. G. Radaelli. *Phys. Rev. Lett.*, **107**(13):137205, 2011.

[275] M. Mostovoy. *Phys. Rev. Lett.*, **96**(6), 2006.

[276] Y.J. Um, A. Subedi, P. Toulemonde, A. Y. Ganin, L. Boeri, M. Rahlenbeck, Y. Liu, C. T. Lin, S.J.E. Carlsson, A. Sulpice, M. J. Rosseinsky, B. Keimer, and M. Le Tacon. *arXiv:1202.0375v2*, 2012.